THE UNIVERSITY
OF MICHIGAN
MAR 16 1960
ENGINEERING
LIBRARY

JOURNAL OF FLUID MECHANICS

VOLUME 7 PART 2

FEBRUARY 1960

PUBLISHED BY

CAMBRIDGE UNIVERSITY PRESS

BENTLEY HOUSE, 200 EUSTON ROAD, LONDON, N.W.1

AMERICAN BRANCH: 32 EAST 57TH STREET, NEW YORK 22, N.Y.

Price 30*s.* (*U.S.A.* $5.00)

The JOURNAL OF FLUID MECHANICS exists for the publication of theoretical and experimental investigations of all aspects of the mechanics of fluids, and is issued in four parts per volume.

EDITOR

DR G. K. BATCHELOR

Department of Applied Mathematics and Theoretical Physics, University of Cambridge, Free School Lane, Cambridge, England

ASSISTANT EDITORS

DR T. B. BENJAMIN, DR I. PROUDMAN, DR P. G. SAFFMAN

Department of Applied Mathematics and Theoretical Physics, University of Cambridge, Free School Lane, Cambridge, England

ASSOCIATE EDITORS

PROF. G. F. CARRIER

Pierce Hall, Harvard University, Cambridge 38, *Massachusetts, U.S.A.*

DR W. C. GRIFFITH

Research and Development Laboratory, Missile Systems Division, Lockheed Aircraft Corporation, Palo Alto, California, U.S.A.

M. J. LIGHTHILL

Royal Aircraft Establishment, Farnborough, Hampshire, England

PROF. R. R. LONG

School of Engineering, The Johns Hopkins University, Baltimore 18, *Maryland, U.S.A.*

Authors wishing to have papers published in the JOURNAL should communicate them to any one of the persons named above, choosing one in their own country where possible.

Authors are urged to ensure that their papers are written clearly and attractively, in order that their work will be readily accessible to readers.

Manuscripts should be typed in double spacing on one side of the paper only, with references listed at the end in alphabetical order of authors. Drawings should be done on a large scale in Indian ink on tracing cloth or drawing paper, the lettering being shown clearly in pencil for reproduction by the printer; the list of captions should be typed at the end of the manuscript. Proofs of papers from overseas will usually be despatched to authors by airmail. There is no charge for publication. Authors are entitled to receive 50 offprints of a paper in the JOURNAL free of charge, and additional offprints can be purchased if ordered in advance.

SUBSCRIPTIONS

The subscription price for a volume of four parts is £5. 10*s*. net, post free, payable in advance; separate parts 30*s*. net, plus postage. Subscriptions may be sent to any bookseller, or to the Cambridge University Press, Bentley House, 200 Euston Road, London, N.W. 1.

Subscribers in the United States should send their orders to the Cambridge University Press, American Branch, 32 East 57th Street, New York 22. The subscription price per volume is $18.50, post free, payable in advance; separate parts $5.00, plus postage.

Quotations for available back volumes and parts may be obtained on application to the Cambridge University Press.

Behaviour of small regions of different gases carried in accelerated gas flows

By GEORGE RUDINGER AND LOWELL M. SOMERS
Cornell Aeronautical Laboratory, Buffalo, New York

(Received 2 April 1959)

Small regions in a flow where the density is different from that of the surrounding gas do not exactly follow accelerated motions of the latter, but move faster or slower depending on whether their density is smaller or larger than that of the main flow. This behaviour cannot be quantitatively explained by treating a gas 'bubble' as a hypothetical solid particle of the same density, because a gas bubble cannot move relative to the surrounding gas without being transformed into a vortex which absorbs part of the energy of the relative motion.

To illustrate the acceleration effect, the flow velocity behind known pressure waves in a shock tube is compared with the observed velocity of a bubble produced by a spark discharge. The displacement of such a bubble by a wave exceeds that of a flow element by more than 20 %, but the bubble density is not known. If the spark discharge is replaced by a small jet of another gas, a pressure wave cuts off a section of this jet which then represents a bubble of known density.

A theory is developed which permits computing the response of such bubbles to accelerations. The ratio of the bubble velocity to the velocity of the surrounding gas depends on the density ratio for the two gases and on the shape of the bubble, but not on the acceleration. Experimental results with H_2, He, and SF_6 bubbles in air, accelerated by shock waves of various strength, are presented and agree well with the theoretical predictions. The results apply regardless of whether accelerations are produced by pressure waves in a non-steady flow or by curvature of streamlines in a steady flow. Various aspects of the experimental observations are discussed.

1. Introduction

The technique of using tracers for the visualization of streamlines in a gas flow, or for the measurement of flow velocity, is well established. It is also known that such tracers do not move exactly with the flow if their density is different from that of the surrounding gas and if they have to undergo accelerated motions. The behaviour of solid particles under such conditions was described in considerable detail, for instance, by Wright (1951), Cady (1954), and Hoenig (1957). While such particles always lag in accelerated flows, gaseous particles ('bubbles') may lead or lag depending on whether their density is smaller or larger than that of the surrounding gas. The behaviour of gas bubbles in accelerated flows is, however, different from that of a hypothetical solid particle of the same density, because a gas bubble cannot move relative to the surrounding gas without being trans-

formed into a vortex which absorbs part of the energy of the relative motion. This effect appears to have received little attention, although its understanding is important not only when gas bubbles are used as tracers but also for other phenomena. For example, if pressure waves interact with a flame, the different responses of the regions of different density lead to a deformation of the flame front; this modifies the rate of heat release, and causes secondary waves to be emitted by the flame. Such waves were observed, for instance, by Markstein (1957), and the theoretical and experimental aspects of such interactions were reviewed by Rudinger (1958).

Gaseous tracer bubbles can be produced by various methods, and such techniques, developed mainly for the measurement of constant flow velocities, were reviewed by Cady (1954). A method to measure not only velocities but also velocity distributions is due to Townend (1937), who discharged straight sparks between two electrodes and determined the subsequent motion and deformation of the spark columns. A spark column, consisting of hot gas, can be observed by means of a schlieren system. In an alternative method, a number of sparks, discharged in rapid succession, can be photographed directly. In the latter method, each spark tends to follow the ionized path of the preceding one, and, since the spark columns are carried with the flow, their displacements and deformations indicate the local flow velocity. This multiple-spark technique has also been studied by Saheki (1947), and by Bomelburg (1956), Herzog (1957), Herzog & Weske (1957), and Weske (1958). The errors made by neglecting the response of the spark column in accelerated flows are not negligible, and Herzog & Weske (1957) propose a semi-empirical method of correction.

In §§ 2 and 3, shock-tube experiments are described in which the flow velocities, produced by pressure waves of known properties, are compared with the velocities of spark-heated bubbles to illustrate the large errors that may result if such bubbles are used as tracers in a flow. Since the effective density of a spark-column is not known, a new technique for producing bubbles of known density is described in § 4, and a theory of wave interaction with such bubbles is derived in § 5. The theoretical and experimental results are compared and discussed in § 6.

2. Apparatus for spark experiments

The response of gas bubbles to accelerations is conveniently studied by means of a shock tube. In the first experiments, bubbles are produced by an electric spark discharge, and their motion is observed with the aid of a schlieren system.

A vertical shock tube is used for these experiments. It has a square cross-section of 3 in. width and a total length of about 9 ft. The diaphragm is located 3 ft. from the top, and the last 9 in. from the bottom represent the test section which is provided with two glass walls for the schlieren observations. To produce shock or expansion waves of desired strength, the initial pressure in the test section is always atmospheric and the pressure in the driver section is raised or lowered as needed. One or more layers of photographic film are used as diaphragms and are punctured by a solenoid-operated plunger needle. Details of the construction of the shock tube have been published elsewhere (Markstein 1957).

A spark gap is formed between one wall of the test section and the point of a steel needle, introduced through the opposite wall. The spark is produced by charging a 1μF condenser to 400 V and then discharging it through an automobile spark coil in series with a 3 D 22 thyratron. The latter acts as a switch for proper timing control. In agreement with observations by previous investigators (Townend 1937, Saheki 1947 and Bomelburg 1956), reproducible straight sparks can be obtained if the needle electrode is negative and if the gap does not exceed about $\frac{3}{8}$ in. To assure that the spark is discharged at right angles to the shock-tube wall, the latter is covered with an insulating sheet (photographic film) with a pin hole opposite the needle. The spark-heated column of air is clearly visible on schlieren photographs obtained with a short-duration spark light source.

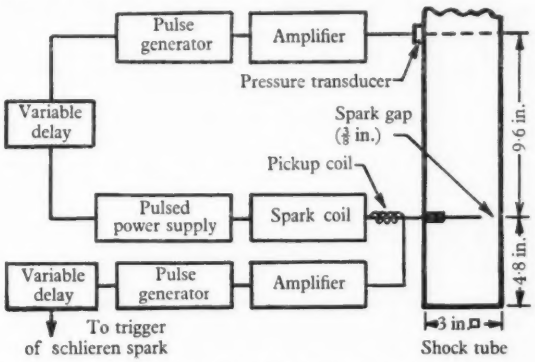

FIGURE 1. Schematic arrangement of shock tube and instrumentation for spark experiments.

The experimental set-up is shown schematically in figure 1. Proper timing of the spark discharge and of the schlieren spark is achieved by means of two variable-time delays. A pressure transducer is mounted near the top of the test section, so that the amplified signal from a pressure wave propagating down the tube triggers a thyratron several hundred microseconds before the wave reaches the spark gap. The thyratron circuit produces a single pulse which, in turn, triggers the spark discharge after a desired delay. A pick-up coil, consisting of a few turns of wire wrapped around the high-tension lead of the spark, produces a signal which, through a second thyratron pulse generator and the second delay unit, triggers the schlieren spark.

3. Measurements of flow velocity behind pressure waves

In the first series of experiments, the displacement of the spark column in the wake of a weak shock wave is measured as a function of time and compared with the corresponding displacement of an element in the surrounding gas. The spark is discharged shortly before the arrival of the wave at the spark gap, and a schlieren photograph is taken after some interval. Figure 2*a*, plate 1, shows a typical record.

Such photographs can be evaluated with reference to the wave diagram in figure 3*a* which shows the motion of the shock wave, the spark column, and

a corresponding gas element. Let x_S be the distance of the shock wave from the spark gap at the time the schlieren photograph is taken. If this distance is plotted as a function of the delay setting for the schlieren spark, one obtains a straight line which intercepts the line $x_S = 0$ at the instant that the shock wave passes the spark gap. Let Δt be the time interval in which the wave has travelled the distance x_S. These data determine the shock velocity and, together with the initial speed of sound in the test section a_0, the shock Mach number M_S. For the weak shocks used in these experiments, the results agree well with calculated data based on the theory of an ideal shock tube.

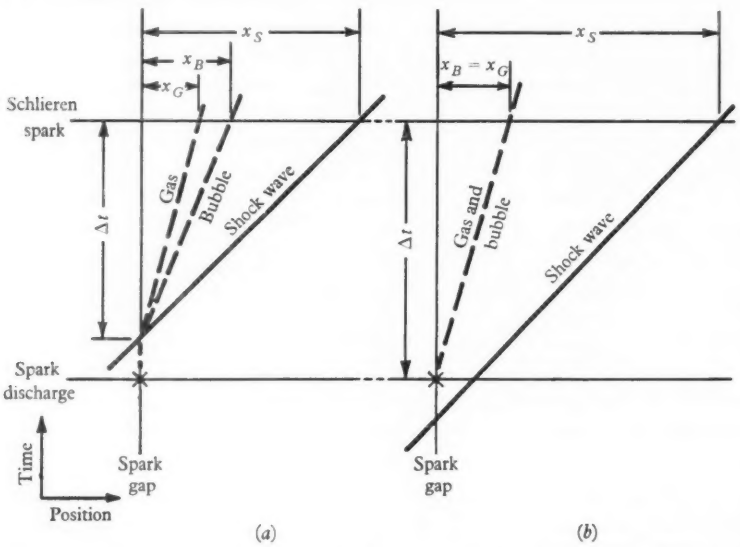

FIGURE 3. Wave diagrams for spark experiments with the spark discharged: (*a*) before, and (*b*) after, passage of a shock wave.

The spark bubble remains at rest until the shock wave arrives; it then travels the distance x_B during the time Δt. During the same time, a gas element that initially was located at the spark gap travels the distance x_G. If the flow were accurately represented by the bubble motion, the ratio of the two displacements should be unity. Since $\Delta t = x_G/u_G = x_S/(a_0 M_S)$, where u_G is the flow velocity of the gas, the actual displacement ratio is given by

$$\frac{x_B}{x_G} = \frac{x_B}{x_S}\frac{a_0 M_S}{u_G}. \tag{1}$$

The first factor on the right-hand side of this equation can be obtained directly from the schlieren photographs, and the second factor varies only with M_S, since u_G is related to M_S and a_0 by

$$u_G = \frac{2}{\gamma+1} a_0 \left(M_S - \frac{1}{M_S}\right), \tag{2}$$

where γ is the ratio of the specific heats. The displacement ratios observed for shock Mach numbers of about 1·12, 1·22 and 1·28, corresponding to shock-pressure ratios of 1·29, 1·58 and 1·74, respectively, are plotted in figure 4. This plot indicates that the velocity of a spark-heated bubble immediately after interaction with a shock wave is about 60 % higher than the flow velocity. Subsequently, the bubble velocity decreases and gradually approaches the flow velocity. In spite of the scatter of the data, the uncertainty of the measured bubble displacements is considerably smaller than the deviation of the displacement ratio from unity, as can be seen in figure 2*a*, plate 1, where the value of x_G is also indicated.

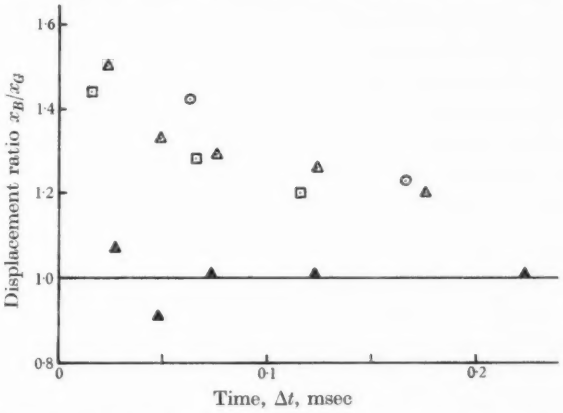

FIGURE 4. Displacement ratios of spark bubbles for shock waves of various strength as a function of the travel time of the bubbles. Spark is discharged either before (open symbols) or after (filled symbols) passage of the shock wave. Shock pressure ratio: ⊙, 1·29; △, ▲, 1·58; □, 1·74.

To verify that the observed deviations of the displacement ratio from unity are caused by the interaction of the shock wave with the spark volume, the bubble displacement is also determined in experiments in which the spark is discharged after the shock wave has passed the spark gap. A typical schlieren photograph is shown in figure 2*b*, plate 1, and the wave diagram corresponding to these experiments is given in figure 3*b*. The travel time of the bubble Δt is determined by the setting of the second delay unit (see figure 1), but a correction must be applied because of unavoidable fixed delays in the spark circuits. This correction is obtained by plotting x_B as a function of the delay setting and extrapolating to $x_B = 0$. The displacement ratio x_B/x_G is then obtained from the measured value of x_B and from $x_G = u_G \Delta t$. The results are indicated in figure 4 by the filled-in symbols and verify that the bubble moves with the flow as long as accelerations are absent.

From the data presented in figure 4, it appears that the excess bubble velocity depends only little, if at all, on the strength of the shock wave. Although the shock accelerations are extremely high, the shock Mach number is varied over a small range only. The effect of accelerations of a different order of magnitude can be studied by experiments in which the spark column is accelerated by an

expansion wave. Such waves are produced by partially evacuating the driver section of the shock tube, and their properties can be determined from oscilloscope records of the pressure variations at the location of the pressure transducer (see figure 1). The expansion wave is reflected from the closed end of the shock tube and leaves a region of reduced density and zero velocity. If the spark is discharged before arrival of the wave and the schlieren photograph taken after passage of the reflected wave, the bubble displacement x_B is readily compared with the corresponding displacement of a gas element x_G. To test for proper timing of the events, the starting pulse from the second time-delay (see figure 1) is also used to produce a signal on a second channel of the oscilloscope to mark the instant of the spark discharge. The instant of the schlieren spark is similarly indicated on the pressure record. Figure 5, plate 1, shows a schlieren photograph with the corresponding oscilloscope record, where it can be seen that the spark is discharged before the pressure starts to decrease, and that the photograph is taken after the pressure again has become steady. The interval between the spark discharge and the taking of the photograph is about 4·5 msec. A spark column of this 'age' no longer appears as a straight line but as a bubble of irregular shape. The mean of the maximum and minimum distances of the bubble boundaries from the spark gap is, therefore, taken as x_B.

During the passage of the incident and reflected expansion waves, the density decreases from ρ_0 to ρ_∞, and this change can be computed from the corresponding pressure change since the flow is isentropic. Let L be the distance of the spark gap from the closed end of the shock tube. The value of x_G is then related to the densities and pressures by

$$\frac{x_G + L}{L} = \frac{\rho_0}{\rho_\infty} = \left(\frac{p_0}{p_\infty}\right)^{1/\gamma}. \tag{3}$$

The pressure ratio p_∞/p_0 for these experiments is in the neighbourhood of 0·7. For the record in figure 5, plate 1, $p_\infty/p_0 = 0{\cdot}66$, and the value of x_G computed from equation (3) is indicated in the figure. Because of the uncertainty of x_B, the displacement ratios scatter considerably, and the observed values range from about 1·15 to 1·25. Since gradual cooling of the bubble during its acceleration and deceleration by the waves tends to reduce the excess displacement, these values seem sufficiently close to those observed for shock accelerations (figure 4) to support the previous conjecture that the displacement ratio is independent of the applied acceleration.

4. Experiments with bubbles of known density

The experiments described above give a good indication of how pressure waves interact with bubbles the density of which is different from that of the surrounding gas, but the experimental results cannot be used to check a theoretical analysis because the density of a spark-heated bubble is not known. A technique was developed, therefore, to produce bubbles of known density.

At first, soap bubbles filled with various gases were tried, but this approach was soon abandoned. The displacement of large bubbles amounts to only a few bubble diameters and cannot be measured accurately because of changes of bubble shape.

For small bubbles, the mass of the soap film represents a significant fraction of the total mass, so that the bubble density becomes uncertain.

In the technique finally adopted, a fine jet of some gas, discharged across the shock tube, represents a 'bubble' of known density. For this purpose, the needle electrode of the spark gap is replaced by a piece of hypodermic tubing of 0·033 in. internal diameter. A second tube of about 0·25 in. diameter is mounted in the opposite wall of the test section to receive the jet discharged by the fine tube. The larger tube is connected to an aspirator pump to remove the jet flow before it can contaminate the air in the test section. The gap between the two tubes is about 0·3 in. so that a passing shock wave cuts off this exposed length of the jet. The motion of this jet element can then be observed with the aid of a schlieren system.

Figure 6, plate 2, shows four schlieren photographs obtained by this technique for a shock-pressure ratio of about 1·3. The gases used are hydrogen, helium, and sulphurhexafluoride. Such records can be evaluated by the procedure already described in connexion with the spark experiments, and the values of x_G corresponding to the experimental conditions are marked in the figure. It is seen that the displacements of the bubbles are larger than x_G for the light gases H_2 and He, and smaller for the heavy gas SF_6.

One interesting feature of these photographs is that all bubbles are inclined although the jet is discharged horizontally. This phenomenon is readily explained. The pure gas that leaves the jet tube mixes with air as it advances across the test section. Consequently, the effective density of the bubble changes continuously from that of the pure gas to that of a mixture of this gas with air. The bubble end nearest the jet tube, therefore, travels faster than the other end for H_2 and He, and slower for SF_6. Because of the rapid deterioration of the SF_6 bubble, which is discussed in § 6, the inclination of this bubble is clearly visible only on photographs taken early enough after passage of the shock wave (lower right picture of figure 6, plate 2).

The extent to which the jet mixes with air, and therefore the inclination of the bubble, depends on the diffusion rate and on the jet velocity which controls the time available for mixing. No attempt was made to keep the jet velocity the same for all gases, and the photographs indicate that the velocity of the H_2 jet was considerably higher than that of the He jet, because the He bubble is more inclined than the H_2 bubble in spite of the 10 % larger diffusion coefficient for H_2-air as compared to He-air (Hirschfelder, Curtis & Bird 1954).

In view of the foregoing discussion, all bubble displacements must be measured on the side of the bubble nearest to the jet tube. Experimental results obtained with the described technique are discussed in § 6.

5. Theory of wave interaction with gas bubbles

For an observer moving with the gas, the acceleration by a wave is equivalent to that of a gravitational field. In this field, two forces act on a bubble in the gas, namely, its weight in the equivalent gravitational field and a buoyancy force equal to the corresponding weight of the gas displaced by the bubble. Those two forces act in opposite directions and are of equal magnitude only if the density of the bubble is the same as that of the surrounding gas. If the bubble moves because the

resultant force is not zero, its surface becomes a sheet of vorticity. Subsequently, this sheet rolls up with the result that the entire bubble is transformed into a vortex. The effect of this transformation corresponds to a drag on the translational bubble motion relative to the gas which must supply the energy absorbed by the vortex flow.

Vortex formation is not readily apparent in the described experiments because the bubbles are too small to reveal sufficient details of the flow, although figures 2*a* and *b*, plate 1, indicate the more 'turbulent' character of a bubble that has undergone interaction with a shock wave as compared to the smooth surface of a bubble that has not interacted. The development of a vortex can be clearly seen in figure 7, plate 3, which shows three stages of the interaction of a shock wave with a flame bubble. These schlieren photographs are taken from a series obtained by Markstein (1958) in the course of another investigation. A combustible mixture in the test section of the shock tube is ignited by a spark between the electrodes, visible at the centre of each photograph, and a bubble of burned gas is contained within the flame front. The latter advances so slowly that its progress during the time of interest here is unimportant. The first photograph shows the approximate spherical flame bubble just before interaction with a downward-travelling shock wave. The second photograph shows the wave emerging from the bubble and also a reflected wave. In the third photograph, the waves have moved away from the bubble which has now, clearly, been transformed into a vortex ring.

The following analysis by-passes a detailed study of this vortex formation and yields the final translational velocity of the bubble directly on the basis of a few plausible assumptions. Consider, first, accelerations by shock waves. The time during which a shock wave passes through the bubble, i.e. the time during which acceleration takes place, is so short that the vortex must essentially be formed in a second, subsequent stage. This view is supported by figure 7, plate 3, where no indication of vortex formation can be seen at the time when the shock wave has left the bubble. The analysis will, therefore, proceed in two steps, corresponding to the initial acceleration of the bubble and to its subsequent transformation into a vortex. Later, it will be shown that, within the accuracy of the assumptions made, the same two-step analysis may also be applied to waves, other than shock waves, for which acceleration and vortex formation take place simultaneously.

During the acceleration stage, the bubble distortion may be ignored (centre of figure 7, plate 3), and it seems permissible to treat the initial phase of the motion in the following way. Let the subscript P identify the quantities associated with the bubble motion immediately following the passage of the shock, and let the subscript G identify the quantities associated with the ambient gas particles. Assuming that one may neglect the modification of the pressure field caused by the presence of the bubble, the impulse per unit volume I which the bubble experiences during the shock passage is precisely that which the ambient gas would have experienced, namely, $I = \rho_G u_G$, where u_G is the gas velocity after the shock has passed.

This impulse must accelerate the bubble from rest to the speed u_P and must also accelerate some of the surrounding gas from the speed u_G to a velocity distribution associated with the motion of the bubble. Since the latter is not

distorted during this early phase, the bubble may be treated as if it were a solid particle. One may thus invoke the well-known concept of 'apparent additional mass' (virtual mass) for such a situation and obtain

$$I = \rho_G u_G = \rho_P u_P + k\rho_G(u_P - u_G), \tag{4}$$

with k as the apparent additional mass fraction (i.e. inertia coefficient). For a spherical bubble, $k = 0{\cdot}5$, and for a long circular cylinder moving at right angles to its axis, $k = 1{\cdot}0$ (Lamb 1945, p. 155). Equation (4) yields directly

$$u_P = \frac{1+k}{\sigma+k} u_G, \tag{5}$$

where

$$\sigma = \frac{\rho_P}{\rho_G} = \frac{\rho_B}{\rho_G} \tag{6}$$

is the density ratio. For real solid particles, such as are customarily used for flow visualization, σ is of the order of 1000, so that u_P is practically zero. For σ less than unity, the particle velocity exceeds that of the gas. The foregoing part of the analysis is closely related to calculations described by Birkhoff & Caywood (1949) who considered accelerated motions of gas bubbles in a liquid.

The second step of the analysis deals with the transformation of a gas bubble into a vortex as a result of the initial motion relative to the surrounding gas. Since the kinetic energy of the initial motion must supply the energy absorbed by the vortex, the relative velocity is reduced from $u_P - u_G$ to $u_B - u_G$, where u_B is the desired final bubble velocity. Let the ratio of these relative velocities be denoted by β, so that

$$u_B - u_G = \beta(u_P - u_G). \tag{7}$$

The quantity β^2 thus represents the fraction of the kinetic energy of the initial relative bubble motion that is available for the final relative translational motion. Substitution of equation (5) into equation (7) yields the final bubble velocity relative to the duct as

$$u_B = \left(1 + \beta \frac{1-\sigma}{\sigma+k}\right) u_G, \tag{8}$$

where β is yet to be determined.

Figure 7, plate 3, indicates that a spherical bubble is transformed into a vortex ring, and it seems plausible that an infinitely long cylindrical bubble would become a linear vortex pair. These two cases can be treated theoretically, and the bubble motions observed in the described experiments should then fall between those corresponding to these extremes.

The calculations for a vortex ring are based on a study by Taylor (1953). He considers a flat circular disk that is suddenly set in motion along the axis of symmetry, in a perfect fluid, and without separation of the flow. If the material of the disk were then suddenly 'dissolved away', the flow could also be considered as being caused by a distribution of vortex lines over the plane of the disk. The strongest vortex lines near the edge of the disk tend to roll up the weaker ones until, finally, a vortex ring remains for which it is assumed that the vorticity is uniformly distributed over a core of small diameter compared to the diameter of the ring. Such a vortex cannot remain at rest in the surrounding gas, but moves with a velocity that depends on its dimensions and strength. To apply Taylor's

results to the present problem, the assumption is made that this vortex ring represents a reasonable approximation of the vortex into which a spherical gas bubble is transformed, provided the initial velocity of the bubble is equal to that of the disk. Taylor derives the ratio of the velocity of the vortex relative to the fluid to the initial velocity of the disk. This ratio has been defined here as β, and Taylor's results is $\beta = 0{\cdot}436$.

If the circular disk in Taylor's analysis is replaced by an infinite lamina, a linear vortex pair is formed which, by analogy with the preceding case, is considered to be an approximation to the vortex into which a cylindrical bubble is transformed. This analysis is presented in the Appendix and yields $\beta = 0{\cdot}203$.

The foregoing treatment gives no indication of the time required for the vortex to form, but figure 7, plate 3, shows that the vortex is fully developed before the bubble has travelled one bubble diameter. Since the displacements of interest have a magnitude of many such diameters (see figure 6, plate 2), it may be assumed that the vortex motion is instantaneously established. As a consequence of this assumption, equation (8) may be applied also to waves other than shock waves. Such waves can always be approximated as closely as desired by a sequence of discontinuous wave elements for each of which the ratio of the velocity increments $\Delta u_B/\Delta u_G$ has the same value. If the two steps of the analysis were applied to each element consecutively, the final result would thus be the same as if the analysis had been applied to the entire wave, provided only that the bubble density is not significantly changed by diffusion during the time of wave interaction with the bubble.

Two possible sources of error in the analysis should be discussed. Buoyancy of a bubble in the gravitational field of the earth causes a bubble motion that is superposed on the motion produced by a wave. Although the acceleration of this motion is several orders of magnitude smaller than the wave acceleration, it acts during the entire experiment while the wave acts only during its passage across the bubble. For the conditions of the present experiments, it is readily verified that this effect is utterly negligible if the travel time of the bubble is less than 1 msec, and even for travel times of 5 msec, as in the experiments with the expansion waves (figure 5, plate 1), the displacement caused by gravity alone is less than 3 % of the total bubble displacement.

The other effect to be considered is related to differences in compressibility of the two gases involved. In the derivation of equation (8), it has been implied that the density ratio remains constant during the acceleration of the bubble. This condition is satisfied only if the gases have the same compressibility. If the compressibilities are not equal, the density ratio changes during passage of the wave from σ_0 to σ_∞, which is given by

$$\sigma_\infty = \sigma_0 \left(\frac{p_\infty}{p_0}\right)^{(1/\gamma_B)-(1/\gamma_G)}, \tag{9}$$

where p_∞/p_0 is the pressure ratio across the wave. The relation for isentropic changes of state may be used because only weak waves are considered here. Since an effective value of the density ratio must lie between σ_0 and σ_∞, the influence of this uncertainty of σ on u_B in equation (8) is less than 0·5 % for the conditions of

the reported experiments ($p_\infty/p_0 < 2$, $\gamma_G = 1{\cdot}40$ for air, $\gamma_B = 1{\cdot}10$ for SF_6, and $\gamma_B = 1{\cdot}67$ for He).

In the described experiments, the ratio of bubble length to its diameter is about 9. If this shape is considered as an elongated ellipsoid of revolution, the inertia coefficient (Lamb 1945, p. 155) is approximately 0·94. In view of the uncertainty of the effective shape of the bubbles, the value $k = 1{\cdot}0$, corresponding to an infinite cylinder, is used. The effect on u_B of such a variation of k in equation (8) is unimportant.

			u_B/u_G	
Gas	σ	u_P/u_G	Vortex ring	Vortex pair
H_2	0·0695	1·87	1·38	1·18
He	0·138	1·76	1·33	1·15
SF_6	5·03	0·33	0·71	0·86

TABLE 1. Theoretical results

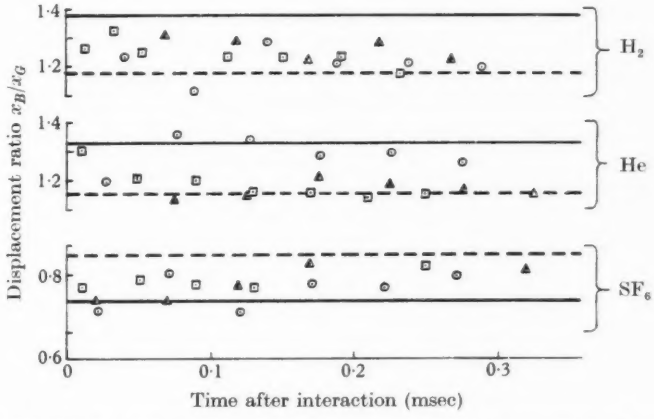

FIGURE 8. Observed and theoretical displacement ratios for the interaction of shock waves with gas bubbles of different densities (see also Table 1). ——, Vortex ring; – – –, vortex pair. Shock pressure ratio: ⊙, 1·29; △, 1·58; ⊡, 1·74.

Experimental results should lie between the values predicted by equation (8) for the two values of β, corresponding to a vortex ring and a linear vortex pair, respectively. For the gases used, the initial and final velocity ratios, u_P/u_G and u_B/u_G, as computed from equations (5) and (8), are collected in table 1.

Figure 8 shows the theoretical and experimental displacement ratios plotted as a function of the time elapsed after interaction of the shock wave with the bubble. The pressure ratios of the shock waves used in the experiments are 1·29, 1·58 and 1·74, and the experimental points are identified accordingly. The theoretical values are independent of time and are thus represented by horizontal lines.

6. Discussion

The effect of accelerations in a gas flow on the motion of gas bubbles of different density has been studied both theoretically and experimentally. In the present investigation only one-dimensional flows accelerated by pressure wave are considered, but it should be emphasized that it is irrelevant whether the accelerations occur in a non-steady flow or are caused by curvature of streamlines in a steady flow. The behaviour of gas bubbles in an accelerated flow is quite different from that of solid particles and cannot be explained by the difference in density alone. If a shock wave passes over a solid particle, which may be about 1000 times as dense as the surrounding gas, the initial particle velocity is practically zero. Subsequently, the particle speeds up under the influence of its aerodynamic drag until it moves with the flow. A gas bubble, on the other hand, acquires almost instantaneously, a velocity that may be larger or smaller than the gas velocity, depending on whether the density ratio is smaller or larger than unity. This velocity is, however, different from that of a hypothetical solid particle of the same density because a gas bubble in relative motion with respect to its surroundings is transformed into a vortex which absorbs part of the energy. Subsequently, the relative bubble velocity gradually decreases as a result of viscous dissipation.

The theory is based on the assumption that a spherical bubble is transformed into a vortex ring, and a cylindrical bubble into a linear vortex pair. One obtains for these limiting cases bubble velocities that differ by less than 20 % for the gases used here, and the velocities for other bubble shapes should fall between these rather narrow limits. The experimental data in figure 8 are in good agreement with this requirement and thus support the main features of the theory, namely, that the vortex is formed practically instantaneously (before the bubble has travelled one bubble diameter), and that the velocity and displacement ratios are independent of the magnitude of the acceleration.

According to equation (7), β^2 represents the fraction of the energy of the initial relative bubble motion that is available for translational motion after a vortex is formed. The effective value of β should lie between 0·203 and 0·436, so that the major fraction of the energy is absorbed by the vortex, and only about 10 % remain for the translational motion.

It is interesting to compare the results for gas bubbles with those for solid tracer particles, for example, those given by Hoenig (1957). A shock wave of Mach number 10, propagating in argon of 273 °K, at a pressure of 1 cm of mercury, produces a flow velocity of $2{\cdot}42 \times 10^5$ cm/sec. A particle of 10^{-3} cm diameter and a density of 3 g/cm^3 remains practically at rest immediately after passage of the shock wave, and reaches 95 % of the gas velocity after about 0·15 msec. After this time, the particle follows the flow closely. By comparison, the decrease of the relative velocity of a gas bubble behind a shock wave is so slow that it is barely noticeable in figure 8. The displacement ratios for H_2 and He show a tendency to decrease and those of SF_6 to increase with time, but the decay of the relative motion is still smaller than the scatter of the experimental points even after 0·3 msec.

The displacement of a gas bubble that initially is moving with the flow can always be considered as the vector sum of two displacements, one that would be observed if the flow velocity remained constant, and the other caused by accelerations. The former exactly represents the corresponding motion of the flow, while the latter differs from that of the flow by the factor $1+\beta(1-\sigma)/(\sigma+k)$, according to equation (8). This factor is independent of the manner in which the acceleration takes place as long as σ may be treated as a constant. If the acceleration lasts long enough for σ to change significantly as a result of diffusion and/or heat conduction, the foregoing constant factor no longer applies. Dissipation of vorticity because of viscosity also reduces the relative bubble motion. The effect of diffusion, which causes the sloping appearance of the bubbles in figure 6 (plate 2), has been discussed in § 4. Although one is dealing there with variations of σ in space rather than in time, these effects are closely related.

Another interesting feature of the behaviour of gas bubbles is the instability of bubbles that are heavier than their surroundings. Figure 6, plate 2, illustrates the rapid disintegration of SF_6 bubbles, while H_2 and He bubbles maintain their appearance for considerably longer times. Similar observations about the stability of buoyant vortices were reported by Turner (1957), who also provided the explanation that a light vortex core stabilizes the motion in a manner comparable to that of a stable stratification of two gases in a gravitational field, except that, in the vortex, gravity is replaced by the centrifugal force due to rotation.

Figure 4 shows that the displacement ratio of spark-heated bubbles decreases rather rapidly, while figure 8 indicates almost constant values for bubbles of the three gases used. The main difference between these experiments is that spark-heated bubbles are much hotter than the surrounding gas, while the temperature of the gas bubbles differs only a little if at all. It is readily verified that the compression produced by the strongest shock waves used in the experiments causes differences between bubble and gas temperatures of 0 °K for H_2, 23 °K for He, and -23 °K for SF_6 if the initial air temperature is 300 °K. Heat conduction and viscosity effects should, therefore, become significant mainly for the spark-heated bubbles. The consequences of these effects are not included in the theory, and only a tentative explanation of the observed behaviour is offered here. It should first be noted that, although the density of a spark-heated bubble is not known, the value of the displacement ratio computed from equation (8) cannot exceed $1+\beta$, corresponding to $\sigma = 0$, and for $k = 1{\cdot}0$. Extrapolation of the experimental data in figure 4 to the origin of the time scale should, therefore, yield a value between about 1·2 and 1·4, depending on the effective value of β, but the experimental data indicate an initial displacement ratio in the neighbourhood of 1·6. The observed results for small values of Δt seem, therefore, too high to represent the decay of a vortex. The data lie between the values corresponding to a fully developed vortex, as given by equation (8) and those corresponding to the initial bubble velocity before a vortex is formed, as given by equation (5), but there seems to be no reason why the transformation of a hot bubble into a vortex should be slower than that of a cold bubble. The high bubble velocities may be explained by considering the effect of cooling on the vortex. The propagation velocity of a vortex relative to the surrounding gas is proportional to the circula-

tion and inversely proportional to the size of the vortex (see, for example, equation (A 5) of the Appendix). While cooling does not affect the circulation, it causes the vortex to contract and, therefore, to speed up. According to this hypothesis, the behaviour of spark-heated bubbles, as shown in figure 4, is an indication of the extent to which the slowing down of the bubble because of vortex formation is counteracted by a speeding up due to cooling.

The large viscosity of air at elevated temperatures should cause a rapid dissipation of vorticity. An analysis of the slope of the relation between the displacement ratio and time (figure 4) shows indeed that after about 0·2 msec, the bubble velocity is already reduced to within a few per cent. of the flow velocity. It appears therefore that, immediately after interaction, the behaviour of a spark-heated bubble is significantly affected by cooling, while later, the viscosity effects dominate.

If spark-heated bubbles are used for tagging a flow, a correction for acceleration effects may have to be made to avoid appreciable errors, particularly immediately after accelerations. For bubbles formed by different gases, the acceleration effects can be greatly reduced by selecting density ratios as close to unity as the sensitivity of the detection system permits. In the described experiments, rather extreme conditions are used to demonstrate the phenomena clearly and to provide a sensitive test for the theory. The described results not only have a direct bearing on the use of tracer bubbles in gas flows, but they may also contribute to the understanding of various phenomena in flows of non-uniform density.

The authors wish to thank their colleagues G. H. Markstein and A. Gail for stimulating discussions in the course of this work. This work was started as an internal research project of Cornell Aeronautical Laboratory, and continued under the auspices of Project SQUID which is supported by the Office of Naval Research under Contract *Nonr*-1825(25).

Appendix

Impulsive motion of an infinite lamina and subsequent formation of a linear vortex pair

Taylor (1953) analysed the formation of a ring vortex under the condition that an impulse is given to a circular disk and the latter is then 'dissolved away'. A similar analysis is carried out in the following for an infinite lamina.

Assume that a lamina of width $2b$ is suddenly moved with a velocity U at right angles to its plane and that no flow separation occurs. A discussion of the resulting potential flow is given by Lamb (1945, p. 85), and one obtains for the kinetic energy of the motion

$$T = -\tfrac{1}{2}\pi\rho b^2 U^2, \tag{A 1}$$

and for the potential of the flow at the surface of the lamina

$$\phi = \pm U(b^2 - y^2)^{\frac{1}{2}}, \tag{A 2}$$

where y is the co-ordinate in the plane of the lamina, measured from its centre. The impulse of the motion is given by

$$P = dT/dU = \pi\rho b^2 U, \tag{A 3}$$

and the surface velocity by

$$d\phi/dy = \pm Uy(b^2-y^2)^{-\frac{1}{2}}. \tag{A 4}$$

If the lamina were suddenly dissolved away, the flow could be considered as being produced by a distribution of rectilinear vortices over the surface of the lamina. These vortices tend to roll up to form a linear vortex pair with the centres of the cores located near the edges of the lamina where the vorticity is strongest. It is assumed that the vorticity is uniformly distributed over the cores. Let the distance between the centres of the cores be denoted by $2B$. The velocity of a vortex pair relative to the surrounding gas, and its impulse, are given by (Lamb 1945, pp. 221, 229)

$$v = K/4\pi B \tag{A 5}$$

and

$$P' = 2BK\rho, \tag{A 6}$$

respectively, where the circulation around the cores is $+K$ and $-K$. With the aid of equation (A 4), one obtains for the circulation

$$K = 2\int_0^b Uy(b^2-y^2)^{-\frac{1}{2}}\,dy = 2Ub. \tag{A 7}$$

Rolling up of the vortex elements does not affect the impulse of the motion, so that $P' = P$ and equations (A 3), (A 6) and (A 7) yield

$$B = \tfrac{1}{4}\pi b. \tag{A 8}$$

If this result is substituted into equation (A 5), one obtains

$$v = (2/\pi^2)\,U = 0{\cdot}203\,U. \tag{A 9}$$

In view of the hypothesis made for the motion of a gas bubble, U and v must be identified with the velocities of the initial and final bubble motion relative to the surrounding gas, so that $U = u_P - u_G$ and $v = u_B - u_G$. Equation (A 9) thus yields the final result $\beta = 0{\cdot}203$.

REFERENCES

Birkhoff, G. & Caywood, T. E. 1949 *Fluid flow patterns. J. Appl. Phys.* **20**, 646.

Bomelburg, H. J. 1956 A method for the measurement of the flow of air by means of series of electric sparks. *Univ. of Marland, Tech. Note* BN–68, AFOSR-TN-56-38.

Cady, W. M. 1954 In *Physical Measurements in Gas Dynamics and Combustion, High Speed Aerodynamics and Jet Propulsion*, pp. 139–58, vol. ix. Princeton: Princeton University Press.

Herzog, J. 1957 A new experimental approach to the analysis of compressor performance. *Univ. of Maryland, Tech. Note* BN-90, AFOSR-TN-57-3.

Herzog, J. & Weske, J. R. 1957 Characteristics of the technique of aerodynamic investigation by means of electric sparks. *Univ. of Maryland, Tech. Note* BN-105, AFOSR-57-359.

Hirschfelder, J. O., Curtis, C. F. & Bird, R. B. 1954 *Molecular Theory of Gases and Liquids*. New York: Wiley.

Hoenig, S. A. 1957 Acceleration of dust particles by shock waves. *J. Appl. Phys.* **28**, 1218.

Lamb, H. 1945 *Hydrodynamics*, 6th ed. New York: Dover.

Markstein, G. H. 1957 A shock tube study of flame front-pressure wave interaction. *6th Symposium (International) on Combustion*, pp. 387–98. New York: Reinhold.

Markstein, G. H. 1958 Discussion of Rudinger 1958.

RUDINGER, G. 1958 Shock wave and flame interactions. *Combustion and Propulsion*, pp. 153–82. Third AGARD Coll. London: Pergamon.

SAHEKI, Y. 1947 On the measurement of wind (tunnel) velocity (distributions) by the electric spark method. *Hokkaido Univ., Faculty of Engineering Memoirs*, **8**, 185; transl. by E. Hope, *Nat. Res. Counc. Can. Tech. Trans.* TT-100 (1950).

TAYLOR, G. I. 1953 Formation of a vortex ring by giving an impulse to a circular disk and then dissolving it away. *J. Appl. Phys.* **24**, 104.

TOWNEND, H. C. H. 1937 Visual and photographic methods of studying boundary layer flow. *Aero. Res. Counc. (Gt Brit.), Res. and Mem.* no. 1803.

TURNER, J. S. 1957 Buoyant vortex rings. *Proc. Roy. Soc.* A, **239**, 61.

WESKE, J. R. 1958 Ein Beitrag zur Untersuchung stetiger und unstetiger dreidimensionaler Strömungsfelder in Turbomaschinen. *ZAM* IXb (5/6) 721 (J. Ackeret Anniversary issue).

WRIGHT, F. H. 1951 The particle-track method of tracing fluid streamlines. *Jet Propulsion Lab., Calif. Inst. of Technology, Progress Rept*, no. 3–23.

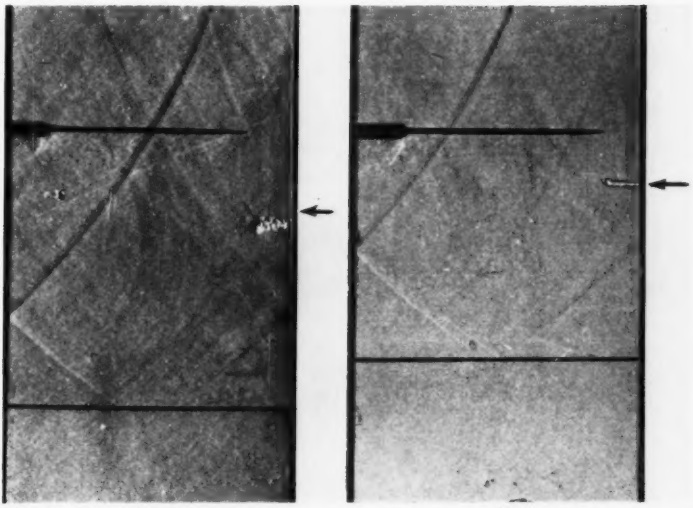

(*a*) (*b*)

FIGURE 2. Typical schlieren photographs of spark columns with the spark discharged (*a*) before, and (*b*) after, passage of a shock wave (pressure ratio 1·58). Arrows indicate calculated displacements of an unheated air element that initially was at the location of the spark gap.

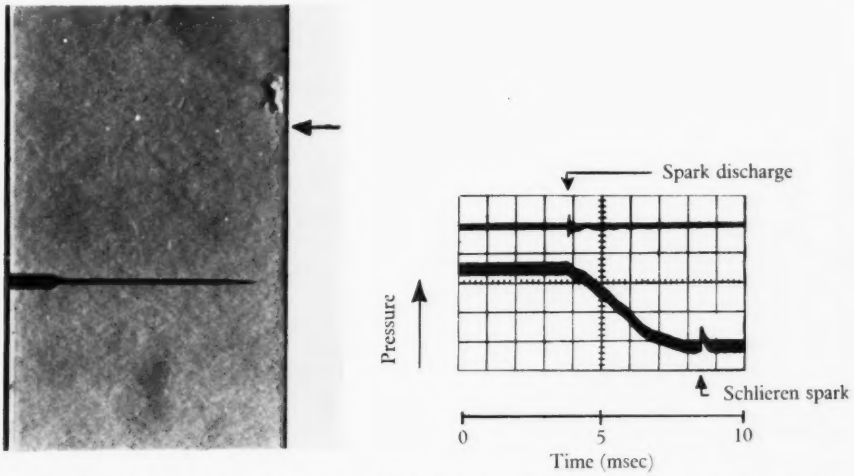

FIGURE 5. Schlieren photograph of spark bubble after acceleration by expansion wave and its reflexion from the closed bottom of the shock tube (overall pressure ratio 0·66). Pressure record is taken a few inches above spark gap. Arrow indicates calculated displacement of an unheated air element that initially was at the location of the spark gap.

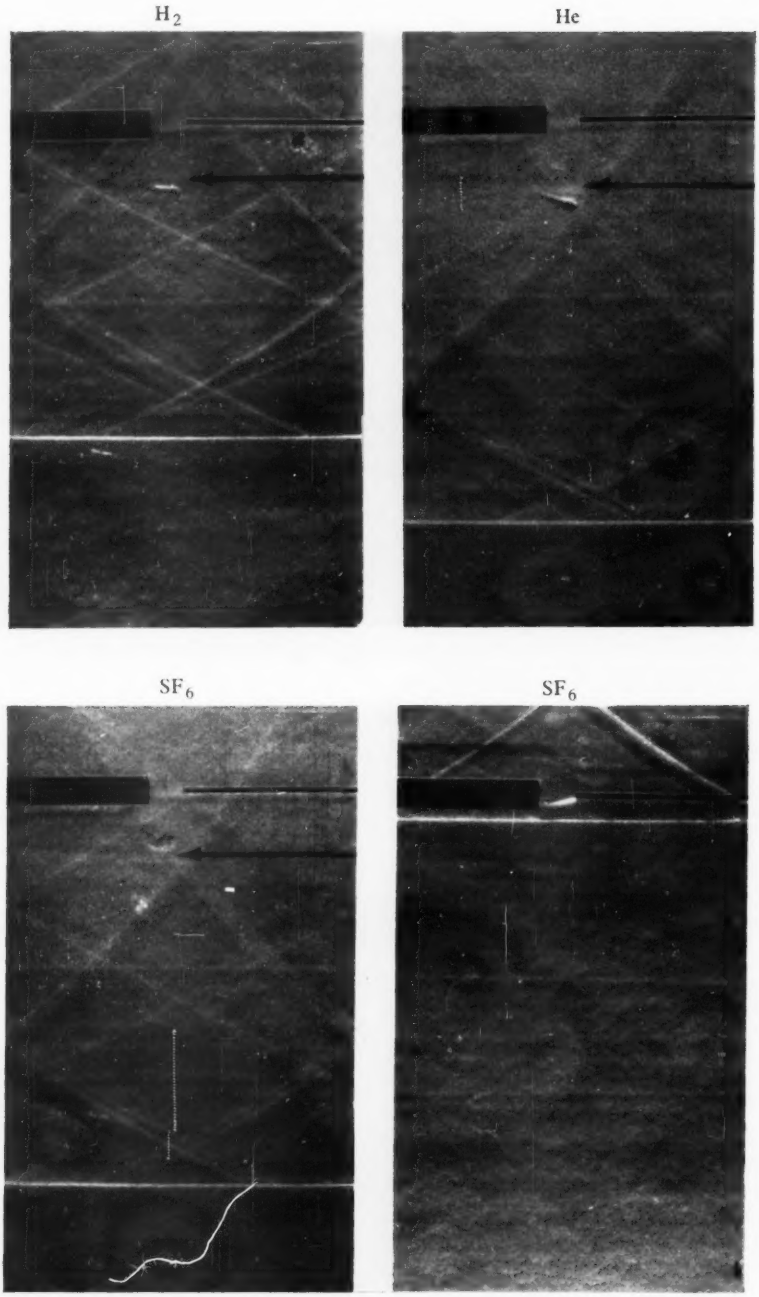

FIGURE 6. Typical gas jet/shock-wave interactions (shock pressure ratio 1·58).

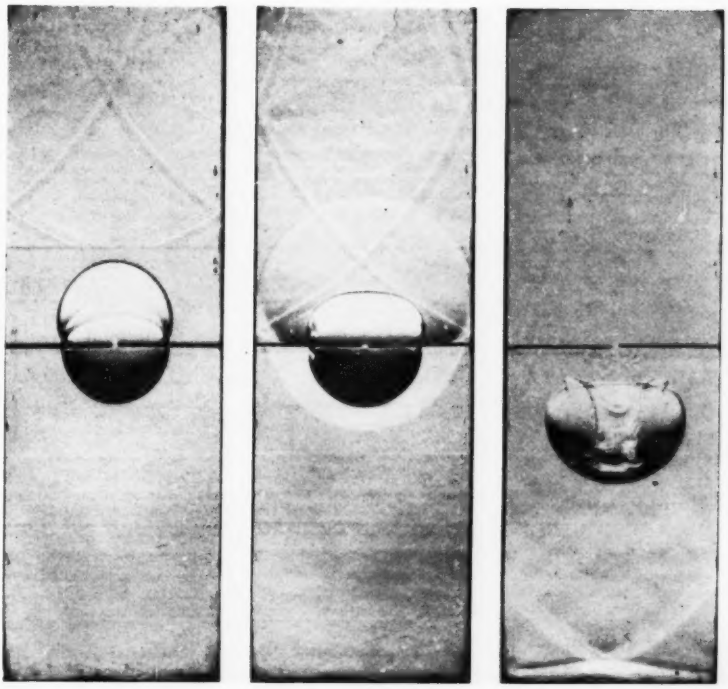

FIGURE 7. Interaction of a shock wave (pressure ratio about 1·3) with a bubble of burned gas (stoichiometric butane–air mixture).

Taylor instability of finite surface waves

By H. W. EMMONS, C. T. CHANG and B. C. WATSON
Harvard University, Cambridge, Mass.

(Received 20 May 1959)

The instability of the accelerated interface between a liquid (methanol or carbon tetrachloride) and air has been investigated experimentally for approximate sinusoidal disturbances of wave-number range from well below to well above the cut-off. The growth rates are measured and compared with theoretical results. A third-order theory shows the phenomena of overstability which is found in the experimental results. Some measurements of later stages of growth agree moderately well with the available theory and disclose some additional phenomena of bubble competition, Helmholtz instability with transition to turbulence, and jet instability with production of drops.

1. Introduction

If a glass were held upside down with water held magically, in its usual position, and then released, the water would fall out. This process occurs in underwater explosions, in the acceleration by combustion of liquid fuels, in the acceleration of stellar material, and, perhaps, in the molten layer, if any, on the leading edge of a blunt re-entry body. These acceleration-unstable liquid surface phenomena were studied by G. I. Taylor in the early 1940's with the first publication in 1950. He showed that in the absence of viscosity and surface tension all small surface irregularities are unstable and grow in time.

An initial test of the correctness of Taylor's ideas, apart from comparison with explosion photographs where the accelerations were uncertain, was made by Lewis (1950). As discussed later, the agreement was well within experimental scatter, but the investigation was limited to a wavelength (or acceleration) range in which the effect of surface tension was slight.

That surface tension and viscosity have modifying effects is clear, and it was shown by Bellman & Pennington (1954) that surface tension produces a cut-off wave-number (or wavelength) above which the surface disturbance merely oscillates and below which the disturbances grow. Viscosity, on the other hand, merely decreases the rate of growth at low wave-number and causes damping of the oscillatory solutions at high wave-numbers.

Allred & Blount (1953) with apparatus similar to that used by Lewis have, by using two fluids with densities close to each other to reduce the growth rate, studied the stability in a range where surface tension would be expected to play a part. Their results indicated a growth rate appreciably lower than the rate indicated by Bellman & Pennington's theory.

Experimental results show that the linear growth discussed in the theories can

apply only for very short times. The liquid surface rapidly changes to liquid spikes falling into the gas and gas bubbles rising* through the liquid.

Attempts to analyse these later developments have been made by Ingraham (1954) analytically, and Pennington *et al.* (1953) numerically. Both analyses showed the type of distortion of sinusoidal waves as observed, but neither carried the work to very large displacements.

Certain large displacement effects have been examined. Davies & Taylor (1950) studied the constant rate of rise of bubbles through a stationary liquid, while Birkhoff (1954) and Garabedian (1957) have computed with high precision the bubble-rise velocity.

On the other hand, the spikes have been shown analytically by Carrier (1953) and numerically by Pennington *et al.* (1953) to be simply left behind. Thus relative to the acceleration field the spikes are simply in free fall.

These very approximate analyses fall far short of describing the later stages of development. The régime established after spikes and rising bubbles have appeared could remain until the spikes 'hit the bottom', while the bubbles 'rise to the top'; but in fact such a motion is found unstable. The rising bubbles compete with one another, the large ones growing at the expense of the small ones. Some indications of this type of behaviour is given in figure 1 (plate 1). The gas-liquid interface on the sides of the spikes and bubbles are in relative (tangential) motion which produces additional surface instability of the Helmholtz type. These experimentally observed phases have been recognized by Lewis (1950) and Birkhoff (1954), but no detailed attempt to obtain analytical nor experimental knowledge of the processes has been made. In particular the final stage of mixing could only be of interest in its various statistical properties (it being hopelessly complex for detailed description), yet it could be analysed only by a statistic which was strongly biased by spacial and time variations of very large magnitude.

2. Growth of surface waves

A. *Theoretical consideration—finite waves with surface tension*

For the purposes of analysis, we shall treat the medium as a non-viscous, incompressible fluid. Surface tension is included. The upper fluid is taken as air whose density we may neglect relative to that of the liquid. The flow-field is assumed to be two-dimensional, with the x'-axis taken in the unperturbed plane of the interface. For simplicity, we shall assume that the motion of the whole system is started from rest and the initial surface disturbance is a simple sinusoidal standing wave with amplitude η_0' and wave-number k'. For the proper interpretation of the results, all the physical parameters concerned will be expressed in dimensionless forms. As standards of measurement we shall take the wave-number k' and the wave velocity $\sqrt{(g'/k')}$, of the initial disturbances, as scales of length and velocity, respectively, where g' is the acceleration relative to a force-free frame of reference. $\rho g'$ is a virtual gravity force taken as positive in a direction normal to the surface

* The terms 'rising' and 'falling' refer of course to the familiar gravity effects on an upside down glass of water. For the general case, 'downwards' is the direction of the effective gravity component, directed for instability from the heavier toward the lighter medium.

from the heavier toward the lighter medium. Thus for liquids at rest on the surface of the earth, $g' = -981\,\mathrm{cm/sec^2}$.

The dimensionless independent variables of the problem will be taken as

$$x = k'x', \quad y = k'y', \quad t = \sqrt{(+g'k')}t'. \tag{2.1}$$

In terms of these dimensionless variables, the governing equations and the boundary conditions for the velocity potential $\phi(x, y, t)$ (defined by $\mathbf{u} = -\operatorname{grad}\phi$) and the surface displacement $\eta(x, t)$ in the y-direction are:

Governing equations:

$$\phi_{xx} + \phi_{yy} = 0$$

for
$$\infty > x > -\infty, \quad \eta > y > -\infty, \quad t \geqslant 0. \tag{2.2}$$

Boundary conditions:

The liquid surface moves with the liquid,

$$\eta_t - \eta_x\phi_x + \phi_y = 0. \tag{2.3}$$

The pressure in the liquid differs from atmospheric by the effect of surface tension and the curvature,

$$-\eta - \phi_t + \tfrac{1}{2}(\phi_x^2 + \phi_y^2) = k^2[\eta_{xx}(1+\eta_x^2)^{-\frac{3}{2}}] \tag{2.4}$$

on $y = \eta(x, t)$.

Initial conditions:
$$\eta(x, 0) = \eta_0 \cos x, \tag{2.5}$$

$$\eta_t(x, 0) = 0. \tag{2.6}$$

In equation (2.4) k is given by,

$$k = \frac{k'}{k'_c}, \tag{2.7}$$

where k'_c, the cut-off wave-number, is given by

$$k'_c = \sqrt{\frac{\rho g'}{T}}, \tag{2.8}$$

where T is the surface tension. The parameter k can also be interpreted as the ratio of the surface tension forces to the gravity forces.

In order to proceed analytically, let us assume that the surface disturbance admits an expansion of the following type:

$$\eta = \sum_{r=1}^{\infty} \eta_0^r \eta_r(x, t). \tag{2.9}$$

If η_r and all its derivatives are further assumed to be of the same order of magnitude, it follows from equation (2.3) that

$$\phi = \sum_{r=1}^{\infty} \eta_0^r \phi_r. \tag{2.10}$$

Since equation (2.2) is linear, it must be satisfied by every ϕ_r. Our general scheme of solution is to introduce equations (2.9) and (2.10) into (2.3), (2.4), (2.5) and (2.6) and equate like powers of η_0 to find the corresponding boundary and initial conditions for ϕ_r and η_r. The values of ϕ_r and its derivatives required at

$y = \eta(x,t)$ are found from the values at $y = 0$ by use of Taylor expansions. We then determine each ϕ_r and η_r in succession to complete the solution. First, we have

$$\eta_r(x,0) = \begin{cases} \cos x & \text{for } r = 1, \\ 0 & \text{for } r \neq 1. \end{cases} \tag{2.11}$$

The following notation will be used throughout:

$$\eta_{r,t} \equiv \frac{\partial \eta_r}{\partial t} \quad \text{for all } r. \tag{2.12}$$

Then, the boundary conditions obtained by the above process from equations (2.3) and (2.4), wherein all quantities are evaluated at $y = 0$, are:

$$\eta_{1,t} + \phi_{1,y} = 0, \tag{2.13a}$$

$$\eta_1 + \phi_{1,t} + k^2 \eta_{1,xx} = 0, \tag{2.13b}$$

$$\eta_{2,t} + \phi_{2,y} = \phi_{1,x}\eta_{1,x} - \phi_{1,yy}\eta_1, \tag{2.13c}$$

$$\eta_2 + \phi_{2,t} + k^2\eta_{2,xx} = \tfrac{1}{2}(\phi_{1,x}^2 + \phi_{1,y}^2) - \phi_{1\ ty}\eta_1, \tag{2.13d}$$

$$\eta_{3,t} + \phi_{3,y} = \phi_{1,x}\eta_{2,x} + (\phi_{1,xy}\eta_1 + \phi_{2,x})\,\eta_{1,x} - \phi_{2,yy}\eta_1 - \tfrac{1}{2}\phi_{1,yyy}\eta_1^2 - \phi_{1,yy}\eta_2, \tag{2.13e}$$

$$\eta_3 + \phi_{3,t} + k^2\eta_{3,xx} = \phi_{1,x}\phi_{2,x} + \phi_{1,y}\phi_{2,y} + (\phi_{1,xy}\phi_{1,x} + \phi_{1,yy}\phi_{1,y})\,\eta_1 + \tfrac{3}{2}k^2\eta_{1,xx}(\eta_{1,x})^2 - \phi_{2,yt}\eta_1 - \tfrac{1}{2}\phi_{1,yyt}(\eta_1)^2 - \phi_{1,yt}\eta_2. \tag{2.13f}$$

At each step in approximation, the boundary conditions are now linear, all non-linearity involving lower-order functions which will have been determined as earlier approximations. All such terms have been placed on the right-hand side and are, at any given stage, known.

As expected, the first approximation, ϕ_1, η_1 are the solutions given earlier by Bellman & Pennington:

$$\phi_1 = -\mu_1 \sinh(\mu_1 t)\, e^y \cos x \,(\equiv -B_{11,t} e^y \cos x), \tag{2.14a}$$

$$\eta_1 = \cosh(\mu_1 t)\cos x \qquad (\equiv B_{11}(t)\cos x), \tag{2.14b}$$

where

$$\mu_1^2 = 1 - k^2. \tag{2.14c}$$

These solutions show the phenomena of cut-off wave-number since $\mu_1 = 0$ at $k = 1$ and below this μ_1 is positive so that surface waves grow. Note that for waves shorter than the cut-off wavelength ($k > 1$) μ_1 is imaginary and the waves oscillate; they are not damped.

The second approximation ϕ_2, η_2, extends the results published by Ingraham (1954) to include surface tension, although we solve only for a massless upper fluid:

$$\phi_2 = \frac{\mu_1}{4}\sinh 2\mu_1 t + \left(\frac{\mu_1}{4}\sinh 2\mu_1 t - \frac{B_{22}(t)}{2}\right) e^{2y}\cos 2x, \tag{2.14d}$$

$$\eta_2 = B_{22}(t)\cos 2x, \tag{2.14e}$$

where

$$\mu_2^2 = 2[1 - (2k)^2], \tag{2.14f}$$

$$B_{22}(t) = \frac{1}{2}\left(\frac{\mu_1}{\mu_2}\right)^2 \left\{1 + \frac{1}{4(\mu_1/\mu_2)^2 - 1}\left[\cosh 2\mu_1 t - 4\left(\frac{\mu_1}{\mu_2}\right)^2 \cosh \mu_2 t\right]\right\}. \tag{2.14g}$$

The equation of the surface shows the growth of the first harmonic while the velocity potential shows the first harmonic and a purely time-dependent term which arises because of the additional pressure in the liquid required to produce the velocity of the rising fluid. The first harmonic is seen on analysis of these expressions to grow only by energy addition from the fundamental if the first harmonic wave-number is above the cut-off (i.e. the fundamental $k > \frac{1}{2}$), while for first harmonic wave-numbers below the cut-off they grow also by direct energy addition from the acceleration field, once they are started.

The third approximation introduces some new features. When the first and second approximations are introduced into the boundary conditions, equations (2.13*e*) and (2.13*f*), they become

$$\eta_{3,t} + \phi_{3,y} = P_{31}(t)\cos x + P_{33}(t)\cos 3x, \tag{2.14h}$$

$$\eta_3 + \phi_{3,x} + k_2\eta_{3,xx} = Q_{31}(t)\cos x + Q_{33}(t)\cos 3x, \tag{2.14i}$$

where the P and Q functions of t are given in Appendix I. These equations show that as a result of the excitation of lower approximations not only a new mode appears ($\cos 3x$) but also a feedback of excitation to the fundamental ($\cos x$) occurs. The solution can be expressed as

$$\phi_3 = C_{31}(t)\cos x + C_{33}(t)\cos 3x, \tag{2.15}$$

$$\eta_3 = B_{31}(t)\cos x + B_{33}(t)\cos 3x, \tag{2.16}$$

where the B and C functions of t are given in Appendix II. The second harmonic behaves as the fundamental and first harmonic with respect to a cut-off wave-number above which it grows only at the expense of energy from the lower wave-number waves. The second harmonic is at the cut-off for the fundamental at $\frac{1}{3}$ cut-off wave-number. Thus the distortion of the fundamental changes nature at each wave-number $1/n$ ($n = 1, 2, 3, \ldots$) as each successive harmonic changes from direct growth to becoming oscillatory.

The final solution for the growth of harmonic disturbances on the surface against air of an accelerated fluid is to the present order of approximation:

$$\eta = \sum_{r=1}^{\infty} \eta_0^r \eta_r = \eta_0 \cosh \mu_1 t \cos x + \eta_0^2 B_{22}(t)\cos 2x + \eta_0^3(B_{31}(t)\cos x + B_{33}(t)\cos 3x) + \ldots. \tag{2.17}$$

A corresponding sum holds for

$$\phi(x, y, t) = \sum_{r=1}^{\infty} \eta_0^r \phi_r = -\eta_0 \mu_1 \sinh \mu_1 t\, e^y \cos x + \eta_0^2 \left[\frac{\mu_1}{4}\sinh 2\mu_1 t + \left(\frac{\mu_1}{4}\sinh 2\mu_1 t - \frac{B_{22,t}}{2}\right) e^{2y}\cos 2x\right] + \eta_0^3(C_{31}\cos x + C_{33}\cos 3x) + \ldots. \tag{2.18}$$

These series can be expressed as Fourier series by rearrangement:

$$\eta = \sum_{m=1}^{\infty} A_m(k, t)\cos mx, \tag{2.19}$$

where $A_m(k, t) = \sum_{r=m}^{\infty} B_{rm}(k, t)\,\eta_0^r$ and the $B_{rm}(k, t)$ are given in Appendix II up to B_{33}. Thus is displayed the harmonic content of the distorted growing disturbance.

From the hyperbolic function nature of the B_{mr} functions already obtained and the manner of their formation, it appears that the entire series, if obtained, would change to a group of irrationally spaced time harmonic terms when the fundamental wave-number exceeds unity. This appears contrary to experimental results discussed in the next section. In any case, the present solution to the third approximation is still limited to small wave amplitudes; certainly not exceeding $\eta = \eta' k' = 2\pi$, i.e. the wave amplitude equal to the wavelength.

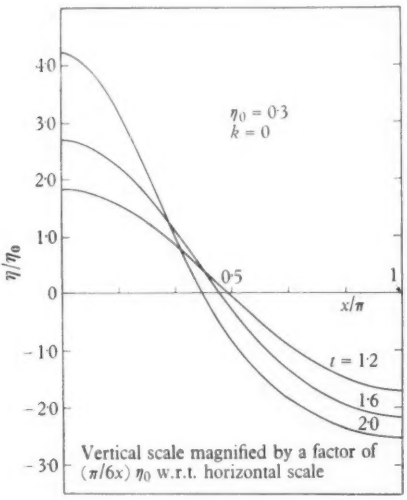

FIGURE 2. Calculated wave profiles at different times.

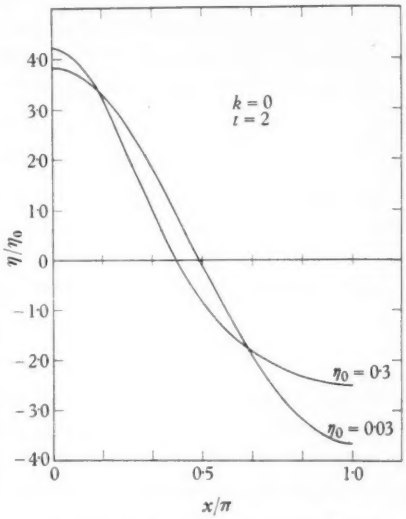

FIGURE 3. Calculated wave profiles with different initial amplitudes.

Results of the analysis indicate that in order to get a reasonable representation of the wave-form even at comparatively early stages, at least a third approximation is required. An example of the growth of a surface wave is given in figure 2 where three consecutive shapes of the surface are shown for an initial sinusoidal disturbance of amplitude $\eta_0 = 0{\cdot}3$ and wave-number $k = 0$ (i.e. the effect of surface tension has been neglected). The asymmetrical growth of the surface is clearly indicated by the narrowing of the crest and the broadening of the trough of the wave with time. The influence of the amplitude and wave-number of the initial disturbance on its subsequent growth are shown in figures 3 and 4, respectively. As is to be observed there, asymmetry of the surface occurs much earlier for initial disturbances of larger amplitudes than for those of smaller amplitudes. Disturbances having wave-numbers close to 'cut-off' values (i.e. $k = 1{\cdot}0$) are more stable than those having lower wave-numbers. Neglecting the effect of surface tension is equivalent to considering the limiting case of $k = 0$. Surface tension, therefore, has a definite stabilizing effect. Alternately, the limiting case $k = 0$ can be considered as a case of infinite acceleration for which all harmonics are below cut-off wave-number and are inherently unstable once they are started.

The present third-order theory also shows that, contrary to the prediction of a modified first-order theory (Bellman & Pennington 1954), the surface disturbance still grows at the 'cut-off' wave-number (i.e. $k = 1{\cdot}0$) in the manner given by

$$\eta = \eta_0 + \tfrac{3}{16}\eta_0^3 t^2 \cos x + \tfrac{3}{64}\eta_0^3[\cos(2\sqrt{6}t) - 1]\cos 3x. \tag{2.20}$$

The crest and trough of the wave, however, are growing at equal rates. By further increasing the wave-number of the initial disturbance, as a consequence

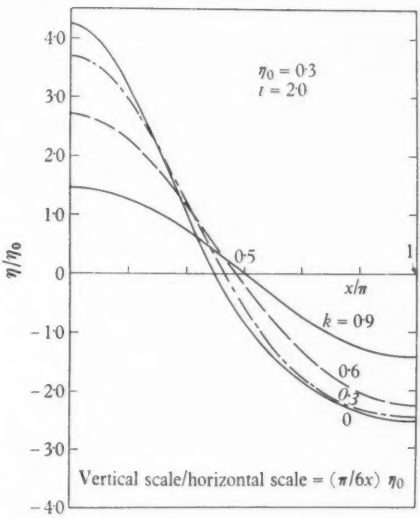

FIGURE 4. Calculated wave profiles with different wave-numbers.

	$k < 1{\cdot}0$	$k = 1{\cdot}0$	$k > 1{\cdot}0$
Taylor's original theory	$\eta_0 \exp(t)$	$\eta_0 \exp(t)$	$\eta_0 \exp(t)$
Bellman & Pennington's theory	$\eta_0 \exp\{\sqrt{(1-k^2)}\, t\}$	η_0	$\eta_0 \cos\{\sqrt{(k^2-1)}\, t\}$
Third-order theory	$\eta_0 \exp\{\sqrt{(1-k^2)}\, t\}$	$\frac{3}{16}\eta_0^3 t^2$	$e_{31}(k)\, \eta_0\{\sqrt{(k^2-1)}\, t\} \sin\{\sqrt{(k^2-1)}\, t\}$*

* Note. The term compared is the dominating one appearing in the amplitude $A_1(k, t)$ of the basic mode $A_1(k, t)\cos x$. For $e_{31}(k)$, see Appendix II.

TABLE 1. Comparison between various theories regarding the growth of the basic mode in the earlier period

of the feedback to the basic mode from the second harmonic, the surface disturbance, instead of growing exponentially in time as compared with those having wave-numbers $k < 1{\cdot}0$, tends to be 'overstabilized', i.e. it oscillates in time with an ever-increasing amplitude. As a comparison between the predictions of the various theories, we have indicated qualitatively in table 1 the behaviour of the basic mode with variation of the wave-number.

B. *Experimental apparatus*

The experimental results reported here were performed in an apparatus consisting of a glass-sided frame partially filled with liquid, a means of accelerating this frame and its contents, and various pieces of equipment for recording the behaviour of the liquid surface as the frame is accelerated. A schematic of the accelerator is given in figure 5. The frame which is accelerated is made of

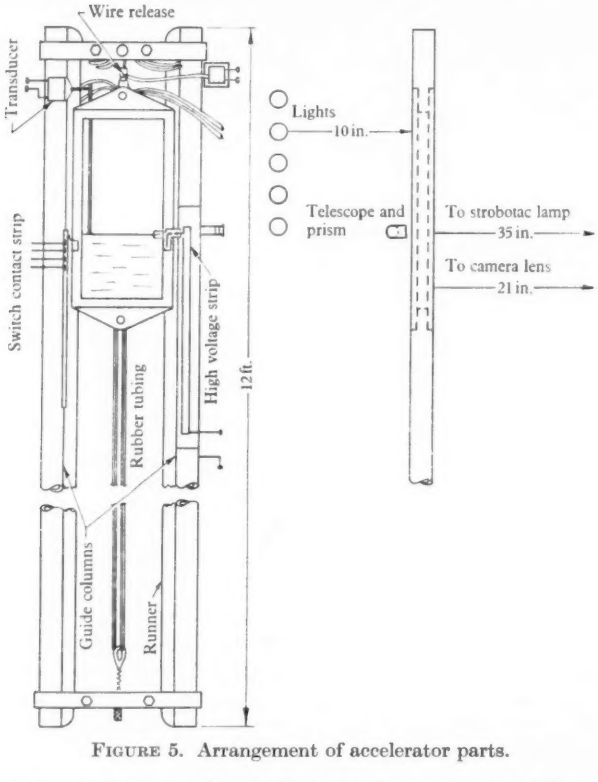

FIGURE 5. Arrangement of accelerator parts.

aluminium with a glass front and back. Its inside dimensions are 12 in. × 5 in. × 1 in. This frame is restrained to travel in a vertical direction by the two guide columns.

At the start of an experimental run the frame is held at the top of the guide columns by a steel wire while tension is applied to the rubber tubes attached to the bottom of the frame. To begin the run an electric current is passed through the steel wire, melting it and releasing the frame. After the frame has left the area of interest another set of rubber tubes attached to the upper end of the frame comes into play and arrests the moving frame.

In order to provide an initial disturbance to the surface of the liquid contained in the frame, a small paddle, its blade resting at the surface, is oscillated by a transducer driven by an audio oscillator and amplifier.

An indication of the initial amplitude of the travelling wave created by the paddle is obtained by observing the surface profile with a 30-power microscope. A stroboscope, flashing at a frequency close to the frequency at which the waves pass a fixed point, provides the illumination and creates the impression of a slowly moving wave profile which may be measured by means of a graduated reticle in the microscope.

Photography is used for recording the time and position of the surface waves and also the position of the frame at millisecond intervals. A camera is placed in

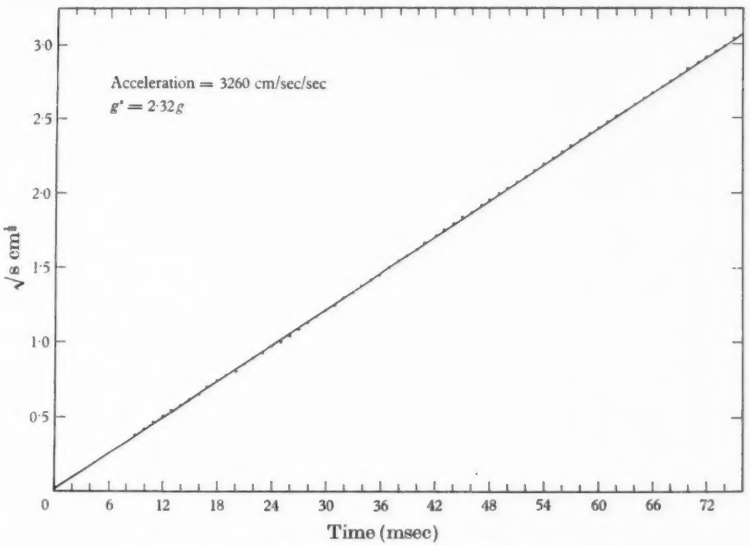

FIGURE 7. Square root of frame displacement *vs* time.

front of the frame, while behind the frame are positioned ten flash bulbs which are fired by switches tripped by the descending frame. Also located on the frame is a spark gap at which appears a spark discharge every millisecond. Because the camera shutter is open during the time that the frame is descending the film records: (*a*) the sparks giving the position of the frame every millisecond, (*b*) the ten positions of the interface at the times the flash bulbs were fired, and (*c*) the position of the spark gap at the time of the firing of the flash bulbs. The images of (*b*) and (*c*) above allow a precise determination of the relative times of the several events. A typical photograph is given in figure 6 (plate 2).

The analysis of the film by travelling microscope and photographic enlarger provides the quantitative data. The travelling microscope is used to measure the position of the spark discharges, the wavelengths, and the wave amplitudes in the earliest stage of growth. The enlarger is used in the study of the later stages of growth.

By plotting the square root of the distance from the initial position to the individual spark discharges against time (figure 7), the rate of acceleration and the relative time at which the acceleration began is obtained.

From extreme enlargements of the wave-forms of the later stages of growth an indication of the wave behaviour is obtained. A measurement of the distance from the wave spike or crest and of the bottom of the wave troughs from a mean horizontal line is made. The mean horizontal line is established by making the cross-sectional area occupied by the spikes equal to the area of the vacuated fluid in the troughs. This definition of a 'mean horizontal line' is used instead of a fixed line on the frame, because the meniscus growth changes the mean level of the waves relative to the frame. Figure 8 is an illustration of this later growth.

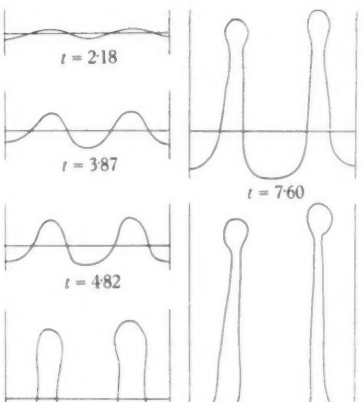

FIGURE 8. Later growth outlines.

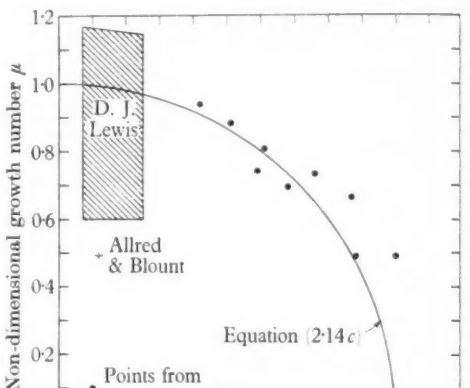

FIGURE 9. Initial growth rate.

C. *Experimental results on surface waves, small amplitudes*

The results of initial growth-rate experiments can best be discussed with the aid of figure 9 which is based on two non-dimensional numbers μ, a measure of the rate of wave-amplitude increase, as the ordinate and k, the ratio of wave-number to the cut-off wave-number, as abscissa.

For $k < 1$ the predominate growth rate is that predicted by the linear theory of Bellman & Pennington (1954) and given here by equations 2.14*b* and 2.14*c*. This linear theory prediction is represented by a solid line forming a quarter circle in the μ, k-plane of figure 9.

The value of μ from experimental results of wave growth in the $k < 1$ range is taken as the solution of the equation

$$\mu = \frac{1}{t_m} \cosh^{-1} \frac{\eta_m}{\eta_0}, \tag{2.21}$$

where η_m/η_0 is the ratio of the measured height to the initial wave height (for experimental convenience the double amplitude or crest-to-trough distance is used) and t_m is the non-dimensional time at which the wave reached the height η_m.

If the results of a large number of experiments performed by Lewis (1950) of a water-air interface are interpreted by the above method, then these results will fall in the shaded area of figure 9. As a result of the large accelerations and moderately long wavelengths used by Lewis the effects of surface tension would not be expected to be revealed.

The single point placed by the names, Allred & Blount, represent the results of an experiment reported by them in which they used *n*-heptane and air as the two fluids. Unfortunately, this is the only experiment of this type reported by them; their other experiments involved the interface between two fluids with densities close to each other in value and, therefore, cannot be represented entirely as functions of the two dimensionless numbers used in this figure.

Film	k' cm^{-1}	g'/g	k	$\eta_0 k_c$	μ
D-3	8·64	2·32	1·00	0·11	0·49
H-4	5·91	2·18	0·68	0·098	0·57
M-7	6·64	2·24	0·76	0·11	0·64
H-10	7·00	1·86	0·87	0·12	0·62
H-11	7·26	1·96	0·88	0·024	0·46
K-2	7·77	6·81	0·51	0·064	0·63
L-1	9·37	6·86	0·61	0·046	0·63
L-3	6·53	6·94	0·42	0·032	0·61
L-6	9·04	6·96	0·59	0·15	0·57

TABLE 2. Initial wave-growth data

The rest of the points in figure 9 are the results of the present work; the dimensional wave-numbers and accelerations of the experimental runs corresponding to the points in the μ, k-plane are given in table 2. Although there is a definite decrease in growth rate as the wave-number approaches cut-off, all the photographs of initially disturbed surfaces showed some evidence of wave growth. The experimental scatter is largely due to inaccuracies in the determination of the initial amplitudes.

Beyond the cut-off wave-number as shown in figure 10 (plate 3) there is an indication of a type of behaviour here called over-stability. The photographs taken of wave growth under these conditions indicate a standing oscillation of the waves with amplitude increasing in time. In figure 10 the points A, B and C designate the same position in the space of the frame, and it is seen that the waves have been caught in different positions of oscillation.

No more than a single oscillation has been observed; apparently after passing through one reversal of direction the wave grows to a large size and well-developed third-stage growth appears with the resulting competition between bubbles soon reducing the number of bubbles in a given space. There is some evidence that the larger the value of k for waves behaving in the over-stable manner, the higher the frequency at which the wave oscillates, as would be expected from equation (2.14*c*).

D. *Later stage wave-growth experiments*

The films which were analysed for third-stage growth showed considerable scatter of results even though a selective process was applied in the choice of which group of waves were to be studied; i.e. those waves were chosen which

appeared to be in a group of waves of a fairly uniform nature. The scatter was largely due to two things: the presence of odd modes of vibration imposed on the steady growth, and to small variations in initial conditions which become magnified at later times.

Except for the prediction of over-stability, the third-order theory does not check well with the experimental results. The theory predicts an ever-growing oscillation while the experiments never show more than one cycle of oscillation

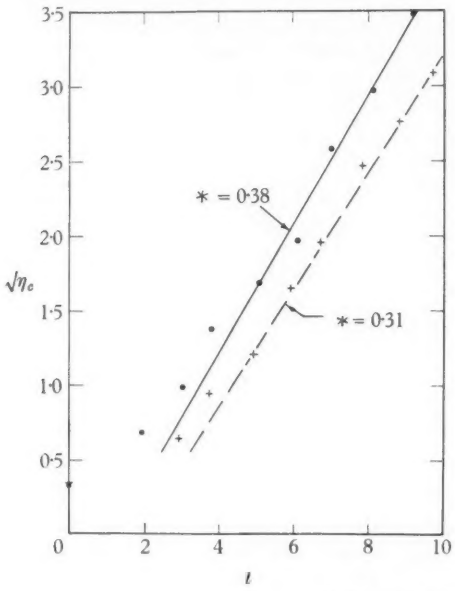

FIGURE 11. Spike acceleration. $* = \dfrac{\text{Spike acceleration}}{\text{Acceleration of free fall}}$

before monotonic growth occurs. It is not known at present whether the inadequacy is in the theoretical treatment or in the experimental boundary conditions.

Spike acceleration is illustrated by figure 11. Of the photographs measured for spike growth all indicated an acceleration of less than half the rate of free fall in the particular virtual gravity field applied. This may be compared with Carrier's (1953) work and the machine calculations of Pennington *et al.* (1953), which indicated a rate of acceleration equal to the free-fall rate. Since both of these theoretical predictions assume the surface tension to be zero, they would indicate a higher rate of growth because the surface tension forces act against the direction of acceleration of the spikes.

On the other hand, experimental results on bubble velocity resulted in good agreement with the theoretical predictions. The results, which are illustrated by two examples given in figure 12, in general give the conclusion that the value of c in the equation, $v = c\sqrt{g\lambda}$, lies between 0·2 and 0·3. This agrees with the theory

of Birkhoff (1954) and the work of Garabedian (1957), even though they did not consider surface tension effects in their analyses.

Examples of competition between bubbles are observed in every photograph taken of the wave disturbance type.

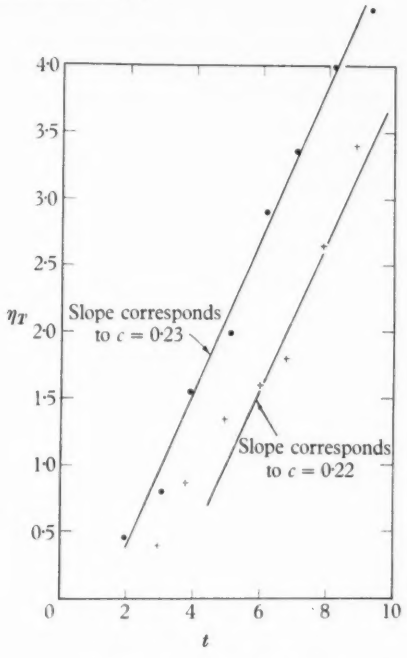

FIGURE 12. Bubble velocity.

3. Experiments involving a liquid sheet at the wall

If the surface is not disturbed by the vibrating paddle, a distortion of the surface still results from the liquid meniscus around the edge of the accelerated container as is illustrated by figure 13 (plate 4). Point A is the position reached by a very thin sheet of liquid next to the glass. Point B is the top of a thin wall of liquid that is in the exact centre between the glass walls. Points C and D are the tips of two two-dimensional bubbles which occupy the space between the sheets at the wall and the liquid wall in the centre. The more or less round bubbles of which there are four, one in each corner, are at the points E and F. The above is further illustrated by figure 14 (plate 5) in which an oblique view of the same type of phenomenon is offered.

Some study was made on the behaviour of the liquid sheet at the side wall. The results of this study are given in figure 15. Two liquids, methanol and carbon tetrachloride, were used in these experiments, and little difference was found between the two except that in the case of the carbon tetrachloride a second thickening of the sheet was seen to occur some distance back from the leading edge. This thickening was seen to catch up with the leading edge, after the leading-

edge acceleration began to slacken, and to provide fresh impetus allowing acceleration to continue at the original rate for a further distance. This point is illustrated by a comparison of figures 15 and 16. In figure 16 the line, labelled second wave line, represents the region where the thickening has caught up with the leading edge.

A graph, figure 17, of the ratio of the leading-edge acceleration to the applied gravity field versus the applied gravity field indicates that the leading edge

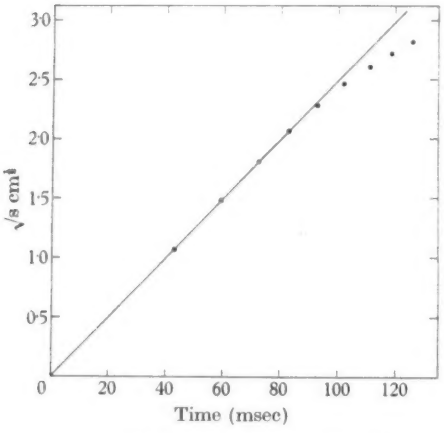

FIGURE 15. Square root of the relative displacement of the leading edge of the methanol sheet at the wall *vs* time.

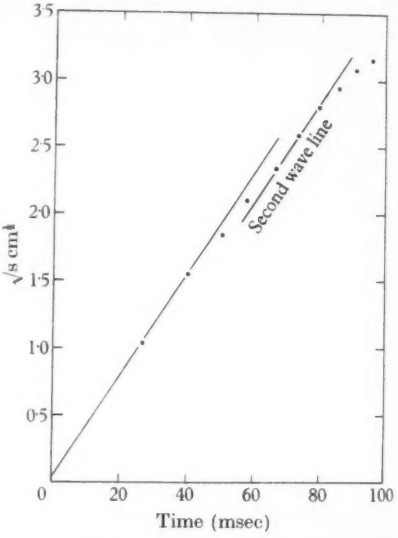

FIGURE 16. Square root of the relative displacement of the leading edge of the carbon tetrachloride sheet at the wall *vs* time.

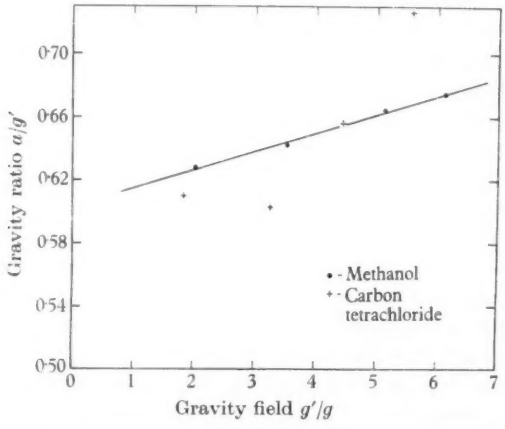

FIGURE 17. The ratio of the acceleration of the leading edge of the liquid sheet at the wall to the acceleration of free fall in the applied gravity field *vs* the applied gravity field.

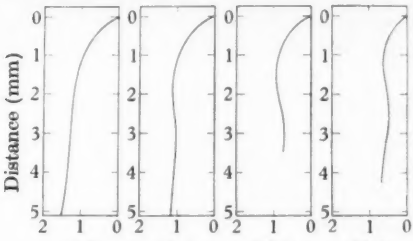

Time (msec)	43·7	60·0	72·8	83·3
Displacement (cm)	1·17	2·22	3·30	4·30

FIGURE 18*a*. Liquid sheet profiles at a low acceleration rate.

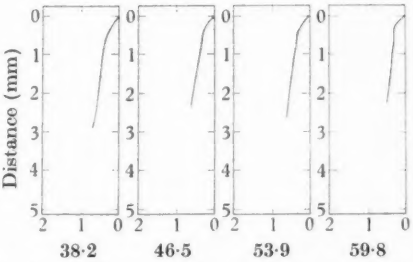

Time (msec)	38·2	46·5	53·9	59·8
Displacement (cm)	3·12	4·40	5·80	7·09

FIGURE 18*b*. Liquid sheet profiles at a high acceleration rate.

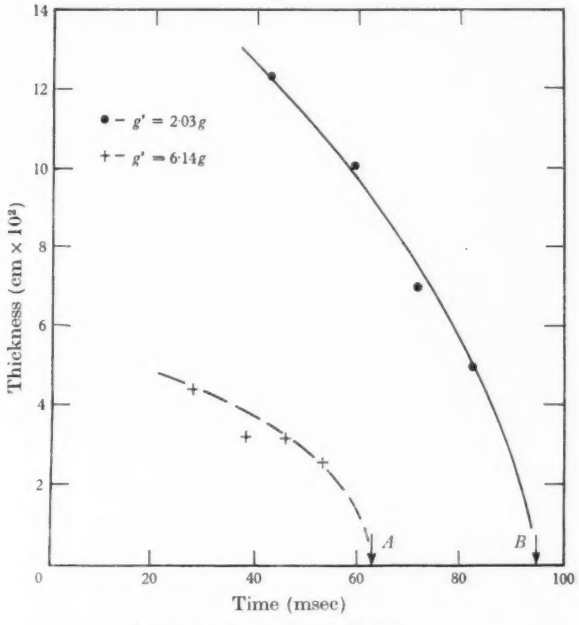

FIGURE 19. Profile thickness.

travels, in the ranges of applied gravities used here, at from 0·6 to 0·7 as fast as a free falling body. This is a higher acceleration than any observed in the case of wave spikes.

In order to get more information on the manner in which the accelerating sheet acts, the profiles of the sheet at the wall were determined at the highest and lowest rates at which the experiments with methanol were run. These results are given in figures 18*a* and 18*b*.

From the profile, a characteristic thickness can be measured and plotted versus time as in figure 19. The points marked *A* and *B* in this figure represent the time at which the displacement of the leading edge no longer maintained its constant acceleration. From this it can be deduced that at the time *A* for the experiment giving the profile shown in figure 18*a* and at the time *B* for the experiment giving the profile shown in figure 18*b* the liquid sheet ran out of fluid in the sense that the rate of supply from the main body of liquid was insufficient to allow things to continue as they had been.

The authors gratefully acknowledge the support of this work by the Office of Ordnance Research, U.S. Army, through Combustion Research Contract No. DA-19-920-ORD-1029.

Appendix I

Amplitudes of forcing functions of the third approximation, equation (2.14*h*, *i*)

$$P_{31}(t) = -\frac{\mu_1}{32}\left\{\frac{32(\mu_1/\mu_2)^4 - 8(\mu_1/\mu_2)^2 - 3}{4(\mu_1/\mu_2)^2 - 1}\right\}\sinh(\mu_1 t) + \frac{\mu_1}{32}\left\{\frac{3 - 8(\mu_1/\mu_2)^2}{4(\mu_1/\mu_2)^2 - 1}\right\}\sinh(3\mu_1 t)$$
$$+\frac{\mu_1-\mu_2}{2}\frac{(\mu_1/\mu_2)^4}{4(\mu_1/\mu_2)^2-1}\sinh(\mu_1+\mu_2)t + \frac{\mu_1+\mu_2}{2}\frac{(\mu_1/\mu_2)^4}{4(\mu_1/\mu_2)^2-1}\sinh(\mu_1-\mu_2)t,$$

$$P_{33}(t) = \frac{\mu_1}{32}\left\{\frac{96(\mu_1/\mu_2)^4 - 48(\mu_1/\mu_2)^2 + 9}{4(\mu_1/\mu_2)^2 - 1}\right\}\sinh(\mu_1 t) + \frac{9}{32}\frac{\mu_1}{4(\mu_1/\mu_2)^2-1}\sinh(3\mu_1 t)$$
$$-\tfrac{3}{2}(\mu_1+\mu_2)\frac{(\mu_1/\mu_2)^4}{4(\mu_1/\mu_2)^2-1}\sinh(\mu_1+\mu_2)t - \tfrac{3}{2}(\mu_1-\mu_2)\frac{(\mu_1/\mu_2)^4}{4(\mu_1/\mu_2)^2-1}\sinh(\mu_1-\mu_2)t.$$

$$Q_{31}(t) = -\left\{\frac{9}{33}\frac{1-\mu_1^2}{\mu_1^2} - \frac{\mu_1^2}{32}\left[\frac{32(\mu_1/\mu_2)^4 - 1}{4(\mu_1/\mu_2)^2 - 1}\right]\right\}\cosh(\mu_1 t)$$
$$-\left\{\frac{3}{32}\frac{1-\mu_1^2}{\mu_1^2} - \frac{\mu_1^2}{32}\left[\frac{16(\mu_1/\mu_2)^2 + 5}{4(\mu_1/\mu_2)^2 - 1}\right]\right\}\cosh(3\mu_1 t)$$
$$-\tfrac{1}{2}(\mu_1+\mu_2)^2\frac{(\mu_1/\mu_2)^4}{4(\mu_1/\mu_2)^2-1}\cosh(\mu_1+\mu_2)t - \tfrac{1}{2}(\mu_1-\mu_2)^2\frac{(\mu_1/\mu_2)^4}{4(\mu_1/\mu_2)^2-1}\cosh(\mu_1-\mu_2)t,$$

$$Q_{33}(t) = \left\{\frac{9}{32}\frac{1-\mu_1^2}{\mu_1^2} + \frac{\mu_1^2}{32}\left[\frac{32(\mu_1/\mu_2)^4 - 8(\mu_1/\mu_2)^2 + 5}{4(\mu_1/\mu_2)^2 - 1}\right]\right\}\cosh(\mu_1 t)$$
$$+\left\{\frac{3}{32}\frac{1-\mu_1^2}{\mu_1^2} - \frac{\mu_1^2}{32}\left[\frac{8(\mu_1/\mu_2)^2 - 7}{4(\mu_1/\mu_2)^2 - 1}\right]\right\}\cosh(3\mu_1 t)$$
$$-\tfrac{1}{2}(\mu_1^2+\mu_2^2)\frac{(\mu_1/\mu_2)^4}{4(\mu_1/\mu_2)^2-1}\{\cosh(\mu_1+\mu_2)t + \cosh(\mu_1-\mu_2)t\}.$$

E

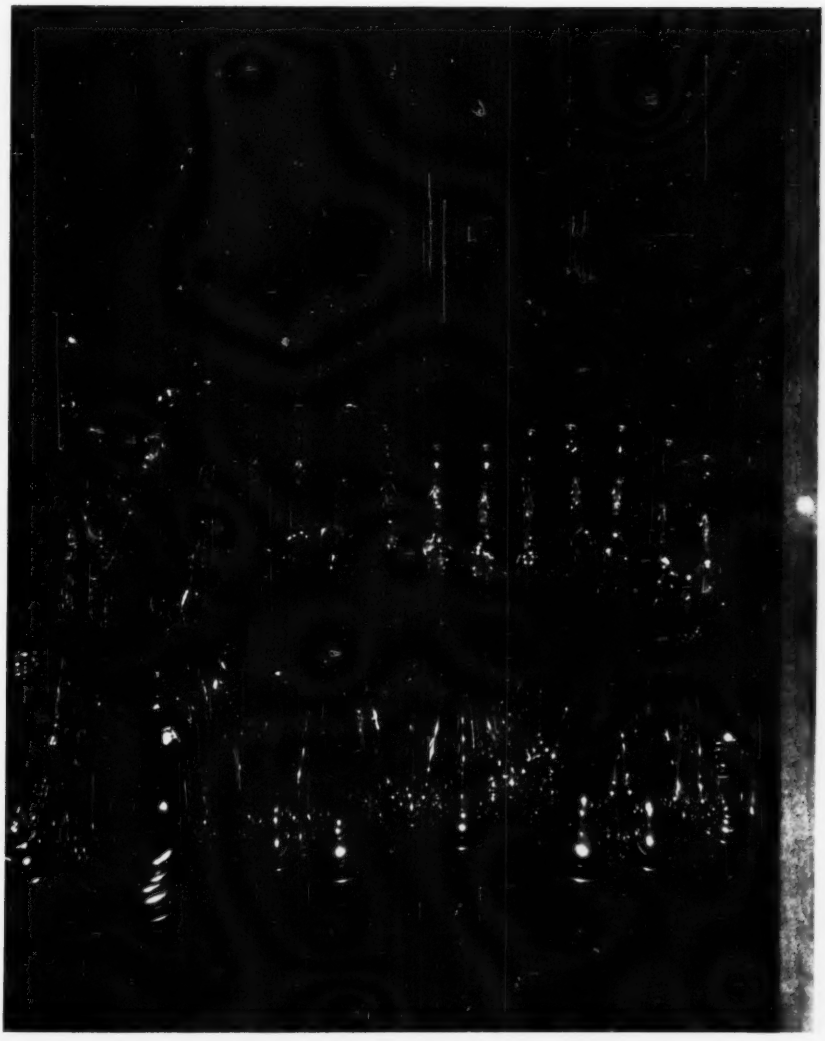

FIGURE 1. A later stage of wave development.

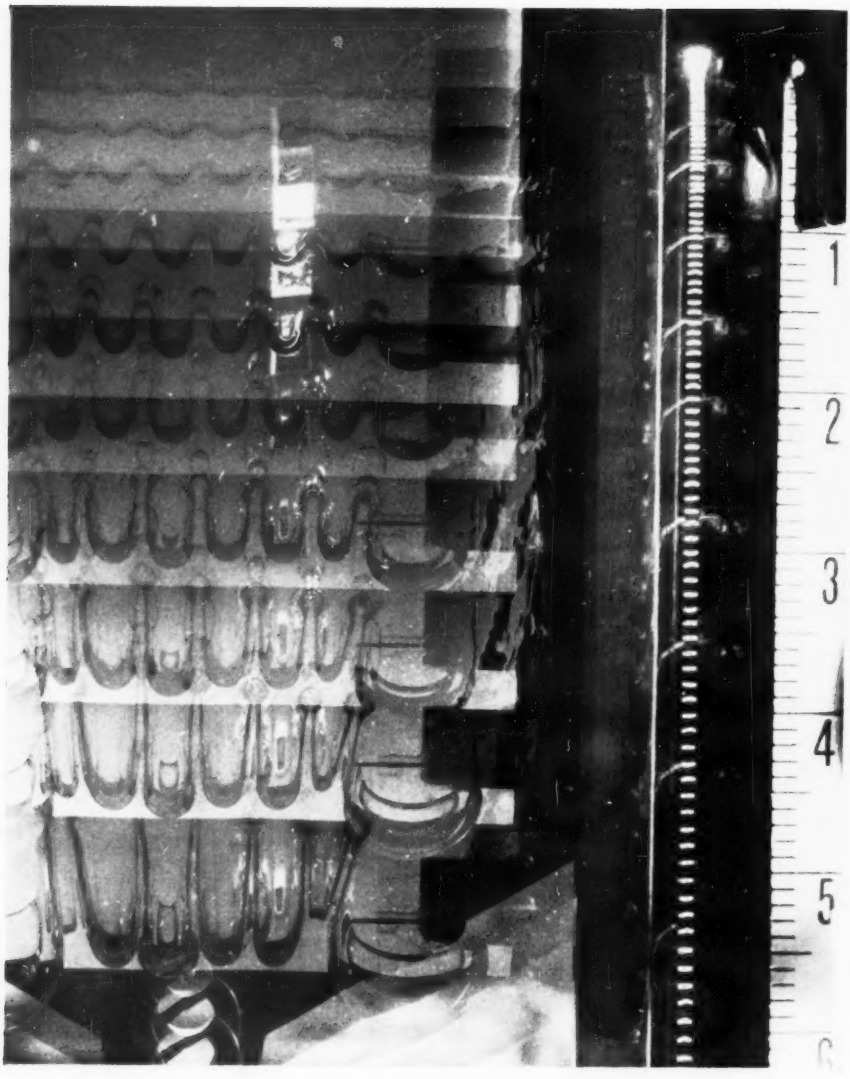

FIGURE 6. Typical photograph of position of interface at ten stages of growth.

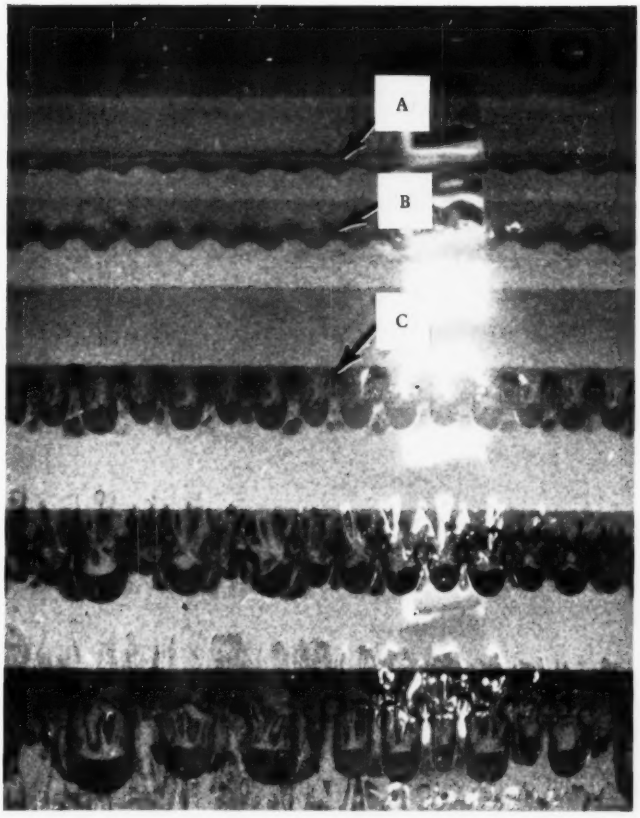

FIGURE 10. Example of over-stable growth.

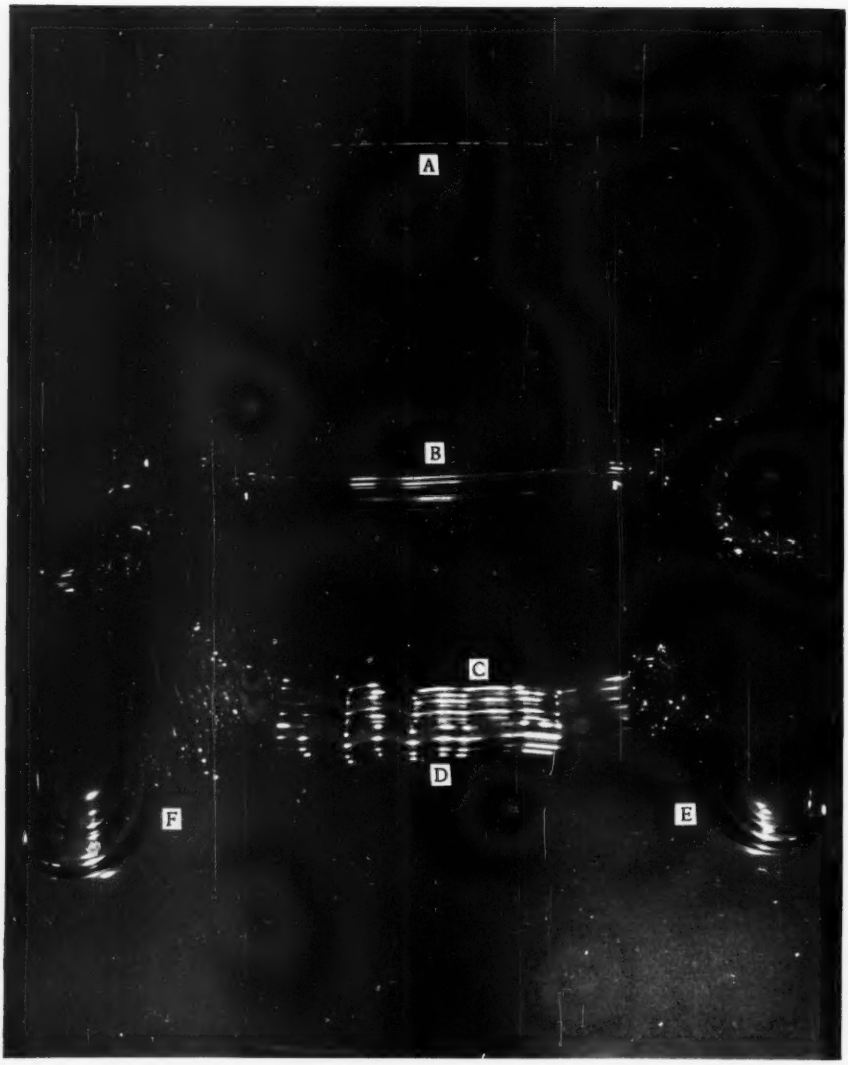

FIGURE 13. The growth of an initially undisturbed surface.

FIGURE 14. Oblique view of the growth of an initially undisturbed surface.

Appendix II

Amplitude functions of the third-stage approximation, equations (2.15) *and* (2.16)

$$C_{31}(t) = P_{31}(t) - B_{31}(t), \quad C_{33}(t) = P_{33}(t) - \tfrac{1}{3}B_{33}(t),$$

$$B_{31}(t) = a_{31}\cosh(\mu_1 t) + b_{31}\cosh(3\mu_1 t) + c_{31}\cosh(\mu_1 t)\cosh(\mu_2 t) + d_{31}\left(\frac{\mu_1}{\mu_2}\right)\sinh(\mu_1 t)\sinh(\mu_2 t) + e_{31}\mu_1 t\sinh(\mu_1 t),$$

$$B_{33}(t) = a_{33}\cosh(\mu_3 t) + b_{33}\cosh(3\mu_1 t) + c_{33}\cosh(\mu_1 t)\cosh(\mu_2 t) + d_{33}\left(\frac{\mu_1}{\mu_2}\right)\sinh(\mu_1 t)\sinh(\mu_2 t) + e_{33}\cosh(\mu_3 t),$$

where $P_{31}(t)$ and $P_{33}(t)$ are given in Appendix I, $\mu_r^2 = r(1-r^2k^2)$, and

$$a_{31} = -(b_{31}+c_{31}), \quad b_{31} = \frac{1}{8}\left\{\frac{3}{32}\frac{1-\mu_1^2}{\mu_1^2} - \frac{1}{4}\left[\frac{5(\mu_1/\mu_2)^2-1}{4(\mu_1/\mu_2)^2-1}\right]\right\},$$

$$c_{31} = 2\frac{(\mu_1/\mu_2)^6}{[4(\mu_1/\mu_2)^2-1]^2}, \quad d_{31} = 2\left(\frac{\mu_1}{\mu_2}\right)^4\frac{2(\mu_1/\mu_2)^2-1}{[4(\mu_1/\mu_2)^2-1]^2},$$

$$e_{31} = \frac{9}{64}\frac{1-\mu_1^2}{\mu_1^2} - \frac{1}{16}\left[\frac{16(\mu_1/\mu_2)^4 - 2(\mu_1/\mu_2)^2 - 1}{4(\mu_1/\mu_2)^2-1}\right],$$

$$a_{33} = -\frac{1}{1-(\mu_3/\mu_1)^2}\left\{\frac{27}{32}\frac{1-\mu_1^2}{\mu_1^2} + \frac{3}{16}\frac{4(\mu_1/\mu_2)^2+1}{4(\mu_1/\mu_2)^2-1}\right\},$$

$$b_{33} = -\frac{1}{9-(\mu_3/\mu_1)^2}\left\{\frac{9}{32}\frac{1-\mu_1^2}{\mu_1^2} - \frac{3}{16}\frac{4(\mu_1/\mu_2)^2+1}{4(\mu_1/\mu_2)^2-1}\right\},$$

$$c_{33} = 12\frac{(\mu_1/\mu_2)^2}{4(\mu_1/\mu_2)^2-1}\frac{1}{(\mu_3/\mu_1)^4 - 2[1+(\mu_2/\mu_1)^2](\mu_3/\mu_1)^2 + [1-(\mu_2/\mu_1)^2]^2},$$

$$d_{33} = -6\frac{(\mu_1/\mu_2)^2}{4(\mu_1/\mu_2)^2-1}\frac{1+(\mu_2/\mu_1)^2-(\mu_3/\mu_1)^2}{(\mu_3/\mu_1)^4 - 2[1+(\mu_2/\mu_1)^2](\mu_3/\mu_1)^2 + [1-(\mu_2/\mu_1)^2]^2}.$$

REFERENCES

Allred, J. & Blount, G. 1953 Experimental studies of Taylor instability. *Report Los Alamos Scientific Laboratory of the University of California*, no. LA-1600.

Bellman, R. & Pennington, R. H. 1954 Effects of surface tension and viscosity on Taylor instability. *Quart. J. Appl. Math.* **12**, 151.

Birkhoff, G. 1954 Taylor instability and laminar mixing. *Report Los Alamos Scientific Laboratory of the University of California*, no. LA-1862.

Carrier, G. F. 1953 On Taylor instability with large motions. *Un-numbered report Los Alamos Scientific Laboratory of the University of California.*

Davies, R. M. & Taylor, G. I. 1950 The mechanics of large bubbles rising through extended liquids and through liquids in tubes. *Proc. Roy. Soc.* A, **200**, 375.

Garabedian, P. R. 1957 On steady state bubbles generated by Taylor instability. *Applied Mathematics and Statistics Laboratory, Stanford University, Tech. Rep.* no. 59.

Ingraham, R. L. 1954 Taylor instability of the interface between superposed fluids. *Proc. Phys. Soc. Lond.* B, **67**, 748–52.

Lewis, D. J. 1950 The instability of liquid surfaces when accelerated in a direction perpendicular to their planes. II. *Proc. Roy. Soc.* A, **202**, 81–96.

Pennington, R. *et al.* 1953 Machine calculation of the growth of Taylor instability in an incompressible fluid. *Project Matterhorn Report*, no. PNJ-LA-11, p. 659.

Taylor, G. I. 1950 The instability of liquid surfaces when accelerated in a direction perpendicular to their planes. I. *Proc. Roy. Soc.* A, **201**, 192–6.

Dispersion due to molecular diffusion and macroscopic mixing in flow through a network of capillaries

By P. G. SAFFMAN
Cavendish Laboratory, Cambridge

(Received 27 May 1959)

This paper is concerned with the dispersion of a material quantity in the steady flow of a viscous fluid through a random network of capillaries (which is a useful model of a porous medium), for the case in which molecular diffusion and macroscopic mixing, due to the randomness of the streamlines, are both important. A Lagrangian correlation function is introduced and the longitudinal and lateral effective diffusivities are thereby calculated for all values of Ul/κ less than some large value. Here, l denotes the length of a capillary, U the mean velocity of the fluid, and κ the molecular diffusivity of the material quantity. The theory is compared with experimental observations of dispersion in flow through granular beds.

1. Introduction

In a recent paper (hereafter referred to as I), Saffman (1959) has investigated the dispersion of a dynamically neutral material quantity in a viscous fluid flowing through a porous medium, on the basis that the porous medium may be regarded as equivalent to a statistically isotropic network of straight capillaries. The discussion was restricted to the case in which the dispersion is primarily due to macroscopic mixing. This arises from the randomness of the streamlines through the network, and has an effective diffusivity of order Ul, where l is the length scale of the capillaries and U is the mean velocity of the fluid (the interstitial velocity). The results of I are then only valid when

$$\kappa \ll Ul, \tag{1.1}$$

where κ is the molecular diffusivity of the material quantity.

The method of I utilized the fact that the path of a fluid particle through a random network of capillaries can be treated as a random walk of randomly orientated steps, the velocity in a step depending upon its direction. This approach is clearly valid only if (1.1) is satisfied. An alternative approach, involving the idea of Lagrangian correlation functions which are well known in the theory of turbulent diffusion (see § 3 below), was suggested to the author by Dr T. H. Ellison in a private communication. As it happens, this method seems to be in general (although not always†) less useful than the random walk approach for the cases

† For example, it gives the dispersion in certain cases for small values of the time from the initial instant, whereas the random walk approach is an asymptotic theory for large values of this time.

considered in I. However, it affords a means of calculating the dispersion when (1.1) is not satisfied, i.e. when the effect of molecular diffusion is comparable with or greater than the macroscopic mixing, and this is the purpose of the present paper. The theory is not without practical importance since a network of capillaries is not an altogether unreasonable model of a porous medium and actual flows in which $Ul/\kappa \leqslant O(1)$ are not uncommon, e.g. the flow of gases through porous media.

2. The flow in the network

The work is restricted to the case in which the mean (macroscopic) velocity in the network is uniform and unidirectional, and the Reynolds number of the flow in the capillaries is sufficiently small for viscous effects to be dominant (this is equivalent to supposing that the mean flow satisfies Darcy's law). We also suppose (primarily for simplicity, as in I) that the pores are circular of radius a and of equal length l, where $a \ll l$. Then to a reasonable approximation, the average velocity in a capillary making an angle θ ($0 < \theta < \frac{1}{2}\pi$) with the direction of mean motion may be taken as

$$q = 3U\cos\theta, \tag{2.1}$$

where U is the average velocity of the entire fluid (see I, equation (2.19), where q is denoted by $\hat{q}$).

Since this paper is primarily concerned with the dispersion when κ is comparable with or greater than Ul, we shall suppose further that

$$\frac{Ul}{\kappa} \ll \frac{8l^2}{a^2} \quad \text{or} \quad \frac{l}{U} \gg \frac{a^2}{8\kappa}. \tag{2.2}$$

Now $a^2/8\kappa$ is the time scale for molecular diffusion to smooth out variations in concentration across the cross-section of a capillary, and the condition (2.2) expresses the condition that this is small compared with the time spent by a fluid particle in a capillary. The work of Taylor (1953; 1954) and Aris (1956) shows that in this case the concentration is approximately uniform over the cross-section and disperses, relative to axes moving with the velocity q, according to a diffusivity

$$\kappa + \frac{a^2q^2}{48\kappa} = D, \quad \text{say.} \tag{2.3}$$

Thus, when (2.2) is satisfied, the dispersion in the network is the same as if the velocity in each capillary were uniform throughout it, with the value q, and the material is subject to a diffusion process along the capillary with a diffusivity D (which depends upon the direction of the capillary). Note that

$$\frac{a^2q^2}{48\kappa^2} < \frac{3}{16}\frac{a^2}{l^2}\left(\frac{Ul}{\kappa}\right)^2 \ll \frac{3}{2}\frac{Ul}{\kappa}$$

by virtue of (2.2); so that $D \doteqdot \kappa$ if Ul/κ is not large compared with unity, and for all Ul/κ if $a \lll l$.

3. The Lagrangian correlation function

If $u(t)$ is the velocity component in the x-direction of a marked particle participating in a random process, the Lagrangian correlation function or covariance of the velocity u at time t and at a later time t' is $\overline{u(t)\,u(t')}$, where the bar denotes an average taken in an appropriate way (which will depend upon the precise nature of the random process). As was first pointed out by Taylor (1921), the displacement in the x-direction after time t is $X(t) = \int_0^t u(t')\,dt'$, and $dX/dt = u(t)$. Hence

$$\frac{d}{dt}\overline{X^2(t)} = 2\overline{X(t)\,u(t)} = 2\int_0^t \overline{u(t)\,u(t')}\,dt'. \tag{3.1}$$

For the case in which $u(t)$ is a stationary random function of the time (e.g. turbulent diffusion along a pipe; see Batchelor & Townsend 1956), $\overline{u(t)\,u(t')} = R(t-t')$, where $R(\tau)$ is the correlation function of the velocity u for a time interval τ (and depends only on τ and not on the time from any given instant), and the axes are chosen so that $\bar{u} = \bar{X} = 0$. The overbar here denotes an ensemble or stochastic average. Then (3.1) becomes

$$\frac{d\overline{X^2}}{dt} = 2\int_0^t R(\tau)\,d\tau, \tag{3.2}$$

and hence

$$\overline{X^2} = 2\int_0^t (t-\tau)\,R(\tau)\,d\tau. \tag{3.3}$$

Thus when t is large compared with the time scale for which the velocities at successive times are effectively correlated,

$$\overline{X^2} \sim 2t\int_0^\infty R(\tau)\,d\tau - 2\int_0^\infty \tau R(\tau)\,d\tau, \tag{3.4}$$

assuming that the integrals converge.

Thus,

$$\frac{\overline{X^2}}{2t} \sim \int_0^\infty R(\tau)\,d\tau,$$

and hence $\int_0^\infty R(\tau)\,d\tau$ may be regarded as the effective diffusivity. It should perhaps be pointed out for the benefit of readers unfamiliar with this analysis that (3.4) does not prove that the dispersion of a cloud of marked particles is given (asymptotically) by solutions of the diffusion equation with this effective diffusivity. To do this, it is necessary to prove that the probability distribution of X is normal, and that the displacement of different fluid particles in the same realization of the flow become statistically uncorrelated. However, there are usually no reasons for believing that these requirements are not satisfied, even though in most cases the formulation of rigorous proofs appears to present great difficulties.

If now $u(t)$ denotes the longitudinal component (i.e. in the direction of mean flow) of the velocity of a marked particle in steady flow through a random network of capillaries, we may proceed in an identical manner, provided the network is

statistically homogeneous. For convenience, we refer u and X to axes moving with the mean velocity, so that

$$u = (q+q_D)\cos\theta - U = U(3\cos^2\theta - 1) + q_D\cos\theta, \tag{3.5}$$

where $\theta = \theta(t)$ refers to the capillary containing the particle at time t. q_D is the random part of the velocity along the capillary due to the diffusion process with diffusivity D; it can be regarded as the velocity due to a Brownian motion equivalent to the diffusion process. That is, the velocity of a marked particle along a capillary fluctuates randomly because of the actual Brownian motion (caused by the collisions with other molecules) and because, as it moves to and fro across the capillary cross-section, the local mean velocity varies. These effects are mathematically equivalent to diffusion with diffusivity D and a corresponding fictitious Brownian velocity q_D with the properties

$$\langle q_D\rangle = 0 \quad \text{and} \quad \int_0^\infty \langle q_D(0)\, q_D(\tau)\rangle\, d\tau = D, \tag{3.6}$$

where $\langle\ \rangle$ denotes an average with respect to the Brownian motion.

This argument is, of course, valid only if the time interval over which successive values of q_D are correlated is small compared with the average time spent by a marked particle in a capillary. The former is at most $a^2/8\kappa$ (and will be much less if molecular transport dominates the diffusion process), whereas the order of magnitude of the latter is the lesser of l/U and $l^2/2\kappa$, and the argument is therefore valid by virtue of (2.2) and the condition $a \ll l$.

For the case of turbulent flow, the average denoted by the overbar is an ensemble average over all realizations of the flow. For the case of steady flow in a random network, the average is over all configurations of the network, but this is equivalent, owing to the statistical homogeneity of the network, to an average over the initial position and velocity of the particle. Thus, if f denotes a property of a marked particle which at time $t = 0$ was in a pore making an angle θ ($0 < \theta < \frac{1}{2}\pi$) with the direction of mean motion and with azimuthal angle ϕ ($0 < \phi < 2\pi$) about the same direction, was at a distance $l\xi$ ($0 < \xi < 1$) from the entrance of the capillary, and had a 'Brownian velocity' q_D, where the values of ξ, ϕ and $\mu = \cos\theta$ are uniformly distributed (since the proportion of pores in the range θ to $\theta + d\theta$ is $\sin\theta\, d\theta$), then

$$\bar{f} = \int_0^{\frac{1}{2}\pi}\int_0^1\int_0^{2\pi}\int_0^1 f\sin\theta\, d\theta\, d\xi\frac{d\phi}{2\pi}\, dp\,(q_D), \tag{3.7}$$

where $p(q_D)$ is the probability that the 'Brownian velocity' is less than q_D. Note that

$$\langle f\rangle = \int_0^1 f\, dp\,(q_D).$$

The value of $\bar{f}$ is independent of the precise origin of the time. Moreover, because of the statistical homogeneity, $\overline{u(t)} = \overline{u(0)} = 0$, and $\overline{u(t)\,u(t')}$ is a function of $(t'-t)$ only, equal to $R(t'-t)$, say. Thus the covariance is given by

$$R(\tau) = \overline{u(0)\,u(\tau)},$$

with the dispersion following from (3.3) and (3.4).

4. Calculation of the covariance

Let primed quantities denote values after a time τ from some initial instant. We have, writing $\mu = \cos\theta$, $\mu' = \cos\theta'$,

$$\overline{uu'} = U^2\overline{(3\mu^2-1)(3\mu'^2-1)} + \overline{\mu\mu' q_D q_D'} + U\{\overline{\mu q_D(3\mu'^2-1)} + \overline{\mu' q_D'(3\mu^2-1)}\}. \quad (4.1)$$

The last term in (4.1) is zero since $\langle q_D\rangle = 0$ and μ is independent of q_D.

Consider now the second term. The time interval over which q_D and q_D' are effectively correlated is small compared with the average time for the particle to leave the initial capillary and enter another. In other words $\langle q_D q_D'\rangle$ is non-negligible only for values of τ so small that the value of μ does not change (except for a negligible range of values of ξ for which a particle is next to a pore junction). Hence, to a reasonable approximation,

$$\overline{\mu\mu' q_D q_D'} = \overline{\mu^2 q_D q_D'} = \int_0^1 \mu^2 \langle q_D q_D'\rangle \, d\mu,$$

on integrating with respect to ξ and ϕ. (This is permissible since $\langle q_D q_D'\rangle$ will depend, to the present approximation, only on τ and the mechanics of the diffusion process with diffusivity D.)

It now follows from (3.6) that

$$\begin{aligned}\int_0^t \overline{\mu\mu' q_D q_D'}\, d\tau &= \int_0^1 D\mu^2\, d\mu \quad (\text{if } t \gg a^2/8\kappa) \\ &= \frac{\kappa}{3} + \frac{3}{80}\frac{a^2U^2}{\kappa} \end{aligned} \quad (4.2)$$

on substituting from (2.3) and (2.1).

Thus the problem reduces to the calculation of the first term in (4.1), namely,

$$\overline{(3\mu^2-1)(3\mu'^2-1)} = S(\tau), \quad \text{say.}$$

There are two distinct contributions to $S(\tau)$. First, there is the integral over those initial conditions such that the marked particle has not reached either of the ends of the initial capillary after time τ, so that $\mu = \mu'$; this gives a contribution $S_1(\tau)$, say. Secondly, there is the integral over the conditions for which the particle is in a different capillary after time τ (or has returned to the initial capillary after having passed through one of the junctions at its ends), giving a contribution $S_2(\tau)$, say. Then $S(\tau) = S_1(\tau) + S_2(\tau)$.

4.1. *The calculation of* $S_1(\tau)$

Let $P(\xi_0, \mu, \tau)$ denote the probability that a marked particle released at time $\tau = 0$ at a distance $l\xi_0$ from the entrance of the capillary has not reached one of the ends after time τ. Since $\mu = \mu'$ for a particle which remains in the initial capillary,

$$S_1(\tau) = \int_0^1\int_0^1\int_0^{2\pi} (3\mu^2-1)^2 P\, d\mu\, d\xi_0 \frac{d\phi}{2\pi}. \quad (4.3)$$

($P(\xi_0, \mu, \tau)$ is in fact the integral of $dp(q_D)$ over those modes of the 'Brownian motion' such that $\xi \neq 0$ or 1 in time τ.)

To calculate P, we note that the marked particles are convected along the capillary with velocity q ($= 3U\mu$) and diffuse relative to an origin moving at this speed with a diffusivity D. If they reach the ends of the capillary, they no longer contribute to $S_1(\tau)$. Hence the probability that the particle lies between $l\xi$ and $l(\xi+d\xi)$ after time τ (not having passed through $\xi = 0$ or 1) is $c\,d\xi$, where $c(\xi,\tau)$ is the solution of

$$\frac{\partial c}{\partial \tau} + \frac{q}{l}\frac{\partial c}{\partial \xi} = \frac{D}{l^2}\frac{\partial^2 c}{\partial \xi^2}, \tag{4.4}$$

subject to the initial condition $c = \delta(\xi-\xi_0)$ when $\tau = 0$ ($\delta(\xi)$ is the Dirac delta function) and the boundary conditions $c = 0$ when $\xi = 0$ and 1 for all τ. Then

$$P(\xi_0,\mu,\tau) = \int_0^1 c\,d\xi. \tag{4.5}$$

The solution of (4.4) is straightforward. It is easily verified that

$$C = \sum_1^\infty a_n \sin n\pi\xi\, e^{M\xi} \exp\{-(n^2\pi^2+M^2)\,D\tau/l^2\},$$

where

$$M = \frac{ql}{2D} = \frac{\frac{3}{2}Ul\mu}{\kappa + 3a^2U^2\mu^2/16\kappa}, \tag{4.6}$$

is a solution of the differential equation which satisfies the boundary conditions. It satisfies the initial conditions if

$$\delta(\xi-\xi_0) = \sum_1^\infty a_n \sin n\pi\xi\, e^{M\xi},$$

from which it follows by the usual methods of Fourier series that

$$a_n = 2\,e^{-M\xi_0}\sin n\pi\xi_0.$$

Then (4.5) gives

$$P(\xi_0,\mu,\tau) = \sum_1^\infty \frac{2n\pi}{n^2\pi^2+M^2}\{1-(-1)^n e^M\} e^{-M\xi_0}\sin n\pi\xi_0 \exp\{-(n^2\pi^2+M^2)\,D\tau/l^2\}. \tag{4.7}$$

On substituting in (4.3) and integrating with respect to ξ_0 and ϕ, we obtain

$$S_1(\tau) = \int_0^1 4\,d\mu\,(3\mu^2-1)^2 \sum_1^\infty \frac{n^2\pi^2}{(n^2\pi^2+M^2)^2} \times \{1-(-1)^n\cosh M\}\exp\{-(n^2\pi^2+M^2)\,D\tau/l^2\}, \tag{4.8}$$

where, in general, D and M are functions of $\mu = \cos\theta$.

This expression is fairly complicated. However, for the purpose of finding the effective diffusivity we only require the value of $\int_0^\infty S_1(\tau)\,d\tau$. Integrating (4.8) term by term and summing the infinite series, we find

$$\int_0^\infty S_1(\tau)\,d\tau = \int_0^1 4\,d\mu\,(3\mu^2-1)^2 \sum_1^\infty \frac{l^2}{D}\frac{n^2\pi^2}{(n^2\pi^2+M^2)^3}\{1-(-1)^n\cosh M\}$$

$$= \int_0^1 d\mu\,\frac{l^2}{4D}(3\mu^2-1)^2\left(\frac{1}{M}\coth M - \frac{1}{M^2}\right). \tag{4.9}$$

We have here made use of the following formulae (which may be obtained by expressing $\cosh \lambda x$ as a Fourier cosine series in x and putting $x = 0$ and π):

$$\frac{\cosh\lambda - 1}{2\lambda^2} = \sum_1^\infty \frac{1-(-1)^n\cosh\lambda}{n^2\pi^2+\lambda^2},$$

$$\frac{\lambda - \sinh\lambda}{2\lambda^2\sinh\lambda} = \sum_1^\infty \frac{(-1)^n}{n^2\pi^2+\lambda^2},$$

and the formulae which can be obtained by differentiating them with respect to λ.

4.2. *The calculation of* $S_2(\tau)$

The determination of $S_2(\tau)$ is rather more difficult. We shall assume, first, that the values of μ for successive capillaries are statistically independent; that is, when a particle reaches a junction the choice of the next capillary is independent of the previous one. The larger κ/Ul the better will be this assumption, because molecular diffusion has a much smaller correlation time scale than the macroscopic mixing.

It might now be thought that

$$S_2(\tau) = [\overline{(3\mu^2-1)(3\mu'^2-1)}]_{\mu\neq\mu'} = \overline{(3\mu^2-1)}\,\overline{(3\mu'^2-1)} = 0.$$

However, this argument is false because it ignores the fact that although μ' is independent of μ, it is not independent of the fact that the particle has passed through a junction during the time τ and this, as will be seen below, affects the probability distribution of μ'. Nevertheless, it is in fact true that $\int_0^\infty S_2(\tau)\,d\tau = 0$, so that $S_2(\tau)$ does not contribute to the effective diffusivity. $\int_0^\infty \tau S_2(\tau)\,d\tau \neq 0$, so there is a contribution to $\overline{X^2}$. The remainder of this section is devoted to the calculation of $S_2(\tau)$, or, to be more precise, its Laplace transform which is sufficient for our purposes.

Let $Q(\mu,t)\,d\mu$ denote the probability that a marked particle released at a junction at $t = 0$ is in a capillary in the range μ to $\mu + d\mu$ after time t.

The probability that a particle released at $t = 0$ at a distance $l\xi$ from the entrance to a capillary with a given value of μ reaches a junction in the time interval from t to $t + dt$ is

$$\frac{\partial}{\partial t}\{1 - P(\xi,\mu,t)\}\,dt,$$

where $P(\xi,\mu,t)$ is given by (4.7). Hence the probability that this particle is in a capillary in the range μ' to $\mu' + d\mu'$ after time τ from the initial instant of release is

$$d\mu' \int_0^\tau Q(\mu', \tau - t)\frac{\partial}{\partial t}\{1 - P(\xi,\mu,t)\}\,dt = L(\xi,\mu,\mu',\tau)\,d\mu', \quad \text{say.} \tag{4.10}$$

Then by definition

$$S_2(\tau) = \int_0^1\int_0^1\int_0^1 d\xi\,d\mu\,d\mu'(3\mu^2-1)(3\mu'^2-1)\,L(\xi,\mu,\mu',\tau). \tag{4.11}$$

If all the pores leading from a junction had equal probability of being entered by a marked particle, then $Q(\mu, t) = 1$ and $S_2(\tau) \equiv 0$. However, this is not the case since there is a tendency for particles to enter pores in which q is large rather than those in which it is small. (If $\kappa \ll Ul$, the probability of a particle leaving a junction by a pore in the range of width $d\mu$ is $2\mu\, d\mu$, and $Q(\mu, t) = 2\mu$ for $t \ll lU$.) On the other hand, for large values of t the particle will (so to speak) forget where it was at $t = 0$ and the probability of the particle being in a capillary in a particular direction will become independent of the direction, i.e. $Q(\mu, t) \to 1$ as $t \to \infty$. But since $S_2(\tau)$ depends upon the values of $Q(\mu, t)$ for all values of t between 0 and τ, $S_2(\tau)$ will not in general vanish.

It is useful now to take Laplace transforms with respect to the time. These will be denoted by an asterisk, i.e. the transform of $f(t)$ is $f^*(p)$. Then since (4.10) is a convolution, we have on integrating with respect to ξ,

$$S_2^*(p) = \int_0^1 \int_0^1 d\mu\, d\mu' (3\mu^2 - 1)(3\mu'^2 - 1)\, Q^*(\mu', p)\{1 - pP_1^*(\mu, p)\}, \tag{4.12}$$

where

$$P_1^*(\mu, p) = \sum_1^\infty \frac{4n^2\pi^2}{(n^2\pi^2 + M^2)^2} \frac{1 - (-1)^n \cosh M}{p + (n^2\pi^2 + M^2) D/l^2}. \tag{4.13}$$

Now for the effective diffusivity, we really require only $\int_0^\infty S_2(\tau)\, d\tau$ and this is $S_2^*(O)$. It now follows from (4.11) and (4.12) that $S_2^*(O) = 0$, provided

$$\lim_{p \to 0} \int_0^1 (3\mu'^2 - 1)\, Q^*(\mu', p)\, d\mu' \tag{4.14}$$

is finite. We know intuitively that $Q(\mu', t) \to 1$ as $t \to \infty$, and if we assume that $Q(\mu', t) - 1$ is integrable from 0 to ∞, it follows that $Q^*(\mu', p) = p^{-1} + O(1)$ as $p \to 0$, and hence that (4.14) is finite. However, this last assumption is far from obvious ($Q(\mu', t) - 1$ might be $O(1/t)$) and it therefore seems worth while presenting an explicit calculation of $Q^*(\mu', p)$.

Let $E(\mu', t)\, d\mu'$ denote the probability that a particle released at a junction is after time t in a capillary leading from this junction in the range μ' to $\mu' + d\mu'$, and in this time t has not returned to the junction or gone to the other end of the pore. The value of μ' in (and only in) $E(\mu', t)$ ranges from -1 to $+1$ (elsewhere $0 \leqslant \mu' \leqslant 1$), to take account of the fact that the particle may diffuse into a capillary against the direction of the stream. Then $Q(\mu', t)$ is related to $E(\mu', t)$ by

$$Q(\mu', t) = E(\mu', t) + E(-\mu', t) + \int_0^t dt'\, Q(\mu', t - t') \frac{\partial}{\partial t'} \left[1 - \int_{-1}^{+1} E(\mu, t')\, d\mu\right], \tag{4.15}$$

the last term being the probability that it was at a junction sometime during the interval 0 to t and went on from there into a pore with μ' in the appropriate range. Taking Laplace transforms of (4.15), we obtain

$$Q^*(\mu', p) = E^*(\mu', p) + E^*(-\mu', p) + Q^*(\mu', p)\left[1 - p \int_{-1}^{+1} E^*(\mu, p)\, d\mu\right], \tag{4.16}$$

since $\int_{-1}^{+1} E(\mu, 0)\, d\mu = 1$.

Hence
$$Q^*(\mu', p) = \frac{E^*(\mu', p) + E^*(-\mu', p)}{p\int_{-1}^{+1} E^*(\mu, p)\, d\mu}. \tag{4.17}$$

Now $E(\mu, t)$ may be determined in a manner similar to that for $P(\xi, \mu, t)$, except that care is required because the particle starts at a junction. We overcome this difficulty by taking $c = 1/\Delta T$, for $\xi = 0$ and $0 < t < \Delta T$, as the boundary condition on the concentration $c(\xi, t)$ along the capillary, where $c(\xi, t)$ satisfies (4.4); and $c = 0$ initially, $c = 0$ at $\xi = 1$ for all t, and $c = 0$ at $\xi = 0$ for $t > \Delta T$. Then, we take

$$E(\mu, t) = \lim_{\Delta T \to 0} \int_0^1 c(\xi, t)\, d\xi, \quad \text{and} \quad E^*(\mu, p) = \lim_{\Delta T \to 0} \int_0^1 c^*(\xi, p)\, d\xi.$$

Taking the Laplace transform of (4.4), we find that $c^*(\xi, p)$ satisfies

$$\frac{\partial^2 c^*}{\partial \xi^2} - 2M\frac{\partial c^*}{\partial \xi} - \frac{l^2 p}{D} c^* = 0, \tag{4.18}$$

which has to be solved subject to the boundary conditions

$$c^*(1, p) = 0, \quad c^*(0, p) = \frac{1}{p\Delta T}[1 - e^{-p\Delta T}] \to 1 \quad \text{as} \quad \Delta T \to 0.$$

The solution of (4.18) is perfectly straightforward (it is a linear equation with constant coefficients) and we find after a little algebra that

$$E^*(\mu, p) = \frac{M \sinh (M^2 + l^2 p/D)^{\frac{1}{2}} + (M^2 + l^2 p/D)^{\frac{1}{2}} \{\cosh (M^2 + l^2 p/D)^{\frac{1}{2}} - e^M\}}{(l^2 p/D) \sinh (M^2 + l^2 p/D)^{\frac{1}{2}}}. \tag{4.19}$$

(4.19), (4.17), (4.13) and (4.12) thus give an explicit expression for $S_2^*(p)$, and hence determine, in principle, $S_2(\tau)$. We find from (4.19) and (4.17) that, as $p \to 0$,

$$pQ^*(\mu, p) = 1 + \tfrac{1}{4} l^2 p \left[\frac{1 - M \coth M}{M^2 D} - \int_0^1 d\mu\, \frac{1 - M \coth M}{M^2 D}\right], \tag{4.20}$$

thus verifying that (4.14) is finite and that

$$\int_0^\infty S_2(\tau)\, d\tau = 0. \tag{4.21}$$

5. The longitudinal dispersion

Collecting together the results of § 4, we have from (4.2), (4.9) and (4.21), the result that the longitudinal dispersion in a network of capillaries is asymptotically described by an effective diffusivity

$$\kappa_l = \frac{\kappa}{3} + \frac{3}{80}\frac{a^2 U^2}{\kappa} + \frac{l^2 U^2}{4}\int_0^1 (3\mu^2 - 1)^2 \frac{M \coth M - 1}{DM^2}\, d\mu. \tag{5.1}$$

where
$$M = \frac{3}{2}\frac{Ul\mu}{D} \quad \text{and} \quad D = \kappa + \frac{3a^2 U^2 \mu^2}{16\kappa}. \tag{5.2}$$

The expression for κ_l is valid provided we may replace the upper limit of integration in the expression (3.3) for $\overline{X^2}$ by $t = \infty$. This is permissible when the

exponential term in (4.8) involving the time is small compared with unity and $S_2^*(1/t) \doteqdot S_2^*(0)$, which is the case if $t \gg l^2/\kappa$.

When there is no convection and no macroscopic mixing (i.e. $U = 0$), it follows from (5.1) that $\kappa_l = \frac{1}{3}\kappa$. Now experiments on dispersion in granular beds (e.g. Carberry & Bretton 1958) give values of $\kappa_l \doteqdot \frac{2}{3}\kappa$, when convection is negligible. The discrepancy seems to be due quite simply to a granular bed not being a random network of capillaries.

However, this is not to say that the present theory is not applicable to dispersion in granular beds; it is at least of qualitative value. Moreover, when there is flow through a granular bed, the streamlines will approximate to those through a random network of capillaries, and it is not too unreasonable to suppose that the macroscopic mixing due to the meanderings of the streamlines is given approximately by the terms in (5.1) involving U. In other words, we suggest that (for the purposes of comparison with experiments in granular beds) the above expression for κ_l be replaced by

$$\kappa_l = \kappa_m + \frac{3}{80}\frac{a^2U^2}{\kappa} + \tfrac{1}{4}l^2U^2\int_0^1 (3\mu^2-1)^2\frac{M\coth M - 1}{DM^2}\,d\mu, \tag{5.3}$$

where κ_m is the measured diffusivity when $U = 0$ (and M and D are given by (5.2)). The closer the geometry of the bed approaches that of a random network, then presumably the closer will be κ_m to $\frac{1}{3}\kappa$. The calculating of κ_m presents great difficulties; however, it may be readily measured by means of an electrical analogue (see, for example, Wooding 1959).

The expression (5.3) for κ_l still contains two quantities, a and l, whose values have to be fixed in some way from the properties of the granular bed. For a, a reasonable value is $a = (24k/\sigma)^{\frac{1}{2}}$, where k and σ are the permeability and porosity, respectively, of the bed. The bed and the random network will then have the same permeability (see I, § 2). In any case, the values of κ_l are fairly insensitive to changes in a, provided a/l is not greater than about $\frac{1}{5}$ (which is about the largest permissible value consistent with the assumptions about the flow through the capillaries).

As regards l, probably the best value to take is the mean diameter of the grains, and it is not possible to be more precise than this. However, it may be an underestimate, especially if there are cracks or fissures or channels running through the bed. The presence of these would be equivalent to increasing the value of l, since they roughly correspond to longer capillaries. We can in fact work out the theory for a network of capillaries of varying lengths; this simply gives (5.1) averaged over the lengths of the capillaries, but since the distribution of capillary lengths is unknown, there is no real loss in supposing them to be all equal to some suitably chosen value which may be somewhat larger than the mean particle diameter if channels run through the bed or the packing is not too uniform.

The longitudinal diffusivity as given by (5.3) may be evaluated numerically for given values of a/l and Ul/κ. For $Ul/\kappa \ll 1$,

$$\kappa_l \doteqdot \kappa_m + \frac{1}{15}\frac{U^2l^2}{\kappa}, \tag{5.4}$$

and for $Ul/\kappa \gg 1$ (but not so large that (2.2) is violated), it can be shown that

$$\kappa_l \doteq \frac{Ul}{6}\left(\log_e \frac{3}{2}\frac{Ul}{\kappa} - \frac{17}{12} - \frac{1}{8}\frac{a^2}{l^2}\frac{Ul}{\kappa}\right) + \kappa_m + \tfrac{4}{9}\kappa + O\left(\frac{\kappa^2}{Ul}\right). \tag{5.5}$$

The expression (5.5) may be compared with the equivalent expression obtained in I (equations (4.4a) and (4.5)) by means of the random walk analysis, namely

$$\kappa_l \doteq \frac{Ul}{6}\left(\log_e \frac{3Ul}{2\kappa} - \frac{1}{4}\right). \tag{5.6}$$

The leading terms agree, providing a useful check on the analysis. The difference in the other terms seems to arise from the fact that in I molecular diffusion was taken into account only in an approximate manner.

Hiby (1959) gives the following empirical formula for longitudinal dispersion in beds of glass spheres:

$$\kappa_l = 0{\cdot}67\kappa + \frac{0{\cdot}65\,Ul}{1 + 6{\cdot}7(\kappa/Ul)^{\frac{1}{2}}}, \tag{5.7}$$

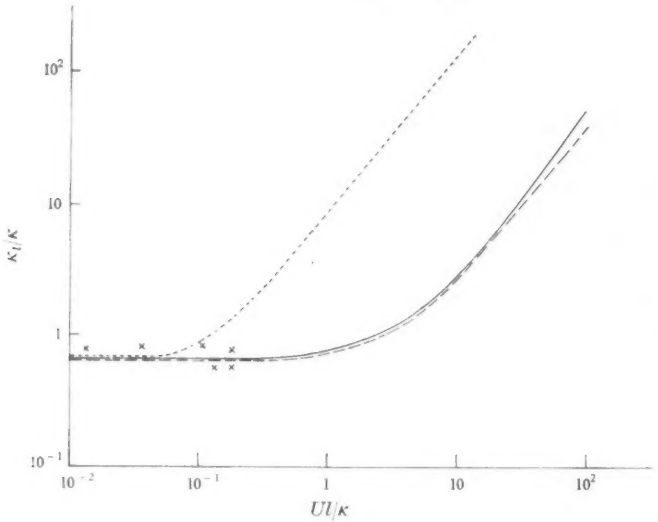

FIGURE 1. Comparison of theory and experiment for the longitudinal dispersion. — — —, Hiby (1959); - - - - -, Blackwell *et al.* (1959); ×, Carberry & Bretton (1958); ——, calculated values from (5.3) with $a/l = \frac{1}{5}$ and $\kappa_m = \frac{2}{3}\kappa$.

where l is the mean diameter of the spheres. According to this expression, macroscopic mixing is completely negligible for $Ul/\kappa < 0{\cdot}5$. On the other hand, Blackwell, Rayne & Terry (1959) suggest on the basis of experiments in beds of sand the empirical expression:

$$\frac{\kappa_l}{\kappa} = 8{\cdot}8\left(\frac{Ul}{\kappa}\right)^{1{\cdot}17} \quad \text{for} \quad \frac{Ul}{\kappa} > 0{\cdot}5, \tag{5.8}$$

where l is the mean particle diameter. Also, they find that macroscopic mixing becomes significant at about $Ul/\kappa = 0{\cdot}04$.

These results are shown on figure 1, together with the theoretical curve taking $a/l = \frac{1}{5}$ and $\kappa_m = \frac{2}{3}\kappa$ ($a/l = \frac{1}{10}$ is probably a better value for a bed of sand but the difference in the calculated values is slight). It will be seen that the theory predicts that macroscopic mixing is negligible for $Ul/\kappa < 0{\cdot}5$, and the calculated values are in remarkably good agreement with the expression of Hiby. Nevertheless, the discrepancy between the experimental observations is such that it is not possible to say definitely whether or not the theory is valid when applied to granular beds. A possible explanation of the differences might be that the packing of the sand in some of the experiments was not uniform, in particular there may have been gaps or channels along the walls of the cylinders containing the medium. Hiby states that he was unable to obtain uniform packing right up to the walls of his apparatus, and he went to great trouble to eliminate the wall effect which could affect the results to a factor of two or more. As mentioned previously, non-uniform packing or the presence of channels along the walls would be equivalent to an increase in the value of l, and would thereby reduce the discrepancy between the calculated values and the empirical curve of Blackwell *et al.*; but it is not yet possible to say whether this explanation is sufficient.

6. The skewness of the longitudinal dispersion

In the previous section, it was tacitly assumed that the longitudinal distribution of concentration was Gaussian, so that it is meaningful to regard $\overline{X^2}/2t$ as an effective diffusivity. We shall now obtain an estimate of $\overline{X^3}$ in order to see how Gaussian the distribution actually is. This calculation is not without practical importance since observed concentration profiles are often skew.

By arguments similar to those in § 3, it follows that

$$\frac{d}{dt}\overline{X^3} = 3\overline{X^2(t)\,u(t)} = 3\int_0^t\int_0^t \overline{u(t)\,u(t')\,u(t'')}\,dt'\,dt''$$

$$= 6\int_0^t d\tau_2 \int_0^{\tau_2} R_3(\tau_1, \tau_2)\,d\tau_1, \tag{6.1}$$

where

$$R_3(\tau_1, \tau_2) = \overline{u(0)\,u(\tau_1)\,u(\tau_2)} \tag{6.2}$$

is a triple Lagrangian correlation function.

Now there are two types of contribution to $R_3(\tau_1, \tau_2)$. First, there are the contributions from the cases in which the particle is in the same capillary after time τ_2 from the instant of release; and secondly, from the cases in which it is in a different capillary after time τ_2. We shall assume that the second contribution has negligible effect on the value of $\overline{X^3}(t)$ for large values of t (as is the case for $\overline{X^2}$). Although this assumption is highly plausible, a rigorous proof seems to present great difficulties.

To calculate the first contribution, we require the probability that a particle released at a given position is in the same capillary after time intervals τ_1 and τ_2, where $\tau_1 < \tau_2$, and the particle has not been to one of the ends of the capillary and

come back again (this is counted as being in a different pore). This probability is just $P(\xi_0, \mu, \tau_2)$, as given by (4.7). Hence, for $\tau_1 < \tau_2$,

$$R_3(\tau_1, \tau_2) = U^3 \int_0^1 \int_0^1 (3\mu^2 - 1)^3 P(\xi_0, \mu, \tau_2)\, d\xi_0\, d\mu$$
$$= 4U^3 \int_0^1 (3\mu^2 - 1)^3\, d\mu \sum_1^\infty \frac{n^2\pi^2}{(n^2\pi^2 + M^2)^2}$$
$$\times \{1 - (-1)^n \cosh M\} \exp\{-(n^2\pi^2 + M^2)\, D\tau/l^2\}, \quad (6.3)$$

since the contribution from the 'Brownian velocity' vanishes. Then

$$\overline{X^3} \sim t \int_0^\infty d\tau_2 \int_0^{\tau_2} R_3\, d\tau_1$$
$$= 4U^3 t \int_0^1 (3\mu^2 - 1)^3 \left(\frac{l^2}{D}\right)^2 \sum_1^\infty \frac{n^2\pi^2}{(n^2\pi^2 + M^2)^4} \{1 - (-1)^n \cosh M\}\, d\mu$$
$$= \frac{U^3 l^4 t}{24} \int_0^1 (3\mu^2 - 1)^3 \frac{1}{D^2} \left\{\frac{1}{M^2} + \frac{3}{M^2 \sinh^2 M} - \frac{3}{M^4}\right\} d\mu. \quad (6.4)$$

If $Ul/\kappa \ll 1$, then

$$\overline{X^3} \doteq \frac{U^3 t l^4}{120\kappa^2}; \quad (6.5)$$

and if $Ul/\kappa \gg 1$, it can be shown that

$$\overline{X^3} \doteq -\frac{U^2 t l^3}{40\kappa}. \quad (6.6)$$

(An estimate of $\overline{X^3}$ for large values of Ul/κ is given in equation (3.20) of I. The expressions are the same, except for the numerical coefficient.)

It is clear that $\overline{X^3}$ increases linearly with t and in this sense the distribution becomes more skew as the time increases. However, the skewness factor $\overline{X^3}/(\overline{X^2})^{\frac{3}{2}}$ tends to zero like $t^{-\frac{1}{2}}$, and since there is no reason to doubt that the higher moments tend to those of a Gaussian distribution as $t^{-\frac{1}{2}} \to 0$ (a rigorous proof of this statement is difficult and will not be attempted here), we may say that the distribution is asymptotically Gaussian.

A measure of the departure from normality is given by the value of the skewness factor. If $Ul/\kappa < O(1)$, the skewness factor is always small. The more interesting case is when $Ul/\kappa \gg 1$. The condition that the skewness factor be small compared with unity is then

$$\left(\frac{Ut}{l}\right)^{\frac{1}{2}} \gg \frac{Ul}{20\kappa} \left(\log \frac{3Ul}{2\kappa}\right)^{-\frac{3}{2}}. \quad (6.7)$$

(This condition is similar to that given in I, equation (4.4*a*), but it is a little less restrictive.)

7. Lateral dispersion

The dispersion in a fixed direction perpendicular to the mean velocity can be calculated in a similar manner as that in the longitudinal direction. We take y- and z-axes perpendicular to the mean velocity, and denote by ϕ the azimuthal angle between the y-axis and the projection of the capillary on the yz-plane. That

is, if q is the velocity of fluid in a capillary, the components of velocity parallel to the axes are $q\cos\theta$, $q\sin\theta\cos\phi$, $q\sin\theta\sin\phi$. It follows from the assumption of statistical isotropy that all values of ϕ ($0 \leqslant \phi < 2\pi$) are equally likely.

The velocity of a particle in the y-direction is

$$v(t) = 3U\cos\theta\sin\theta\cos\phi + q_D\sin\theta\cos\phi, \tag{7.1}$$

and the lateral diffusivity is

$$\kappa_l = \int_0^\infty \overline{v(0)\,v(\tau)}\,d\tau. \tag{7.2}$$

We have, as in § 4,

$$\overline{vv'} = 9U^2\overline{\cos\theta\sin\theta\cos\phi\cos\theta'\sin\theta'\cos\phi'} + \overline{q_D q_D'\sin^2\theta\cos^2\phi}. \tag{7.3}$$

The last term on the right-hand side of (7.3) makes a contribution to κ_l of amount

$$\begin{aligned}\overline{D\sin^2\theta\cos^2\phi} &= \frac{\kappa}{3} + \frac{3a^2U^2}{16\kappa}\int_0^1 \mu^2(1-\mu^2)\,d\mu \\ &= \frac{\kappa}{3} + \frac{1}{80}\frac{a^2U^2}{\kappa}.\end{aligned} \tag{7.4}$$

Now to calculate

$$S_l(\tau) = 9U^2\,\overline{\cos\theta\sin\theta\cos\phi\cos\theta'\sin\theta'\cos\phi'},$$

it is necessary to make some assumption about the statistical correlation between the values of ϕ in successive capillaries occupied by a marked particle. In the present paper, we shall assume that these are statistically independent, and also that the value of ϕ is independent of θ. The contribution to $S_l(\tau)$ from particles which have changed capillaries in time τ is then identically zero, and hence

$$S_l(\tau) = 9U^2\int_0^1\int_0^1\int_0^{2\pi} \mu^2(1-\mu^2)\cos^2\phi\,P(\xi_0,\mu,\tau)\,d\xi_0\,d\mu\,d\phi, \tag{7.5}$$

where $P(\xi_0,\mu,\tau)$ is given by (4.7).

The assumption of the statistical independence of the values of ϕ in different capillaries is somewhat dubious when $Ul/\kappa \gg 1$ (as discussed in more detail in I). Roughly speaking, this is because the lateral meanderings of the streamlines are restricted by continuity requirements. However, the smaller is Ul/κ, the better will be the assumption, since the capillaries by which a marked particle leaves a junction are equally likely if molecular diffusion is dominant.

$S_l(\tau)$ may be integrated with respect to τ, giving

$$\int_0^\infty S_l(\tau) = \frac{9U^2l^2}{8}\int_0^1 \mu^2(1-\mu^2)\frac{1}{D}\left(\frac{1}{M}\coth M - \frac{1}{M^2}\right)d\mu. \tag{7.6}$$

Then κ_l is the sum of (7.4) and (7.6). Altering the terms independent of U so that $\kappa_l = \kappa_m$ when $U = 0$ (for the same reasons as given in § 5), we have

$$\kappa_l = \kappa_m + \frac{1}{80}\frac{a^2U^2}{\kappa} + \frac{9U^2l^2}{8}\int_0^1 \mu^2(1-\mu^2)\frac{1}{D}\left(\frac{1}{M}\coth M - \frac{1}{M^2}\right)d\mu. \tag{7.7}$$

It will be noticed that $\kappa_l \neq \kappa_l$, in accord with intuition and experience.

When $Ul/\kappa \ll 1$,

$$\kappa_l \doteqdot \kappa_m + \frac{U^2 l^2}{40\kappa}. \tag{7.8}$$

At the other extreme when $Ul/\kappa \gg 1$, then

$$\kappa_l \doteqdot \tfrac{3}{16} Ul + \frac{1}{40}\frac{a^2U^2}{\kappa} + \kappa_m - \frac{\kappa}{3} + O\left(\frac{\kappa^2}{Ul}\right). \tag{7.9}$$

The leading term of this expression agrees with that obtained by the random walk analysis.

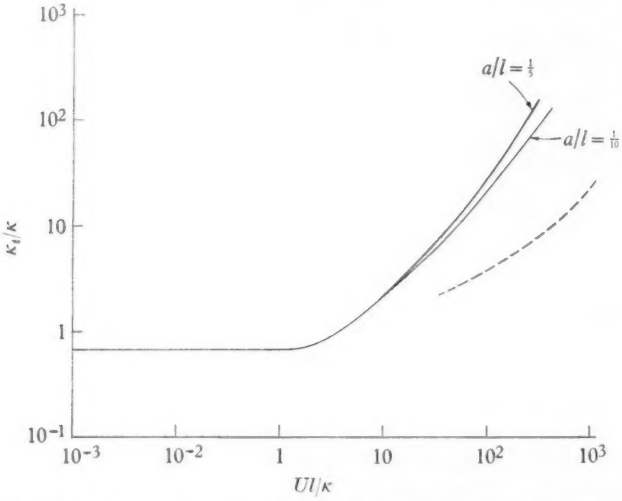

FIGURE 2. The lateral dispersion. ——, Calculated values with $\kappa_m = \frac{2}{3}\kappa$ and $a/l = \frac{1}{5}$ and $\frac{1}{10}$; – – –, observed values (Hiby 1959).

The theoretical values with $\kappa_m = \frac{2}{3}\kappa$ and $a/l = \frac{1}{5}$ and $\frac{1}{10}$ are shown on figure 2. Also shown are some measured values by Hiby (1959), in beds of spheres, for large values of Ul/κ. The agreement is not good but a statistical correlation between successive values of ϕ, consistent with a restricted lateral displacement of the streamlines, could reduce the calculated values of κ_l considerably. The neglect of this correlation probably accounts for the differences between theory and experiment, and it is hoped to investigate this in later work.

REFERENCES

ARIS, R. 1956 *Proc. Roy. Soc.* A, **235**, 67.

BATCHELOR, G. K. & TOWNSEND, A. A. 1956 Article in *Surveys in Mechanics* (ed. G. K. Batchelor and R. M. Davies), p. 352. Cambridge University Press.

BLACKWELL, R. J., RAYNE, J. R. & TERRY, W. M. 1959 *J. Petrol Tech.* **217**, 1.

CARBERRY, J. J. & BRETTON, R. H. 1958 *J. Amer. Inst. Chem. Engrs*, **4**, 367.

HIBY, J. W. 1959 Paper presented at conference on displacement in porous media, Imperial College, London, March 1959.

SAFFMAN, P. G. 1959 *J. Fluid Mech.* **6**, 321.

TAYLOR, G. I. 1921 *Proc. Lond. Math. Soc.* **20**, 196.

TAYLOR, G. I. 1953 *Proc. Roy. Soc.* A, **219**, 186.

TAYLOR, G. I. 1954 *Proc. Roy. Soc.* A, **225**, 473.

WOODING, R. W. 1959 *Proc. Roy. Soc.* A, **252**, 120.

Wave resistance to vertical motion in a stratified fluid

By F. W. G. WARREN
Imperial College, London

(Received 14 March 1959, and in revised form 12 July 1959)

When a body moves through a stratified fluid, i.e. one whose density decreases upwards, gravity waves are set up and this causes a resistance to motion. An axisymmetric case is considered in which a body moves steadily and vertically through a fluid whose density decreases exponentially upwards. The fluid is supposed perfect, incompressible, and unbounded in all directions. The equations of motion are linearized, and with a fairly general initial motion of the surrounding fluid, the limit of the solution as $t \to \infty$ is evaluated. Transform methods are used to solve the equation of motion, and the methods of steepest descents and stationary phase are used to obtain approximate solutions.

Streamlines and the distortion of the constant density levels for a spindle-shaped body are shown. The curves of resistance against a function of the velocity for the circular cylinder, the sphere, and a spindle-shaped body are also given. A criterion is given for when the maximum wave resistance for a sphere may be expected, and an estimate of this maximum resistance is made.

1. Introduction

The problem of a body rising through a stratified fluid has applications in the study of buoyant convection currents rising through stable surroundings. This type of motion frequently occurs in the atmosphere when a thermal rises through a cumulus cloud. In this case the expansion of the thermal during its ascent causes a condensation of the water vapour within it. The release of latent heat warms the thermal, and this causes a further expansion and a further decrease in density of the rising air mass. This offsets the loss in buoyancy as the thermal rises to higher, less dense regions, and the upward motion is maintained (Scorer 1958). For the purposes of this problem, the atmosphere may be regarded as an incompressible fluid whose density decreases upwards, and whose static stability parameter is the same as that of the atmosphere (Scorer 1950, 1958); and the thermal can be taken to have a fixed, spherical shape. What is required is a measure of the energy used to generate the gravity waves set up in the stable surroundings of the cumulus cloud as the thermal rises, so that the importance of this effect on the motion and growth of the thermal can be estimated. This is obtained in § 10.

The problem considered in this paper may also be regarded as a first approach to the study of the dispersion of stirring motions into gravity waves. A criterion is suggested for when the maximum amount of energy is used to make waves, and hence for when the maximum amount of energy is absorbed and dispersed by gravity waves.

2. The equation of motion

Perturbation methods are applied to the basic equations of flow to obtain a linear equation governing the stream function of the perturbation.

The notation employed, is, using, cylindrical co-ordinates:

z = height (the z-axis is coincident with that of the body),

r = horizontal co-ordinate,

(u, w) = velocity of the fluid,

W = steady vertical velocity of the body (positive upwards),

β = static stability parameter $= -\dfrac{1}{\rho_0}\dfrac{d\rho_0}{dz}$ = constant > 0,

where $\rho_0(z)$ = undisturbed density,

$$\alpha^2 = g\beta,$$

and

$$k_0 = \left|\frac{\alpha}{W}\right|.$$

If we write

$$\frac{D}{Dt} = \frac{\partial}{\partial t} + u\frac{\partial}{\partial r} + (w - W)\frac{\partial}{\partial z},$$

the equations of motion relative to axes fixed in the body are

$$\frac{Du}{Dt} + \frac{1}{\rho}\frac{\partial p}{\partial r} = 0, \tag{1}$$

and

$$\frac{Dw}{Dt} + \frac{1}{\rho}\frac{\partial p}{\partial z} = -g. \tag{2}$$

Since the fluid is incompressible

$$\frac{D\rho}{Dt} = 0, \tag{3}$$

and the equation of continuity reduces to

$$\frac{\partial}{\partial r}(ru) + \frac{\partial}{\partial z}(rw) = 0. \tag{4}$$

Equation (4) implies the existence of a stream function, $\psi(r, z, t)$, such that

$$u = \frac{1}{r}\frac{\partial \psi}{\partial z} \quad \text{and} \quad w = -\frac{1}{r}\frac{\partial \psi}{\partial r}.$$

We now write $\rho = \rho_0 + \rho'$ and $p = p_0 + p'$, where ρ' and p' are small perturbations of the undisturbed density and pressure, ρ_0 and p_0, respectively. If we substitute $\rho_0 + \rho'$ for ρ, and $p_0 + p'$ for p in equations (1), (2) and (3) and neglect products of u, w, p', ρ' and their derivatives, these three equations become

$$\rho_0\left(\frac{\partial}{\partial t} - W\frac{\partial}{\partial z}\right)u + \frac{\partial p'}{\partial r} = 0, \tag{1}'$$

$$\rho_0\left(\frac{\partial}{\partial t} - W\frac{\partial}{\partial z}\right)w + \frac{\partial p'}{\partial z} = -\rho' g \tag{2}'$$

and

$$\left(\frac{\partial}{\partial t} - W\frac{\partial}{\partial z}\right)\rho' + w\frac{\partial \rho_0}{\partial z} = 0. \tag{3}'$$

The elimination of ρ' and p' from these equations and the substitution for u and w in terms of ψ leads to the following equation of motion:

$$\left(\frac{\partial}{\partial t} - W\frac{\partial}{\partial z}\right)^2\left\{\frac{\partial}{\partial r}\left(\frac{1}{r}\frac{\partial\psi}{\partial r}\right) + \frac{\partial}{\partial z}\left(\frac{1}{r}\frac{\partial\psi}{\partial z}\right) - \frac{\beta}{r}\frac{\partial\psi}{\partial z}\right\} + \alpha^2\frac{\partial}{\partial r}\left(\frac{1}{r}\frac{\partial\psi}{\partial r}\right) = 0. \tag{5}$$

The first two terms in the curly brackets represent the vorticity, the term containing β is an inertia term which arises because the density decreases upwards, and the last term represents the effect of gravity.

If it assumed that a steady motion exists for which $\partial/\partial t \equiv 0$, then equation (5) becomes

$$\frac{\partial^2}{\partial z^2}\left\{\frac{\partial}{\partial r}\left(\frac{1}{r}\frac{\partial\psi}{\partial r}\right) + \frac{\partial}{\partial z}\left(\frac{1}{r}\frac{\partial\psi}{\partial z}\right) - \frac{\beta}{r}\frac{\partial\psi}{\partial z}\right\} + k_0^2\frac{\partial}{\partial r}\left(\frac{1}{r}\frac{\partial\psi}{\partial r}\right) = 0. \tag{5}'$$

Equation (5)′ has the same form for both W and $-W$. Thus the equation of steady motion makes no distinction between ascent and descent at equal speeds. The assumption that there is no perturbation of the fluid at large distances from the body, together with the boundary condition at the surface of the body, leads to a solution of equation (5)′ in which a wave pattern appears below the body. This seems unreasonable if the body is in descent. On the other hand, if the assumption of no perturbation at infinity is dropped, the solution of equation (5)′ is indeterminate. In some cases it may be argued that the term containing β may be neglected because it is small compared with the other terms of equations (5) and (5)′. These equations then become

$$\left(\frac{\partial}{\partial t} - W\frac{\partial}{\partial z}\right)^2\left\{\frac{\partial}{\partial r}\left(\frac{1}{r}\frac{\partial\psi}{\partial r}\right) + \frac{\partial}{\partial z}\left(\frac{1}{r}\frac{\partial\psi}{\partial z}\right)\right\} + \alpha^2\frac{\partial}{\partial r}\left(\frac{1}{r}\frac{\partial\psi}{\partial r}\right) = 0 \tag{6}$$

and

$$\frac{\partial^2}{\partial z^2}\left\{\frac{\partial}{\partial r}\left(\frac{1}{r}\frac{\partial\psi}{\partial r}\right) + \frac{\partial}{\partial z}\left(\frac{1}{r}\frac{\partial\psi}{\partial z}\right)\right\} + k_0^2\frac{\partial}{\partial r}\left(\frac{1}{r}\frac{\partial\psi}{\partial r}\right) = 0 \tag{6}'$$

respectively. The same equations are obtained if β and g are regarded as variable parameters, and $\beta \to 0$, $g \to \infty$, in such a way that α^2 remains constant.

However, the solution of the equation of steady motion (6)′ is indeterminate, even if the assumption of no perturbation at infinity is made. Also the circumstances in which the term in equation (5) containing β may be neglected do not seem obvious. For these reasons it is better to use the equation of unsteady motion (5), and with a general type of initial motion to look for a limiting value of the solution as $t \to \infty$.

3. The boundary conditions

If line sources and sinks are placed on the z-axis, the separating streamlines may be regarded, in the usual manner, as the outline of a body. The strength of these line sources may be written conveniently as

$$-2\pi W f'(z) f(z),$$

the accent denoting differentiation with respect to z. At points near the axis,

$$u = \frac{1}{r}\frac{\partial\psi}{\partial z} = -\frac{W}{r}f'(z)f(z),$$

and hence

$$\psi(0, z, t) = -\frac{W}{2}\{f(z)\}^2 = \psi_a, \quad \text{say}, \tag{7}$$

where ψ is defined so that the constant of integration is zero. If the axisymmetric body whose shape is given by $r_a = f(z)$ is a slender one, so that r_a is small, then

$$\frac{\partial}{\partial z}\psi(r_a, z, t) \simeq \frac{\partial}{\partial z}\psi(0, z, t),$$

and

$$\frac{u(r_a, z, t)}{W - w} \simeq \frac{1}{Wf(z)}\frac{\partial}{\partial z}\psi(0, z, t) \quad \text{if} \quad |w| \ll |W|.$$

However, if $r_a = f(z)$ is a boundary of the fluid, then

$$-\frac{u(r_a, z, t)}{W - w} = f'(z).$$

Hence equation (7) holds for a body whose shape is given approximately by $r_a = f(z)$, if the body is a slender one.

The flow pattern at $t = 0$ is given (compatibly) as

$$\left.\begin{aligned} \psi(r, z, 0) &= \psi_0 \\ \text{and} \quad \frac{\partial}{\partial t}\psi(r, z, 0) &= \dot{\psi}_0. \end{aligned}\right\} \tag{8}$$

The initial motion described by ψ_0 and $\dot{\psi}_0$ is taken to be of a general nature and may contain waves. Alternatively, the body may be started suddenly from rest in a still fluid. The solution of the equation of impulsive motion (i.e. equation (5)′ with $g = 0$) is equivalent to a potential flow solution multiplied by a factor $\cos \frac{1}{2}\beta r$. Thus the motion in the horizontal direction has a 'wavelength' of $2/\beta$; but this seems of theoretical interest only since the amplitude of the motion dies away rapidly in an exponential manner.

4. The transformation of the equation of motion

Equation (5) is transformed by means of a Fourier transform in the vertical direction and a Hankel-like transform in the horizontal direction:

$$\Psi(r, k, t) = \frac{1}{\sqrt{2\pi}}\int_{\infty}^{-\infty} dz\, e^{ikz}\psi(r, z, t). \tag{9}$$

$$\chi(m, k, t) = \int_0^{\infty} dr\, J_1(mr)\,\Psi(r, k, t). \tag{10}$$

The transforms corresponding to ψ_0, $\dot{\psi}_0$ and ψ_a are

$$\Psi_0, \chi_0;\ \dot{\Psi}_0,\ \dot{\chi}_0 \quad \text{and} \quad \Psi_a(k) = \Psi(0, k, t)$$

respectively. If we multiply equation (5) by e^{ikz} and integrate with respect to z from $-\infty$ to $+\infty$, and assume ψ vanishes at $\pm\infty$, we obtain

$$\left(\frac{\partial}{\partial t} + iWk\right)^2\left\{\frac{\partial}{\partial r}\left(\frac{1}{r}\frac{\partial \Psi}{\partial r}\right) - k^2\frac{\Psi}{r} + i\beta k\frac{\Psi}{r}\right\} + \alpha^2\frac{\partial}{\partial r}\left(\frac{1}{r}\frac{\partial \Psi}{\partial r}\right) = 0.$$

If this equation is multiplied by $rJ_1(mr)$ and integrated with respect to r from 0 to ∞, it becomes

$$\left[\left(\frac{\partial}{\partial t} + iWk\right)^2(k^2 - i\beta k + m^2) + \alpha^2 m^2\right]\chi = m(\alpha^2 - W^2k^2)\,\Psi_a(k). \tag{11}$$

To derive equation (11), it has been assumed that $J_1(mr)\,(\partial/\partial r)\,\Psi(r,k,t)$ vanishes at $r=0$ and $r=\infty$ and that $\Psi(r,k,t)$ vanishes at $r=\infty$; it then follows that

$$\int_0^\infty dr\, rJ_1(mr)\,\frac{\partial}{\partial r}\left(\frac{1}{r}\frac{\partial \Psi}{\partial r}\right) = m\Psi(0,k,t) - m^2\chi(m,k,t).$$

Equation (11) is an ordinary differential equation with t as the independent variable. Its solution may be written as the sum of a particular integral and a complementary function: $\chi = \chi_1 + \chi_2$. Correspondingly, $\Psi = \Psi_1 + \Psi_2$ and $\psi = \psi_1 + \psi_2$.

5. The particular integral

The particular integral of equation (11) is obtained by putting $\partial/\partial t \equiv 0$, since the right-hand side is independent of time. This gives $\chi_1 = m\Psi_a/(m^2-\lambda^2)$, where

$$\lambda^2 = \frac{k^4 - i\beta k^3}{k_0^2 - k^2}.$$

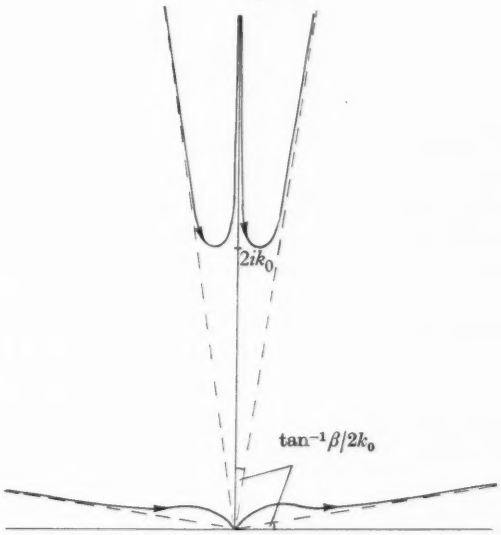

FIGURE 1. Path for λ in the complex λ-plane as k varies.

The inverse of the transformation (10) is

$$\Psi(r,k,t) = r\int_0^\infty dm\, mJ_1(rm)\,\chi(m,k,t).$$

Hence,

$$\Psi_1(r,k,t) = r\Psi_a(k)\int_0^\infty dm\,\frac{m^2 J_1(rm)}{m^2-\lambda^2}.$$

This integral is evaluated in Watson (1944, p. 424).† Substituting its value, we obtain

$$\Psi_1(r,k,t) = (\tfrac{1}{2}\pi i)\, r\lambda H_1^{(1)}(r\lambda)\,\Psi_a(k),$$

where

$$\mathrm{Im}\,(\lambda) > 0.$$

† The integral $\int \frac{z^2 H_1^{(1)}(rz)\,dz}{z^2-\lambda^2}$ taken round an infinite semicircle in the upper half-plane gives the results immediately.

The inverse of the transform (9) then gives

$$\psi_1(r,z,t) = \frac{\pi i}{2\sqrt{2\pi}} \int_{-\infty}^{\infty} dk\, e^{-ikz} r\lambda H_1^{(1)}(r\lambda)\, \Psi_a(k),$$

where $\mathrm{Im}\,(\lambda) > 0$. The path of λ, as k varies from $-\infty$ to $+\infty$, is shown in figure 1. If $\beta/k_0 \ll 1$, this path lies approximately on the real and imaginary axes. If it is assumed that the body is symmetrical about its centre so that $r_a = f(z) = f(-z)$, then $\Psi_a(k)$ is an even function of k. ψ_1 may then be written

$$\psi_1 = -\sqrt{\frac{\pi}{2}}\, \mathrm{Im} \int_0^{\infty} dk\, \Psi_a(k)\, e^{ikz} r\Lambda H_1^{(1)}(r\Lambda), \tag{12}$$

where

$$\Lambda = \begin{cases} \lambda_1 & \text{if} \quad k < k_0, \\ i\lambda_2 & \text{if} \quad k > k_0 \end{cases}$$

and

$$\lambda_1^2 = \frac{k^4}{k_0^2 - k^2} \quad (\lambda_1 > 0),$$

$$\lambda_2^2 = \frac{k^4}{k^2 - k_0^2} \quad (\lambda_2 > 0).$$

6. The complementary function

Since the particular integral is independent of time, the behaviour of ψ as $t \to \infty$ depends solely upon the behaviour of ψ_2 as $t \to \infty$. The complementary function is obtained if we write $\Psi_a(k) = 0$ in equation (11). This gives

$$\chi_2 = A_1(k,m)\, e^{\gamma_1 t} + A_2(k,m)\, e^{\gamma_2 t},$$

where A_1 and A_2 are functions of k and m, and γ_1 and γ_2 are the roots of

$$(\gamma + iWk)^2 (k^2 - i\beta k + m^2) + \alpha^2 m^2 = 0. \tag{13}$$

At $t = 0$, χ and $\partial\chi/\partial t$ have the given values χ_0 and $\dot{\chi}_0$, respectively, and A_1 and A_2 are found from these conditions. We thus obtain

$$A_1 = [\gamma_2(\chi_0 - \chi_1) - \dot{\chi}_0]/[\gamma_2 - \gamma_1],$$
$$A_2 = [\gamma_1(\chi_0 - \chi_1) - \dot{\chi}_0]/[\gamma_1 - \gamma_2].$$

The inverse of the transforms (8) and (9) gives

$$\psi_2 = \frac{r}{\sqrt{2\pi}} \int_{-\infty}^{\infty} dk \int_0^{\infty} dm\, e^{-ikz} m J_1(rm)\, [A_1 e^{\gamma_1 t} + A_2 e^{\gamma_2 t}].$$

A transformation to polar co-ordinates is now made, so that one range of integration is finite. We write $k = \rho \sin\theta$, $m = \rho\cos\theta$ and thus obtain

$$\psi_2 = \frac{r}{\sqrt{2\pi}} \int_{-\frac{1}{2}\pi}^{\frac{1}{2}\pi} d\theta \int_0^{\infty} d\rho\, \rho^2 \cos\theta \exp[-iz\rho\sin\theta] \times J_1(r\rho\cos\theta)\, [A_1(\rho,\theta)\, e^{\gamma_1 t} + A_2(\rho,\theta)\, e^{\gamma_2 t}],$$

where

$$\gamma_{1,2} = -iW\rho\sin\theta \pm i\alpha\cos\theta \sqrt{\frac{\rho}{\rho - i\beta\sin\theta}}.$$

We write

$$I_1^{(+)} = \frac{r}{\sqrt{2\pi}} \int_0^{\frac{1}{2}\pi} d\theta \int_0^{\infty} d\rho\, \rho^2 \cos\theta \exp\left[-iz\rho\sin\theta\right] J_1(r\rho\cos\theta)\, A_1(\rho,\theta)\, e^{\gamma_1 t},$$

$$I_1^{(-)} = \frac{r}{\sqrt{2\pi}} \int_{-\frac{1}{2}\pi}^{0} d\theta \int_0^{\infty} d\rho\, \rho^2 \cos\theta \exp\left[-iz\rho\sin\theta\right] J_1(r\rho\cos\theta)\, A_1(\rho,\theta)\, e^{\gamma_1 t}.$$

Similarly the notations $I_2^{(+)}$ and $I_2^{(-)}$ are used for integrals containing A_2.

To find the limit of the integrals as $t \to \infty$, we consider the ρ-integration first, and deform the paths of integration in the complex ρ-plane to regions where $\mathrm{Re}\,(\gamma_{1,2}) < 0$.† Two cases arise, corresponding to ascent and descent of the body. For ascent, it is found that if certain assumptions about the initial conditions are made, no poles are crossed in the deformation in the ρ-plane. The whole path may be deformed to regions where $\mathrm{Re}\,(\gamma_{1,2}) < 0$. Hence in this case the integrals tend to zero as $t \to \infty$. For the case of descent, the same assumptions are made, but poles of χ_1 are crossed at points where $\gamma = 0$, and the residues give rise to a steady term as $t \to \infty$. A difficulty arises for the integrals $I_1^{(-)}$ and $I_2^{(+)}$ because it is not possible to deform the whole of the path in the ρ-plane to regions where

$$\mathrm{Re}\,(\gamma_{1,2}) < 0.$$

The second integration with respect to θ then shows that these integrals do not have limits as $t \to \infty$. However, if the assumption is made that $\beta/k_0 \ll 1$ this difficulty is partly overcome in the sense that the integrals $I_1^{(-)}$ and $I_2^{(+)}$ taken along the deformed paths remain negligible for a certain interval of time. During this time the integrals are approximately equal to the residue terms from the poles crossed by the deformations. From these residues the limit of ψ_2 is obtained. Thus it may be shown that

$$\lim_{t\to\infty} \psi_2 = \begin{cases} 0, & \text{if } W > 0 \\ \sqrt{2\pi} \displaystyle\int_0^{k_0} dk\, \Upsilon_a(k)\, r\Lambda J_1(r\Lambda) \sin kz & \text{if } W < 0. \end{cases} \tag{14}$$

The remainder of this section gives a proof of the expression (14) and discusses some points which arise from the preceding paragraph.

Case I. Ascent $W > 0$

It is assumed that A_1 and A_2 are $O(\exp[b\,|\mathrm{Im}\,\rho|]\rho^{-3-\Delta})$ as $|\rho| \to \infty$, where $\Delta > 0$ and $b \geqslant 0$. Equation (13) shows that if $\gamma = 0$, then $m^2 = \lambda^2$. Hence χ_1 has poles at points where $\gamma = 0$, A_1 has a pole at $\gamma_1 = 0$ and A_2 has a pole at $\gamma_2 = 0$. Figure 2 shows the ρ-plane. Regions where $\mathrm{Re}\,(\gamma) < 0$ are shaded, and the poles of $A_{1,2}$ at $\gamma_{1,2} = 0$ are shown at the points marked Γ. γ has a pole at $\rho = i\beta\sin\theta$ and a branch point at the origin. A cut is made along the imaginary ρ-axis to join these points, so that γ is single valued in the cut plane.

We consider the upper bounds of the integrands of the integrals $I_1^{(+)}$, etc., taken along the deformed paths. Upper bounds for the integrals taken along the deformed paths may then be found. The range of the θ-integration is divided into the ranges $(0, \pm\epsilon)$ and $(\pm\epsilon, \pm\frac{1}{2}\pi)$, where ϵ is a small positive number.

† The transformation $\rho \to \rho(\gamma)$ is not a simple one and it is better to keep to the independent variables (ρ, θ).

Discussion of the integral $I_1^{(+)}$

(i) No deformation is made in the interval $0 < \theta < \epsilon$, and it may be shown that $\left|\int_0^\infty d\rho\right| < M$, for some fixed M.

(ii) In $\epsilon < \theta < \frac{1}{2}\pi$, the path of integration in the ρ-plane is deformed as shown in figure 3.

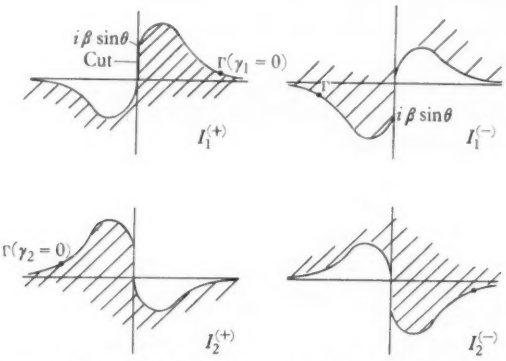

FIGURE 2. Case I. Paths of Re $(\gamma) = 0$ in the complex ρ-plane.

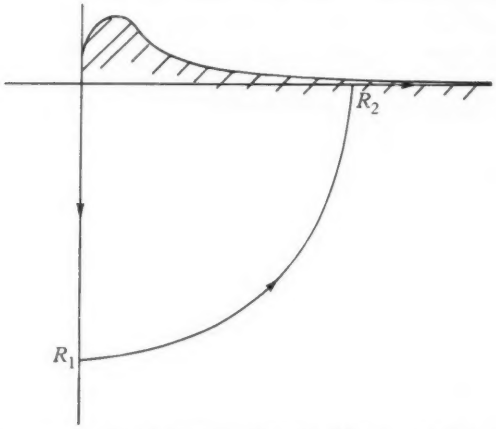

FIGURE 3. Case I. Deformation for $I_1^{(+)}$ in $\epsilon < \theta < \frac{1}{2}\pi$.

It follows that

$$\left|\int_{R_1 R_2 \infty} d\rho\right| < K\epsilon$$

by suitable choice of R_1, and that

$$\left|\int_{0 R_1} d\rho\right| < \frac{K}{Wt\sin\theta - 2(r + |z| + b)}$$

if $Wt\sin\theta > 2(r + |z| + b)$. where K is a fixed number.

Discussion of the integral $I_1^{(-)}$.

(i) In the interval $-\epsilon < \theta < 0$ the path is deformed as shown in figure 4.

It may be shown that $\left|\int_{0,\infty} d\rho\right| < M\, e^{ck_0(r+|z|+b)}$, where c is some constant which depends on β and k_0 only.

(ii) In $-\frac{1}{2}\pi < \theta < -\epsilon$, the deformation is similar to that used in $I_1^{(+)}$, see figure 5.

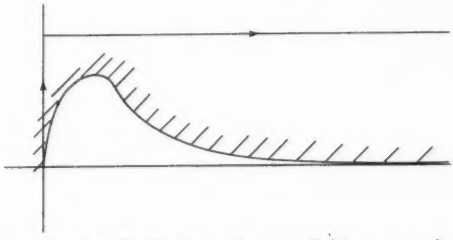

FIGURE 4. Case I. Deformation for $I_1^{(-)}$ in $-\epsilon < \theta < 0$.

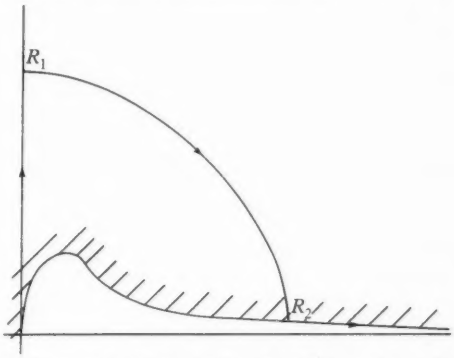

FIGURE 5. Case I. Deformation for $I_1^{(-)}$ in $-\frac{1}{2}\pi < \theta < -\epsilon$.

In this case it may be shown that

$$\left|\int_{0R_1R_2\infty} d\rho\right| < K\epsilon + \frac{K}{Wt\sin\theta - 2(r+|z|+b)}.$$

Similar results hold for the integrals $I_2^{(+)}$ and $I_2^{(-)}$, when the paths are deformed in a similar manner. If we collect these results for the integrals $I_1^{(+)}$, etc., and consider upper bounds for varying θ, we obtain the following upper limit for the θ-integration:

$$\left|\int_{-\frac{1}{2}\pi}^{\frac{1}{2}\pi} d\theta \int_{\text{paths}} d\rho\right| < K\left\{(1+\exp\left[ck_0(r+|z|+b)\right])\epsilon + \frac{1}{Wt_0\sin\epsilon - 2(r+|z|+b)}\right\},$$

where $Wt_0\sin\epsilon > 2(r+|z|+b)$.

For poles crossed by the deformations there will be contributions from the residues, which give terms like

$$\int_{-\frac{1}{2}\pi}^{\frac{1}{2}\pi} d\theta\, \Theta\, e^{\gamma_p t}. \tag{15}$$

Here Θ is some function of θ and a pole occurs at $\rho = \rho_p(\theta)$, say, where

$$\gamma = \gamma(\rho_p, \theta) = \gamma_p(\theta).$$

If $\mathrm{Re}\,(\gamma_p) < 0$, the expression (15) will decrease with time, but if $\mathrm{Re}\,(\gamma_p) > 0$ (e.g. for the deformation used for $I_2^{(-)}$), this may not be so. In general, if it is possible to deform the path of integration in the θ-plane to regions where $\mathrm{Re}\,(\gamma_p) < 0$ (where γ_p is such that $\mathrm{Re}\,(\gamma_p(\pm\frac{1}{2}\pi)) \leqslant 0$), the expression (15) will decrease with time. However, this deformation is not always possible, and, for example, we may have $\mathrm{Im}\,(\gamma_p) = \text{constant} = Wl$, say, and $\mathrm{Re}\,(\gamma_p) = 0$. There is then a steady fluctuation present throughout the motion. This type of motion is easier to see if we use equation (6). The assumption that

$$\psi \propto e^{-ikz} r J_1(mr)\, e^{iWlt}$$

then gives

$$(l+k)^2\,(k^2+m^2) = k_0^2 m^2. \tag{13'}$$

Hence equation (6) has a solution

$$\psi = r\, e^{iWlt} \int_0^\infty dk\, \Psi_a(k)\, e^{-ikz}\, m J_1(rm),$$

where m satisfies equation (13') and l is fixed.

This fluctuating type of motion does not seem to be of practical interest since it must be present in the initial conditions and it is not easy to see how this motion could arise in the first instance, unless a fluctuating type of disturbance were present.

With regard to the θ-integration for the residues in the case where

$$\mathrm{Im}\,(\gamma_p) = \text{constant}, \quad \mathrm{Re}\,(\gamma_p) > 0,$$

the fluctuation would increase with time. In this case the linear theory is inadequate to say what eventually happens.

If it is now assumed that poles of the above description do not occur in A_1 and A_2 and hence in χ_0 and $\dot{\chi}_0$, i.e. that certain types of waves are absent from the initial condition, then

$$|\psi_2| < K\left\{(1+\exp\left[ck_0(r+|z|+b)\right])\,\epsilon + \frac{1}{Wt\sin\epsilon - 2(r+|z|+b)}\right\}.$$

This holds for all (r_1, z_1, t) if $r_1 + |z_1| < r + |z|$ and $t > t_0$. Hence $\psi_2 \to 0$ as $t \to \infty$ if $W > 0$ for all regions of the flow. This result holds for any $\beta > 0$.

Case II. Descent $W < 0$

The same methods are used as in Case I, but it is no longer possible to deform the paths of integrations for the integrals $I_1^{(-)}$ and $I_2^{(+)}$ in the ρ-plane so that they lie completely in regions where $\mathrm{Re}\,(\gamma) < 0$. The singularities of γ prevent this. Figure 6, which corresponds to figure 2 of Case I, shows the ρ-plane.

The paths for the integrals $I_1^{(-)}$ and $I_2^{(+)}$ are deformed as shown in figures 8, 9 and 10. In the regions were $\mathrm{Re}\,(\gamma) > 0$, the paths are deformed so as to pass through a col as in the method of steepest descent. An upper bound for the contributions from segments of the paths where $\mathrm{Re}\,(\gamma) > 0$ is then made. The track of the cols for varying θ is shown in figure 7.

The position of the cols is given by $\rho = \rho_c(\theta)$, say, and at these points

$$\gamma = \gamma(\rho_c, \theta) = \gamma_c(\theta).$$

We write $$\operatorname{cosec}\theta^* \cot\theta^* = \frac{3\sqrt{3}}{8}\frac{\beta}{k_0} \quad (\tfrac{1}{2}\pi > \theta^* > 0)$$

and $$\operatorname{cosec}\theta^{**} \cot\theta^{**} = \frac{1}{2}\frac{\beta}{k_0} \quad (\tfrac{1}{2}\pi > \theta^{**} > 0).$$

Then if $|\theta| > \theta^*$, it may be shown that two cols lie on the cut; and that if $|\theta| > \theta^{**}$ both zeros of γ lie on the cut. We suppose that β and g are variable parameters

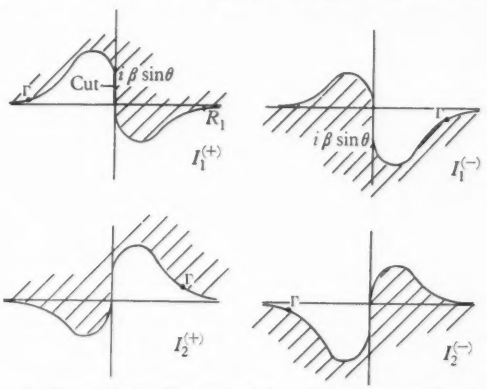

FIGURE 6. Case II. Paths of $\mathrm{Re}(\gamma) = 0$ in the complex ρ-plane.

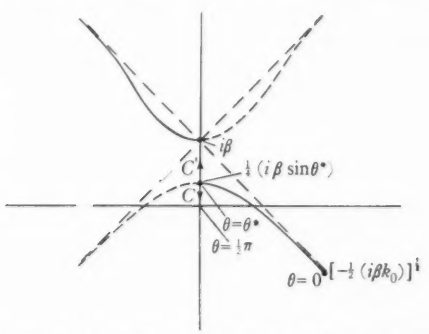

FIGURE 7. Case II. Path of the cols for varying θ in the complex ρ-plane.

with α, k_0 and W held fixed, and that $0 < \beta/k_0 \ll 1$. The range of the θ-integration is divided into the ranges $(0, \pm\epsilon)$; $(\pm\epsilon \pm \tfrac{1}{2}\pi \mp \delta)$; and $(\pm\tfrac{1}{2}\pi \mp \delta, \pm\tfrac{1}{2}\pi)$; where ϵ and δ are small positive numbers. β is chosen so that $\tfrac{1}{2}\pi - \theta^* < \delta$ in order to restrict the contributions from the paths in regions where $\mathrm{Re}(\gamma) > 0$.

Discussion of the integral $I_1^{(+)}$

(i) There is no deformation of the path in $0 < \theta < \epsilon$ and it may be shown that

$$\left|\int_0^\infty d\rho\right| < M.$$

(ii) In $\epsilon < \theta < \frac{1}{2}\pi$, the path is deformed to $\mathrm{Re}\,(\gamma) = 0$. On this path it may be shown that

$$\left|\frac{d\gamma/d\rho}{W\sin\theta}\right| > 1.$$

With the assumption that $A(\rho, \theta)$ is of bounded variation on any finite length of the path, it follows that

$$\left|\int_{0,\infty} d\rho\right| < \frac{K\exp[ck_0(r+|z|+b)]}{Wt\sin\theta} + M\epsilon.$$

Similar results hold for $I_2^{(-)}$.

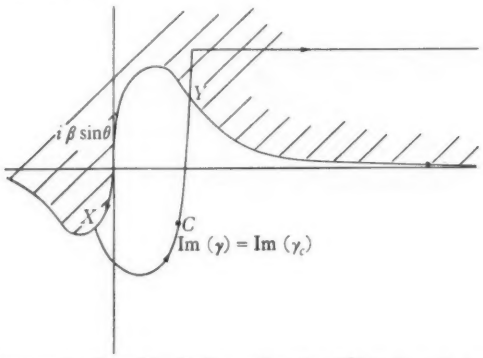

FIGURE 8. Case II. Deformation for $I_2^{(+)}$ in $0 < \theta < \epsilon$.

Discussion of the integral $I_2^{(+)}$

(*a*) *Contributions from the paths which lie in regions where* $\mathrm{Re}\,(\gamma) \leqslant 0$

(i) In $0 < \theta < \epsilon$, the path is deformed as shown in figure 8.

It may be shown that

$$\left|\int_{OX+Y\infty} d\rho\right| < M\exp[ck_0(r+|z|+b)].$$

(ii) In $\epsilon < \theta < \frac{1}{2}\pi - \delta$, the path is deformed as in figure 9. Here

$$\left|\int_{OX} d\rho\right| < \frac{K\exp[ck_0(r+|z|+b)]}{Wt\sin\theta},$$

as may be shown by a discussion similar to that used above for the integral $I_1^{(+)}$, (ii).

If $\beta/k_0 \ll \sin\delta$, it may be shown that

$$\left|\frac{d\gamma/d\rho}{W\sin\theta}\right| > \frac{1}{2}$$

and that the integrand is uniformly bounded with respect to β and θ on the deformed path.

It then follows that

$$\left|\int_{YZ} d\rho\right| < \frac{K\exp[ck_0(r+|z|+b)]}{Wt\sin\theta},$$

where $|OZ| = k_0$, say.

As in Case I, integral $I_1^{(+)}$, it may also be shown that

$$\left|\int_{Z\infty} d\rho\right| < \frac{K}{Wt\sin\theta - 2(r+|z|+b)} + M\epsilon.$$

(iii) In $\frac{1}{2}\pi - \delta < \theta < \frac{1}{2}\pi$, the paths are deformed in the three subintervals

$$\tfrac{1}{2}\pi - \delta < \theta < \theta^*; \quad \theta^* < \theta < \theta^{**}; \quad \theta^{**} < \theta < \tfrac{1}{2}\pi;$$

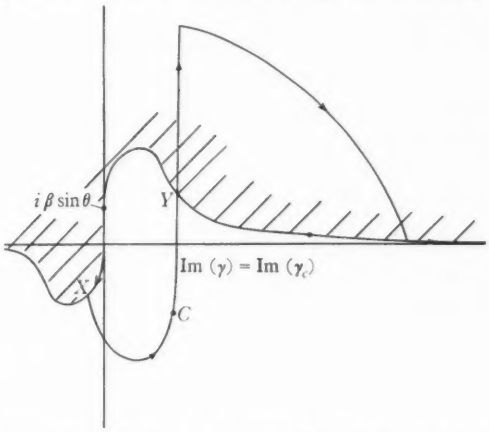

FIGURE 9. Case II. Deformation for $I_2^{(+)}$ in $\epsilon < \theta < \frac{1}{2}\pi$.

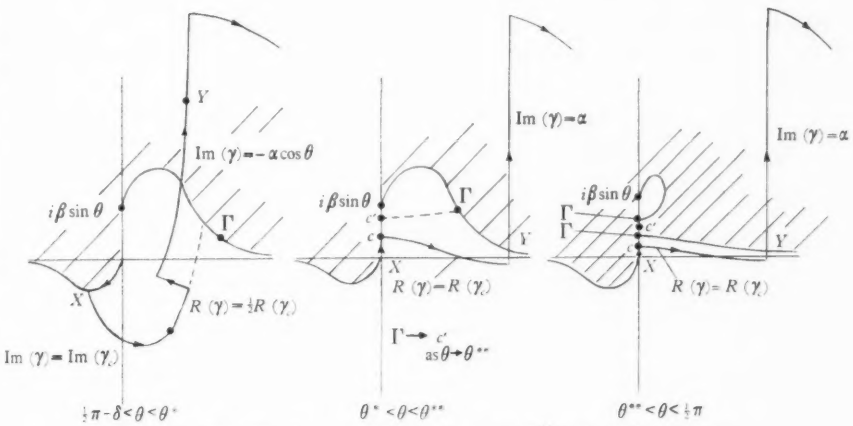

FIGURE 10. Case II. Various deformations for $I_2^{(+)}$ in $\frac{1}{2}\pi - \delta < \theta < \frac{1}{2}\pi$.

as shown in figure 10. For points on the segment $Y\infty$ of the deformed path, where $|OY| = k_0$, it may be shown that

$$\left|\frac{d\gamma/d\rho}{W\sin\theta}\right| > \frac{1}{2}$$

Similar arguments hold for $\left|\int_{Y\infty} d\rho\right|$ as in (ii) above.

(*b*) *Contributions from the paths which lie in regions where* $\mathrm{Re}\,(\gamma) \geqslant 0$

If we consider the path of the col, we may show that in the interval

$$0 < \theta < \theta^*, \quad \mathrm{Re}\,(\gamma_c/W) < 5\sqrt{(\beta k_0)};$$

and that in

$$\theta^* < \theta < \tfrac{1}{2}\pi, \quad \mathrm{Re}\,(\gamma_c/W) < \tfrac{1}{8}\beta.$$

(i) In $0 < \theta < \frac{1}{2}\pi - \delta$, it may be shown that the length of the path XY is less than

$$K\sqrt{(\beta k_0)}.$$

(ii) In $\frac{1}{2}\pi - \delta < \theta < \frac{1}{2}\pi$, the length of the path in the region where

$$\mathrm{Re}\,(\gamma) \geqslant 0 \quad \text{is} \quad O(k_0).$$

It may also be shown that the integrand is uniformly bounded with respect to β and θ on the deformed paths. From these results it may then be shown that

$$\left|\int_0^{\frac{1}{2}\pi} d\theta \int_{XY} d\rho\right| < K[\sqrt{(\beta k_0)} + \delta]\exp[ck_0(r+|z|+b)]\exp[5W\sqrt{(\beta k_0)}\,t].$$

The integral $I_1^{(-)}$ may be discussed in a manner similar to $I_2^{(+)}$.

From the above results for the integrals $I_1^{(+)}$, etc., we obtain the following upper limit for the θ-integration:

$$\left|\int_{-\frac{1}{2}\pi}^{\frac{1}{2}\pi} d\theta \int_{\text{paths}} d\rho\right| < K\exp[ck_0(r+|z|+b)]\left\{\epsilon + \frac{1}{Wt\sin\epsilon} + \frac{1}{Wt\sin\epsilon - 2(r+|z|+b)} + [\sqrt{(\beta k_0)} + \delta]\exp[5W\sqrt{(\beta k_0)}\,t]\right\}.$$

This holds for all $0 < \beta < \bar{\beta}$, for some $\bar{\beta} > 0$. (c does not increase if β decreases.) It also holds for all (r_1, z_1, t), where $r_1 + |z_1| < r + |z|$, and $t > t_0$.

If we choose $t_1 \gg t_0$ and β such that $\sqrt{(\beta k_0)} \ll 1/5Wt_1$ (i.e. $\sqrt{(\beta/k_0)} \ll 1/5\alpha t_1$), then

$$\left|\int_{-\frac{1}{2}\pi}^{\frac{1}{2}\pi} d\theta \int_{\text{paths}} d\rho\right| < K\exp[ck_0(r+|z|+b)](3\epsilon + 4\delta) \tag{16}$$

during some interval of time (t_1, t_2), $t_2 > t_1$. If (ϵ, δ) is chosen so that the expression on the right-hand side of (16) is small compared with the average value of

$$|\psi_1 + \text{residue terms}|\,\dagger$$

in the region $r_1 + |z_1| < r + |z|$, then

$$\left|\int_{-\frac{1}{2}\pi}^{\frac{1}{2}\pi} d\theta \int_{\text{paths}} d\rho\right|$$

may be neglected in the interval $t_1 < t < t_2$. This interval may be called a 'quasi-limit' interval. An estimate of $\psi_2 = \int_{-\frac{1}{2}\pi}^{\frac{1}{2}\pi} d\theta \int_0^{\infty} d\rho$ for large t may be found from the asymptotic expression of $\int_{XY} d\rho$. The method of steepest descent through the col gives the first n-terms in the form‡

$$\sum_{r=1}^{n} \int_{-\frac{1}{2}\pi}^{\frac{1}{2}\pi} d\theta\, \Theta_r \exp[\gamma_c(\theta)\,t]\,t^{-r-\frac{1}{2}},$$

† ψ_1 and the residue terms change little as $\beta \to 0$.

‡ A modification is needed at $\theta = \theta^*$ since $d\gamma/d\rho = 0$ there.

where the Θ_r are functions of θ, and $\mathrm{Re}\,(\gamma_c(\pm\frac{1}{2}\pi)) = \mathrm{Re}\,(\gamma_c(0)) = 0$. A different form of deformation of the path in the ρ-plane occurs at $\theta = \theta^*$ and hence not all the Θ_r are holomorphic at this point. Hence complete deformation of the path of integration in the θ-plane to regions where $\mathrm{Re}\,(\gamma_c) \leqslant 0$ is not possible,† and

$$\int_{-\frac{1}{2}\pi}^{\frac{1}{2}\pi} d\theta \int_{XY} d\rho$$

gives terms

$$O\left(\frac{\exp\left[\frac{1}{8}(\beta|W|t)\right]}{t^{r+\frac{1}{2}}}\right) + \ldots.$$

where r is some integer. Hence $|\psi_2|$ diverges as $t \to \infty$, and eventually the motion increases without limit.

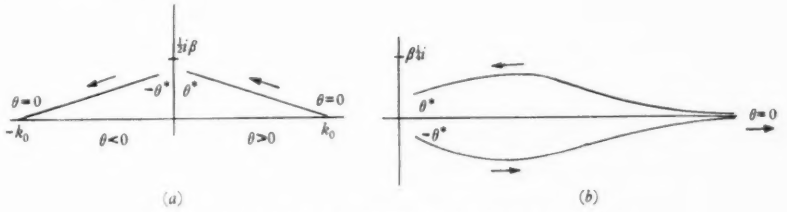

FIGURE 11. Paths of integration for k, (*a*), and λ, (*b*).

The assumption that second-order terms are small no longer holds at this stage and the linear theory seems inadequate. Physically, the medium is a dispersive one in which local disturbances are propagated outwards in all directions. The gradually increasing inertia forces retard the propagation to deeper levels, and waves ahead cannot disperse so rapidly in descent as in ascent.

Similar assumptions concerning the poles of χ_0 and $\dot{\chi}_0$ are made as in Case I. In the case where the motion is started suddenly from rest, a pole of χ_0 occurs at $\rho = i\beta\sin\theta$. It seems better to treat this pole separately, since the arguments used earlier would not hold in this case.

With the above assumptions, the limit of the complementary function in the 'quasi-limit' interval is found from the residues of the poles of χ_1 at $\gamma = 0$, which are crossed by the deformations used for $I_1^{(-)}$ and $I_2^{(+)}$. If we substitute for the residues, after a little manipulation we obtain

$$-\sqrt{\frac{\pi}{2}}\, ir \int_L dk\, \Psi_a(k)\, e^{-ikz}\, \lambda J_1(r\lambda)\, \mathrm{sgn}\,\theta,$$

where L is the path in the k-plane shown in figure 11. Figure 11 also shows the corresponding path for λ.

If $\beta r \ll 1$ and $\beta z \ll 1$, then these paths may be taken to lie approximately on the real axes. With the assumption that $\Psi_a(k)$ is even, this leads to the expression

$$\sqrt{2\pi} \int_0^{k_0} dk\, \Psi_a(k)\, r\Lambda J_1(r\Lambda) \sin kz. \tag{17}$$

† Other paths may be chosen, but a different form of deformation occurs at some stage because the contours of γ change their form at $\theta = \theta^*$ and at $\theta = \theta^{**}$.

In conclusion, for Case II, if $\beta/k_0 \ll 1$, there is a region around the body where, for a given time interval, ψ_2 is given by the expression (17). The length of this interval becomes infinite as $\beta/k_0 \to 0$.

7. The complete solution

The results of §§5 and 6 give the following expression for ψ as $t \to \infty$:

$$\psi = \frac{W}{2} \operatorname{Im} \int_0^\infty dk\, F(k)\, r\Lambda H_1^{(1)}(r\Lambda) \exp[i\,(\operatorname{sgn} W)\, kz], \tag{18}$$

where

$$F(k) = \int_0^\infty dz \cos kz \{f(z)\}^2.$$

Hence the wave pattern produced by a descending body is the same as that produced by an ascending one. The waves are downstream in each case. When the initial conditions are those of a steady, numerically greater velocity, and ψ_0 is given by expression (18), it may be shown that the same wave pattern eventually emerges.

Methods similar to those used in §§4–6, may be employed to solve equation (6). There is no essential singularity of the integrand in the corresponding double integral expression for ψ_2. The paths of $\operatorname{Re}(\gamma) = 0$ coincide with the real ρ-axis. The poles of χ_1 also occur on the real ρ-axis, and the double integral expressions for ψ_1 and ψ_2 are improper integrals. If principal values of the integrals are taken we obtain after one integration

$$\psi_1 = \frac{W}{2} \operatorname{Im} \int_0^\infty dk\, F(k)\, r\Lambda H_1^{(1)}(r\Lambda) \cos kz$$

and

$$\lim_{t\to\infty} \psi_2 = \frac{W}{2} \operatorname{Im} \int_0^{k_0} dk\, F(k)\, r\Lambda H_1^{(1)}(r\Lambda)\, i(\operatorname{sgn} W) \sin kz.$$

These two results differ from the corresponding expressions when $\beta \neq 0$. However, the sum $\psi = \psi_1 + \psi_2$ is the same in both cases, and in this sense the limit of the solution of equation (5) as $\beta \to 0$ is the same as the solution of the limiting form of equation (5) as $\beta \to 0$.

8. Asymptotic approximation to the motion

An asymptotic expression for the streamlines and the distortion of the constant density levels can be obtained by the method of steepest descents. The displacement of the streamlines is given approximately by

$$\Delta_s = \int_z^\infty dz \frac{u}{W} = -\frac{\psi}{Wr},$$

and the displacement Δ_{ρ_0} of the constant density levels by

$$\Delta_{\rho_0} = \int_z^\infty dz \frac{w}{W}.$$

If we write $k = k_0 \sin\xi$ and use the asymptotic expression for $H_1^{(1)}(x)$

$$H_1^{(1)}(x) \simeq \sqrt{\frac{2}{\pi x}} \exp[i(x - \tfrac{3}{4}\pi)],$$

then expression (18) yields

$$\Delta_s \simeq -\sqrt{\frac{k_0^3}{2\pi r}}\,\mathrm{Im}\int_M d\xi\, F(k_0\sin\xi)\sin\xi\cos^{\frac{1}{2}}\xi\exp\left[ik_0\sin\xi(z+r\tan\xi)-\tfrac{3}{4}\pi i\right],$$

when $W > 0$. M is the path shown in figure 12. It is deformed to pass through the col at C. This col contributes an exponentially small term to the asymptotic approximation to Δ_s and is omitted. It may be regarded as the potential flow displacement.

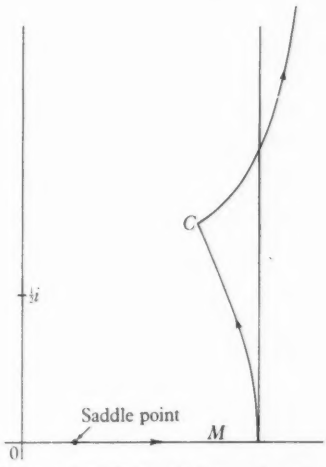

FIGURE 12. Path of integration for ξ.

When $z < 0$ a saddle point appears on the real axis between the origin and $(\frac{1}{2}\pi, 0)$. The method of stationary phase then gives

$$\Delta_s \simeq \frac{1}{r}\frac{k_0 F(k_0\sin\xi^*)}{\sqrt{(2+\sin^2\xi^*)}}\sin\xi^*\cos^2\xi^*\cos\left(\frac{zk_0\sin\xi^*}{1+\cos^2\xi^*}\right) \quad \text{if} \quad z<0$$
$$\simeq 0 \quad \text{if} \quad z>0$$

for the asymptotic value of Δ_s. Here ξ^* satisfies the equation $dG/d\xi = 0$, where

$$G(\xi) = irk_0\sin\xi\left(\tan\xi+\frac{z}{r}\right),$$

and where $z/r = \tan\phi$, say. This gives

$$\tan^3\xi^* + 2\tan\xi^* + z/r = 0$$

or

$$\sin 2\xi^* + 2\tan(\xi^*-\phi) = 0.$$

A similar result holds for Δ_{ρ_0}:

$$\Delta_{\rho_0} \simeq -\frac{1}{r}\frac{k_0 F(k_0\sin\xi^*)}{\sqrt{(2+\sin^2\xi^*)}}\sin^2\xi^*\cos\xi^*\cos(rk_0\tan^2\xi^*\sec\xi^*) \quad \text{if} \quad z<0$$
$$\simeq 0 \quad \text{if} \quad z>0.$$

If $W < 0$ the reverse holds with Δ_s and Δ_{ρ_0} asymptotically zero if $z < 0$.

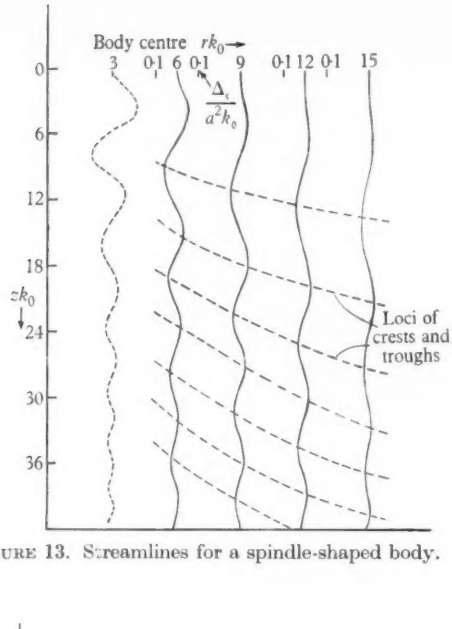

FIGURE 13. Streamlines for a spindle-shaped body.

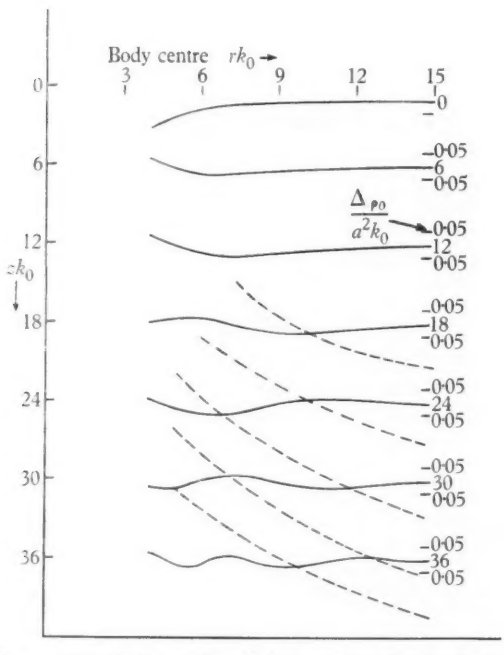

FIGURE 14. Deformation of the constant density levels for a spindle-shaped body.

If ξ^* is used as a parameter we may write the displacements as

$$\frac{1}{r} \times \text{amplitude factor} \times \cos\{(r \text{ or } z) \times \text{phase factor}\}.$$

The results for a spindle-shaped body whose shape is given by

$$f(z) = a\cos\frac{\pi z}{2b} \quad \text{if} \quad |z| < b$$
$$= 0 \qquad\qquad \text{if} \quad |z| > b$$

have been plotted and are shown in the figures 13 and 14. a and b are the half-breadth and half-length of the body and k_0^{-1} has been used as a unit length to measure distances from the body. a^2k_0 has been used as a unit displacement to draw the streamlines and the constant density levels. It may be shown that the slopes of the curves joining the crests and troughs (shown dotted in the figures) are asymptotically $-\cot\xi^*$ so that the approximate rate at which the disturbance spreads outwards is $\frac{1}{2}rW$. A value of $\frac{3}{2}\pi$ for bk_0 was used in the calculations.

9. The wave resistance

The wave resistance to the motion of the body is found from a consideration of the pressures on its surface. If the static thrust is neglected the upthrust is

$$R = 2\pi\int_{-b}^{b} dz\, p\sin\eta\frac{ds}{dz}f(z),$$

as shown in figure 15. p is the perturbed pressure. Euler's equation of motion relative to the body for horizontal motion under steady conditions is

$$W\frac{\partial u}{\partial z} = \frac{1}{\rho}\frac{\partial p}{\partial r}$$

when products of small quantities have been dropped. The assumption that $1/\rho \simeq 1/\rho_0$ gives

$$p = W\rho_0\int_r^\infty \frac{dr}{r}\frac{\partial^2\psi}{\partial z^2} = \frac{W^2\rho_0}{2}\int_0^\infty dk\, k^2F(k)\,H_0^{(1)}(r\Lambda)\exp[i(\operatorname{sgn}W)\,kz].$$

Further, we assume that the body is slender so that $ds/dz \simeq 1$ and $\sin\eta \simeq f'(z)$. If we write $\rho_0(z) \simeq \rho_0(1-\beta z)$, where ρ_0 = density at $z = 0$, then we obtain

$$\frac{R}{\pi\rho_0W^2} = \operatorname{Im}\int_{-b}^{b} dz(1-\beta z)f(z)f'(z)\int_0^\infty dk\, k^2F(k)\exp[i(\operatorname{sgn}W)\,kz]\,H_0^{(1)}(r_a\Lambda).$$

Since $f(z)$ is even, this becomes

$$\frac{R}{2\pi\rho_0W^2} = (\operatorname{sgn}W)\int_0^{k_0} dk\, k^2F(k)\int_0^b dz f'(z)f(z)\sin kz\,J_0(r_a\lambda_1)$$
$$-\beta\operatorname{Im}\int_0^\infty dk\, k^2F(k)\int_0^b dz f'(z)f(z)\cos kz\,H_0^{(1)}(r_a\Lambda).$$

The latter integral represents the effect of the change in virtual mass, and is

neglected because it is multiplied by β. If $r_a\lambda_1$ is small over a large part of the range $0 < k < k_0$, so that $J_0(r_a\lambda_1) \simeq 1$, then approximately

$$R = -(\operatorname{sgn} W)\,\pi\rho_0 W^2 \int_0^{k_0} dk\, k^3\{F(k)\}^2,$$

since

$$\int_0^b dz f'(z)f(z)\sin kz = -\frac{k}{2}\int_0^b dz \cos kz\,\{f(z)\}^2 = -\frac{k}{2}F(k).$$

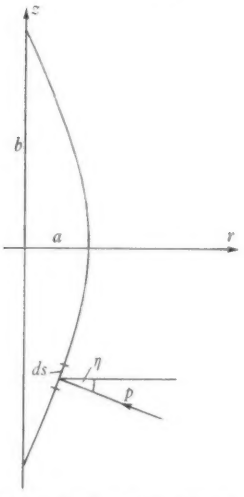

FIGURE 15. Calculation of the wave resistance.

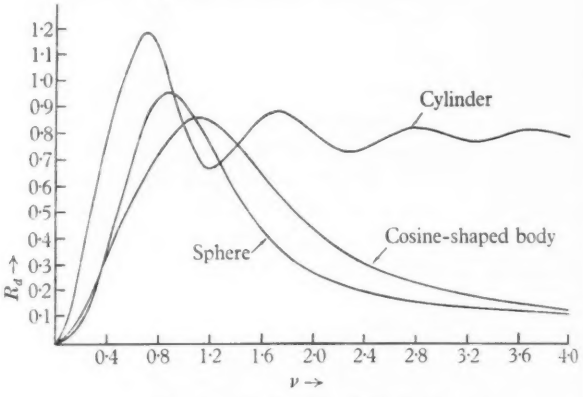

FIGURE 16. Curves of R_d against ν.

$$R_d = \frac{\text{Wave resistance}}{\beta a^4 g\rho_0},$$

$$\nu = \frac{b\sqrt{(g\beta)}}{\pi W}.$$

If the shape of the body is written as $r_a = af_1(z/b)$, where a = half-breadth and b = half-width of the body, the wave resistance is given by

$$\frac{R}{\rho_0 a^4 g\beta} = \frac{1}{\pi\nu^2}\int_0^{\pi\nu} dk\, k^3\{F_1(k)\}^2 = R_d, \quad \text{say}, \tag{19}$$

where $\nu = bk_0/\pi$ and

$$F_1(k) = \int_0^1 dz \cos kz\{f_1(z)\}^2.$$

For small ν, $R_d \propto \nu^2$. In many cases the right-hand side of equation (19) will tend to zero as $\nu \to \infty$, and hence, in general there will be some condition of maximum resistance.

Wave resistance curves for the spindle-shaped body, the sphere and the circular cylinder (whose shape is given by $f(z) = a$, if $|z| < b$, $f(z) = 0$ if $|z| > b$), are shown plotted against ν, that is against a function of velocity, in figure 16. Many assumptions break down for the circular cylinder and its resistance curve is of theoretical interest only.

10. Applications and conclusions

The rise of a thermal through the atmosphere has a velocity given, approximately, by Scorer (1957) $W = \sqrt{(gBa)}$,

where B = buoyancy = density difference/density, and $2a$ = width of the thermal. To estimate the wave resistance it is assumed that the thermal is a sphere whose diameter is the width of the thermal. The ratio of the wave resistance to the buoyancy is then

$$\frac{\text{resistance}}{\text{buoyancy}} = \frac{3}{4\pi}\frac{a\beta}{B}R_d\left(\sqrt{\frac{a\beta}{\pi^2 B}}\right) = 0{\cdot}05\left(\frac{a\beta}{B}\right)^2,$$

roughly, if $a\beta/B < 3$. For the following values of the constants (which may occur in the atmosphere)

$$a = 10^4\,\text{cm.}, \quad B = 10^{-2}, \quad \beta = 10^{-7}\,\text{cm}^{-1},$$

this ratio is about 0·0005. Thus in these cases the wave resistance to motion is negligible. This remains true over a large range of values of B and β. On the other hand, the following values of the constants:

$$a = 10^5\,\text{cm}, \quad B = 3.10^{-3}, \quad \beta = 10^{-7}\,\text{cm}^{-1},$$

give a ratio of about 0·5.

As a rough guide, a sphere will experience most wave resistance at a speed given by

$$\frac{a\sqrt{g\beta}}{W} = 3.$$

The ratio of the wave resistance to the weight of the displaced fluid is then about $\frac{1}{4}a\beta$, where a is the radius of the sphere.

Hence in general the dispersion of energy due to wave motion is small. However, when the situation is specially favourable to the surrounding fluid, and the forces involved are small, this dispersion may play a major part in the behaviour of the fluid, as in the case of the larger thermal with a smaller buoyancy (e.g. towards the end of the ascent).

In a similar manner, it may also be possible for these waves to affect the behaviour of turbulent eddies. For instance, if the eddies are large, and if their outer regions move slowly, a considerable proportion of energy may be dispersed by gravity waves. A criterion for this energy disperion to be a maximum would be

$$\frac{a\sqrt{g\beta}}{W} = n,$$

where the number n depends on the shape of the eddy, a is a typical dimension, say the eddy size, and W a velocity typical of its outer regions.

I would like to express my thanks to Dr R. S. Scorer for the very many helpful discussions and guidance he has given me throughout this work.

REFERENCES

Scorer, R. S. 1950 *Proc. Roy. Soc.* A, **201**, 137.

Scorer, R. S. 1957 *J. Fluid Mech.* **2**, 583.

Scorer, R. S. 1958 *Natural Aerodynamics.* London: Pergamon Press.

Watson, G. N. 1944 *Theory of Bessel Functions*, p. 424. 2nd edition. Cambridge University Press.

The viscosity of a suspension of spheres

By A. D. MAUDE
City of Liverpool College of Technology

(Received 6 May 1959)

It is shown that in Stokes's flow the perturbation field, due to the addition of one more sphere to a shear flow of a fluid containing a number of non-interacting spheres, has the property that the total additional shearing force, acting on any plane normal to the direction of velocity change, is zero. However, the perturbation velocity, integrated over such a plane, takes a constant value, positive if the plane lies on one side of the sphere and negative if it lies on the other side. It follows that the effect of all the spheres is not to alter the shearing stress at all, but to reduce the mean shear by a factor $1-2{\cdot}5c$, where c is the concentration. This suggests that Einstein's viscosity law should be altered to $\eta = \eta_0/(1-2{\cdot}5c)$ when c is not small.

1. Introduction

If a number of spheres is added to a fluid the viscosity of the fluid appears to increase. Einstein (1906, 1911) has shown that if the density of the fluid is the same as that of the spheres, if the Reynolds number is sufficiently low for all inertial effects to be neglected, if the spheres are much smaller than the vessel containing the liquid, and if the spheres do not exert an attractive or a repulsive force between themselves, then for very low concentrations

$$\eta = \eta_0(1+2{\cdot}5c), \tag{1}$$

where η and η_0 are the viscosities of the suspension and fluid respectively, and c is the volume of spheres in unit volume of suspension. Many attempts have been made to extend this equation to higher powers of c for the case of equi-sized spheres. In most previous work, simplifying assumptions have had to be made, and the present work is an attempt to extend (1) without the use of such assumptions.

2. General considerations

The liquid is considered as being sheared in an idealized viscometer consisting of two infinite planes $y = 0$ and $y = H$, the latter being moved with a velocity U_x in the positive direction of x by a force F per unit area. The viscosity is then given by

$$\eta_0 = FH/U_x.$$

The introduction of spheres into this liquid will disturb the flow pattern, and it is convenient to consider the disturbance such that it vanishes at infinity. It is shown below that this implies that the average value of F is unaffected, although

the average value of U_x is reduced. The perturbation velocity in the x-direction, v_x, will cause the velocity to vary over any plane $y = \text{const.}$, but when the plane considered is far from the spheres, and when the perturbations of many spheres are superimposed, the variation over the plane will vanish. This variation over the planes $y = 0$ and $y = H$ is called a wall effect, and will be neglected in the present work.

The flow pattern may be calculated in theory by the method of successive reflexions. The first-order perturbation velocity caused by each sphere placed in the original flow is first calculated. The sum of all these perturbation velocities is then taken as the initial velocity field, and the second perturbation field due to each sphere placed in it is calculated. Third and higher-order perturbation velocity fields can be calculated similarly, leading to an infinite series of terms. It will be shown below that second and higher-order perturbation velocity fields cannot affect the viscosity of the suspension.

It appears to be difficult to prove the convergence of the above series, and, while it is expected to hold for low concentrations, there may well be a critical concentration above which it diverges.

Lamb (1945) gives a general solution of the linearized Navier Stokes equation as follows:

$$v_x = \frac{1}{\eta}\Sigma\left\{\frac{r^2}{2(2n+1)}\frac{\partial p_n}{\partial x} + \frac{nr^{2n+3}}{(n+1)(2n+1)(2n+3)}\frac{\partial}{\partial x}\frac{p_n}{r^{2n+1}}\right\} + \Sigma\left\{\frac{\partial \phi_n}{\partial x} + z\frac{\partial X_n}{\partial y} - y\frac{\partial X_n}{\partial z}\right\} \tag{2}$$

with two similar expressions for v_y and v_z obtained by cyclic permutation of x, y, z. Here $r^2 = x^2+y^2+z^2$, and p_n, ϕ_n, X_n are arbitrary solid harmonics of degree n, and the pressure $p = \Sigma p_n$.

If the origin is now taken at the centre of the added sphere, the restriction that the perturbation velocity and pressure must vanish at infinity implies that $n < 0$. For mathematical rigour, a proof is needed showing that it is always possible to satisfy the required boundary condition at the sphere surface; such a proof could easily be constructed using the method of § 7, but will not be given here.

3. Lemma 1

The force in the x-direction on any plane $y = \text{const.} \neq 0$ due to a perturbation velocity field is zero.

The force on a plane $y = \text{const.}$ will be given by

$$\eta\int_{z=-\infty}^{\infty}\int_{x=-\infty}^{\infty}\left(\frac{\partial v_y}{\partial x}+\frac{\partial v_x}{\partial y}\right)dx\,dz;$$

and as this must be independent of y for there to be no accelerating force on an infinite slab between two planes $y = \text{const.}$, only harmonics which give rise to v_x and v_y of degree -1 need be considered.

Neither ϕ nor X can give rise to terms in v of degree -1, and if the sphere moves so that it experiences no resultant force, the significant term in p_n—that is, p_{-2}—must be zero.

4. Lemma 2

The value of $\iint v_x\,dx\,dz$ in a perturbation field is constant for all positive and negative values of y.

From lemma 1 the total force in the x-direction on any plane $y = \text{const.}$ is zero. That is,

$$\eta \int_{z=-\infty}^{\infty} \int_{x=-\infty}^{\infty} \left(\frac{\partial v_y}{\partial x} + \frac{\partial v_x}{\partial y}\right) dx\,dz = 0.$$

But $$\eta \int_{z=-\infty}^{\infty} \int_{x=-\infty}^{\infty} \frac{\partial v_y}{\partial x}\,dx\,dz = \eta \int_{z=-\infty}^{\infty} [v_y]_{x=-\infty}^{\infty}\,dz = 0.$$

Therefore $$\int_{z=-\infty}^{\infty} \int_{x=-\infty}^{\infty} \frac{\partial v_x}{\partial y}\,dx\,dz = \frac{\partial}{\partial y} \int_{z=-\infty}^{\infty} \int_{x=-\infty}^{\infty} v_x\,dx\,dz = 0,$$

and $$\int_{z=-\infty}^{\infty} \int_{x=-\infty}^{\infty} v_x\,dx\,dz = \text{const.} \tag{3}$$

5. Lemma 3

The average value of $(\partial v_y/\partial x + \partial v_x/\partial y)$ and of $\partial^2 p/\partial x\,\partial y$ over the surface of any sphere $r = \text{const.}$ is zero.

If expressions for $\partial v_x/\partial x$, $\partial v_y/\partial y$ and $\partial^2 p/\partial x\,\partial y$ are found from equations (2), and are integrated over the surface of a sphere, only a very limited number of values of n will be found to give a non-zero value, and in each case $n > 0$, so that this term will not occur in the perturbation velocity.

For example, consider the contribution of ϕ_n to the integral of $\partial v_x/\partial y$ over the surface of a sphere, which is

$$\int \frac{\partial^2 \phi_n}{\partial x\,\partial y}\,dA.$$

As ϕ_n is a solid harmonic, $\partial^2 \phi_n/\partial x\,\partial y$ is also a solid harmonic, and by the orthogonal properties of harmonic functions this integral will be zero unless $\partial^2 \phi_n/\partial x\,\partial y$ is of degree 0 or -1. Therefore, $v_x = \partial \phi_n/\partial x$ will be of degree 1 (the degree zero not giving $\partial^2 \phi_n/\partial x\,\partial y$ of degree -1). But as v_x must vanish at infinity this term cannot be included in the perturbation velocity field, so that no velocity due to the term ϕ_n can contribute to the integral.

A similar argument applied to each possible harmonic proves the proposition.

6. Expression of the significant parts of the integral (3) in terms of p_n, ϕ_n, X_n

As the integral (3) is a constant, only terms in v_x of degree -2 can contribute to it, so that we are restricted to p_{-3}, ϕ_{-1}, X_{-2}. Let

$$v_{x1} = -\frac{r^2}{10}\frac{\partial p_{-3}}{\partial x} + \frac{3}{30r^3}\frac{\partial}{\partial x}(r^5 p_{-3}) = \tfrac{1}{2} p_{-3} x,$$

$$v_{x2} = \frac{\partial \phi_{-1}}{\partial x},$$

$$v_{x3} = z\frac{\partial X_{-2}}{\partial y} - y\frac{\partial X_{-2}}{\partial z}.$$

If we express p_{-3}, ϕ_{-1}, X_{-2} in spherical polar co-ordinates, using the axis of y as the line $\theta = 0$ and the positive (y, z)-plane as the plane $\omega = 0$, considerations of symmetry show that the only terms which contribute to the integral and give a value which is different for positive and negative values of y are as follows. First, there is

$$p_{-3} = Ar^{-3}\cos\omega P_2^1(\cos\theta),$$

where $P_2^1(\cos\theta)$ denotes the associated Legendre polynomial $\cos\theta\sin\theta$. This gives

$$\int_{z=-\infty}^{\infty}\int_{x=-\infty}^{\infty} v_{x1}\,dx\,dz = \begin{cases}\pi A/3\eta & \text{for positive } y,\\ -\pi A/3\eta & \text{for negative } y.\end{cases}$$

Secondly, there is $\qquad X_{-2} = Br^{-2}\sin\omega P_1^1(\cos\omega),$

which gives

$$\int_{z=-\infty}^{\infty}\int_{x=-\infty}^{\infty} v_{x1}\,dx\,dz = \begin{cases}-2\pi B & \text{for positive } y,\\ 2\pi B & \text{for negative } y.\end{cases}$$

It should be noted that terms which make the integral give the same value for positive and negative y may be neglected since they do not affect the rate of shear, and hence the viscosity, of the suspension.

7. Expression of A and B in terms of the original flow

To avoid the complication of the movement of the sphere we may impress a translational and a rotational velocity upon our axes, and thus upon the original flow, such that

$$[4\pi a^3\,\mathrm{curl}\,\mathbf{v}]_{r=0} = 0,$$
$$[6\pi\eta a\mathbf{v} + \pi a^3\,\mathrm{grad}\,p]_{r=0} = 0.$$

The bracket [ ] is used to indicate that the function is to be calculated for the original flow, and the suffix $r = 0$ to indicate that its value at the origin is to be taken. Here a is the radius of the sphere.

By Faxen's theorem (proved simply by Pérès in 1929), this implies the absence of movement or rotation of the sphere if no external force or couple is exerted on it. This choice of axes will not affect the perturbation velocity field.

Lamb gives

$$rv_r = \frac{1}{\eta}\Sigma\frac{nr^2}{2(2n+3)}p_n + \Sigma n\phi_n, \tag{4}$$

$$r\,\mathrm{curl}_r\,\mathbf{v} = \Sigma n(n+1)X_n. \tag{5}$$

The left-hand side of both these is determined by the original flow at $r = a$.

In both the original flow and in the perturbation flow

$$\mathrm{div}\,\mathbf{v} = \frac{1}{r^2}\frac{\partial}{\partial r}(r^2v_r) + \frac{1}{r\sin\theta}\frac{\partial}{\partial\theta}(v_\theta\sin\theta) + \frac{1}{r\sin\theta}\frac{\partial v_\omega}{\partial\omega} = 0.$$

As v_θ and v_ω are equal and opposite in the original flow and in the perturbation flow at $r = a$, $\partial(r^2v_r)/\partial r$ must also be equal and opposite in the two flows at $r = a$. But from (4) we have

$$\frac{\partial}{\partial r}(r^2v_r) = \frac{1}{\eta}\Sigma\frac{n(n+3)r^2}{2(2n+3)}p_n + \Sigma n(n+1)\phi_n, \tag{6}$$

and the left-hand side of this is determined by the original flow at $r = a$.

If both sides of (4) and (5) are multiplied by $\cos\omega P_2^1(\cos\theta)$ and are integrated over the surface of a sphere, the orthogonal property of surface harmonics allows us to write

$$I_1 = -\int_{-1}^{1}\int_0^{2\pi} [rv_r]_{r=a}\cos\omega P_2^1(\cos\theta)\,d\omega\,d\cos\theta$$
$$= \frac{6\pi}{5}\frac{1}{\eta}\frac{A}{a} - \frac{36\pi}{5}\frac{C}{a^3},$$
$$I_2 = -\int_{-1}^{1}\int_0^{2\pi}\left[\frac{\partial}{\partial r}r^2 v_r\right]_{r=a}\cos\omega\, P_2^1(\cos\theta)\,d\omega\,d\cos\theta$$
$$= \frac{72\pi}{5}\frac{C}{a^3},$$

where C is the constant of the harmonic

$$\phi_{-3} = Cr^{-3}\cos\omega P_2^1(\cos\theta).$$

Similarly,

$$I_3 = -\int_{-1}^{1}\int_0^{2\pi}[r\,\mathrm{curl}_r\,\mathbf{v}]_{r=a}\sin\omega P_1^1(\cos\theta)\,d\omega\,d\cos\theta$$
$$= \frac{8\pi}{3}\frac{B}{a^3}.$$

This gives $$A = \frac{5}{12}\frac{\eta a}{\pi}(2I_1 + I_2), \quad B = \frac{3}{8}\frac{a^3}{\pi}I_3.$$

As I_1, I_2 and I_3 are determined by the original flow, A and B may be found for an arbitrary original flow. A similar procedure could be made to yield the constant for each of the harmonics in the perturbation velocity field, and thus to solve the problem of a sphere in an arbitrary velocity field.

8. Expression of I_1 and I_3 in terms of the original flow at the origin

Let the original flow be expressed as a series of spherical harmonics in the manner of equation (2). As it contains no singularities within $r = a$, only harmonics with $n \geqslant 0$ are included.

Consider the harmonics

$$[p_2] = [A'r^2\cos\omega P_2^1(\cos\theta)],$$
$$[X_1] = [B'r\sin\omega P_1^1(\cos\theta)],$$
$$[\phi_2] = [C'r^2\cos\omega P_2^1(\cos\theta)].$$

Then in a similar manner to the last section we get

$$I_1 = -\frac{12\pi}{35}\frac{a^4}{\eta}A' - \frac{24\pi}{5}a^2C',$$
$$I_2 = -\frac{12\pi}{7}\frac{a^4}{\eta}A' - \frac{72\pi}{5}a^2C',$$
$$I_3 = -\frac{8\pi}{3}aB'.$$

Therefore $$A = -a^5A' - 10a^3\eta C',$$

and $$B = -aB'.$$

Consider now $[\partial^2 p/\partial x\,\partial y]_{r=0}$. Clearly, only harmonics of degree 2 can contribute to its value, as higher degrees will vanish when r is put as zero. Application of the double differentiation to all possible harmonics of degree 2 shows that

$$\left[\frac{\partial^2 p}{\partial x\,\partial y}\right]_{r=0} = A';$$

similarly,

$$\left[\frac{\partial v_y}{\partial x}+\frac{\partial v_x}{\partial y}\right]_{r=0} = 2C',$$

and

$$[\mathrm{curl}_z\,\mathbf{v}]_{r=0} = B',$$

which is zero by the hypothesis at the beginning of §7.

It follows that the difference between the values of $\iint v_x\,dx\,dz$ over each viscometer plate is altered by an amount

$$S = \tfrac{4}{3}\pi a^3\left(\frac{5}{2}\left[\frac{\partial v_y}{\partial x}+\frac{\partial v_x}{\partial y}\right]_{r=0}+\frac{a^2}{2\eta}\left[\frac{\partial^2 p}{\partial x\,\partial y}\right]_{r=0}\right).$$

9. Viscosity of a suspension

If there are n spheres in unit volume, the value of U_x is reduced by an amount $nH\bar{S}$, where $\bar{S}$ is the average of S averaging over all the sphere centres. But from lemma 3, the perturbation velocity cannot affect the average value of S, so that it is determined solely by the original flow. That is,

$$\bar{S} = \frac{u_x}{H}\tfrac{5}{2}\cdot\tfrac{4}{3}\pi a^3.$$

Therefore U_x is reduced to

$$U_x(1-\tfrac{5}{2}n\,\tfrac{4}{3}\pi a^3) = U_x(1-2{\cdot}5c).$$

The viscosity is thus

$$\eta = \eta_0/(1-2{\cdot}5c). \tag{7}$$

10. Limitations of the theory

It has been implicity assumed in the last section that no ordering has taken place. That is, any one sphere will be situated in perturbation fields which arise evenly throughout space. In fact, some ordering will occur. It is well known that the probability of finding a second sphere centre a distance r from a given sphere centre is zero up to $r = 2a$, rises to a maximum and falls again, giving an oscillatory function of r of rapidly decreasing amplitude. The maxima become sharper as the concentration increases. However, except near to a wall, no ordering of direction occurs, and as the average values of $\partial v_y/\partial x+\partial v_x/\partial y$ and $\partial^2 p/\partial x\,\partial y$ are zero for any value of r, the ordering with respect to distance will not affect the result.

The possible divergence of the series mentioned in §2 might produce a change of the law at some concentration. Experiments by Higginbotham, Oliver & Ward (1958) show that the viscosity of a suspension of spheres obeys the law

$$\eta = \eta_0/(1-Kc)$$

up to a concentration of 28 %, above which concentration there is a marked departure from this relation. The value of K obtained was slightly less than 2·5. It is suggested that this change of the law at $c = 0{\cdot}28$ is due to the divergence of the series at higher concentrations.

Equation (7) above agrees with Einstein's result (equation (1)) if the square and higher powers of c are neglected. It also agrees with a theoretical expression derived by Kynch (1956) on what he calls a 'rigid envelope' model. Kynch's expression is

$$\eta = \eta_0(1 + 2{\cdot}5c + 6{\cdot}25c^2 + \ldots).$$

However, equation (7) does not agree with most of the other theoretical expressions which have been published.

The author wishes to express his thanks to his wife and to Mr H. Mulholland for help in preparation of the manuscript of this paper.

REFERENCES

Einstein, A. 1906 *Ann. Phys., Lpz.*, **19**, 289.

Einstein, A. 1911 *Ann. Phys., Lpz.*, **34**, 591.

Higginbotham, G. H., Oliver, D. R. & Ward, S. G. 1958 *Brit. J. Appl. Phys.* **9**, 372.

Kynch, G. J. 1956 *Proc. Roy. Soc.* A, **239**, 90.

Lamb, H. 1945 *Hydrodynamics*, 6th ed. New York: Dover Publications.

Pérès, J. 1929 *C.R. Acad. Sci., Paris*, **188**, 310.

Force-momentum fields in a dual-jet flow

By DAVID R. MILLER* AND EDWARD W. COMINGS†
Purdue University, Lafayette, Indiana

(Received 17 April 1959)

Measurements of mean velocity, mean flow direction, normal turbulent stress in the direction of flow, and mean static pressure are reported for the subsonic flow field generated by identical twin jets of air issuing from parallel slot nozzles in a common wall and mixing turbulently with ambient room air. At the low nozzle velocity employed (72 ft./sec), the two-dimensional plano-symmetric flow was effectively incompressible. Since the end walls prevented interjet air entrainment from the surroundings, a region of highly convergent flow was formed near the nozzles. In this region, contour maps clearly reveal (1) the sub-atmospheric static pressure trough that accounts for the jet convergence, (2) a free stagnation point on the plane of symmetry, (3) stable symmetrical contrarotary vortices which recycle air on the concave side of each converging jet, and (4) the super-atmospheric static pressure mound that redirects the merging jet streams in a common downstream direction. Comparisons are made between the development of the flow, in both the region of jet convergence and the region of combined jet flow, and that of the single-jet counterpart which was previously reported.

1. Introduction

In an earlier paper by the present authors (Miller & Comings 1957), measurements of the force-momentum fields in a two-dimensional incompressible free air jet were reported. Particular emphasis was placed on the role of the mean static pressure stresses in the Reynolds equations of motion. It was shown that the pressure stresses and stress gradients are of the same order of magnitude as the normal turbulent stresses $\rho\overline{u'^2}$ and $\rho\overline{v'^2}$ and their gradients, but of opposite sign. As consequences of this near cancellation of stresses in the region of turbulence, the deceleration of the mean flow along a streamline depends almost entirely on the lateral gradient of turbulent shear stress τ, and mean flow accelerations lateral to a streamline are quite small, i.e. the streamlines are nearly straight. In this paper a jet flow is considered in which static pressure effects are far more pronounced in accelerating the mean flow both along and across the streamlines.

The two-dimensional flow in question is that produced by the subsonic flow of air from twin nozzles set in a common end wall, as illustrated in figure 1. All solid boundaries, shown in cross-section, extend sufficiently far in the z-direction to ensure two-dimensionality at the plane ($z = 0$) depicted in the figure. In addition, the extension of the end wall (the plane $x = 0$) in the y-directions is effectively

* Now at Research and Engineering Division, Monsanto Chemical Company, Dayton, Ohio.
† Now at University of Delaware, Newark.

infinite. The centre-plane ($y = 0$) is the plane of symmetry for both flow and boundaries.

Practically no information on dual-jet flows is available in the literature. Corrsin (1944) investigated the unstable flow from seven parallel slot nozzles in a common wall, with emphasis on flow stabilization methods. His nozzles had a width of only 0·20 in., but were geometrically similar to the nozzles of this study. Temperature, total head, and flow directions were reported. Bollinger (1950) measured mean velocity traverses in the combined flow region of twin round jets set with their axes at various angles to each other with the flows converging. The

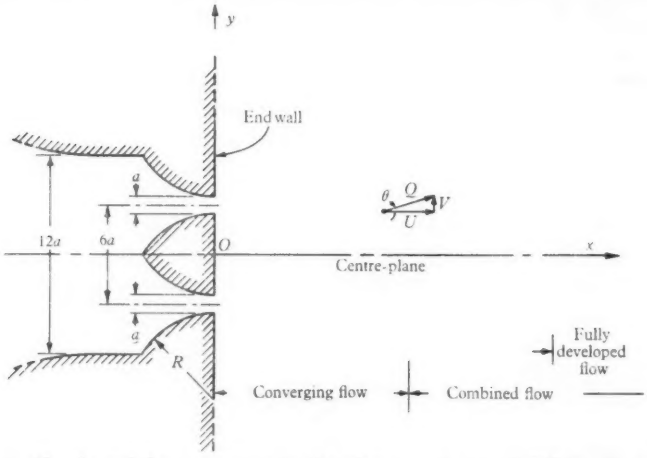

FIGURE 1. Nozzle and flow geometry in the plane $z = 0$. $a = 0{\cdot}500$ in., $R = 2{\cdot}617$ in.

momentum flux distribution in the combined flow region differed greatly from the distribution calculated by adding the momentum flux from the separate jets at the same point in space. Considerable curvature of the streamlines was indicated. Laurence & Benninghoff (1957) have reported extensive mean velocity and turbulence measurements in the fields of multiple interfering air jets produced by several multiple nozzle configurations. In all cases studied, however, the jets were allowed to mix freely with ambient air, and static pressure effects were consequently minimized.

Despite the paucity of previous data, the major features of the dual-jet flow may be inferred *a priori* from the behaviour of simpler turbulent jets and wakes. Thus one would expect to find a region of pronounced negative gauge static pressure $\bar{p}$ between the jets near the end wall, due to the pumping effect of turbulent momentum transfer from the individual jets to the central region. Consequences of the negative pressure are converging curvature of the individual jets and non-conservation of x-momentum. As the two jets are about to merge, one would expect static pressure gradients to be largely responsible for redirecting their momenta in the x-direction and for reversing that portion of the flow earlier entrained on the concave sides of the jets. After the jets have merged, the resultant single-jet flow can be expected to resemble a classical single-jet flow,

the similarity becoming more marked with downstream distance. A downstream transition from large to small static pressure gradients serves to delineate a boundary between the converging and combined flow regions as illustrated in figure 1. As might be expected, the mean x-velocity (U) profile achieves full development a short distance downstream from this boundary.

2. Equations of motion

Under the restrictions placed on the dual-jet flow (and its single-jet counterpart), the appropriate equations of motion in customary Cartesian notation, using Cartesian co-ordinates, are

$$\text{(Continuity)} \qquad \frac{\partial U}{\partial x}+\frac{\partial V}{\partial y}=0, \tag{1}$$

$$(x\text{-Reynolds}) \qquad \frac{\partial}{\partial x}(\rho U^2+\rho\overline{u'^2}+\overline{p})+\frac{\partial}{\partial y}(\rho UV-\tau+\mu\zeta)=0, \tag{2}$$

$$(y\text{-Reynolds}) \qquad \frac{\partial}{\partial y}(\rho V^2+\rho\overline{v'^2}+\overline{p})+\frac{\partial}{\partial x}(\rho UV-\tau-\mu\zeta)=0, \tag{3}$$

where $\tau=-\rho\overline{u'v'}$ is the turbulent shear stress and $\zeta=\partial V/\partial x-\partial U/\partial y$ is the mean vorticity. The mean x- and y-components of velocity U and V define a vector field identically described by two new scalar field variables—Q, the vector magnitude, and θ, the vector angle measured counter-clockwise from the positive x-axis. While these variables, defined in (7), are hereafter called the mean velocity and flow direction, they are not generally identical to the mean magnitude and mean direction of the instantaneous velocity vector.

At any point in the flow, the above equations of motion may be transformed to a local co-ordinate system aligned with the flow by a rotation of the (x, y)-axes through the angle θ. In the local co-ordinate system, s measures distance in the direction of flow and m (rotated y-axis) measures distance perpendicular to s. The transformed equations are

$$\text{(Continuity)} \qquad \frac{\partial Q}{\partial s}+Q\frac{\partial \theta}{\partial m}=0, \tag{4}$$

$$(s\text{-Reynolds}) \qquad \frac{\partial}{\partial s}(\tfrac{1}{2}\rho Q^2+\rho\overline{u_s'^2}+\overline{p})-\frac{\partial}{\partial m}(\tau_s-\mu\zeta)=0, \tag{5}$$

$$(m\text{-Reynolds}) \qquad \kappa\rho Q^2+\frac{\partial}{\partial m}(\rho\overline{v_s'^2}+\overline{p})-\frac{\partial}{\partial s}(\tau_s+\mu\zeta)=0. \tag{6}$$

The subscript s on the turbulent stresses indicates that they are the (s, m)-components of the turbulent stress tensor; and $\kappa=\partial\theta/\partial s$ is recognized as the local streamline curvature. Several of the important transform relations are

$$Q\cos\theta=U, \quad Q\sin\theta=V, \tag{7}$$

$$\rho\overline{u_s'^2}=\rho\overline{u'^2}\cos^2\theta-2\tau\cos\theta\sin\theta+\rho\overline{v'^2}\sin^2\theta, \tag{8}$$

$$\rho\overline{v_s'^2}=\rho\overline{u'^2}\sin^2\theta+2\tau\cos\theta\sin\theta+\rho\overline{v'^2}\cos^2\theta, \tag{9}$$

$$\tau_s=\tau(\cos^2\theta-\sin^2\theta)+(\rho\overline{u'^2}-\rho\overline{v'^2})\cos\theta\sin\theta, \tag{10}$$

$$\zeta=\kappa Q-\frac{\partial Q}{\partial m}=\frac{\partial V}{\partial x}-\frac{\partial U}{\partial y}. \tag{11}$$

Equations (4), (5) and (6) apply to the entire flow field when s and m are interpreted as distances along the orthogonal curvilinear co-ordinates formed by the streamlines and their orthogonals. We now define the stream function ψ which satisfies (1) and is zero on the plane of symmetry:

$$\psi = \int_0 U\,dy = \int_0 Q\cos\theta\,dy. \tag{12}$$

Streamline slope and curvature are now given by the relations

$$dy_\psi/dx = \tan\theta, \quad \kappa = d\theta_\psi/ds = \partial\theta/\partial s. \tag{13}$$

The use of curvilinear co-ordinates in analysing the flow in the converging region of the dual jet simplifies comparisons with the single-jet flow. In the single jet, the mid-nozzle streamline is a straight line coinciding with the x-axis: in the dual jet, each mid-nozzle streamline is highly curved until the individual jets have merged into a single jet. In comparisons based on the mid-nozzle streamlines, s is equivalent to x in the single jet. A new straight-line co-ordinate n, perpendicular to the mid-nozzle streamline and tangential to the local curvilinear m-co-ordinate, is equivalent to y in the single jet.

In the jet flows under consideration, all flow variables except the stream function must approach zero as y approaches $\pm\infty$. This fact, with the conditions of symmetry of the variables, leads to the total mass and momentum integrals from (1) and (2):

$$\rho\int_0^\infty U\,dy = \rho\psi_\infty \quad \text{(a constant)}, \tag{14}$$

$$\int_0^\infty (\rho U^2 + \rho\overline{u'^2} + \overline{p})\,dy = J \quad \text{(a constant)}. \tag{15}$$

A convenient definition of the jet width b is

$$b(x) = \int_0^\infty (U/U_c)^2\,dy, \tag{16}$$

where U_c is the centre-plane ($y = 0$) value of U at the x-station of the integration.

3. Apparatus

But for the removal of a dummy converging wall originally blocking flow from one of the twin nozzles, the flow equipment was identical to that described in the earlier paper. A low-speed wind tunnel provided a uniform low-turbulent horizontal flow of room air to the dual nozzles of aspect ratio 40:1 depicted in horizontal section in figure 1. The nominal nozzle velocity U_r was 72 ft./sec, corresponding to a nozzle Reynolds number aU_r/ν of $1{\cdot}78\times10^4$. Ceiling and floor boundaries over and under the jet flow helped maintain the two-dimensional character of the flow while permitting free horizontal mixing of the jets with ambient air.

Mean and fluctuating velocities were measured with a constant temperature hot-wire anemometer similar to one described by Laurence & Landes (1952). The single tungsten wire, of 0·0002 in. diameter and 0·080 in. active length, was supported vertically in the flow, i.e. parallel to the z-axis. Measurements of mean

static pressure were obtained with a static pressure probe of the disk type and connecting Prandtl micromanometer. These same two instruments were employed in the single-jet study; a more detailed description appears in the earlier paper.

Two instrument probes were used in measuring and indicating local flow direction. The first was a rotatable impact tube supported vertically in the flow. A side impact opening, of 0·021 in. diameter, was located near the upper sealed end of the tube, which was of 0·065 in. outside diameter and 2·5 in. length. The lower end of the tube formed the journal of a fine half-bearing machined in the end of the horizontal supporting member; it also carried a 0·5 in. diameter coaxial sheave for angular control, and provided a pressure connexion via small bore rubber tubing with the micromanometer. A remote graduated hand dial and spring loaded piano wire loop communicated known angular settings to the impact tube. In use, the direction of maximum indicated pressure was taken as the average of two angles of equal indicated pressure straddling the peak angle.

The second flow-direction probe consisted of a light aluminum foil vane, of 1·5 in. vertical length and 0·2 in. width, attached along its vertical leading edge to a wire spindle carried in the conical end bearings of a fork support. No provision was made or needed for accurate vane-angle measurement, since this probe was primarily used in regions of high streamline curvature where positional accuracy is more important than angular accuracy.

Measuring probes were individually positioned in the (x, y)-plane, midway between the ceiling and floor boundaries, with a precision of several thousandths of an inch by means of a lead-screw traversing mechanism. A detailed description of apparatus and procedures is available (Miller 1957).

4. Interpretation of measurements

Some uncertainty is inevitable in the interpretation of 'point' measurements obtained in turbulent flows. Townsend (1956) notes that such measurements commonly concern those quantities that are easy to measure rather than those which have an easily understood significance. Two reasons may be cited: (1) the 'easily understood' quantities are abstractions of a type precluding *direct* measurement by present techniques, and (2) no existing measuring process is so perfectly understood and so free of indeterminate influences as to permit an assumption-free definitive formulation of its cause-to-effect relation. The confidence placed in a given interpretation, therefore, can only be justified by incomplete circumstantial evidence; examples are incomplete theory, comparisons between different instruments, and findings of internal or external consistencies. A brief discussion of interpretation practices employed in this investigation follows.

Hot-wire measurements

The single hot-wire and associated constant-temperature anemometer circuits produces a voltage e assumed to be uniquely and instantaneously related (through steady flow calibration) to the magnitude q of the velocity vector

perpendicular to the wire. When the fluctuation of q, i.e. q', is small relative to its mean $\bar{q}$, then

$$f(\bar{e}) = \bar{q} = Q \quad \text{and} \quad \overline{e'^2}\left[\frac{df(\bar{e})}{de}\right]^2 = \overline{q'^2} = \overline{u_s'^2},$$

where f represents the functional e *vs* q relation obtained by calibration. Measurements of $\bar{e}$ and the mean square of e' were converted to Q and the mean square of u_s' by means of these relations. In flow regions of high turbulence intensity, the above expressions no longer hold. At a point where Q is actually zero (for example, at the free stagnation point and the vortex centre),

$$f(\bar{e}) \doteqdot \bar{q} = \sqrt{(\overline{u_s'^2 + v_s'^2})} > Q,$$

and

$$\overline{e'^2}\left[\frac{df(\bar{e})}{de}\right]^2 \doteqdot q'^2 = \overline{u_s'^2} + \overline{v_s'^2} - \bar{q}^2 \doteqdot \overline{u_s'^2}.$$

These approximate equalities recognize the non-linearity of f at low q (a linearizing circuit was not employed). Q values are readily corrected in the neighbourhood

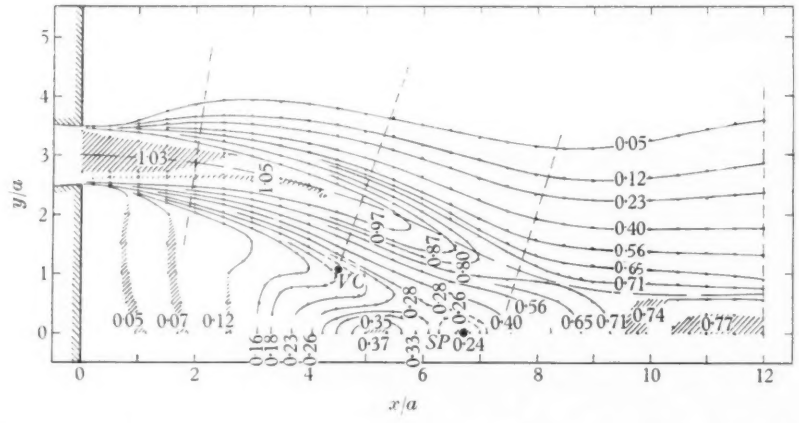

FIGURE 2. Mean velocity contours. Shaded areas are regions of constant velocity within the accuracy of hot-wire measurements. The points marked *VC* and *SP* are respectively the vortex centre and free stagnation point. The mid-nozzle streamline ($\psi = 0{\cdot}48$) starting at $x = 0$, $y = 3a$ is shown, as well as the paths of the four lateral traverses whose profiles are given in figures 5 to 8. Values of Q/U_r.

of singular points by interpolation from surrounding regions of low turbulence intensity, using the location of the point fixed by vane-probe measurements. The method is illustrated in the U/U_r profile of figure 10. All computations involving Q, e.g. the streamline mapping of figure 3, incorporated this method of correction. For purposes of discussion, the Q contours of figure 2 were not corrected. Turning to the fluctuation term $\overline{u_s'^2}$, no correction could be applied since no independent estimate of $\overline{v_s'^2}$ was available. Reported values of this variable are subject to considerable error within a radius of $\frac{1}{2}a$ of the two singular points.

Flow direction

The impact direction probe gave measures of the direction of maximum impact pressure as contrasted to the flow angle θ previously defined. As is demonstrated in figure 3, the two quantities may differ by as much as 40° in a turbulent jet flow, where strong lateral gradients of velocity and static pressure exist. Most of this error was removed by a method of streamline plotting. This method, discussed in

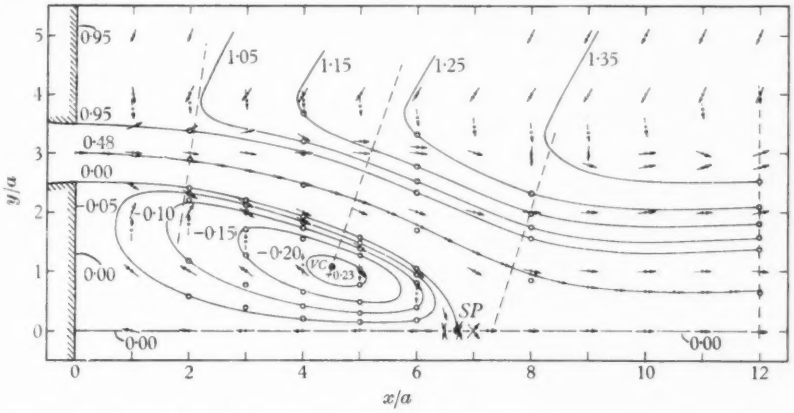

FIGURE 3. Mean flow directions and streamlines determined from the impact probes (solid arrows) and the vane (broken arrows). Values of ψ/aU_r.

conjunction with figure 3, depends strongly on the corrected Q-field and is relatively insensitive to impact direction measurements. It is justified by the excellent agreement found between the path of the mid-nozzle streamline so determined and the path established from impact direction measurements alone. Vane directions agreed everywhere with the calculated streamline directions, within the ability of the eye to judge.

Static pressure

Theory is of no assistance in evaluating the reliability of the static pressure measurements, since the external and internal aerodynamics of the probe and connecting passage are too complex and obscure. Confidence is instead based on the internal and external consistency of the single-jet static pressure measurements, as presented in the earlier paper. There is as yet no indication of significant bias in the measurements, in either the single- or dual-jet flows. Hinze (1959) discusses static pressure measurements at some length.

5. Results—converging region ($0 < x/a < 12$)

Complete tables and graphs of experimental data are available elsewhere (Miller 1957). Measurements revealed, as expected, a high degree of flow symmetry about the centre-plane; consequently, data taken only in the positive y half-plane are reported. At $x/a = 12$, the initially individual jets had merged

and the flow variables resembled those in a single-jet flow. This was consequently selected to be the downstream limit of the converging region and the beginning of the combined flow region.

Mean velocity field

Figure 2 is a contour map of the mean velocity or Q-field. Contour levels were arbitrarily selected to give adequate coverage; and points corresponding to a single level were located by traversing the probe through the flow. The value of each level was then determined from hot-wire traverses carried out after the contours were plotted. To facilitate comparisons with other figures, the positions of several characteristic lines and points are indicated in the figure. The reference velocity U_r, previously referred to as the nominal nozzle velocity, is defined as that hypothetical nozzle velocity whose kinetic pressure $\frac{1}{2}\rho U_r^2$ is equal to the measured gauge impact pressure at the centre of the nozzle mouth. This particular definition, selected for convenience in hot-wire calibration and data reduction, does not require that $Q/U_r = 1{\cdot}00$ at the centre of the nozzle mouth.

Flow direction and streamline fields

Mean flow directions and streamlines appear in figure 3. Solid and broken arrows represent flow directions measured with the impact and vane direction probes, respectively. The vortex centre and free stagnation point were found using the vane probe. At the free stagnation point the vane whipped around in all directions at random without favouring any one; at the vortex centre the vane rotated rapidly and continuously. Detection of the two points by the vane method was found to be remarkably sensitive and reproducible; no two measurements of their positions differed by more than $0{\cdot}132a$ or 0·066 in. in either co-ordinate. Crossed arrows in the vicinity of the free stagnation point reflect the fact that two symmetric pressure maxima were found on rotating the impact direction probe about its axis.

The mid-nozzle streamline $\psi/aU_r = 0{\cdot}48$ was established from impact direction measurements exclusively. Using the velocity contours of figure 2, an original estimate of its path was made. The impact direction probe was then traversed along the estimated path with readings of θ taken at $\frac{1}{2}$ in. intervals. These readings were used in a numerical integration of the first relation of (13) to obtain an improved estimate of the path. Three repetitions of this iterative procedure (the last with an x-interval of 0·25 in.) gave satisfactory convergence. Analysis of the final curve yielded its curvature κ from (13) and arc length s as functions of x. All other streamlines were calculated from (12) using the measured flow directions and Q-values from figure 2. Calculated points are indicated by circles in figure 3. In the vicinity of the two nozzle lip streamlines near the nozzle, the agreement between streamline and measured flow directions is poor. This is a result of the gradient error of the impact direction probe discussed earlier. In these regions, the streamlines are more accurate indicators of true flow directions.

Among the features revealed in figure 3 are: (1) one of the two contrarotary stable vortices which recycles air (24 % of that issuing from the nozzles) between the jets, (2) the stagnation of the streamline from the inner lip of the nozzle at

SP, and (3) curvature, spread, and confluence of the jets. Air entrained on the outer side of the jet is seen to approach at an angle near 245°. The corresponding streamlines, if sufficiently extended, would reveal another large vortex system outside the jet in accordance with the requirement of (14).

Static pressure field

Mean static pressure contours appear in figure 4. Comparisons with the previous contour maps give an immediate qualitative picture of the important role of static pressure gradients in accelerating the mean flow, particularly in regard to

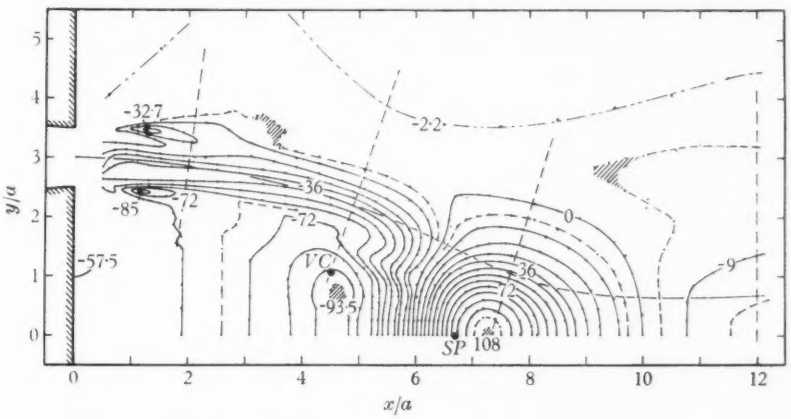

FIGURE 4. Mean static pressure contours. Values of $\overline{p}/\rho U_r^2 \times 10^3$. —, contour interval = 9; – – –, mid-contour.

lateral acceleration resulting in streamline curvature. Except in the static pressure mound between $x/a = 6$ and $x/a = 10$, all regions of the flow were at less than atmospheric pressure (negative $\overline{p}$). The static pressure mound around $x/a = 7$, whose peak is near the free stagnation point, is largely responsible for the stagnation and for the reversal of the flow between jets. Downstream from the mound a return to the modest static pressure gradients typical of a single free jet is observed.

Lateral traverses

Further aspects of the converging flow are best revealed in profile diagrams derived from probe traverses indicated in figures 2–4. Proceeding downstream along the mid-nozzle streamline, the four lateral traverses perpendicular to the streamline and intersecting it at $s/a = 2$, 5, 8, 12·4 correspond to the profiles of figures 5–8 respectively. Traverse measurements included mean velocity Q, turbulent s-stress $\rho\overline{u_s'^2}$, and mean static pressure $\overline{p}$.

The mean velocity profiles of figures 5–7 are fairly symmetrical about $n = 0$ and similar in shape (but not of equal peak height) to single-jet profiles taken at equal distances from the nozzle. A comparison of the widths of the velocity profiles at various downstream distances in table 1 reveals practically identical spreading tendencies in the converging jet and the single free jet out to 8 nozzle-slit widths

from the nozzle. Beyond $8a$ the comparison breaks down due to the confluence of the converging jets in the dual-jet flow. In table 1 jet width is taken to be the lateral distance between the two profile points where the mean velocity is half of

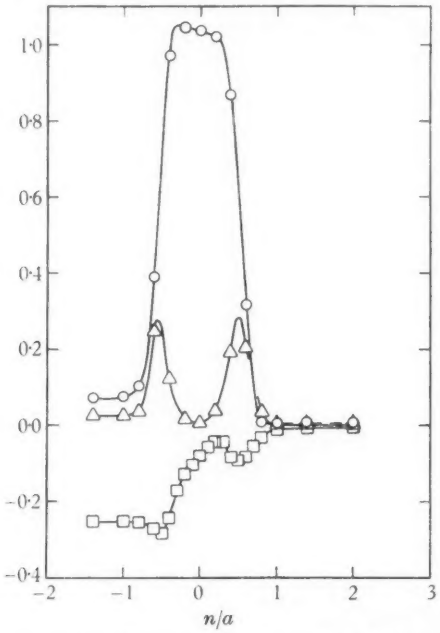

FIGURE 5. Lateral traverse at a distance $s/a = 2$ measured downstream from the nozzle along the mid-nozzle streamline. Circles, triangles and squares refer respectively to mean velocity Q, turbulent stress $\rho\overline{u_s'^2}$, and mean static pressure $\bar{p}$. ○, Q/U_r; △, $10\overline{u_s'^2}/U_r^2$; □, $4\bar{p}/\rho U_r^2$.

	Half velocity jet width / Nozzle width (a)	
x/a or s/a	Dual jet	Single jet
2	1·06	1·14
3	(1·15)	1·20
4	(1·24)	1·26
5	1·33	—
6	(1·46)	1·50
8	1·96	—
10	—	2·24

TABLE 1. Comparison of dual- and single-jet widths near nozzles.

the profile peak value. Numbers in parentheses were obtained from figure 2 and are less accurate than the others. Consequences of the nearly equal profile spreading are developed later in the discussion of the mid-nozzle streamline profiles.

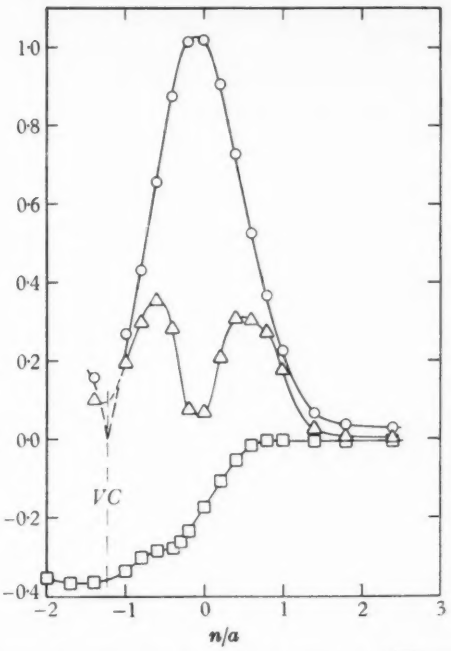

FIGURE 6. Lateral traverses at $s/a = 5$. ○, Q/U_r; △, $10\overline{u_s'^2}/U_r^2$; □, $4\bar{p}/\rho U_r^2$.

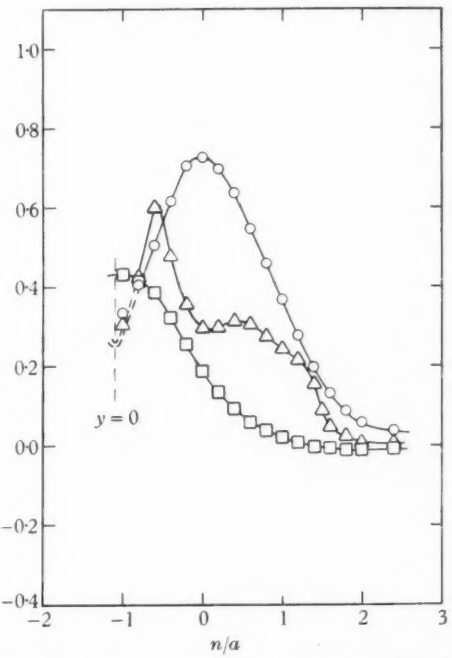

FIGURE 7. Lateral traverses at $s/a = 8$. ○, Q/U_r; △, $10\overline{u_s'^2}/U_r^2$; □, $4\bar{p}/\rho U_r^2$.

Turning to the turbulent stress profiles of figures 5–8, several interesting features are observed in the downstream development of the two-peaked curve when compared to its single-jet counterpart. (In the single-jet flow, of course, the peaks are symmetrical about the x-axis.) Starting near $s/a = 5$, the inner stress peak (negative n) begins a period of rapid growth relative to the outer peak (positive n),

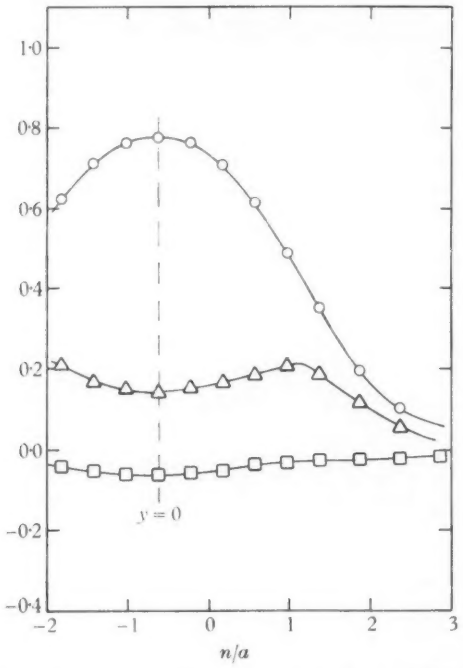

FIGURE 8. Lateral traverses at $s/a = 12{\cdot}4$. ○, Q/U_r; △, $10\overline{u_s'^2}/U_r^2$; □, $4\overline{p}/\rho U_r^2$.

whereas the outer peak spreads more rapidly and develops a hump clearly evident at $s/a = 8$. Downstream from $s/a = 8$, in the region where the two jets intermingle, the inner stress peak decays quite rapidly; at $s/a = 12{\cdot}4$ no trace of an inner peak remains. The limited turbulence measurements reported here preclude a coherent discussion of the reasons for the observed behaviour of the stress profile; it can only be stated that moderate differences exist in the production, transport, and dissipation of turbulence energy between the inner and outer shear regions of the converging jet and either shear region of the single jet.

Static pressure profiles of figures 5–7 bear no resemblance to corresponding single-jet profiles. In the discussion of figure 4, mention was made of the role of static pressure in curving the streamlines. To explore this further, we rearrange (6) in the form

$$\kappa\rho Q^2 + \frac{\partial \overline{p}}{\partial m} = \frac{\partial}{\partial s}(\tau_s + \mu\zeta) - \frac{\partial}{\partial m}(\rho\overline{v_s'^2}), \tag{17}$$

and hypothesize that the right-hand side is zero along the mid-nozzle streamline of the converging jet. Note that in the single jet along the centre-plane each term

of (17) is exactly zero, due to the symmetry of the flow. To test the hypothesis, values of the two left-hand terms were calculated at various points along the mid-nozzle streamline. Resulting values in dimensionless form are listed in table 2. These results show that the lateral static pressure gradient at the mid-nozzle streamline was at least the dominant force causing streamline curvature. That better agreement was not obtained is ascribed more to the diversity of measurement errors involved (velocity, flow direction, static pressure) than to the influence of any term on the right-hand side of (17).

s/a	$\kappa a Q^2/U_\tau^2$	$\partial(\overline{p}/\rho U_\tau^2)/\partial(m/a)$
2	−0·064	0·055
3·5	−0·076	0·090
5	−0·076	0·081
6·5	−0·011	0·011
6·63	0·000	0·000
8	0·088	−0·097
9·5	0·049	−0·023

TABLE 2. Lateral accelerations and static pressure gradients on the mid-nozzle streamline.

Analyses similar to the above have been carried out in other regions of the flow. The general conclusion is that both turbulent stress gradients and static pressure gradients contribute to lateral flow acceleration; the latter dominates where Q is large and κ is small (as along the mid-nozzle streamline), and the former dominates where Q is small and κ is large (as in the regions of entrainment).

Longitudinal traverses

Profiles of Q, $\overline{u_s'^2}$, and $\overline{p}$, obtained by traverse measurements along the mid-nozzle streamline and along the centre-plane, appear in figures 9 and 10, respectively. Considering the former first, the effect of the static pressure gradient along the streamline on the mean velocity is evident. In particular, the static pressure peak near $x/a = 8$ is largely responsible for the dip in the mean velocity decay curve. The turbulent stress profile contains a peak, also near $x/a = 8$, which is sharper and 45 % higher than the corresponding peak in the single-jet flow.

Neglecting the viscous stress term, the Reynolds equation (5) respective to the s-direction is

$$\frac{\partial}{\partial s}(\tfrac{1}{2}\rho Q^2 + \rho\overline{u_s'^2} + \overline{p}) - \frac{\partial \tau_s}{\partial m} = 0. \tag{18}$$

The quantity in parentheses was computed at various stations along the mid-nozzle streamline for both the converging and single jets. Results are compared in table 3. Good agreement indicates that the distribution of the turbulent shear stress τ_s about the mid-nozzle streamline was practically identical in the two flows despite differences in the mean velocity levels. Equal spreading of the two jet flows, discussed in conjunction with table 1, further establishes the similarity of the turbulent shear stress fields in the cores of the jets.

Turning to the centre-plane profiles of figure 10, note the (x, y)-co-ordinates and components are used because of the coincidence of the traverse with the x-axis.

Plotting U instead of Q reveals more clearly the reversal of the mean flow and the nature of the previously mentioned error in mean velocity measurement near the free stagnation point. The data of this figure were analysed in a manner similar

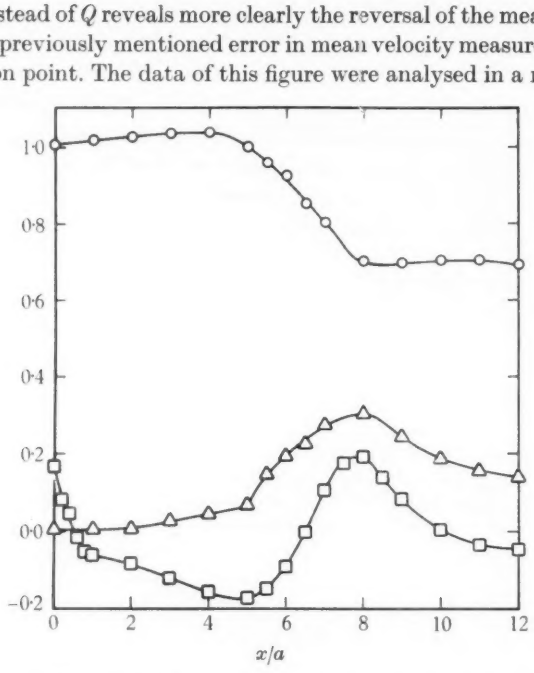

FIGURE 9. Longitudinal tranverses along the mid-nozzle streamline. ○, Q/U_r; △, $10\overline{u_s'^2}/U_r^2$; □, $4\bar{p}/\rho U_r^2$.

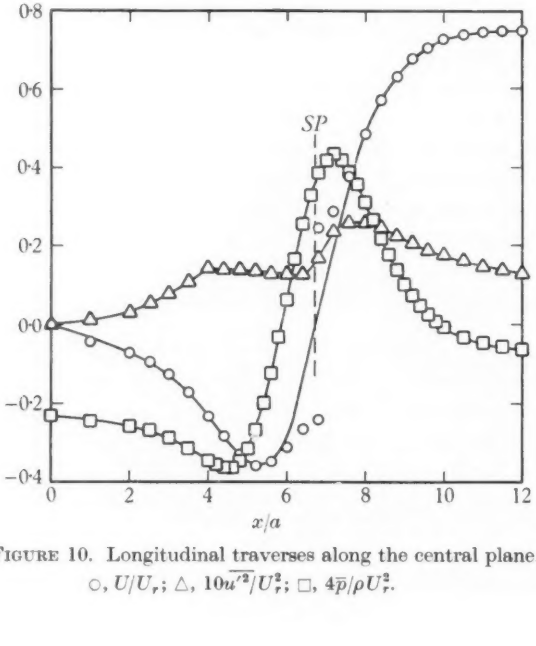

FIGURE 10. Longitudinal traverses along the central plane. ○, U/U_r; △, $10\overline{u'^2}/U_r^2$; □, $4\bar{p}/\rho U_r^2$.

to that of the preceding figure. Equation (18) when written for the centre-plane streamline is

$$\frac{\partial}{\partial x}(\tfrac{1}{2}\rho U^2+\rho\overline{u'^2}+\overline{p})-\frac{\partial \tau}{\partial y}=0. \tag{19}$$

Again the quantity in parentheses was computed at a number of stations along the centre-plane. A plot of these data against x yielded a smoothed curve remarkably symmetrical about $x/a = 6{\cdot}57$ (very near the free stagnation point) and quite well represented by a Gaussian error integral curve as follows:

$$(\tfrac{1}{2}\rho U^2+\rho\overline{u'^2}+\overline{p})/\rho U_\tau^2 = 0{\cdot}337\int_{-\infty}^{w}\Phi(w')\,dw'-0{\cdot}059, \tag{20}$$

where

$$\Phi(w')=\frac{1}{\sqrt{(2\pi)}}\exp(-\tfrac{1}{2}w'^2), \quad w=0{\cdot}658(x/a-6{\cdot}57).$$

	$\dfrac{\rho Q^2+2\rho\overline{u_s'^2}+2\overline{p}}{\rho U_\tau^2}$	
s/a, x/a	Dual jet	Single jet
4	1·00	1·01
6	0·86	0·87
8	0·69	0·70
10	0·55	0·57
12	0·49	0·49

TABLE 3. Comparison of mid-nozzle streamline decay.

Differentiating (20) with respect to x/a gives the turbulent shear stress gradient,

$$\frac{\partial}{\partial(y/a)}\left(\frac{\tau}{\rho U_\tau^2}\right)=0{\cdot}089\exp[-0{\cdot}216(x/a-6{\cdot}57)^2], \tag{21}$$

which is a Gaussian error curve centred at $x/a = 6{\cdot}57$ with a peak value of 0·089. These relations hold in the range $0 < x/a < 11$. In view of flow symmetry, τ itself is zero along the centre-plane.

From the foregoing it is apparent that the turbulent shear stress gradient tends to accelerate the mean flow in the positive x-direction at all points along the centre-plane out to $x/a = 11$; the maximum tendency occurs very near the free stagnation point. Alternately reinforcing and opposing this tendency is the effect due to the static pressure gradient along the x-axis. In the range $4{\cdot}5 < x/a < 7{\cdot}2$, the static pressure gradient tends to accelerate the flow in the negative x-direction against the influence of the turbulent shear stress. Flow stagnation occurs at the point (*SP*) where the two forces are equal and opposite. The x-gradient of the normal turbulent stress $\rho\overline{u'^2}$ in (19) was generally negligible in comparison to the static pressure and turbulent shear stress forces.

6. Results—combined jet region ($x/a > 12$)

On merging, the converging jets of the dual-jet flow lose their individual identities and behave as a single jet. The analysis of the flow in the combined jet region is therefore identical to that of the previously reported single-jet flow

(Miller & Comings 1957). Indeed, the combined jet flow is so nearly similar to the single-jet flow that it will suffice to describe the similarities and differences without repeating the more detailed development of the earlier paper.

Mean velocity and jet width

A fully developed turbulent jet is characterized by (1) linear spread with downstream distance, (2) power-law decay of the centre-plane mean velocity with downstream distance, and (3) similarity of the lateral mean velocity profile. These three properties are expressed in the relations

$$b/a = c(x/a - x_0/a), \tag{22}$$

$$U_c^2/U_r^2 = K(x/a - x_0/a)^{-C}, \tag{23}$$

$$U/U_c = f(\eta), \quad \text{where} \quad \eta = y/b. \tag{24}$$

In these equations c, x_0, K and C are experimental constants, b is the jet width (a function of x) defined in (16), and U_c is the centre-plane mean velocity at a given value of x. Certain restrictions are imposed on the values of the experimental constants by the condition of momentum conservation expressed in (15). These restrictions, listed in the last lines of table 4 together with values of the various experimentally determined quantities, are necessarily approximate since momentum alone is not strictly conserved, even in the single jet.

Factor	Combined dual jet	Single jet
Region of fully developed flow		
$x/a >$	23	7
c	0·072	0·0723
x_0/a	−5·50	−1·572
K	11·1	6·74
C	1·03	1·028
$f(\eta)$	$\exp(-\frac{1}{8}\pi\eta^2)$	$\exp(-\frac{1}{8}\pi\eta^2)$
Restrictions		
$C \doteq$	1·0	1·0
$cK \doteq J/\rho U_r^2 =$	0·86	0·48

TABLE 4. Comparison of mean velocity properties in the fully developed jet.

The data of table 4 with equations (22), (23) and (24) give a complete description of the mean velocity fields of the two flows after the mean velocity profiles achieved similarity. The station where this occurred, listed on the first line, was considerably farther from the nozzle in the dual-jet case because of the extended region of convergence of the individual jets. Rates of spread and decay of the profiles were identical in the two flows as indicated by the equality of c and C in each case. Also identical were the dimensionless analytic functions $f(\eta)$ best fitting the experimental data. The only marked differences found were in the position of the 'virtual origin' x_0 and in the value of the velocity level constant K.

All comparisons thus far made can be summarized in a single statement as follows: if the two nozzles of the dual-jet flow were replaced by a single nozzle of the same size as either, located on the centre-plane at $x/a = -3{\cdot}93$ and having

a nozzle mouth velocity 1·29 times that of the original dual nozzles, then the mean velocity field at $x/a > 23$ would be indistinguishable in all respects from the original field.

Dimensionless mean velocity profiles appear in figure 11. It is noted that the data have not been corrected to remove the slight influence of the lateral velocity V on the hot-wire in the region $2{\cdot}5 < \eta < 4{\cdot}0$. The smooth curve through the points obtained at $x/a = 20$, 30, 40 is identical to the best curve through the uncorrected data of the single jet. Points of the $x/a = 12$ profile do not conform to the curve since the flow had not reached full development at that station.

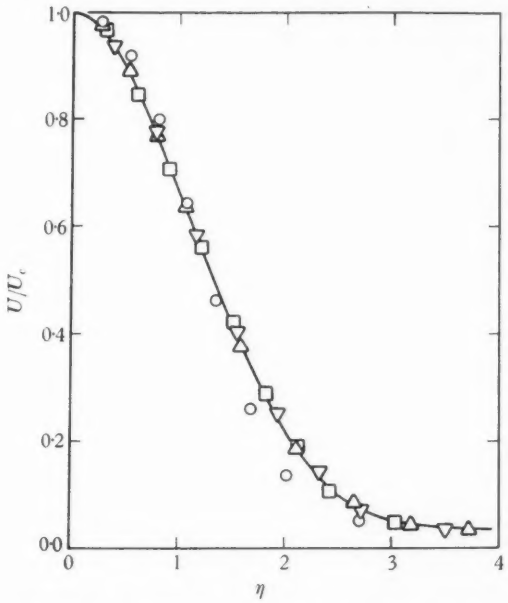

FIGURE 11. Mean velocity profiles for $x/a \geqslant 12$. ○, 12; △, 20; ▽, 30 and □, 40. The solid curve is identical with that obtained for a single jet.

Turbulent x-stress and static pressure profiles

As should be expected, the downstream development of the turbulent x-stress and static pressure profiles resembles that of the single-jet flow. The turbulent stress profiles of figure 12 exhibit 'partial self-preservation' at $x/a = 20$, 30 and 40, as evidenced by a coincidence of the curves at large η and an apparent tendency to converge on a single fully self-preserving curve as x approaches infinity. A convergence of the static pressure profiles on a self-preserving form is apparent in figure 13. With the exception of the turbulent stress profile at $x/a = 12$, all of the curves are typical in shape and height to those obtained in a single-jet flow. This, however, is as far as the similarities go. No simple equivalence was found in the distance histories of the profiles. This is shown in the data of table 5, which lists the approximate downstream station of the single-jet flow at which the given dual-jet profile was most nearly duplicated. These data reveal a near-normal

development of the static pressure field, accompanied by an initially retarded but rapid development of the x-stress field. Finally, at $x/a = 40$, the x-stress profile is 'in step' with the static pressure profile; both are nearly identical to the corresponding single-jet profiles at $x/a = 35$.

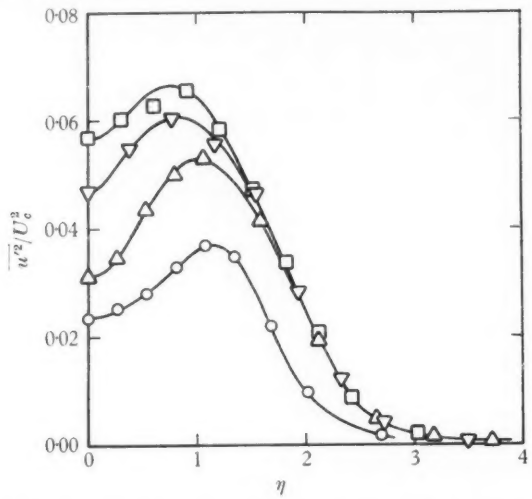

FIGURE 12. Turbulent x-stress profiles. $x/a \geqslant 12$: ○, 12; △, 20; ▽, 30; □, 40.

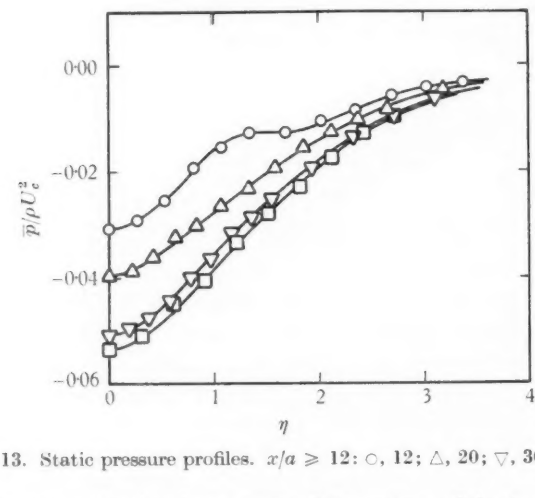

FIGURE 13. Static pressure profiles. $x/a \geqslant 12$: ○, 12; △, 20; ▽, 30; □, 40.

Thus so far no mention has been made of the nature of the turbulent y-stress $\rho\overline{v'^2}$ and shear stress τ fields. In the earlier paper it was shown that in the fully developed single jet (1) dimensionless y-stress profiles are nearly identical to coincident static pressure profiles with the sign inverted, and (2) the shear stress profile reaches full self-preservation at the same station as the mean velocity profile does. We also note that the turbulent x- and y-stresses are identical to twice the

x- and y-components of the energy of turbulence. These facts taken all together give some insight into the precedence of approach to self-preservation (or dynamic equilibrium) of the turbulent motion and energy in the combined jet region. First to reach full self-preservation is the turbulent shear stress at $x/a = 23$. The turbulent y-stress or y-energy distribution quickly assumes a characteristic single-jet form and approximate growth rate downstream from the region of convergence. Lagging behind but rapidly catching up to single-jet proportions is the x-stress or x-energy. It is assumed, but without supporting evidence, that the dual-jet flow downstream from $x/a \doteqdot 40$ would have been found to be completely indistinguishable from a single-jet flow originating in a suitably placed single nozzle.

Dual-jet profile station, x/a	Equivalent single-jet profile station, x/a	
	Turbulent x-stress	Static pressure
12	None	13
20	8	20
30	22	32
40	35	34

TABLE 5. Profile equivalence.

7. Conclusions

Based on the experimental data presented and on the results of a previous investigation of a single free jet, a reasonably clear description of the mean and turbulent motion in a two-dimensional dual-jet flow is possible. In the region of jet convergence near the nozzles, the structure of the flow in the core of either jet is quite similar to that of a single free jet provided due account is taken of the mean flow accelerations attributable to a radically different static pressure field. A region of sub-atmospheric static pressure between the converging jets accounts for their convergence and for the reversal of a considerable fraction of the total flow at the centre-plane against a strong downstream force of turbulent shear. Associated with the flow reversal is the appearance of a pair of symmetrical contrarotary stable vortices and a free stagnation point on the centre-plane. Where the two jets merge, a super-atmospheric static pressure mound redirects their momenta into a single resultant jet symmetrical about the centre-plane. The flow structure of the combined jet exhibits all characteristics of a single-jet flow except for an altered evolution of the turbulence toward self-preservation. This is ascribed to differences in upstream conditions.

For valuable assistance in the course of this work, the authors are indebted to Professor Sydney Goldstein of Harvard University and Mr James C. Laurence of the N.A.S.A. Lewis Research Center. Financial support was generously provided by The Barrett Division, Allied Chemical and Dye Corporation, and by the Purdue Research Foundation.

REFERENCES

BOLLINGER, E. H. 1950 M.S. Thesis, University of Illinois.

CORRSIN, S. 1944 *Nat. Adv. Comm. Aero., Wash., Wartime Rep.* no. W-90.

HINZE, J. O. 1959 *Turbulence.* New York: McGraw-Hill.

LAURENCE, J. C. & BENNINGHOFF, J. M. 1957 *Nat. Adv. Comm. Aero., Wash., Tech. Note* no. 4029.

LAURENCE, J. C. & LANDES, L. G. 1952 *Nat. Adv. Comm. Aero., Wash., Tech. Note* no. 2843.

MILLER, D. R. 1957 Ph.D. Dissertation, Purdue University.

MILLER, D. R. & COMINGS, E. W. 1957 *J. Fluid Mech.* **3**, 1–16.

TOWNSEND, A. A. 1956 *The Structure of Turbulent Shear Flow.* Cambridge University Press.

The boundary layer near the stagnation point in hypersonic flow past a sphere

By T. K. HERRING
Department of Mathematics, University of Manchester

(Received 13 May 1959)

When a sphere or other bluff body travels at supersonic speeds, a shock wave is formed close to the front surface. With increase of speed the air behind the shock is further compressed, and the shock wave moves closer to the surface. This paper considers the case where the region close to the stagnation point between the shock and the sphere can be taken to be a steady laminar boundary layer.

The approximate solution of the equations of motion follows closely the classical work of Homann (1936), ideas similar to those of Lighthill (1957) being used to apply it to the problem in hand. It consists mainly in reducing the equations to ordinary differential form by assuming forms of the flow variables which satisfy the boundary conditions, notably at the shock wave. In addition, several transformations are employed in order to simplify the equations and to increase the range of solutions, and also to facilitate the use of the 'Mercury' electronic computer in solving them.

The results give an insight into some aspects of hypersonic flows. Included in this paper are a selection of temperature and transverse velocity profiles across the boundary layer and several graphs relating such quantities as the shock stand-off distance and the skin-friction coefficient with Reynolds number. The last two mentioned are the most interesting. The first set gives the surprising result that the shock stand-off distance increases with increase in Reynolds number, whereas it is known that the boundary-layer thickness decreases. The second set of graphs shows that the skin-friction coefficient is inversely proportional to a decreasing power of the Reynolds number when it is lower than order 10^3, but the indication is that it tends to the expected constant power of $\frac{1}{2}$ when the Reynolds number is of order 10^4.

1. Introduction

In this paper we investigate an interesting case where the region between the shock and the sphere can be taken to be a steady laminar boundary layer. A high-speed flow through a medium of very low density would seem to satisfy this condition. For, at low enough density, the Reynolds number can be so low (say, about 10^4 or less) that the boundary layer will be laminar, but of a thickness comparable to the stand-off distance of the shock.

Now, in the atmosphere at heights of 60–100 km, the densities range from 10^{-6} to $10^{-7.5}$ g/cm^3, and the temperatures vary from 180° to 360° K (Whipple 1943). The Reynolds number of a sphere of diameter 25 cm, travelling at 4 km/sec

at an altitude of 80 km, is about 5×10^3. This region of the atmosphere thus provides a practical setting for the problem under investigation.

We shall assume that the surface of the body has not yet been heated significantly, and thus that it is a good approximation to take the sphere and free stream temperatures to be equal.

By confining ourselves to the region close to the stagnation point, the shock wave can be taken, to a fair approximation, as spherical and concentric with the sphere. This is a result which has been verified under certain conditions both experimentally and theoretically. Oliver (1956) showed in experiments with a sphere and other bluff bodies at a Mach number of 5·8 that this was so, and he included in his paper excellent schlieren photographs of the phenomenon. A number of authors, including Lighthill (1957), Freeman (1956) and Chester (1956), have put forward theoretical treatments. Chester considered a perfect gas with constant specific heats (as we shall), and, by a method of successive approximations in which he assumed the shape of the shock and found the shape of the body, he was able to verify the above results.

Now, close to the stagnation point the speeds are subsonic, and all compressibility effects are due to thermal variations in the fluid properties. The present work can therefore be compared with work on low-speed laminar boundary layers with varying temperatures. For example, Brown & Donoughe (1951) considered the problem of a two-dimensional steady laminar boundary layer on a straight porous wall, and they found solutions to the equations of motion when the wall temperature was varied. They were able to obtain a negative displacement thickness by cooling the wall, a result similar to one in this paper where the stand-off distance of the shock is found to increase with Reynolds number.

The geometry of the problem we are considering is close to that of Homann (1936), who considered the steady incompressible flow in a boundary layer, along a surface of revolution, close to the stagnation point. He neglected terms of the order of the square of the transverse co-ordinate measured along the surface, and found that the form of the flow variables suggested by the axial symmetry and the constant thickness of the boundary layer, which is a correct result in this approximation, satisfied the boundary conditions and the equations of motion.

In the paper by Lighthill (1957), an exact solution to the inviscid incompressible high-speed flow past a sphere was obtained. Lighthill showed that all the equations of motion and boundary conditions could be satisfied assuming a spherical shock concentric with the sphere.

For the present problem we combine the approaches of Homann and Lighthill, using the forms of the flow variables suggested by the boundary conditions behind the shock wave. The use of the strong-shock conditions is found to be necessary to make the density dependent upon the normal co-ordinate yet independent of the transverse co-ordinate to the first order. With this simplification, the assumed forms of the flow variables satisfy the boundary conditions accurately. The inviscid terms of the equations of motion are satisfied accurately, and the viscous terms are satisfied to the first order in the transverse co-ordinate. A note on the approximation involved in using the strong-shock relations is included in §3.

We will assume for simplicity that the fluid is a perfect gas and that the specific heats at constant pressure and volume of the gas mixture are constant throughout the region of interest. In a real flow, however, where there are very large temperature differences in the boundary layer, the variations in the ratio of the specific heats can be as much as 0·3. This is attributable to ionization and dissociation effects as well as to the large range of temperatures. For this reason we shall quote results for different ratios of the specific heats.

The first section of the paper is devoted to the formulation and simplification of the equations of motion, and several transformations are introduced to facilitate subsequent integrations. The second section concerns the derivation of the results and the discussion of interesting physical conclusions.

2. Basic equations

The equation of state of a perfect gas is

$$p = \rho RT, \tag{1}$$

where R is the gas constant per gramme, p the pressure, ρ the density, and T the temperature. To simplify the problem further, we will take the viscosity μ to be proportional to T, and the Prandtl number $\sigma = \mu c_p/k$ to be a constant = 0·72. Here c_p and c_v are the specific heats at constant pressure and volume ($c_p/c_v = \gamma$), and k is the thermal conductivity, which must also be proportional to T.

We shall use spherical polar co-ordinates (r, θ, λ) with origin at the centre of the sphere and the axis $\theta = 0$ pointing upstream, and write the respective velocity components as v_r, v_θ, v_λ, with $v_\lambda = 0$ in the present case of axial symmetry. The radius of the sphere is taken to be a, and that of the shock to be b, and suffixes 0, 1 will refer respectively to the uniform conditions ahead of the shock, and those immediately behind. Also, we will denote the enthalpy by I and let $M_0 = V_0/c_0$, c_0, and V_0 be the values of the Mach number, speed of sound and axial velocity ahead of the shock. It is important to note that throughout this paper we are considering only the region where θ is small (shaded in figure 1).

The strong-shock relations are

$$\frac{\rho_1}{\rho_0} = \frac{\gamma+1}{\gamma-1}, \tag{2}$$

$$v_{r1} = -\frac{\gamma-1}{\gamma+1} V_0 \cos\theta, \quad v_{\theta 1} = V_0 \sin\theta, \tag{3}$$

$$\frac{p_1}{p_0} = \frac{2\gamma}{\gamma+1} M_0^2 \cos^2\theta, \tag{4}$$

and

$$\frac{I_1}{I_0} = \frac{T_1}{T_0} = \frac{\mu_1}{\mu_0} = \frac{2\gamma(\gamma-1)\, M_0^2}{(\gamma+1)^2}. \tag{5}$$

These shock boundary conditions suggest that it may be useful to investigate whether an approximate solution with

$$v_r = v(r)\cos\theta, \quad v_\theta = u(r)\sin\theta, \tag{6}$$

$$\rho = \rho(r), \quad p = p(r) + P(r)\sin^2\theta, \tag{7}$$

may exist. The more complicated form of p is particularly suited to a boundary-layer type of theory, which is well known to be sensitive to the effect of pressure gradient. The assumptions (6) and (7) correspond to those of Homann (1936) and Lighthill (1957).

The equations of motion in spherical polar co-ordinates are reduced to the axisymmetric boundary-layer form by dimensional considerations and are listed below. The continuity equation becomes

$$\frac{\partial}{\partial r}(\rho v_r)+\frac{1}{a\sin\theta}\frac{\partial}{\partial\theta}(\sin\theta\rho v_\theta)=0, \tag{8}$$

and the momentum equation for the θ-direction becomes

$$\rho\left(v_r\frac{\partial v_\theta}{\partial r}+\frac{v_\theta}{a}\frac{\partial v_\theta}{\partial\theta}\right)=-\frac{1}{a}\frac{\partial p}{\partial\theta}+\frac{\partial}{\partial r}\left(\mu\frac{\partial v_\theta}{\partial r}\right), \tag{9}$$

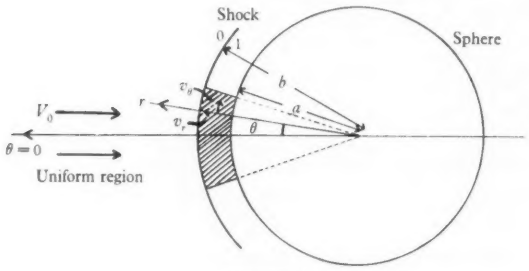

FIGURE 1

whilst the energy equation reduces to

$$\rho\left(v_r\frac{\partial I}{\partial r}+\frac{v_\theta}{a}\frac{\partial I}{\partial\theta}\right)-\frac{v_\theta}{a}\frac{\partial p}{\partial\theta}=\frac{1}{\sigma}\frac{\partial}{\partial r}\left(\mu\frac{\partial I}{\partial r}\right)+\mu\left(\frac{\partial v_\theta}{\partial r}\right)^2, \tag{10}$$

where

$$I=c_p T. \tag{11}$$

In accordance with the usual boundary-layer theory, the pressure gradient across the layer is neglected, so that, in (9), $\partial p/\partial\theta$ is found from its value immediately behind the shock, which is assumed to be within the boundary layer. Thus (4) gives

$$\frac{\partial p_1}{\partial\theta}=-\frac{4\gamma}{(\gamma+1)}M_0^2\sin\theta\cos\theta p_0;$$

and by replacing M_0^2 by V_0^2/c_0^2 and then c_0^2 by $\gamma p_0/\rho_0$, this becomes

$$\frac{\partial p_1}{\partial\theta}=-\frac{4(\gamma-1)}{(\gamma+1)^2}V_0^2\rho_1\sin\theta. \tag{12}$$

On substituting for $\partial p/\partial\theta=\partial p_1/\partial\theta$ in (9), we get

$$\rho\left(v_r\frac{\partial v_\theta}{\partial r}+\frac{v_\theta}{a}\frac{\partial v_\theta}{\partial\theta}\right)=\frac{4(\gamma-1)}{(\gamma+1)^2}\frac{V_0^2}{a}\rho_1\sin\theta+\frac{\partial}{\partial r}\left(\mu\frac{\partial v_\theta}{\partial r}\right). \tag{13}$$

To compare this work with that of Homann, expressed in the boundary-layer co-ordinates (x, y), we simply replace $a\theta$ and $a\sin\theta$ by x, and $r-a$ by y. On

substituting for the flow variables the forms (6) and (7), we are able to reduce the equations of motion to ordinary differential form. Equation (13) becomes

$$\left[\rho\left(v\frac{du}{dr}+\frac{u^2}{a}\right)-\frac{4(\gamma-1)\,V_0^2\rho_1}{(\gamma+1)^2 a}-\frac{d}{dr}\left(\mu\frac{du}{dr}\right)\right]\sin\theta=0; \tag{14}$$

and we shall also use (10) for $\theta = 0$, namely

$$\rho v\frac{dI}{dr}-\frac{1}{\sigma}\frac{d}{dr}\left(\mu\frac{dI}{dr}\right)=0, \tag{15}$$

where henceforth $I(r)$, $T(r)$, $\mu(r)$ will signify values for $\theta = 0$.

To satisfy the continuity equation, we now choose a Stokes stream function ψ, such that

$$a\sin\theta\rho v_r=-\rho_1\frac{\partial\psi}{\partial\theta} \quad \text{and} \quad \sin\theta\rho v_\theta=\rho_1\frac{\partial\psi}{\partial r}; \tag{16}$$

and on substituting (6), we see that ψ takes the form

$$\psi=\Psi(r)\sin^2\theta, \tag{17}$$

and (16) reduces to

$$v=-\frac{2}{a}\frac{\rho_1}{\rho}\Psi \quad \text{and} \quad u=\frac{\rho_1}{\rho}\frac{d\Psi}{dr}. \tag{18}$$

Transformation of the equations

The effect of compressibility is made less marked by choosing a Howarth variable

$$\eta=C\int_a^r\frac{\rho(\beta)}{\rho_1}d\beta, \tag{19}$$

C being a constant. We put also

$$\Psi(r)=Bf(\eta), \tag{20}$$

where B is another constant, and

$$g(\eta)=\frac{I(r)}{I_1}=\frac{T(r)}{T_1}=\frac{\rho_1}{\rho(r)}. \tag{21}$$

Equations (18) now become

$$v(r)=-\frac{2}{a}\frac{\rho}{\rho(\eta)}Bf(\eta), \quad u(r)=BCf'(\eta), \tag{22}$$

where the prime signifies differentiation with respect to η; and substituting (22) in equation (14), we get

$$-2\frac{B^2C^2}{a}ff''+\frac{B^2C^2}{a}f'^2-\frac{4(\gamma-1)}{(\gamma+1)^2}\frac{V_0^2}{a}g-\frac{d}{d\eta}\left(\frac{\mu\rho}{\mu_1\rho_1}f''\right)BC^3\nu_1=0.$$

Now, since $\mu\rho = \text{const.}$, if we choose

$$C=\left(\frac{V_0}{\nu_1 a}\right)^{\frac{1}{2}} \quad \text{and} \quad B=(V_0\nu_1 a)^{\frac{1}{2}}, \tag{23}$$

the above equation reduces to

$$f'''+2ff''-f'^2+\frac{4(\gamma-1)}{(\gamma+1)^2}g=0, \tag{24}$$

and the energy equation (18) becomes

$$g''+2\sigma fg'=0, \tag{25}$$

where the Prandtl number $\sigma = 0{\cdot}72$ for air.

The equations (24) and (25) represent a fifth-order system, but in addition the stand-off distance of the shock is unknown. We require therefore six boundary conditions to solve the equations. These are listed below.

First at the sphere $\eta = 0$, the no-slip conditions give

$$v_r = v_\theta = 0, \quad \text{or} \quad f(0) = f'(0) = 0; \tag{26}$$

and since insignificant heating is supposed to have occurred, $T(0) = T_0$; whence from (5)

$$g(0) = \frac{T_0}{T_1} = \frac{(\gamma+1)^2}{2\gamma(\gamma-1)M_0^2}. \tag{27}$$

The remaining three conditions are found at the shock, $\eta = \eta_1$ say. From the shock relations (2) and (3), and using (22), we have

$$v_1 = -\frac{V_0(\gamma-1)}{(\gamma+1)} = -\frac{2}{a}Bf(\eta_1),$$

where $B = (V_0 \nu_1 a)^{\frac{1}{2}}$: and substituting for ν_1 this becomes

$$B = \left(\frac{4V_0^2 a^2 \gamma(\gamma-1)^2 M_0^2}{(\gamma+1)^3 R_0^2}\right)^{\frac{1}{2}},$$

where

$$R_0 = \frac{2V_0 a \rho_0}{\mu_0} \quad \text{and} \quad M_0 = \frac{V_0}{c_0}$$

are the Reynolds number and Mach number. Hence we find

$$f(\eta_1) = \frac{1}{4}\left(\frac{R_0}{M_0^2}\frac{(\gamma+1)}{\gamma}\right)^{\frac{1}{2}}. \tag{28}$$

Also $$u_1 = V_0 = BCf'(\eta_1) = V_0 f'(\eta_1),$$

whence $$f'(\eta_1) = 1; \tag{29}$$

and $T(\eta_1) = T_1$, whence $$g(\eta_1) = 1. \tag{30}$$

Using a simplified coding technique for a machine such as the Mercury electronic computer, the equations can be integrated from the sphere along an outward normal. Five boundary conditions at the sphere are needed to do this, and so two additional conditions on $f''(0)$ and $g'(0)$ are prescribed, approximate values being guessed from a crude polynomial solution.

As the problem stands, the shock-wave position is determined when $f'(\eta)$ and $g(\eta)$ are simultaneously equal to 1. It would therefore be necessary to try many runs with varying values of $f''(0)$, $g'(0)$ and $g(0)$ before this could be accomplished.

Further transformations

To get over the above difficulty, we first put

$$G = \frac{4(\gamma-1)}{(\gamma+1)^2}g, \tag{31}$$

so that (24) and (25) become

$$f''' + 2ff'' - f'^2 + G = 0, \tag{32}$$

and $$G'' + 2\sigma f G' = 0, \tag{33}$$

whereas the boundary conditions on G are

$$G(0) = \frac{2}{\gamma M_0^2}, \tag{34}$$

$$G(\eta_1) = \frac{4(\gamma-1)}{(\gamma+1)^2}. \tag{35}$$

A shock-wave position is now determined when $f'(\eta_1) = 1$, and represents the solution for that value of γ which satisfies (35). Unfortunately, γ, M_0 and R_0 are now determined uniquely by the boundary conditions (28), (34) and (35), and thus only one shock-wave flow is found for each set of initial conditions. This transformation then offers little improvement in the solution. Our final transformations, however, enable us to determine several flows for each integration.

First we choose a new variable

$$\alpha = \lambda\eta, \tag{36}$$

where λ is a constant, and then by putting

$$f(\eta) = \lambda x(\alpha), \quad G(\eta) = \lambda^4 y(\alpha), \tag{37}$$

we are able to retain (32) and (33) in the same simple form:

$$x''' + 2xx'' - x'^2 + y = 0, \tag{38}$$

$$y'' + 2\sigma x y' = 0, \tag{39}$$

where the primes refer in this case to differentiation with respect to α.

The boundary conditions, however, now include an arbitrary constant λ, and γ, M_0 and R_0 are not fixed by the boundary conditions, but depend on the value λ takes.

We now have the conditions at $\alpha = 0$

$$x(0) = x'(0) = 0, \tag{40}$$

and

$$y(0) = \frac{2}{\gamma M_0^2 \lambda^4}. \tag{41}$$

At $\alpha = \alpha_1$, say, where $\alpha_1 = \lambda\eta_1$, we have

$$x(\alpha_1) = \left(\frac{R_0}{M_0^2}\frac{\gamma+1}{\gamma}\right)^{\frac{1}{2}} \Big/ 4\lambda, \tag{42}$$

$$x'(\alpha_1) = \frac{1}{\lambda^2}, \tag{43}$$

and

$$y(\alpha_1) = \frac{4(\gamma-1)}{(\gamma+1)^2\lambda^4}. \tag{44}$$

It should be noted that real solutions of (43) and (44) exist provided $x'(\alpha_1) > 0$ and $y(\alpha_1) \leqslant 0{\cdot}5$, and that the smaller of the two solutions of (44) for γ is chosen on physical grounds.

The two most important advantages gained by these transformations are: (1) The boundary conditions can now be solved uniquely for γ, M_0 and R_0 at each integral step (subject to the above conditions). (2) There is no loss in generality

if we fix $y(0)$ and thus reduce the initial conditions to be varied from three to two. A convenient value useful in the polynomial solution is seen to be 0·02.

Another advantage is the added usefulness of the crude polynomial series method for finding suitable values of $x''(0)$ and $y'(0)$, since no longer does this type of solution have to apply to specific values of γ, M_0 and R_0. In fact it is only necessary to guarantee that $x'(\alpha)$ and $y(\alpha)$ increase steadily with α to assure satisfactory solutions of (43) and (44) and thus of (41) and (42) also.

3. Presentation of the results

The tables

The results obtained from the Mercury electronic computer by integrating equations (38) and (39) for 60 evenly spaced values of $x''(0)$ and $y'(0)$ were printed in the form of the tables 1 to 4, and others which are included in the author's thesis (Herring 1958).

	1	2	3	4	5	6	7	8	9	10
		$\int_0^\alpha y(\beta)\,d\beta$	$x(\alpha)\,y(\alpha)$	$x'(\alpha)$	$x''(\alpha)/y(\alpha)$	$y(\alpha)$	$y'(\alpha)/y(\alpha)$			
	$\alpha = 0$	0·000	0·000	0·000	30·000	0·020	12·500			
	$\alpha = 0{\cdot}2$	0·009	0·001	0·119	8·445	0·070	3·568			
	$\alpha = 0{\cdot}6$	0·057	0·018	0·347	3·221	0·169	1·436			
	$\alpha = 1{\cdot}0$	0·143	0·075	0·550	1·776	0·262	0·831			
		0·264	0·184	0·717	1·093	0·340	0·505			
		0·412	0·340	0·849	0·730	0·397	0·290			
		0·579	0·527	0·953	0·545	0·433	0·147			
	$\frac{b-a}{a}$	0·756	0·728	1·041	0·464	0·451	0·063			
		0·937	0·938	1·122	0·435	0·458	0·021	γ	M_0	R_0
1	0·1158	1·121	1·156	1·201	0·427	0·460	0·006	1·497	9·82	4,86
*2	0·1020	1·305	1·386	1·280	0·425	0·460	0·001	1·407	10·79	7,70
3	0·0908	1·489	1·629	1·358	0·425	0·461	0·000	1·343	11·72	11,60
*4	0·0816	1·673	1·886	1·436	0·425	0·461	0·000	1·294	12·63	16,81
5	0·0738	1·858	2·158	1·514	0·425	0·461	0·000	1·255	13·52	23,59
6	0·0672	2·042	2·444	1·593	0·425	0·461	0·000	1·225	14·39	32,26
*7	0·0615	2·226	2·745	1·671	0·425	0·461	0·000	1·200	15·25	43,17

TABLE 1. The shock data used in figures 2 and 6 are indicated by *. Rows in this table only are printed at intervals of $\alpha = 0{\cdot}4$ except for the first step.

In each table the columns are numbered from 1 to 10. The columns 2–7 are functions of α, chosen to be directly proportional to the velocity and temperature variables, and columns 1, 8, 9 and 10 give the shock stand-off distances and the values of γ, M_0 and R_0. The rows are printed at intervals of $\alpha = 0{\cdot}2$ except in table 1 where intervals of $\alpha = 0{\cdot}4$ are used for brevity, and those numbered represent the positions of the shock waves. It must be remembered that each table gives a picture of the flow across several completely independent boundary layers. This is clear from the relationships connecting the columns, which are functions of α, with those expressed in terms of r. The constants connecting them, which are different for each shock, are inserted in square brackets, in the following expressions.

Column 1 gives the ratio of the stand-off distances of the shocks to the sphere radius, namely

$$\frac{b-a}{a} = \frac{\gamma+1}{8x(\alpha_1)\,x'(\alpha_1)} \int_0^{\alpha_1} y(\beta)\,d\beta, \tag{45}$$

1	2	3	4	5	6	7	8	9	10
	$\int_0^\alpha y(\beta)\,d\beta$	$x(\alpha)\,y(\alpha)$	$x'(\alpha)$	$x''(\alpha)/y(\alpha)$	$y(\alpha)$	$y'(\alpha)/y(\alpha)$			
	0·000	0·000	0·000	40·000	0·020	12·500			
	0·009	0·001	0·159	11·303	0·070	3·567			
	0·028	0·008	0·316	6·451	0·120	2·063			
	0·057	0·024	0·468	4·417	0·168	1·424			
	0·095	0·054	0·613	3·291	0·215	1·054			
	0·143	0·100	0·751	2·580	0·259	0·801			
$\frac{b-a}{a}$	0·198	0·164	0·880	2·099	0·298	0·609			
	0·261	0·244	1·001	1·766	0·331	0·455	γ	M_0	R_0
*1 0·0945	0·330	0·340	1·114	1·535	0·358	0·330	1·423	9·34	660
2 0·0821	0·404	0·448	1·221	1·377	0·378	0·230	1·351	10·50	1,160
*3 0·0725	0·481	0·565	1·323	1·275	0·393	0·152	1·296	11·62	1,900
4 0·0648	0·560	0·689	1·421	1·211	0·403	0·094	1·253	12·70	2,960
5 0·0584	0·641	0·819	1·518	1·175	0·408	0·054	1·218	13·76	4,410
*6 0·0529	0·723	0·955	1·614	1·155	0·412	0·029	1·190	14·79	6,340
7 0·0482	0·806	1·096	1·709	1·146	0·413	0·014	1·166	15·82	8,870

TABLE 2. The shock data used in figures 3 and 7 are indicated by *.

1	2	3	4	5	6	7	8	9	10
	$\int_0^\alpha y(\beta)\,d\beta$	$x(\alpha)\,y(\alpha)$	$x'(\alpha)$	$x''(\alpha)/y(\alpha)$	$y(\alpha)$	$y'(\alpha)/y(\alpha)$			
	0·000	0·000	0·000	60·000	0·200	32·500			
	0·017	0·004	0·239	7·891	0·150	4·326			
	0·060	0·027	0·472	4·091	0·279	2·289			
	0·128	0·086	0·693	2·660	0·404	1·513			
	0·221	0·194	0·900	1·900	0·522	1·078			
	0·336	0·358	1·089	1·433	0·628	0·783			
	0·470	0·578	1·260	1·127	0·717	0·563			
$\frac{b-a}{a}$	0·621	0·847	1·413	0·925	0·789	0·391			
	0·784	1·152	1·553	0·794	0·841	0·258	γ	M_0	R_0
1 0·1037	0·955	1·484	1·682	0·714	0·876	0·159	1·474	13·85	3,120
*2 0·0921	1·133	1·834	1·804	0·668	0·898	0·091	1·396	15·27	5,030
3 0·0826	1·314	2·198	1·922	0·644	0·910	0·047	1·336	16·63	7,680
*4 0·0747	1·496	2·576	2·039	0·633	0·916	0·022	1·289	17·96	11,270
5 0·0679	1·680	2·969	2·154	0·628	0·919	0·009	1·251	19·26	15,990
*6 0·0620	1·864	3·380	2·270	0·627	0·920	0·004	1·220	20·55	22,070

TABLE 3. The shock data used in figures 4 and 8 are indicated by *.

1	2	3	4	5	6	7	8	9	10
	$\int_0^\alpha y(\beta)\,d\beta$	$x(\alpha)\,y(\alpha)$	$x'(\alpha)$	$x''(\alpha)/y(\alpha)$	$y(\alpha)$	$y'(\alpha)/y(\alpha)$			
	0·000	0·000	0·000	70·000	0·020	32·500			
	0·017	0·004	0·279	9·226	0·150	4·324			
	0·060	0·031	0·552	4·812	0·279	2·284			
	0·128	0·100	0·813	3·164	0·403	1·501			
$\frac{b-a}{a}$	0·220	0·226	1·061	2·301	0·519	1·058			
	0·334	0·417	1·291	1·781	0·621	0·755	γ	M_0	R_0
1 0·1013	0·467	0·670	1·503	1·450	0·705	0·527	1·480	12·36	880
*2 0·0844	0·614	0·978	1·700	1·239	0·769	0·351	1·375	14·50	1,850
*3 0·0724	0·773	1·327	1·886	1·110	0·814	0·219	1·304	16·51	3,480
4 0·0632	0·938	1·705	2·063	1·036	0·842	0·125	1·251	18·45	6,010
*5 0·0558	1·108	2·105	2·235	0·997	0·857	0·065	1·209	20·32	9,750

TABLE 4. The shock data used in figures 5 and 9 are indicated by *.

whereas column 2 gives

$$\int_0^{\alpha} y(\beta)\,d\beta.$$

This can be converted to $(r-a)/a$ upon multiplying by $[(\gamma+1)/8x(\alpha_1)\,x'(\alpha_1)]$, but this is more quickly found from (45) as $\left[(b/a-1)\Big/\int_0^{\alpha_1} y(\beta)\,d\beta\right]$ by dividing the corresponding values in columns 1 and 2. Note that the suffix 1 denotes the values immediately behind the shock and these are given in numbered rows.

The next five columns, 3–7, are connected to the velocities and temperature as follows. Column 3 gives $x(\alpha)\,y(\alpha)$, where the ratio of the radial component of the velocity behind the shock to that ahead is $-v(r)\cos\theta/V_0\cos\theta$, where

$$\frac{v(r)}{V_0} = \left[-\left(\frac{\gamma-1}{\gamma+1}\right)\Big/ x(\alpha_1)\,y(\alpha_1)\right] x(\alpha)\,y(\alpha). \tag{46}$$

The transverse component is quickly found from column 4, which gives $x'(\alpha)$, since

$$\frac{u(r)}{V_0} = \left[\frac{1}{x'(\alpha_1)}\right] x'(\alpha). \tag{47}$$

To obtain $[du(r)/dr]/V_0/a$, column 5 must be multiplied by $[8x(\alpha_1)/(\gamma+1)]$. The temperature ratio is

$$\frac{T(r)}{T_0} = \frac{y(\alpha)}{y(0)} = [50]\,y(\alpha), \tag{48}$$

where $y(\alpha)$ is given in column 6, and finally column 7 gives $y'(\alpha)/y(\alpha)$, where the constant needed to give $[dT(r)/dr]/[T_0/a]$ is

$$\left[\frac{8}{\gamma+1}\,\frac{x(\alpha_1)\,x'(\alpha_1)}{y(0)}\right] = \left[\frac{400}{\gamma+1}\,x(\alpha_1)\,x'(\alpha_1)\right]. \tag{49}$$

Certain information can be found by direct reading of the tables. For instance, the edges of the velocity and temperature boundary layers are approached when columns 5, 6 and 7, which are related to du/dr, T and dT/dr, tend to a constant value. This is very clearly seen in, for example, table 1 (see also figure 2), and in this, as in a few other cases, the shocks are well outside the boundary-layer section. The assumption of a constant pressure throughout the region behind the shock (12) will be less accurate in these cases.

In the table mentioned above the thickness of the velocity and temperature boundary layers are seen to be of the same order, and this is due to the nearness of the Prandtl number (0·72) to unity.

The graphs

Three temperature and two transverse velocity profiles have been drawn for tables 1–4. Figures 2–5 give the temperature and figures 6–9 the velocity profiles for each of these tables, taken in order. The magnitude of the temperatures reached depends directly on the shock relations and a comparison of figures 2 and 4 gives some idea of the range considered.

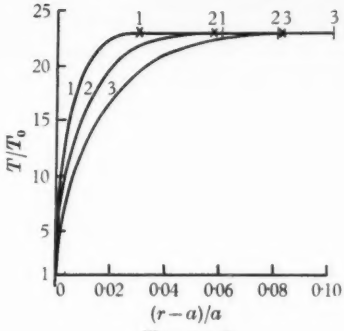

FIGURE 2

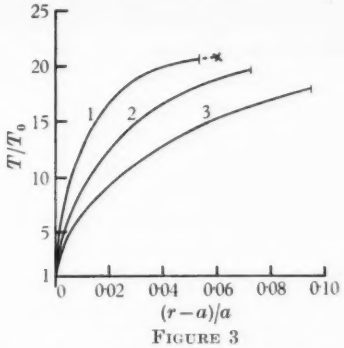

FIGURE 3

FIGURE 2. Temperature profiles plotted from data given in table 1. N.B. In figures 2–9 a shock wave is denoted by a stroke | and approximate boundary-layer edges by a cross × ; the number above is the curve number. Curve 1: $\gamma = 1{\cdot}200$, $M_0 = 15{\cdot}25$, $R_0 = 43{,}170$. Curve 2: $\gamma = 1{\cdot}294$, $M_0 = 12{\cdot}63$, $R_0 = 16{,}810$. Curve 3: $\gamma = 1{\cdot}407$, $M_0 = 10{\cdot}79$, $R_0 = 7700$.

FIGURE 3. Temperature profiles plotted from data given in table 2. In curves 1 of figures 3–5 the shock-wave positions and the boundary-layer edges suggested by the profiles have been marked. In actual fact of course, the boundary layer will end at the shock wave, since ahead of it the temperature assumes the constant value T_0, and so outside the shock the curve is shown as a dotted line. Curve 1: $\gamma = 1{\cdot}190$, $M_0 = 14{\cdot}79$, $R_0 = 6340$. Curve 2: $\gamma = 1{\cdot}296$, $M_0 = 11{\cdot}62$, $R_0 = 1900$. Curve 3: $\gamma = 1{\cdot}423$, $M_0 = 9{\cdot}34$, $R_0 = 660$.

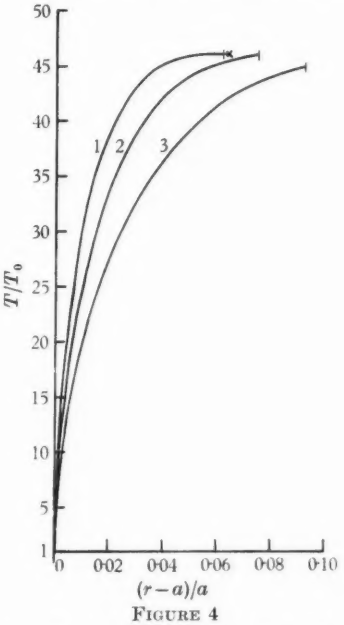

FIGURE 4

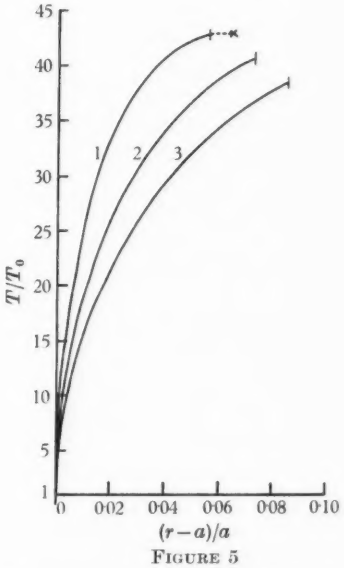

FIGURE 5

FIGURE 4. Temperature profiles plotted from data given in table 3. Curve 1: $\gamma = 1{\cdot}220$, $M_0 = 20{\cdot}55$, $R_0 = 22{,}070$. Curve 2: $\gamma = 1{\cdot}289$, $M_0 = 17{\cdot}96$, $R_0 = 11{,}270$. Curve 3: $\gamma = 1{\cdot}396$, $M_0 = 15{\cdot}27$, $R_0 = 5030$.

FIGURE 5. Temperature profiles plotted from data given in table 4. Curve 1: $\gamma = 1{\cdot}209$, $M_0 = 20{\cdot}32$, $R_0 = 9750$. Curve 2: $\gamma = 1{\cdot}304$, $M_0 = 16{\cdot}51$, $R_0 = 3480$. Curve 3: $\gamma = 1{\cdot}375$, $M_0 = 14{\cdot}50$, $R_0 = 1850$.

Naturally in this problem we are most interested in, for example, the shock stand-off distance, or the boundary-layer thickness as a function of the Reynolds number R_0 or Mach number M_0. To find the variation with R_0, we must maintain γ and M_0 at constant values.

A comparison of curves 1 in figures 2 and 3 and also curves 1 in figures 4 and 5, where in each pair γ and M_0 are approximately constant, gives an indication of this behaviour. The approximate boundary-layer edges have been marked on these graphs with a cross and in these examples as R_0 increases the gradients get larger and thus the boundary-layer thickness decreases. However, at the same time it is surprising that the shock stand-off distance (marked with a dash) increases with R_0. This last result is borne out in a more detailed investigation later.

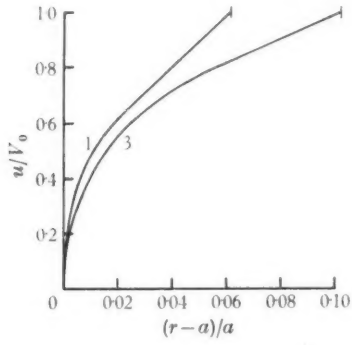

FIGURE 6

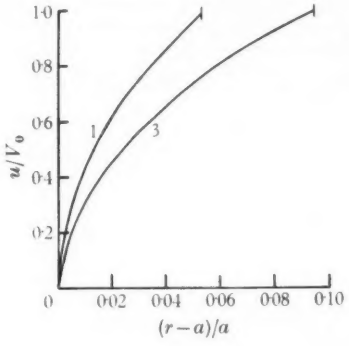

FIGURE 7

FIGURE 6. Transverse velocity profile plotted from data given in table 1. Curve 1: $\gamma = 1{\cdot}200$, $M_0 = 15{\cdot}25$, $R_0 = 43{,}170$. Curve 3: $\gamma = 1{\cdot}407$, $M_0 = 10{\cdot}79$, $R_0 = 7700$.

FIGURE 7. Transverse velocity profile plotted from data given in table 2. Curve 1: $\gamma = 1{\cdot}190$, $M_0 = 14{\cdot}79$, $R_0 = 6340$. Curve 2: $\gamma = 1{\cdot}423$, $M_0 = 9{\cdot}34$, $R_0 = 660$.

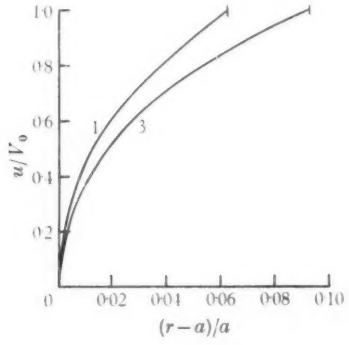

FIGURE 8

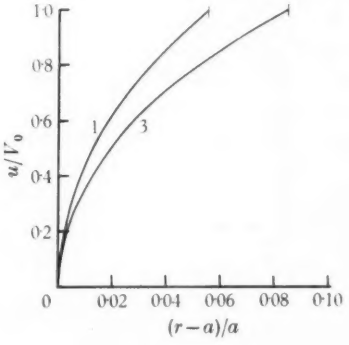

FIGURE 9

FIGURE 8. Transverse velocity profile plotted from data given in table 3. Curve 1: $\gamma = 1{\cdot}220$, $M_0 = 20{\cdot}55$, $R_0 = 22{,}070$. Curve 3: $\gamma = 1{\cdot}396$, $M_0 = 15{\cdot}27$, $R_0 = 5030$.

FIGURE 9. Transverse velocity profile plotted from data given in table 4. Curve 1: $\gamma = 1{\cdot}209$, $M_0 = 20{\cdot}32$, $R_0 = 9750$. Curve 3: $\gamma = 1{\cdot}375$, $M_0 = 14{\cdot}50$, $R_0 = 1850$.

In figures 6–9 showing the transverse velocity profiles, the edge of the boundary layer is defined by a region of approximately constant shear flow. In other words, in a region where viscosity has little effect the vorticity shed by a shock wave of constant curvature is constant. The outer parts of these graphs agree quite well with the exact inviscid incompressible solutions obtained by Lighthill (1957) for a gas with varying specific heats. The effect of viscosity in reducing the velocity quickly to zero is very marked.

The remaining graphs, figures 10–16, show the variation of certain quantities at constant values of γ and M_0, and provide a very interesting insight into their behaviour in a hypersonic flow.

Interpolation on a large scale is an unfortunate necessity in this method, where γ, M_0 and R_0 are not predetermined, and to maintain γ and M_0 constant, a three-point linear scheme between two tables was used.

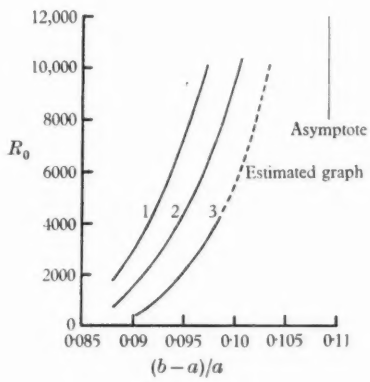

FIGURE 10

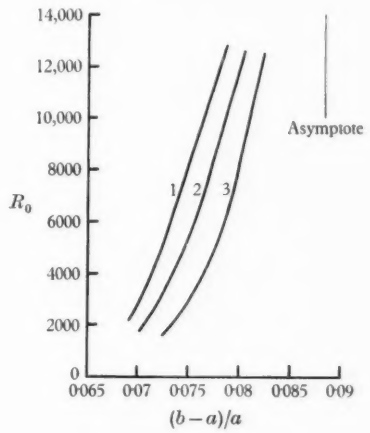

FIGURE 11

FIGURE 10. The Reynolds number as a function of the ratio stand-off distance of the shock to sphere radius, when $\gamma = 1{\cdot}4$. Curve 1: $M_0 = 15$. Curve 2: $M_0 = 12$. Curve 3: $M_0 = 9$.
FIGURE 11. The Reynolds number as a function of the ratio stand-off distance of shock to sphere radius, when $\gamma = 1{\cdot}3$. Curve 1: $M_0 = 18$. Curve 2: $M_0 = 15$. Curve 3: $M_0 = 12$.

Figures 10–12 show the variation of R_0 with the ratio of stand-off distance to sphere radius for a number of constant values of γ and M_0. The interesting result, hinted at previously, that the shock stand-off distance increases with Reynolds number, is here verified, and the asymptotes to the graph (which are independent of Mach number) are drawn for each value of γ. Can this mean that we have negative displacement thicknesses? A comparison of figure 2 with 3, and figure 4 with 5 gives an indication that the boundary-layer thickness decreases with increase in Reynolds number and an examination of the product ρu in these cases shows that it decreases from a maximum at the shock to a minimum at the sphere. In other words, the displacement thickness given by $\int_a^b (u_1\rho_1 - u(r)\rho(r))\,dr$ is positive. The shock distance, however, is not governed by the boundary-layer

thickness, for in table 1 the shocks are outside, and in tables 2–4 they are inside the boundary layer, and thus it is probable that this idea of displacement thickness is erroneous for the region behind the shock. If the shock position depended more upon distribution of mass than of mass flow, i.e. depended more upon ρ and ρu, then a 'mass defect' given by $\int_a^b (\rho_1 - \rho(r))\,dr$ would certainly be negative, and the shock distance would increase with increase in the Reynolds number.

A rough interpolation within figures 10–12 to maintain constant γ, and between them to maintain constant M_0, shows that the shock distance decreases with increase in Mach number and with decrease in γ, respectively. A simple analysis of the boundary conditions on the density at the shock and the sphere, and the knowledge that the density decreases continuously outwards from the sphere

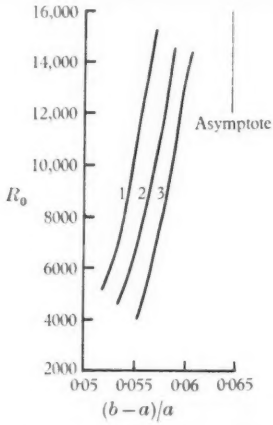

FIGURE 12. The Reynolds number as a function of the ratio stand-off of shock to sphere radius, when $\gamma = 1{\cdot}2$. Curve 1: $M_0 = 18$. Curve 2: $M_0 = 15$. Curve 3: $M_0 = 12$.

provides a simple explanation of these results. The strong shock condition on the density (2) is independent of Mach number, whilst the density at the sphere, which, since $T(0) = T_0$, is dependent only upon the pressure given by (4), increases with Mach number. The region therefore is further compressed and the shock wave moves closer to the body as the Mach number increases. A similar consideration of (2) and (4) shows that as γ increases, the density just behind the shock decreases, whilst at the sphere it remains effectively constant. The shock in this case, therefore, moves away from the sphere as γ increases.

A note here about the error caused by assuming the strong shock conditions on the density will be of value. The oblique shock relation for the density is

$$\frac{\rho_1}{\rho_0} = \left(\frac{\gamma+1}{\gamma-1}\right) \frac{1}{(1+2/(\gamma-1)\,M_0^2)}, \tag{50}$$

where terms $O(\theta^2)$ have been neglected. The strong shock relations are only valid if $\frac{1}{2}M_0^2(\gamma-1) \gg 1$ which means, for example when $\gamma = 1{\cdot}4$, that M_0^2 must be much greater than 5 for these relations to be used. The lowest Mach number considered

at $\gamma = 1{\cdot}4$ is 9, and substituting in (50) gives $\rho_1/\rho_0 \doteqdot 0{\cdot}94(\gamma+1)/(\gamma-1)$. It is clear from this that the strong shock conditions tend to overestimate the density, and so the correction to the graphs involves a small shift to the right to give a compensating increase in the shock stand-off distance. This correction will of course decrease as the Mach number increases.

Figures 13 and 14, where the ratio of $(r-a)$ at $T = 0{\cdot}98T_1$ to $(r-a)$ at $T = T_1$, i.e. $(b-a)$, is plotted against $\log_{10} R_0$, give an indication of the variation of the boundary-layer thickness with Reynolds number. The decrease in the ratio with increase in R_0 shows clearly that the temperature gradients are increasing, and this supports the idea that the boundary-layer width is decreasing with increase

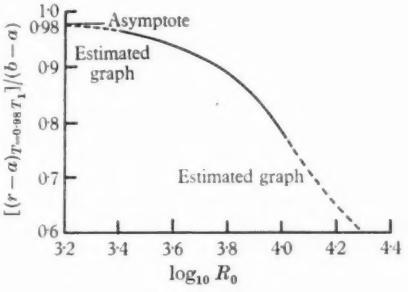

FIGURE 13

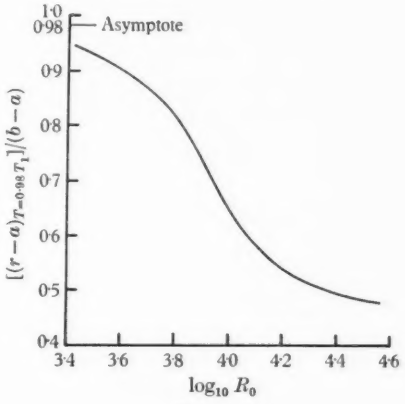

FIGURE 14

FIGURE 13. Boundary-layer thickness as a function of shock stand-off distance, as indicated by the ratio $[(r-a)_{T=0{\cdot}98T_1}]/(b-a)$, for $\gamma = 1{\cdot}3$ and $M_0 = 18$.

FIGURE 14. Boundary-layer thickness as a function of the shock stand-off distance as indicated by the ratio $[(r-a)_{T=0{\cdot}98T_1}]/(b-a)$, for $\gamma = 1{\cdot}2$ and $M_0 = 15$.

in R_0. At low Reynolds number, where the profile approximates to a straight line, the ratio approaches 0·98, and it decreases through a point of inflexion before tending to a further constant value for large values of R_0.

Finally figures 15 and 16 show the variation of skin friction with the Reynolds number, where the skin-friction coefficient is defined as

$$c_f = \frac{\mu_0[du(r)/dr]_{r=a}}{\frac{1}{2}\rho_0 V_0^2} = \frac{400x''(0)}{[\gamma(\gamma+1)]^{\frac{1}{2}} M_0},$$

and it is noticeable that, with γ and M_0 held constant, c_f is solely dependent upon the initial value of $x''(\alpha)$. Once more the influence of the shock wave on the flow can be clearly seen, for, instead of $c_f R_0^{\frac{1}{2}}$ having a constant value as suggested by boundary-layer theory, it is seen to decrease with increase in R_0. In fact, when R_0 is of order 10^3, c_f behaves more like R_0^{-1}. However, the graphs seem to indicate that $c_f R_0^{\frac{1}{2}}$ does approach a constant value at higher Reynolds numbers, and this is not surprising since the tabulated results indicate that when R_0 is of order 10^4 the

shock waves lie well outside the boundary layer, and thus one would expect the normal boundary approximations to apply.

The approximate solutions which have been found for the problem have only been explained in part, but further clarification should be possible as more becomes known about flows at very high speeds.

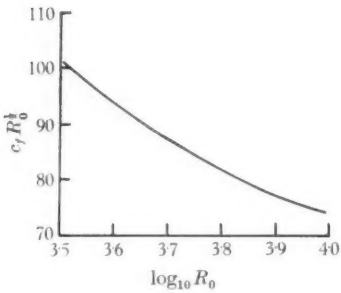

FIGURE 15

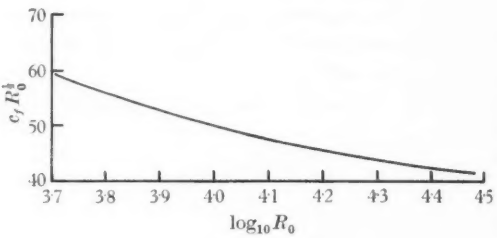

FIGURE 16

FIGURE 15. The skin-friction coefficient as a function of the Reynolds number, for $\gamma = 1{\cdot}3$ and $M_0 = 18$.

FIGURE 16. The skin-friction coefficient as a function of the Reynolds number, for $\gamma = 1{\cdot}2$ and $M_0 = 15$.

I would like to thank Prof. M. J. Lighthill and Mr C. R. Illingworth for their help and encouragement at all times, and also Mr R. Kerr for his advice on programming for the Mercury computer.

REFERENCES

BROWN, W. B. & DONOUGHE, P. L. 1951 *Nat. Adv. Comm. Aero. Tech., Wash., Note* 2479.
CHESTER, W. 1956 *J. Fluid Mech.* **1**, 353, 490.
FREEMAN, N. C. 1956 *J. Fluid Mech.* **1**, 366.
HERRING, T. K. 1958 M.Sc. Thesis, Manchester University.
HOMANN, F. 1936 *Z. Angew. Math. Mech.* **16**, 153.
LIGHTHILL, M. J. 1957 *J. Fluid Mech.* **2**, 1.
OLIVER, R. E. 1956 *J. Aero. Sci.* **23**, 177.
WHIPPLE, F. L. 1943 *Rev. Mod. Phys.* **15**, 246.

A presentation of cnoidal wave theory for practical application

By R. L. WIEGEL
Department of Engineering, University of California, Berkeley

(Received 2 May 1959)

Cnoidal wave theory is appropriate to periodic waves progressing in water whose depth is less than about one-tenth the wavelength. The leading results of existing theories are modified and given in a more practical form, and the graphs necessary to their use by engineers are presented. As well as results for the wave celerity and shape, expressions and graphs for the water particle velocity and local acceleration fields are given. A few comparisons between theory and laboratory measurements are included.

1. Introduction

Mathematical arguments show that the theory of surface waves, commonly known as Stokes's waves, is most useful (i.e. valid without unreasonable restriction as to the wave amplitude) when the depth to wavelength ratio d/L is greater than about 1/8 or 1/10 (Keulegan 1950; De 1955). For shallower water the theory for a wave type known as cnoidal appears to be more satisfactory. The formula for the wave profile involves the Jacobian elliptic function cn u; hence the term 'cnoidal', analogous to 'sinusoidal'. Keulegan has pointed out that the validity of this theory rests on the assumption that the square of the inclination of the water surface is small in comparison with unity. (On the other hand, for Stokes's waves to be valid in shallow water, the wave amplitude is required to be excessively small, thus making the theory unrealistic.) The theory of cnoidal waves has not been developed in the literature to the state where it can be used extensively by engineers; and the object of the present paper is to fill this need.

Korteweg & de Vries (1895) initiated the theory of cnoidal waves. They showed that it accounts for a general class of long waves of permanent type and finite amplitude; one limiting case of the theory gives the solitary wave, while another limiting case gives sinusoidal waves as accounted for by linearized wave theory. Keulegan & Patterson (1940) have studied the cnoidal wave on somewhat different lines. Again, Keller (1948) treated the problem using the general nonlinear shallow-water theory and obtained formulae which are similar to those of Korteweg & de Vries. Littman (1957) has proved the existence of permanent periodic waves of the type in question. The approximate region of validity of the existence proof of cnoidal waves by Littman is shown in figure 1. Benjamin & Lighthill (1954) have advanced the theory considerably with regard to the formation of bores and hydraulic jumps, and Iwasa (1955) has also considered it.

A comparison between the various alternative developments of the theory will not be attempted here; rather, we select those results which appear to be most useful and proceed from them to derive data for practical application.

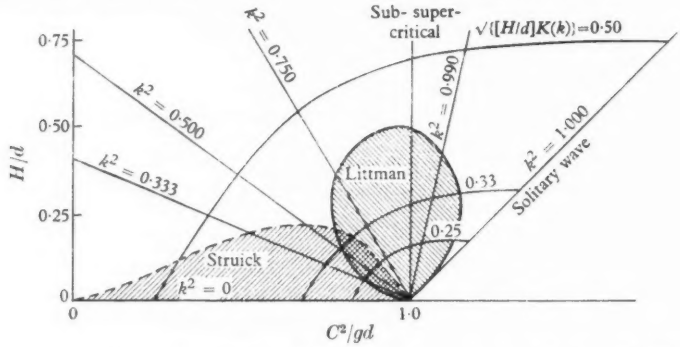

FIGURE 1. Approximate regions of validity of existence proofs by Struik for Stokes's waves and by Littman for cnoidal waves (after Littman 1957).

2. Presentation of the theory

Kortweg & de Vries, Keulegan & Patterson, and Keller use different symbols; however, the critical formulae obtained by them are essentially the same. The wavelength is given by

$$\frac{L}{d} = \frac{4}{\sqrt{3}} K(k) \left(2\bar{L} + 1 - \frac{y_t}{d}\right)^{-\frac{1}{2}}, \tag{1}$$

where d is the still water depth, $K(k)$ is the complete elliptic integral of the first kind with modulus k (it should be noted that $K(k)$ is sometimes denoted by $F_1(k)$). y_t is the vertical distance from the ocean bottom to the wave trough and $\bar{L}$ and k are defined by the following two equations:

$$k^2 = \frac{(y_c/d) - (y_t/d)}{2\bar{L} + 1 - (y_t/d)}, \tag{2}$$

$$\left(2\bar{L} + 1 - \frac{y_t}{d}\right) E(k) = \left(2\bar{L} + 2 - \frac{y_c}{d} - \frac{y_t}{d}\right) K(k), \tag{3}$$

where y_c is the distance from the ocean bottom to the wave crest and $E(k)$ is the complete elliptic integral of the second kind with modulus k. The following inequalities must also hold:

$$2\bar{L} + 1 > \frac{y_c}{d} > \frac{y_t}{d} \quad \text{and} \quad 0 < k^2 \leqslant 1. \tag{4}$$

In using tables of elliptic integrals and functions, the reader is warned that they are often tabulated as functions of the parameter m, where $m = k^2$. Equation (2) can be written

$$\left(2\bar{L} + 1 - \frac{y_t}{d}\right) = \frac{(y_c/d) - (y_t/d)}{k^2} = \frac{H/d}{k^2}. \tag{5}$$

Substituting this into equation (1) and squaring gives

$$\frac{L^2 H}{d^3} = \tfrac{16}{3}[kK(k)]^2. \tag{6}$$

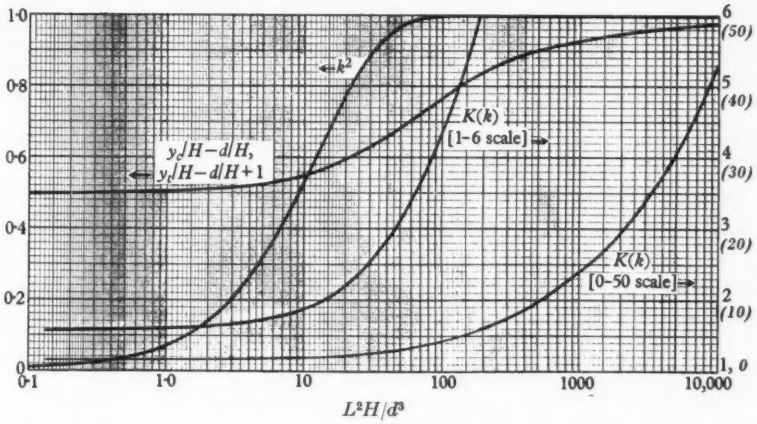

FIGURE 2. Curves obtained from equations (6), (10) and (11*b*), showing relationships between L^2H/d^3 and k^2, $K(k)$, and $y_c/H-d/H = y_t/H-d/H+1$.

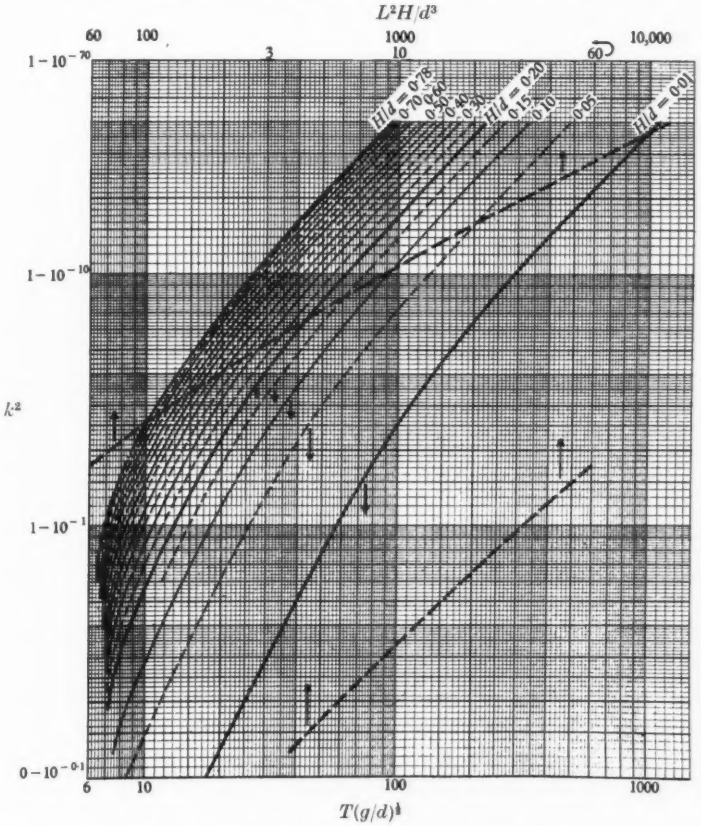

FIGURE 3. Curves showing relationships k^2 *vs* L^2H/d^3, and k^2 *vs* $T(g/d)^{\frac{1}{2}}$ and H/d.

Both Keller (1948) and Littman (1957) also obtain this relationship as their basic approximate solution. L^2H/d^3 is plotted as a function of k^2 in figures 2 and 3. If the wavelength, wave height and water depth are known, then the many formulae of the cnoidal wave theory can be used as they are expressed in terms of various functions of the square of the modulus k. The terminology of the elliptic functions and integrals as used herein are as used by Milne-Thompson (1950).

The wavelength is

$$L = \left(\frac{16d^3}{3H}\right)^{\frac{1}{2}} kK(k). \tag{7}$$

Equation 3 can be rearranged to give

$$E(k) - K(k) = \frac{(1-[y_c/d])}{(2\bar{L}+1-[y_t/d])} K(k). \tag{8}$$

Substituting (1) into the above equation gives

$$\frac{y_c}{d} = \frac{16d^2}{3L^2}\{K(k)[K(k)-E(k)]\}+1; \tag{9}$$

or, multiplying by d/H, we get

$$\frac{y_c}{H} - \frac{d}{H} = \frac{16d^3}{3L^2H}\{K(k)[K(k)-E(k)]\}. \tag{10}$$

Next, y_t can be obtained from the relationship

$$\frac{y_t}{d} = \frac{y_c}{d} - \frac{H}{d} = \frac{16d^2}{3L^2}\{K(k)[K(k)-E(k)]\}+1-\frac{H}{d}, \tag{11a}$$

or

$$\frac{y_t}{H} - \frac{d}{H} + 1 = \frac{16d^3}{3L^2H}\{K(k)[K(k)-E(k)]\}. \tag{11b}$$

These equations have been plotted in figures 2 and 3. The relationships among k^2, $K(k)$ and $E(k)$ have been tabulated over the range $k^2 = 1\text{–}10^{-6}$ by Kaplan (1946, 1948) and partially by Hayashi (1930, 1933) and Airey (1935). In order to extend these functions to the range needed for the study of waves ($k^2 = 1\text{–}10^{-40}$) the following equations were used (Jahnke & Emde 1945):

$$K(k) = \Lambda + \tfrac{1}{4}(\Lambda - 1)\,k'^2 + \tfrac{3}{16}(\Lambda - \tfrac{7}{16})\,k'^4 + \tfrac{25}{256}(\Lambda - \tfrac{37}{30})\,k'^6 + \ldots, \tag{12a}$$

$$E(k) = 1 + \tfrac{1}{2}(\Lambda - \tfrac{1}{2})\,k'^2 + \tfrac{3}{16}(\Lambda - \tfrac{13}{12})\,k'^4 + \tfrac{15}{128}(\Lambda - \tfrac{6}{5})\,k'^6 + \ldots, \tag{12b}$$

where $k' = \sqrt{(1-k^2)}$ and Λ is the natural logarithm of $4/k'$.

The wave profile is

$$y_s = y_t + H\,\mathrm{cn}^2\left[2K(k)\left(\frac{x}{L} - \frac{t}{T}\right), k\right], \tag{13}$$

where cn is the Jacobian elliptic function associated with cosine. The function cn is singly periodic provided k is real number and $0 \leqslant k < 1$. The period becomes infinite when $k = 1$ (in which case we have the solitary wave). While the period of the cn function is $4K(k)$, the period of the cn^2 function is $2K(k)$. The expression $\mathrm{cn}^2[2K(k)(x/L - t/T), k]$ is plotted in figures 4 and 5 as a function of x/L, t/T, with k^2 as parameter. Values of the cn function are available over a limited range

of k^2 (Milne-Thompson 1950; Spenceley & Spenceley 1947; Schuler & Gabelein 1955). Values for $0{\cdot}95 < k^2 < 1$ were calculated to three decimal places using the following series (Milne-Thompson 1950):

$$\mathrm{cn}\,(\bar{u} \mid k^2) = \mathrm{sech}\,\bar{u} - \tfrac{1}{4}k'^2 \tanh\bar{u}\,\mathrm{sech}\,\bar{u}(\sinh\bar{u}\cosh\bar{u} - \bar{u}), \tag{14}$$

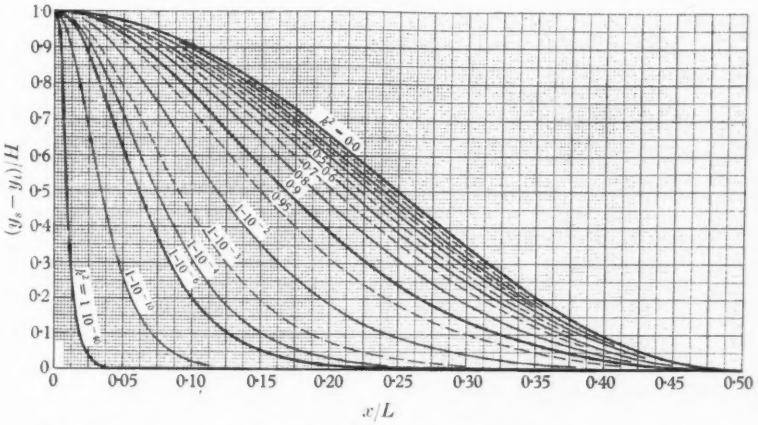

FIGURE 4. Surface profiles of cnoidal waves, obtained from equation (13).

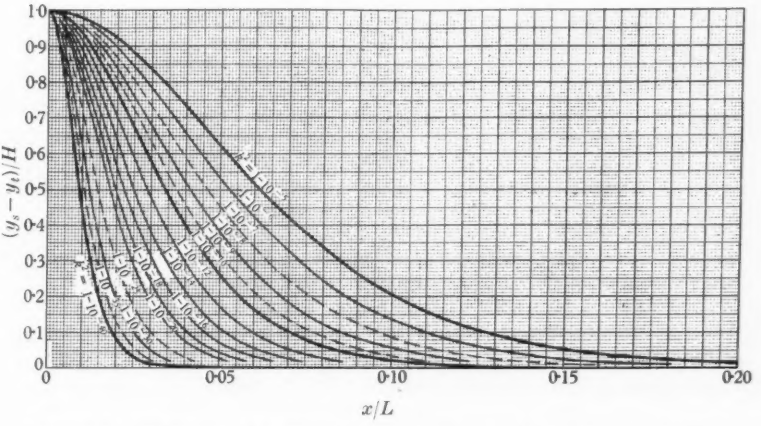

FIGURE 5. Surface profiles of cnoidal waves, obtained from equation (13).

where $\bar{u}$ is the incomplete elliptic integral of the first kind. x/L is the same as $\bar{u}/2K(k)$ for the cn^2 function. $\bar{u}$ has been used rather than the more commonly accepted symbol u to avoid confusion with the horizontal component of water-particle velocity. In figure 6 the theoretical surface profile is compared with some measurements made by Taylor (1955). It can be seen that the cnoidal theory predicts the wave profile very well.

It is interesting to note that when the modulus k is zero,

$$\mathrm{cn}\,(\bar{u} \mid k) = \mathrm{cn}\,(\bar{u} \mid 0) = \cos\bar{u} \quad \text{and} \quad K(k) = \tfrac{1}{2}\pi;$$

hence $4K(k) = 2\pi$, and the wave profile is given by the trignometric functions. When $k = 1$, $\mathrm{cn}(\bar{u} \mid 1) = \mathrm{sech}\,\bar{u}$ and we have the hyperbolic function with $K(k) = \infty$; hence the period becomes infinite and we then have the solitary wave. It can be seen that when k is reduced from 1 to 0·9999 the period $4K$ is reduced from infinity to about 7π, whereas the further reduction of k to 0 reduces $4K$ to only 2π.

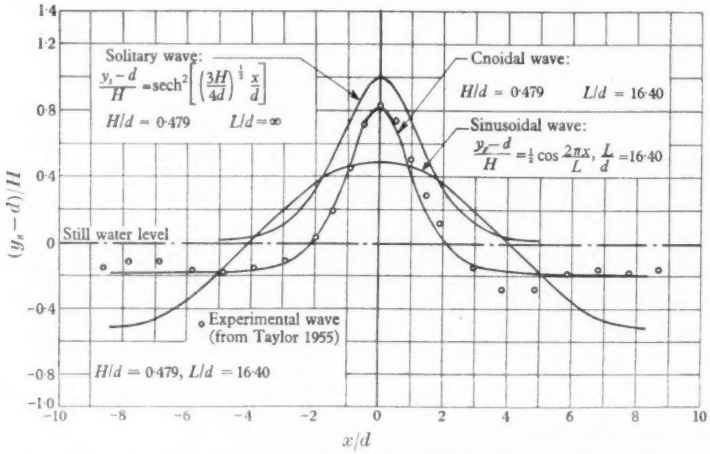

FIGURE 6. Comparison between measured and theoretical wave profiles.

The wave velocity (using Stokes's second definition of wave velocity, which is the velocity of the propagation of the wave-form when the horizontal momentum of the liquid has been reduced to zero by the addition of a uniform motion) is

$$C = (gd)^{\frac{1}{2}}\left[1 + \frac{H}{d}\frac{1}{k^2}\left(\frac{1}{2} - \frac{E(k)}{K(k)}\right)\right], \tag{15a}$$

or, as $\dfrac{16d^3}{3L^2H}K^2(k) = \dfrac{1}{k^2}$,

$$C = (gd)^{\frac{1}{2}}\left[1 + \frac{16d^2}{3L^2}K^2(k)\left(\frac{1}{2} - \frac{E(k)}{K(k)}\right)\right]. \tag{15b}$$

Equation (15a) has been plotted in figure 7.

For one limiting case (the solitary wave), k^2 approaches unity, (k) is unity and $K(k)$ is infinity; hence

$$C = (gd)^{\frac{1}{2}}\left(1 + \frac{H}{2d}\right). \tag{15c}$$

This approximation to

$$C = \left\{gd\left(1 + \frac{H}{d}\right)\right\}^{\frac{1}{2}} \tag{15d}$$

is higher by a maximum of only 2 % even for the case of the solitary wave of maximum steepness ($H/d = 0{\cdot}78$).

For the other limiting case (the linear theory, where $k^2 \to 0$), $E(k)/K(k) \to$ unity and

$$C = (gd)^{\frac{1}{2}}\left(1 - \frac{2\pi^2 d^2}{3L^2}\right), \tag{15e}$$

which is an approximation to

$$C = \left\{gd\left(1 - \frac{4\pi^2 d^2}{3L^2}\right)\right\}^{\frac{1}{2}}. \tag{15f}$$

Now, the linear theory gives (Lamb 1945, p. 366)

$$C = \left\{\frac{gL}{2\pi}\tanh\frac{2\pi d}{L}\right\}^{\frac{1}{2}}. \tag{15g}$$

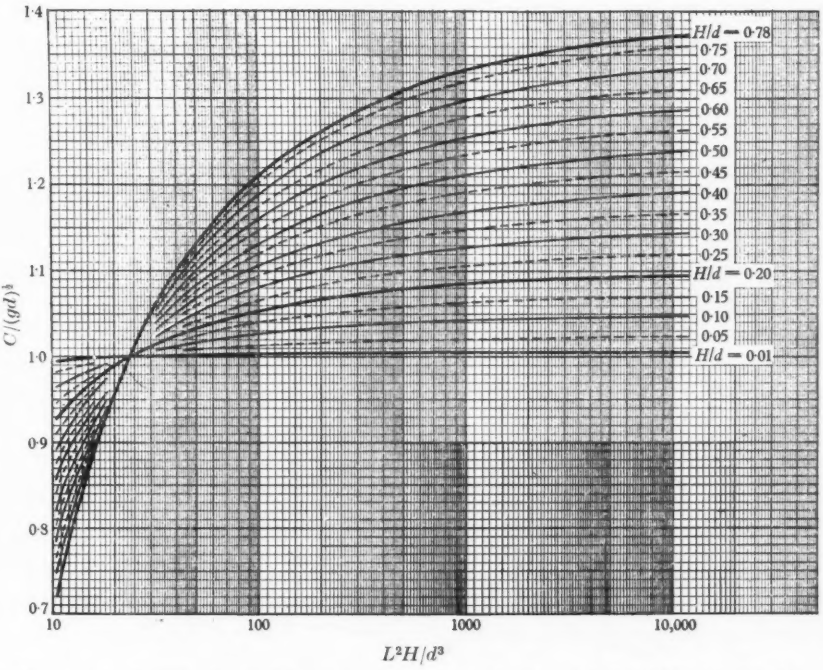

FIGURE 7. Curves obtained from equation (15*a*), showing relationship between the cnoidal wave velocity (Korteweg & de Vries) and L^2H/d^3.

But the first two terms in the expansion of $\tanh(2\pi d/L)$ are

$$\frac{2\pi d}{L} - \frac{8\pi^2 d^3}{3L^3}.$$

So

$$C \doteq \left\{gd\left(1 - \frac{4\pi^2 d^2}{3L^2}\right)\right\}^{\frac{1}{2}}. \tag{15h}$$

which is in agreement with equation (15*f*).

The equation for wave celerity as given by Keulegan & Patterson (1940), and Littman (1957), which is the velocity of the wave crest with respect to fixed co-ordinates, can be written

$$C^2 = gd\left\{1 + \frac{H}{d}\left[-1 + \frac{1}{k^2}\left(2 - 3\frac{E(k)}{K(k)}\right)\right]\right\}. \tag{16}$$

This equation has been plotted in figure 8 as a function of L^2H/d^3, and in figure 9 as a function of $T(g/d)^{\frac{1}{2}}$.

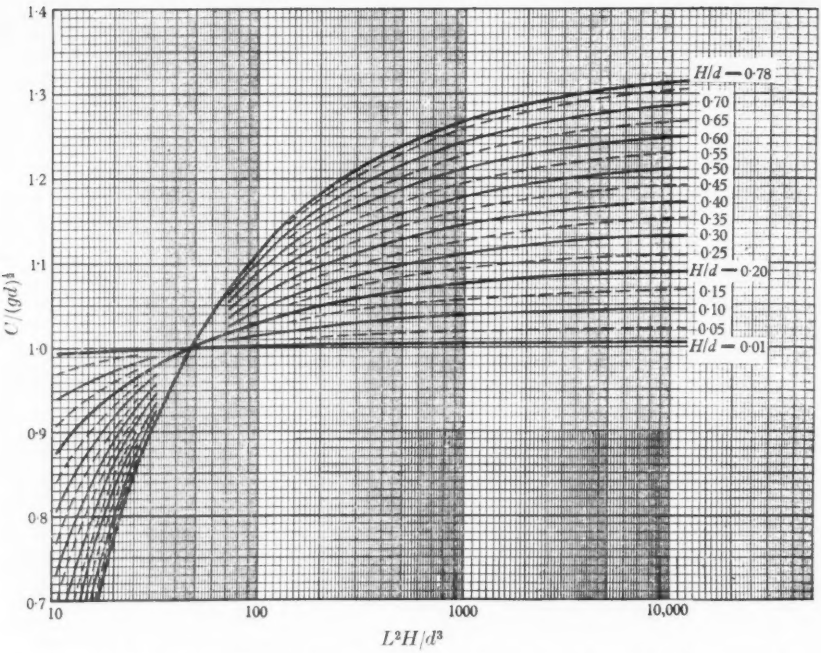

FIGURE 8. Curves obtained from equation (16), showing relationship between the cnoidal wave velocity (Keulegan & Patterson) and L^2H/d^3.

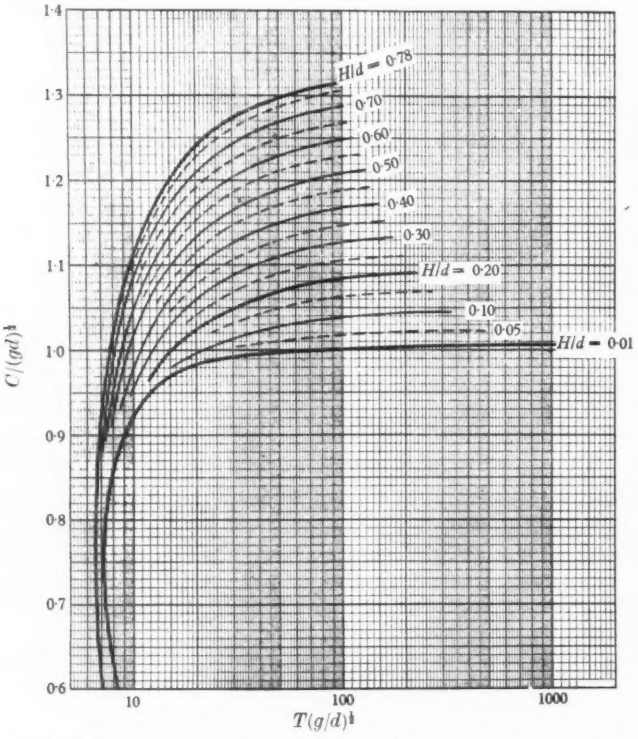

FIGURE 9. Cnoidal wave velocity (Keulegan & Patterson) as a function of $T(g/d)^{\frac{1}{2}}$.

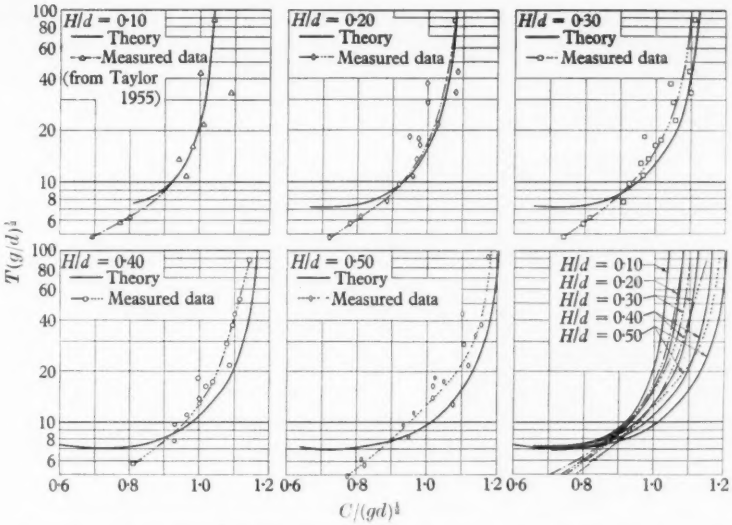

FIGURE 10. Comparisons between theoretical and measured wave velocities.

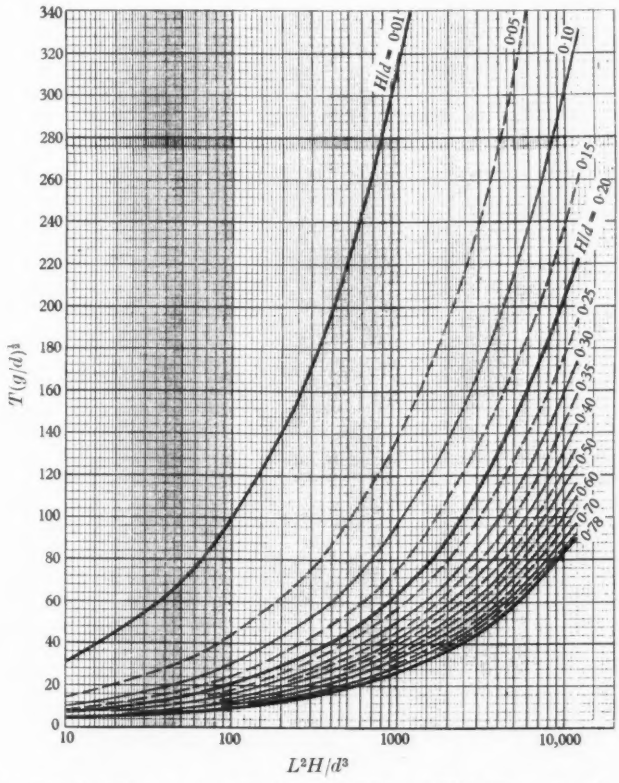

FIGURE 11. Relationships among $T(g/d)^{\frac{1}{2}}$, L^2H/d^3 and H/d (Korteweg & de Vries).

In figure 10 are shown comparisons between the wave velocity as obtained from equation (16) and some measurements of waves in the laboratory.

As cnoidal waves are periodic and of permanent form,

$$L = CT, \quad T = L/C;$$

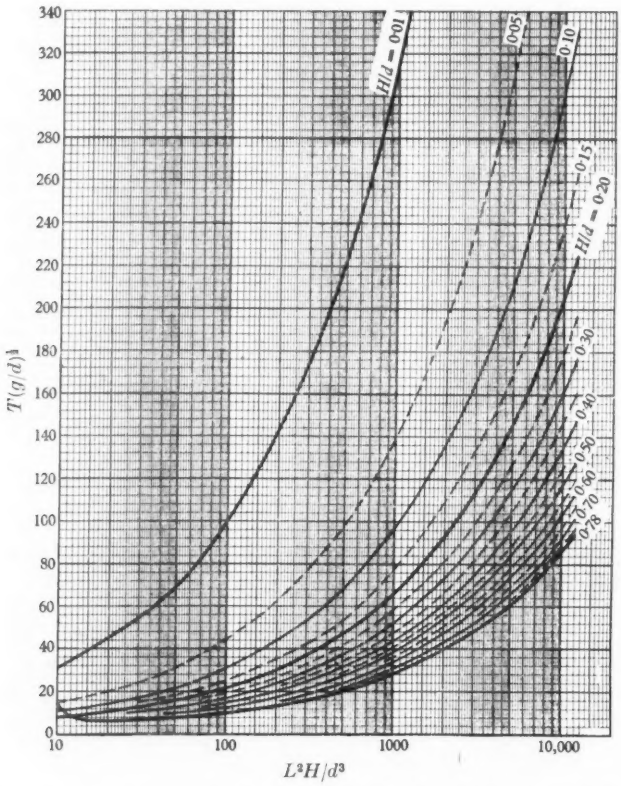

FIGURE 12. Relationships among $T(g/d)^{\frac{1}{2}}$, L^2H/d^3 and H/d (Keulegan & Patterson).

and the wave period is given by

$$T\left(\frac{g}{d}\right)^{\frac{1}{2}} = \left(\frac{16d}{3H}\right)^{\frac{1}{2}} \left[\frac{kK(k)}{1+\dfrac{H}{dk^2}\left(\dfrac{1}{2}-\dfrac{E(k)}{K(k)}\right)}\right], \tag{17}$$

using the velocity as given in equation (15*a*).

From this equation k^2 can be determined as a function of $T(g/d)^{\frac{1}{2}}$ and H/d, and from this L^2H/d^3 can be determined. This has been done and plotted in figure 11.

Using the velocity as given in equation (16) results in

$$T\left(\frac{g}{d}\right)^{\frac{1}{2}} = \left(\frac{16d}{3H}\right)^{\frac{1}{2}} \frac{kK(k)}{\left\{1+\dfrac{H}{d}\left[-1+\dfrac{1}{k}\left(2-\dfrac{3E(k)}{K(k)}\right)\right]\right\}^{\frac{1}{2}}}, \tag{18}$$

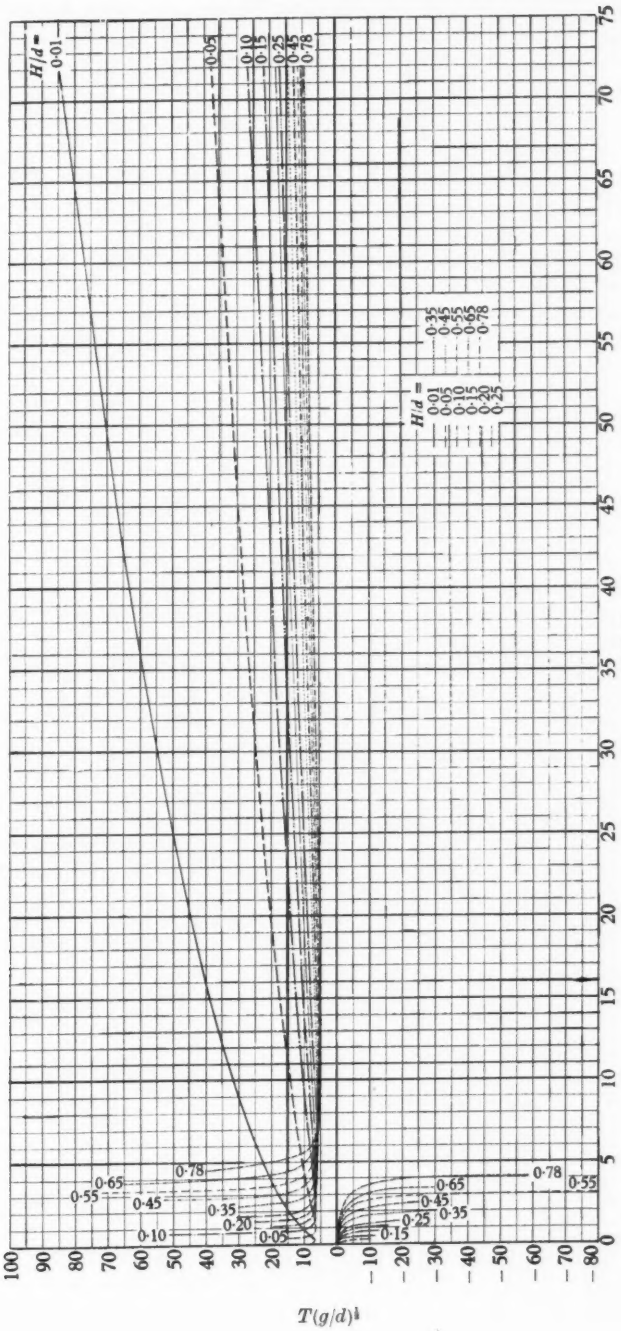

FIGURE 13. Relationships among wave height, wave period, wavelength and water depth for cnoidal waves.

which has been plotted in figure 3 as a function of k^2 and H/d, and in figures 12 and 13 as a function of L^2H/d^3 and H/d. The results in figure 13 show that a wave of a given period and height, and for a given water depth, can have two possible lengths. The physical significance of this is not apparent.

The pressure at any distance y above the bottom has been shown by Keller (1948) to be, to the second approximation,

$$p = \rho g(y_s - y), \tag{19}$$

where ρ is density and y_s is given by (13). It is rather surprising that this simple hydrostatic expression applies.

The horizontal and vertical components of water-particle velocities at any point x, y within the fluid can be obtained from the following equations given by Keulegan & Patterson (1940):

$$\frac{u}{(gd)^{\frac{1}{2}}} = \left[\frac{h}{d} - \frac{h^2}{4d^2} + \left(\frac{d}{3} - \frac{y^2}{2d}\right)\frac{\partial^2 h}{\partial x^2}\right],$$

$$\frac{v}{(gd)^{\frac{1}{2}}} = -y\left[\left(\frac{1}{d} - \frac{h}{2d^2}\right)\frac{\partial h}{\partial x} + \frac{1}{3}\left(d - \frac{y^2}{2d}\right)\frac{\partial^3 h}{\partial x^3}\right],$$

$$h = y_s - d = -d + y_t + H\,\mathrm{cn}^2\left[2K(k)\left(\frac{x}{L} - \frac{t}{T}\right), k\right].$$

These equations become

$$\frac{u}{(gd)^{\frac{1}{2}}} = \left[-\frac{5}{4} + \frac{3y_t}{2d} - \frac{y_t^2}{4d^2} + \left(\frac{3H}{2d} - \frac{y_t H}{2d^2}\right)\mathrm{cn}^2(\,) - \frac{H^2}{4d^2}\mathrm{cn}^4(\,)\right.$$
$$\left. - \frac{8HK^2(k)}{L^2}\left(\frac{d}{3} - \frac{y^2}{2d}\right)(-k^2\,\mathrm{sn}^2(\,)\,\mathrm{cn}^2(\,) + \mathrm{cn}^2(\,)\,\mathrm{dn}^2(\,) - \mathrm{sn}^2(\,)\,\mathrm{dn}^2(\,))\right], \tag{20}$$

$$\frac{v}{(gd)^{\frac{1}{2}}} = y\,.\,\frac{2HK(k)}{Ld}\left[1 + \frac{y_t}{d} + \frac{H}{d}\mathrm{cn}^2(\,) + \frac{32K^2(k)}{3L^2}\left(d^2 - \frac{y^2}{2}\right)(k^2\,\mathrm{sn}^2(\,)\right.$$
$$\left. - k^2\,\mathrm{cn}^2(\,) - \mathrm{dn}^2(\,))\right]\mathrm{sn}(\,)\,\mathrm{cn}(\,)\,\mathrm{dn}(\,), \tag{21}$$

where sn( ) refers to sn$[2K(k)(x/L - t/T), k]$, etc. The local accelerations are

$$\frac{\partial u}{\partial t} = (gd)^{\frac{1}{2}}\frac{4HK(k)}{Td}\left[\left(\frac{3}{2} - \frac{y_t}{2d}\right) - \frac{H}{2d}\mathrm{cn}^2(\,) + \frac{16K^2(k)}{L^2}\left(\frac{d^2}{3} - y^2\right)\right.$$
$$\left. \times (k^2\,\mathrm{sn}^2(\,) - k^2\,\mathrm{cn}^2(\,) - \mathrm{dn}^2(\,))\right]\mathrm{sn}(\,)\,\mathrm{cn}(\,)\,\mathrm{dn}(\,), \tag{22}$$

$$\frac{\partial v}{\partial t} = y(gd)^{\frac{1}{2}}\frac{4HK^2(k)}{LTd}\left\{\left[1 + \frac{y_t}{d}\right][\mathrm{sn}^2(\,)\,\mathrm{dn}^2(\,) - \mathrm{cn}^2(\,)\,\mathrm{dn}^2(\,) + k^2\,\mathrm{sn}^2(\,)\,\mathrm{cn}^2(\,)]\right.$$
$$+ \frac{H}{d}[3\,\mathrm{sn}^2(\,)\,\mathrm{dn}^2(\,) - \mathrm{cn}^2(\,)\,\mathrm{dn}^2(\,) + k^2\,\mathrm{sn}^2(\,)]\,\mathrm{cn}^2(\,) - \frac{32K^2(k)}{3L^2}\left[d^2 - \frac{y^2}{2}\right]$$
$$\times [9k^2\,\mathrm{sn}^2(\,)\,\mathrm{cn}^2(\,)\,\mathrm{dn}^2(\,) - k^2\,\mathrm{sn}^4(\,)(k^2\,\mathrm{cn}^2(\,) + \mathrm{dn}^2(\,))$$
$$\left. + k^2\,\mathrm{cn}^4(\,)(k^2\,\mathrm{sn}^2(\,) + \mathrm{dn}^2(\,)) + \mathrm{dn}^4(\mathrm{sn}^2(\,) - \mathrm{cn}^2(\,))]\right\}. \tag{23}$$

In order to use the equations for water-particle velocities the necessary numbers can be obtained from figures 2, 3, 4 and 5, as

$$\bar{u} \mid k \equiv 2K(k)\,x/L, \tag{24}$$

$$\mathrm{sn}^2(\bar{u} \mid k) \equiv 1 - \mathrm{cn}^2(\bar{u} \mid k), \tag{25}$$

$$\mathrm{dn}^2(\bar{u} \mid k) \equiv 1 - k^2[1 - \mathrm{cn}^2(\bar{u} \mid k)]. \tag{26}$$

A few comparisons of theory with laboratory measurements are shown in figure 14. In considering the vertical velocity it should be noted that the curve

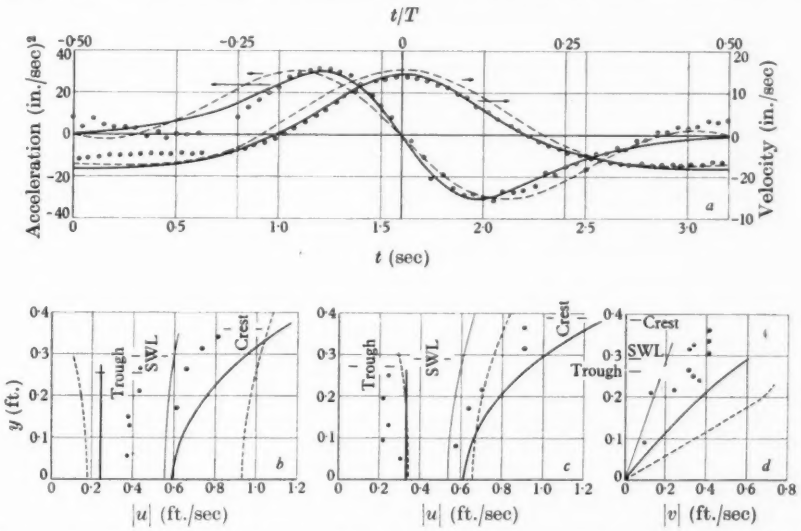

FIGURE 14. Comparisons of horizontal components of water-particle velocity and acceleration with cnoidal wave theory. *a*: ○, Experimental points (Elliott 1953); - - - - -, Stokes's second-order theory; ——, Cnoidal theory. *b* to *d*: ●,○, Experimental points (Morison & Crooke 1953); ——, Linear theory; - - - - -, Stokes's second-order theory; ——, Cnoidal theory. In *b* and *c*, points ●, ○ give $|u|$ under wave troughs and crests respectively; in *d*, points ●, ○ give $|v|$ under SWL leading wave crests and following wave crests respectively.

	H (ft.)	T (sec.)	d (ft.)	L (ft.)
a	0·483	3·20	2·0	24·7
b	0·105	1·62	0·292	5·10
c	0·120	1·27	0·292	3·71
d	0·137	2·09	0·292	6·58

plotted for the cnoidal theory is for the phase of maximum vertical velocity and this occurs prior to the time the wave profile goes through the still water level.

The work presented in this paper was done under Grant G-4630 from the National Science Foundation. The author wishes to express his appreciation to Mrs M. M. Turner for her help in the computations and preparation of the illustrations.

REFERENCES

AIREY, J. R. 1935 Toroidal functions and the complete elliptic integrals. *Phil. Mag.* 7th Series, **19**, 177–88.

BENJAMIN, T. B. & LIGHTHILL, M. J. 1954 On cnoidal waves and bores. *Proc. Roy. Soc.* A, **224**, 448–60.

DE, S. C. 1955 Contributions to the theory of Stokes's waves. *Proc. Camb. Phil. Soc.* **51**, 713–36.

ELLIOTT, J. G. 1953 Interim report, Contract NOy–12561, Hydrodynamics Laboratory, Calif. Inst. of Tech.

HAYASHI, K. 1930 *Tafeln der besselschen, theta-, Kugel, und anderer funktionen.* Berlin: Springer.

HAYASHI, K. 1933 *Tafeln für die differenzenrechnung sowie für die hyperbel-besselschen, elliptischen, und anderer funktionen.* Berlin: Springer.

IWASA, Y. 1955 Analytical considerations on cnoidal and solitary waves. *Memoirs of Faculty of Engineering, Kyoto Univ. (Japan)*, **17**, no. 4.

JAHNKE, E. & EMDE, F. 1945 *Tables of Functions with Formulae and Curves*, 4th ed. New York: Dover.

KAPLAN, E. L. 1946 Auxiliary table of complete elliptic integrals. *J. Math. Phys.* **25**, 26–36.

KAPLAN, E. L. 1948 Auxiliary table for the incomplete elliptic integrals. *J. Math. Phys.* **27**, 11–36.

KELLER, J. B. 1948 The solitary wave and periodic waves in shallow water. *Commun. appl. Math.* **1**, 323–39.

KEULEGAN, G. H. 1950 Wave motion. *Engineering Hydraulics. Proc. Fourth Hydraulics Conf.*, ch. 11, pp. 711–68. Ed. by Hunter Rouse. New York: Wiley.

KEULEGAN, G. H. & PATTERSON, G. W. 1940 Mathematical theory of irrotational translation waves. *J. Res. Nat. Bur. Stand., U.S. Dep. Commerce*, **24**, 47–101.

KORTEWEG, D. J. & DE VRIES, G. 1895 On the change of form of long waves advancing in a rectangular canal, and on a new type of long stationary waves. *Phil. Mag.* 5th Series, **39**, 422–43.

LAMB, H. 1945 *Hydrodynamics*, 6th ed. New York: Dover.

LITTMAN, W. 1957 On the existence of periodic waves near critical speed. *Commun. Pure appl. Math.* **10**, 241–69.

MILNE-THOMPSON, L. M. 1950 *Jacobian Elliptic Function Tables.* New York: Dover.

MORISON, J. R. & CROOKE, R. C. 1953 The mechanics of deep water, shallow water, and breaking waves. *Tech. Mem. U.S. Army, Corps of Engineers, Beach Erosion Board*, no. 40.

SCHULER, M. & GABELEIN, H. 1955 *Eight and Nine Place Tables of Elliptical Functions.* Berlin: Springer.

SPENCELEY, G. W. & SPENCELEY, R. M. 1947 *Smithsonian Elliptic Functions Tables.* Washington, D.C.: Smithsonian Institution.

TAYLOR, D. C. 1955 An experimental study of the transition between oscillatory and solitary waves, M.S. Thesis, Mass. Inst. of Tech.

Optimum power generation from a moving plasma

By JOSEPH L. NEURINGER

Plasma Propulsion Laboratory, Republic Aviation Corporation, Farmingdale, Long Island, New York

(Received 27 April 1959)

The possibility exists of directly using the plasma, resulting from a controlled fusion reaction, to generate electricity by electromagnetic induction. Two special cases of a more general problem are considered here: (1) the extraction of optimum power from the steady one-dimensional flow of an incompressible inviscid plasma across a uniform transverse magnetic field in an externally loaded channel of arbitrarily varying cross-section, and (2) the extraction of optimum power from the steady one-dimensional flow of a compressible inviscid plasma across a uniform transverse magnetic field in a channel of uniform cross-section. In each case, the magnitude of the required external loading at optimum power operation is determined as a function of the parameters which characterize the hydromagnetic interaction. Also determined are the magnitudes of the terminal voltage, power, fluid mechanical to electrical conversion efficiency, and the variation of the fluid dynamical variables along the channel at optimum power.

1. Introduction

With controlled thermonuclear fusion a possibility for the future (Post 1956), the question may be raised as to the best, most efficient way of utilizing the energy liberated for electric power generation. The conventional steam-turbine method of generating electricity, which involves moving parts of heavy cumbersome machinery, may not in this case be the most practical and efficient way of electric generation. A possible method of electric generation which does not involve moving parts is generation by electromagnetic induction using the highly conducting plasma of the reaction products as the working fluid. The inductive action may be described as follows. A plasma moving perpendicular to a magnetic field, both flow and field being horizontal, has induced in it a vertical electric field. If the flow is in a channel with top and bottom walls conductors, and these walls are connected by an external load, then current will flow through the plasma and external load. Further, it is contemplated that by utilizing some of the mechanical energy of the exhausted ionized gases in a plasma pinch engine (Kunen 1958), electric power may be generated to be used either as a prime or auxiliary power unit for the engine system.

The dynamical state of the plasma, characterized by the state variables u_0, p_0, ρ_0 and T_0 exiting from a thermonuclear reactor or exhaust of a pinch engine will probably be fixed by the operating power level of the reactor. Also, the channel entrance width and length may be fixed by space and other limitations. We then pose the following question. For a channel of given entrance cross-section and

length, what must be the shape of the channel, distribution of applied magnetic-field strength and magnitude of applied external loading so that maximum power may be extracted by the external load? The derivation of the conditions for maximum power transfer from conventional generators is developed in elementary texts, but for a plasma generator of the type considered here the situation is much more difficult to analyse because of the complex hydromagnetic interaction between a variable magnetic field and a compressible electrically conducting fluid continuum.

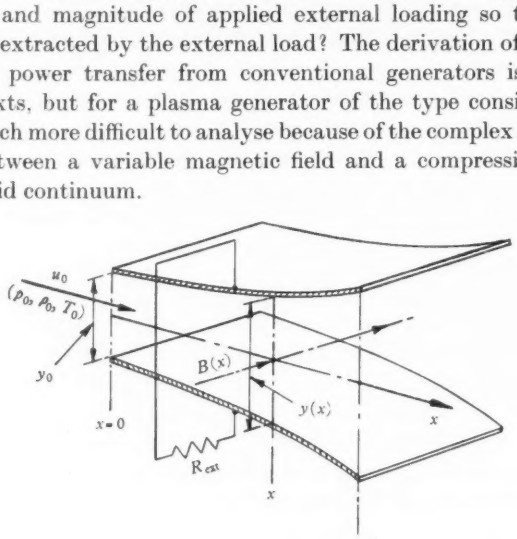

FIGURE 1. Diagram of plasma generator.

To simplify the analysis, consider the two-dimensional channel shown in figure 1. The channel is of unit breadth out of the paper. The plasma moves in the positive x-direction as shown, entering the channel of fixed opening y_0 with fixed values u_0, p_0, ρ_0 and T_0 of the state variables. A magnetic field, normal to the paper and directed into it, is assumed to be an unknown function of x only. The following simplifying assumptions are made:

(a) The flow is one-dimensional, i.e. the fluid dynamical state variables vary in the x-direction but not over the cross-section.

(b) The magnetic Reynolds number (see § 5) is small; that is, any effects on the fluid flow of secondary magnetic fields resulting from the induced current distribution are negligible, because either the secondary magnetic fields are too small or are in the wrong direction to produce appreciable effects.

(c) The induced currents in the x-direction are small compared to those induced in the y-direction, and are neglected.

(d) The plasma behaves like a perfect gas.

(e) The intrinsic properties σ and γ of the plasma are taken to be constant.

(f) The fluid is assumed inviscid and non-heat conducting, so that the only dissipation is electrical.

(g) The plasma is assumed to be electrically neutral so that no space-charge sheaths are developed near the conducting walls.

(h) The motion of the plasma through the channel is smooth, i.e. shock free.

(i) The channel walls are perfectly conducting.

The extremum problem, as outlined above, was formulated in Neuringer (1958), using the techniques of the calculus of variations to obtain the appropriate system

of differential equations and boundary conditions. These equations are each of first order and highly non-linear, and they require machine calculation for their solution. In the special cases where the differential constraints, i.e. the fluid flow equations, are integrable, analytical solutions may be obtained, however, without resorting to the mathematical apparatus of the calculus of variations. The two special cases considered in this paper are:

(1) The flow of an incompressible, inviscid plasma across a uniform transverse magnetic field in a channel of fixed length in which the variation in cross-section along its length is arbitrarily prescribed.

(2) The flow of a compressible, inviscid plasma across a uniform transverse field in a channel of fixed length and uniform cross-section.

In each of these special cases, we shall determine the magnitude of the required external resistance, at optimum power generation, as a function of the parameters which characterize the hydromagnetic interaction. Also, we shall determine the resulting terminal voltage, power, fluid mechanical to electrical conversion efficiency, and distribution of the fluid dynamical state variables along the channel at optimum power.

2. Notation

The rational M.K.S. system is used throughout.

u = velocity
p = pressure
T = temperature
ρ = density
E = electric intensity
B = magnetic induction
H = magnetic intensity
J = current density
I = total current
r = resistance per unit length
R = total resistance
σ = plasma conductivity
μ_e = magnetic permeability
x = distance along channel
y = channel width
l = channel length
γ = ratio of specific heat
P = electric power
k = voltage appearing at the terminals of the generator
η = efficiency
m = constant mass flow rate through channel
c_a = speed of Alfvén waves
P = dimensionless pressure
U = dimensionless velocity
X = dimensionless distance along channel
k' = dimensionless terminal voltage
M_0 = Mach number of flow at channel entrance
$a = l/y_0$
δ = magnetohydrodynamic interaction parameter
α = parameter (function of γ and M_0)
β = parameter (function of γ and M_0)
0 = subscript representing entrance values

3. The circuit and magnetohydrodynamic equations

Let $r(x)$ represent the external unit resistance at station x along the channel. It may be defined as that element of the parallel resolution of the total external resistance which would carry the full current density associated with that station. Let $J(x)$ represent the induced current in the y direction per unit length of channel at station x. The external voltage drop is then $J(x)\,r(x)$. The voltage drop due to the

internal resistance of the plasma is $J(x)\,y(x)/\sigma$. Kirchoff's law then gives for the closed circuit at station x:

$$Ey = Jr + \frac{Jy}{\sigma}, \tag{1}$$

where

$$E = uB. \tag{2}$$

Assumptions i and c imply

$$Jr = k, \tag{3}$$

where k, the voltage drop across the external load, is a constant to be determined.

Using (2) and (3) in (1), we obtain

$$J = \frac{\sigma}{y}\{uBy - k\}. \tag{4}$$

The power generated in the external circuit per unit length is

$$\frac{\hat{P}}{\text{length}} = rJ^2 = kJ = k\sigma\left\{uB - \frac{k}{y}\right\},$$

and the total power generated is

$$P = k\sigma\int_0^l \left(uB - \frac{k}{y}\right)dx. \tag{5}$$

The problem then is to find the velocity distribution $u(x)$ and the constant k which when inserted into (5) maximizes P.

The one-dimensional compressible fluid flow equations, modified to account for the hydromagnetic interaction, are (Resler & Sears 1958):

Continuity equation

$$\rho uy = \rho_0 u_0 y_0 = m, \tag{6}$$

where m represents the constant mass flow rate through the channel.

Momentum equation

$$\rho u\frac{du}{dx} + \frac{dp}{dx} = -JB = -\left(\sigma uB^2 - \frac{\sigma kB}{y}\right), \tag{7}$$

where JB (with proper sign) represents the Lorentz force per unit volume exerted by the magnetic field on the fluid. The last term is obtained using (4) for J.

Energy equation

$$\frac{d}{dx}\left\{\left[\frac{p}{\gamma - 1} + \tfrac{1}{2}\rho u^2\right]uy\right\} + \frac{d}{dx}\{puy\} + uJBy - \frac{J^2}{\sigma}y = 0, \tag{8'}$$

where the first term on the left-hand side represents the net flux of internal plus kinetic energy through the faces of a volume element, the second term represents the rate of mechanical work done by the pressure forces, the third term represents the rate of doing work by the Lorentz force, and the last term represents the Joulean dissipation. (8′) can be written, by means of (4), as

$$\frac{d}{dx}\left\{\left[\frac{\gamma}{\gamma - 1}\frac{p}{\rho} + \tfrac{1}{2}u^2\right]\rho uy\right\} + k\sigma\left\{uB - \frac{k}{y}\right\} = 0. \tag{8}$$

An interesting observation may be made using the energy equation in the form (8). Substituting for the integrand in (5) using (8) and performing the integration, we obtain, using (6),

$$\hat{P} = \left\langle \left[\frac{\gamma}{\gamma - 1} \frac{p}{\rho} + \tfrac{1}{2} u^2 \right] m \right\rangle_0 - \left\langle \left[\frac{\gamma}{\gamma - 1} \frac{p}{\rho} + \tfrac{1}{2} u^2 \right] m \right\rangle_l. \tag{9}$$

That is, the power delivered to the external circuit is equal to the difference in the total, or stagnation, enthalpy flux at the entrance and exit of the channel.

4. Case 1: incompressible inviscid plasma flowing across a uniform transverse magnetic field in a channel of arbitrarily prescribed cross-section

Let $y(x)$ represent the arbitrarily prescribed variation of channel cross-section with length. The fluid density is uniform along the channel, so that the fluid velocity, from (6), is given by $u(x) = m/\rho_0 y$. Substituting for the velocity in the expression for the power (5), we obtain

$$\hat{P} = \left(\frac{k\sigma B m}{\rho_0} - k^2 \sigma \right) \int_0^l \frac{dx}{y(x)}. \tag{10}$$

For maximum power, we require $d\hat{P}/dk = 0$. Carrying out the differentation, we obtain

$$k = \frac{Bm}{2\rho_0} = \frac{u_0 y_0 B}{2}. \tag{11}$$

Two interesting observations may be made using (11).

(1) The value of the external or terminal voltage drop at maximum power is independent of the channel shape.

(2) Using (11) in conjunction with the condition that the induced e.m.f. at each station along the channel equals $uBy = u_0 B y_0 =$ constant, it is seen from Kirchoff's law that the internal voltage drop is equal to the external drop and hence a local matching theorem for maximum power is valid; i.e. the applied external unit loading, $r(x)$, at station x must be equal to the unit internal resistance of the working plasma at that station. It is not too surprising that in the case of incompressibility local matching is required for optimum power extraction. This is so because incompressibility yields the condition that the induced e.m.f. at every station along the channel is the same. This, coupled with the fact that the external voltage drop at each station must be identical (the channel walls are perfectly conducting), means that each station is uncoupled from the others and so can be treated as independently isolated. Conceptually, we may visualize the incompressible plasma generator as one consisting of a continuous distribution of independently acting elemental generators each with its own internal resistance. The elements (generator plus internal resistance) are then connected in parallel and the resulting combination feeding energy to an external load connected to the conducting walls.

The maximum power is, substituting for k from (11) into (10),

$$\hat{P} = \tfrac{1}{4}u_0^2 y_0^2 B^2 \sigma \int_0^l \frac{dx}{y(x)}. \tag{12}$$

The analysis leading to (12) was based purely on electrical energy considerations, i.e. Kirchoff's law and the definition of electrical power in terms of current and resistance. It is instructive, therefore, to reconsider the optimum power formula from a fluid mechanical energy viewpoint. Before doing so, the pressure distribution along the channel, at optimum power operation, is required. Substituting the value for k obtained in (11) into the momentum equation (7), we obtain the following differential equation for the pressure distribution along the channel:

$$\frac{dp}{dx} = \frac{m^2}{\rho_0 y^3}\frac{dy}{dx} - \frac{1}{2}\frac{\sigma B^2 m}{\rho_0 y}.$$

Integrating, and using the boundary condition $p = p_0$ at $x = 0$, we obtain

$$p = p_0 - \frac{m^2}{2\rho_0}\left(\frac{1}{y^2} - \frac{1}{y_0^2}\right) - \frac{\sigma B^2 m}{2\rho_0}\int_0^x \frac{d\xi}{y(\xi)}. \tag{13}$$

Now the fluid mechanical energy density of an incompressible, inviscid fluid is given by the Bernoulli expression $(p + \frac{1}{2}\rho_0 u^2)$. The energy flux at any station x is then $m/\rho_0(p + \frac{1}{2}\rho_0 u^2)$. Energy conservation requires that the difference in the fluid mechanical energy flux at the entrance and exit of the channel goes into electrical energy. Since we have already demonstrated that at optimum power operation the matching theorem is valid, the electrical energy must consist of two equal parts: (1) the electrical energy extracted by the external load, and (2) the electrical energy delivered to the fluid and which is dissipated internally in the form of heat. Mathematically, we have

$$\hat{P} = \frac{m}{2\rho_0}\{[p + \tfrac{1}{2}\rho_0 u^2]_0 - [p + \tfrac{1}{2}\rho_0 u^2]_l\}. \tag{14}$$

Substituting the expression (13) for p into (14), we find that $\hat{P}$ reduces identially to (12).

Incidentally, since the fluid pressure can not be less than zero at the channel exit, we have

$$p_0 - \frac{m^2}{2\rho_0}\left(\frac{1}{y^2(l)} - \frac{1}{y_0^2}\right) - \frac{\sigma B^2 m}{2\rho_0}\int_0^l \frac{d\xi}{y(\xi)} \geqslant 0 \tag{15}$$

as the condition which must be satisfied between the fluid mechanical, electromagnetic, and geometrical properties of the system.

Finally, as an interesting check on the inner consistency of what has gone before, we shall derive the maximum power formula using the techniques of lumped circuit theory. The external conductance in length dx is $dx/r(x)$. The total conductance is then

$$\int_0^l \frac{dx}{r(x)},$$

and the total external resistance is

$$R_{\text{ext}} = \left[\int_0^l \frac{dx}{r(x)}\right]^{-1}.$$

The current flow in the external load is

$$I = \int_0^l J(x)\,dx,$$

and since $J = k/r(x)$, we have $\quad I = k\int_0^l \frac{dx}{r(x)}.$

The total power delivered to the outside circuit is I^2R_{ext}. Using the above expressions for I and R_{ext}, we obtain

$$\hat{P} = I^2R_{\text{ext}} = k^2\int_0^l \frac{dx}{r(x)}. \tag{16}$$

Now at optimum power, $k = \frac{1}{2}(u_0y_0B)$ and $r(x) = y(x)/\sigma$ (local matching). Substituting for k and $r(x)$ into (16), we see that (16) reduces to (12).

For later comparison with the compressible flow case, we repeat the principal result of this section: for an incompressible plasma, the condition for optimum power requires that the external load be equal to the internal resistance of the plasma.

5. Case 2: compressible inviscid plasma moving across uniform transverse magnetic field in a channel of uniform cross-section

Analysis

We treat the optimization problem for the compressible flow case in a different manner than the incompressible case. Instead of seeking to maximize the power integral (5), we shall avoid a complicated integration by considering the maximization of the equivalent expression for the power, namely (9). (9) states that the electric power delivered to the external load is a maximum when the total enthalpy flux at the channel exit is a minimum. However, before we can minimize the total exit enthalpy flux, we must first integrate the fluid mechanical flow equations (6), (7) and (8), in order to determine the appropriate expressions (to be inserted into (9)), for the velocity, pressure and density of the plasma at the channel exit.

Before integrating, it is convenient to introduce the following dimensionless variables:

$$U = \frac{u}{u_0}; \quad X = \frac{x}{y_0}; \quad P = \frac{p}{\rho_0 u_0^2};$$

and the following dimensionless parameters:

$$k' = \frac{u_0y_0B}{k}; \quad \frac{l}{y_0} = a; \quad \frac{p_0}{\rho_0u_0^2} = \frac{1}{\gamma M_0^2}; \quad \frac{B^2y_0^2\sigma}{m}\frac{l}{y_0} = \delta.$$

The meaning of the first three parameters is fairly obvious and needs no further consideration. Let us briefly consider the significance of the fourth. Remembering that $B = \mu_e H$ and the definition of m, we can write δ as

$$\delta = \frac{B^2y_0^2\sigma}{m}\frac{l}{y_0} = \frac{\sigma\mu_e^2H^2l}{\rho_0u_0} = (\mu_e\sigma l u_0)\left(\frac{\mu_eH^2}{\rho_0u_0^2}\right).$$

In the next to the last form, δ represents the ratio of the electrical body force to the dynamic or inertial force on the conducting fluid (Resler & Sears 1958). Hence,

when δ is large we can expect the applied magnetic field to produce significant effects on the fluid motion.

Consider now the resolved form of δ. The term $(\mu_e \sigma l u_0)$ is defined as the magnetic Reynolds number (based on channel length). It is a measure of the effect of the hydromagnetic interaction on the magnetic field, and may be interpreted as the ratio of the motion induced magnetic field strength to the applied magnetic field strength. The term $(\mu_e H^2/\rho_0 u_0^2)$ can be written as

$$\frac{\mu_e H^2}{\rho_0 u_0^2} = \frac{c_a^2}{u_0^2},$$

where $c_a = \sqrt{(\mu_e H^2/\rho_0)}$ represents the speed of propagation of certain magnetohydrodynamic waves, called Alfvén waves. Thus $\sqrt{(\rho_0 u_0^2/\mu_e H^2)}$ is analogous to a Mach number where the usual speed of sonic disturbances is replaced by the speed of the Alfvén wavelike disturbances. The dimensionless number, δ, we shall henceforth call the magnetohydrodynamic interaction parameter.

In terms of the dimensionless variables and parameters, equations (7) and (8) become

$$\frac{dU}{dX} + \frac{dP}{dX} + \frac{\delta}{a}\left(U - \frac{1}{k'}\right) = 0, \tag{7'}$$

$$\frac{d}{dX}\left[\frac{\gamma}{\gamma-1} PU + \tfrac{1}{2}U^2\right] + \frac{\delta}{ak'}\left(U - \frac{1}{k'}\right) = 0. \tag{8'}$$

Eliminating $(U - 1/k')$ from (7') using (8'), (7') becomes

$$\frac{dU}{dX} + \frac{dP}{dX} - k' \frac{d}{dX}\left[\frac{\gamma}{\gamma-1} PU + \tfrac{1}{2}U^2\right] = 0.$$

Integrating, using the boundary conditions $U = 1$ and $P = 1/\gamma M_0^2$ at $X = 0$, we obtain

$$P = \frac{(\alpha + k'\beta) - (U - (\frac{1}{2}k')\, U^2)}{1 - [\gamma/(\gamma-1)]\, k' U}, \tag{17}$$

where

$$\alpha = 1 + \frac{1}{\gamma M_0^2}; \quad \beta = -\left(\frac{1}{\gamma-1}\frac{1}{M_0^2} + \frac{1}{2}\right).$$

Substituting for P in (7') using (17), we obtain, after some differentiations and combination,

$$\frac{dU}{dX}\left[\left(1 - \frac{\gamma}{\gamma-1} k'U\right)^2 - (1 - k'U)\left(1 - \frac{\gamma}{\gamma-1} k'U\right) + \frac{\gamma}{\gamma-1} k'\left\{(\alpha + k'\beta) - \left(U - \frac{k'}{2} U^2\right)\right\}\right] + \frac{\delta}{a}\left(1 - \frac{\gamma}{\gamma-1} k'U\right)^2 \left(U - \frac{1}{k'}\right) = 0. \tag{18}$$

Integrating (18), using the boundary condition $U = 1$ at $X = 0$, we obtain the following expression for U as an implicit function of X:

$$\left\{\frac{\gamma(\gamma-1)}{2} - 1 - \gamma(\gamma-1)\, k'(\alpha + k'\beta)\right\} \log\left(\frac{1 - k'U}{1 - k'}\right) + \left\{\frac{\gamma-1}{\gamma} - \frac{(\gamma^2+1)(\gamma-1)}{2\gamma} + \gamma(\gamma-1)\, k'(\alpha + k'\beta)\right\} \log\left(\frac{1 - [\gamma/(\gamma-1)]\, k'U}{1 - [\gamma/(\gamma-1)]\, k'}\right) + \left\{\frac{\gamma^2}{\gamma-1} k'^2(\alpha + k'\beta) - \frac{\gamma+1}{2} k'\right\}\left\{\frac{U-1}{(1 - [\gamma/(\gamma-1)]\, k'U)\,(1 - [\gamma/(\gamma-1)]\, k')}\right\} = \frac{\delta}{a} X. \tag{19}$$

The total exit enthalpy flux, in terms of the dimensionless variables, is

$$mu_0^2\left\{\frac{\gamma}{\gamma-1}P(a)\,U(a)+\tfrac{1}{2}U^2(a)\right\},$$

where the argument a is the value of X at the channel exit. The necessary condition that the total exit enthalpy flux be a minimum requires the derivative with respect to k' of the above expression to equal zero, or

$$\frac{\gamma}{(\gamma-1)}\left\{\frac{dP(a)}{dk'}U(a)+P(a)\frac{dU(a)}{dk'}\right\}+U(a)\frac{dU(a)}{dk'}=0. \tag{20}$$

Differentiate (17) with respect to k' to obtain $dP(a)/dk'$. Substituting for $dP(a)/dk'$ into (20), rearranging and simplifying, we obtain,

$$\mathbf{A}\frac{dU(a)}{dk'}+\mathbf{B}=0, \tag{20'}$$

where

$$\mathbf{A}=\frac{2\gamma(\gamma-1)(\alpha+k'\beta)-2(\gamma^2-1)U+\gamma(\gamma+1)k'U^2}{2(\gamma-1)^2\{1-[\gamma/(\gamma-1)]k'U\}^2},$$

$$\mathbf{B}=\frac{2\gamma(\gamma-1)\beta U+2\gamma^2\alpha U^2-\gamma(\gamma+1)U^3}{2(\gamma-1)^2\{1-[\gamma/(\gamma-1)]k'U\}^2}.$$

Differentiating (19) with respect to k', rearranging and simplifying, we obtain

$$\{\mathbf{1}+\mathbf{2}+\mathbf{3}\}\frac{dU(a)}{dk'}+\{\mathbf{4}+\mathbf{5}+\mathbf{6}+\mathbf{7}+\mathbf{8}+\mathbf{9}\}=0, \tag{22}$$

where

$$\mathbf{1}=\frac{-k'}{(1-k'U)}\left\{\frac{\gamma(\gamma-1)}{2}-1-\gamma(\gamma-1)k'(\alpha+k'\beta)\right\};$$

$$\mathbf{2}=\frac{-\gamma k'}{(1-[\gamma/(\gamma-1)]k'U)}\left\{\frac{1}{\gamma}-\frac{\gamma^2+1}{2\gamma}+\gamma k'(\alpha+k'\beta)\right\};$$

$$\mathbf{3}=\frac{\{2\gamma^2k'^2(\alpha+k'\beta)-(\gamma^2-1)k'\}}{2(\gamma-1)(1-[\gamma/(\gamma-1)]k'U)^2};$$

$$\mathbf{4}=-\gamma(\gamma-1)(\alpha+2k'\beta)\log\left(\frac{1-k'U}{1-k'}\right);$$

$$\mathbf{5}=\gamma(\gamma-1)(\alpha+2k'\beta)\log\left(\frac{1-[\gamma/(\gamma-1)]k'U}{1-[\gamma/(\gamma-1)]k'}\right);$$

$$\mathbf{6}=\left\{\frac{\gamma(\gamma-1)}{2}-1-\gamma(\gamma-1)k'(\alpha+k'\beta)\right\}\frac{(1-U)}{(1-k'U)(1-k')};$$

$$\mathbf{7}=\frac{\{1-\tfrac{1}{2}(\gamma^2+1)+\gamma^2k'(\alpha+k'\beta)\}\{1-U\}}{(1-[\gamma/(\gamma-1)]k'U)(1-[\gamma/(\gamma-1)]k')};$$

$$\mathbf{8}=\frac{\{\gamma^2/(\gamma-1)(2\alpha k'+3k'^2\beta)-\tfrac{1}{2}(\gamma+1)\}(U-1)}{(1-[\gamma/(\gamma-1)]k'U)(1-[\gamma/(\gamma-1)]k')};$$

$$\mathbf{9}=\frac{[\gamma^2/(\gamma-1)k'^2(\alpha+k'\beta)-\tfrac{1}{2}(\gamma+1)k'][\gamma/(\gamma-1)(U-1)\{(1+U)-[2\gamma/(\gamma-1)]k'U\}]}{(1-[\gamma/(\gamma-1)]k'U)^2(1-[\gamma/(\gamma-1)]k')^2};$$

Eliminating $dU(a)/dk'$ from (20′) and (22), we obtain

$$\{\mathbf{1}+\mathbf{2}+\mathbf{3}\}\,\mathbf{B}-\{\mathbf{4}+\mathbf{5}+\mathbf{6}+\mathbf{7}+\mathbf{8}+\mathbf{9}\}\,\mathbf{A}=0. \tag{23}$$

Equation (23), together with equation (19) (evaluated at $X=\alpha$), form a system of two simultaneous transcendental equations in the two unknowns k' and $U(a)$ as functions of the parameters γ, M_0, and δ.

Results and discussion

A specification of the 'input' parameters γ, M_0, δ and a, and the quantities k' and $U(a)$ obtained from the simultaneous solution of (23) and (19) is sufficient to determine completely all of the electrical and fluid mechanical properties of the interaction. In particular, we shall now derive, in terms of these parameters, explicit formulas for (1) the ratio of the required external resistance at optimum power to the internal resistance of the equivalent incompressible flow, (2) the power, and (3) the generator efficiency.

Eliminating J from (1) and (3), using (2), and solving for r, we obtain

$$r=\frac{ky_0}{\sigma(uBy_0-k)}.$$

Proceeding similarly as in § 4, we sum in parallel the continuous distribution of these elemental resistances, and obtain

$$R_{\text{ext}}=\frac{ky_0}{\sigma}\left[\int_0^l(uBy_0-k)\,dx\right]^{-1}.$$

An element of internal resistance is y_0/σ. The total resistance, R_{int}, of an incompressible plasma moving in a channel of uniform width y_0 is then $y_0/\sigma l$. Forming the resistance ratio, integrating the second term of the above integral, and transforming to dimensionless variables, we obtain

$$\frac{R_{\text{ext}}}{R_{\text{int}}}=\left[\frac{k'}{a}\int_0^a U\,dX-1\right]^{-1}=\left[\frac{k'}{a}\int_1^{U(a)}U\frac{dX}{dU}\,dU-1\right]^{-1}. \tag{24}$$

Forming dX/dU as an explicit function of U by differentiating (19), substituting into the latter integral and performing the integration, we finally obtain

$$\frac{R_{\text{int}}}{R_{\text{ext}}}=\frac{k'}{\delta}[\mathbf{10}+\mathbf{11}+\mathbf{12}]-1, \tag{25}$$

where $$\mathbf{10}=\left\{\frac{\gamma(\gamma-1)}{2k'}-\frac{1}{k'}-\gamma(\gamma-1)\,(\alpha+k'\beta)\right\}\log\left(\frac{1-k'U}{1-k'}\right);$$

$$\mathbf{11}=\left\{\gamma(\gamma-1)\,(\alpha+k'\beta)-\frac{(\gamma-1)^2(\gamma+1)}{2k'\gamma}\right\}\log\left(\frac{1-[\gamma/(\gamma-1)]\,k'U}{1-[\gamma/(\gamma-1)]\,k'}\right);$$

$$\mathbf{12}=(U-1)\left\{\frac{\gamma k'(\alpha+k'\beta)-(\gamma^2-1)/2\gamma}{(1-[\gamma/(\gamma-1)]\,k'U)\,(1-[\gamma/(\gamma-1)]\,k')}-\frac{(\gamma+1)}{2\gamma}\right\};$$

where it is understood that U is evaluated at $X=a$.

We emphasize once again that in the above formulas, R_{int} does not represent the internal resistance of the compressible plasma, but the resistance which would obtain had the plasma been treated as incompressible. It is clear that only in the case of incompressibility, where the induced e.m.f. at each station is the same, can we add in parallel the continuous distribution of elemental internal resistances. We chose to normalize R_{ext} with respect to the incompressible R_{int} because the latter is a resistance property of the system which is independent of the hydromagnetic interaction and depends only on the conductivity of the fluid and the geometry of the system (i.e. the width to length ratio).

The formula for the optimum power is obtained as follows:

$$\hat{P} = I^2 R_{\text{ext}} = k^2 \int_0^l \frac{dx}{r(x)} \quad \text{(see § 4)}.$$

Substituting the expression for $r(x)$, obtained above, into the integrand, and transforming to dimensionless variables, we obtain

$$\hat{P} = \frac{B^2 u_0^2 \sigma y_0 l}{k'^2} \left[\frac{k'}{a} \int_0^a U \, dX - 1 \right].$$

The bracketed term is precisely $(R_{\text{int}}/R_{\text{ext}})$; hence

$$\hat{P} = \frac{B^2 u_0^2 \sigma y_0 l}{k'^2} \frac{R_{\text{int}}}{R_{\text{ext}}}. \tag{26}$$

We define the efficiency or effectiveness, η, of the generator as

$$\eta = \frac{\text{Optimum electric power generated}}{\text{Total input enthalpy flux}}.$$

Forming the ratio of (26) to the total input enthalpy flux, i.e.

$$m \left[\frac{\gamma}{\gamma - 1} \frac{p_0}{\rho_0} + \tfrac{1}{2} u_0^2 \right],$$

and transforming to dimensionless variables, we obtain

$$\eta = -\frac{\delta}{\beta k'^2} \frac{R_{\text{int}}}{R_{\text{ext}}} = 1 + \left[\frac{(\gamma/\gamma - 1)\, P(a)\, U(a) + \tfrac{1}{2} U^2(a)}{\beta} \right], \tag{27}$$

where the last term represents the difference in entrance and exit stagnation enthalpy fluxes divided by the entrance flux. It is seen that the efficiency η is a complicated function (because of the complexity of the resistance ratio term) of the two dimensionless parameters δ and M_0, characterizing respectively the hydromagnetic and compressive properties of the system.

Solutions of the system of equations (23) and (19) (evaluated at $X = a$) for k' and $U(a)$ were obtained on an I.B.M. 704 computer. Solutions were obtained for the particular Mach number $M_0 = 0{\cdot}3$ and for a γ equal to $\frac{5}{3}$ (corresponding to the assumption that the plasma be treated as a monatomic perfect gas). δ was allowed to vary continuously until a maximum $\delta_{\max} \sim 30$ was reached beyond which no solutions could be generated.

Consider table 1 which lists the magnitudes of all the dimensionless electrical and fluid mechanical quantities. It is seen that the solution exhibits an asymptotic behaviour near $\delta_{\text{crit}} \sim 4$. In particular, if attention is focused on the column of exit Mach numbers $M(a)$, it is noted that for the second branch ($\delta > 4$), $M(a)$ is always equal to one. We conclude, therefore, the existence of a finite range of δ, i.e. $\delta_{\text{crit}} \leqslant \delta \leqslant \delta_{\max}$, where the required external loading at optimum power is that which forces a Mach number one flow at the exit.

δ	k'	$2/k'$	$R_{\text{ext}}/R_{\text{int}}$	I/I_{inc}	$\eta\%$	$U(a)$	$P(a)$	$M(a)$
0·1	2·0017	0·99914	0·99166	1·0075	0·1466	1·0067	6·6096	0·30230
0·2	2·0035	0·99823	0·98321	1·0153	0·29519	1·0136	6·5515	0·30468
0·4	2·0076	0·99623	0·96585	1·0315	0·59858	1·0283	6·4321	0·30976
0·6	2·0122	0·99394	0·94781	1·0487	0·91076	1·0441	6·3080	0·31514
0·8	2·0175	0·99131	0·92901	1·0671	1·2324	1·0612	6·1786	0·32101
1·0	2·0236	0·98832	0·90942	1·0868	1·5642	1·0799	6·0434	0·32745
2·0	2·0736	0·96450	0·79390	1·2149	3·4129	1·2093	5·2425	0·37296
4·0	2·0077	0·99617	0·62218	1·6011	9·2909	2·7903	1·6742	1·0000
6·0	1·4202	1·4083	1·2769	1·1029	13·572	2·7237	1·6342	1·0000
8·0	1·2407	1·6120	1·9160	0·84134	15·801	2·6882	1·6130	1·0000
10·0	1·1562	1·7299	2·5444	0·67987	17·127	2·6671	1·6002	1·0000
12·0	1·1083	1·8045	3·1645	0·57024	17·983	2·6533	1·5920	1·0000
14·0	1·0783	1·8547	3·7780	0·49093	18·565	2·6438	1·5863	1·0000
16·0	1·0582	1·8899	4·3865	0·43085	18·976	2·6372	1·5823	1·0000
18·0	1·0442	1·9154	4·9893	0·38389	19·274	2·6323	1·5794	1·0000
20·0	1·0340	1·9342	5·5887	0·34608	19·496	2·6287	1·5772	1·0000
25·0	1·0186	1·9636	7·0735	0·27760	19·845	2·6230	1·5738	1·0000
30·0	1·0105	1·9791	8·5437	0·23165	20·358	2·6146	1·5687	1·0000

TABLE 1. List of the dimensionless electrical and fluid dynamical variables.
$M_0 = 0{\cdot}3; \quad \gamma = \frac{5}{3}$

At least for the branch characterized by $M(a) = 1$, the condition which determines $\delta_{\max}$ may be formulated as follows. The Mach number at any point in the channel in terms of the dimensionless fluid dynamical variables P and U is given by $M = \sqrt{(U/\gamma P)}$. The condition $M(a) = 1$ at the exit yields $P(a) = U(a)/\gamma$. Substituting for $P(a)$ in (23), we obtain

$$\frac{U(a)}{\gamma} = \frac{(\alpha + k'\beta) - [U(a) - (\frac{1}{2}k')\,U^2(a)]}{1 - [\gamma/(\gamma-1)]\,k'U(a)}. \tag{28}$$

The simultaneous solution of (19), (23), and (28) yields $\delta_{\max}$ and the corresponding limiting values of k' and $U(a)$.

Let us consider now the electrical quantities. Referring to the definitions of k and k', both compressible and incompressible, it is seen that $2/k'$ represents the ratio of the compressible terminal voltage to the terminal voltage obtained by assuming the gas to be incompressible. Similarly, I/I_{inc}, the ratio of the compressible to the incompressible current, is given by $(2/k')\,(R_{\text{int}}/R_{\text{ext}})$. It should be emphasized that incompressibility is defined and used here in the sense of § 4; i.e. the density of the fluid is everywhere constant in space and time and not as the limit flow approached as the Mach number is made to approach zero.

Plots of the resistance, voltage and current ratios as functions of the magnetohydrodynamic interaction parameter δ are shown in figure 2. Several general observations can be made. First, for weak interactions (i.e. δ small), the fluid behaves as if it were incompressible; that is, the resistance, terminal voltage and current remain close to the corresponding incompressible values. Secondly, the asymptotic behaviour is clearly marked and is represented in the resistance and current curves as forming cusps at the critical δ. Thirdly, for large δ, the behaviour of the solution is very much different from the corresponding incompressible case. The terminal voltage ratio approaches the asymptotic value two while the external load ratio continues to increase sharply with δ. This behaviour is very significant, for it indicates (as is often done in fluid dynamics in order to obtain a first estimate

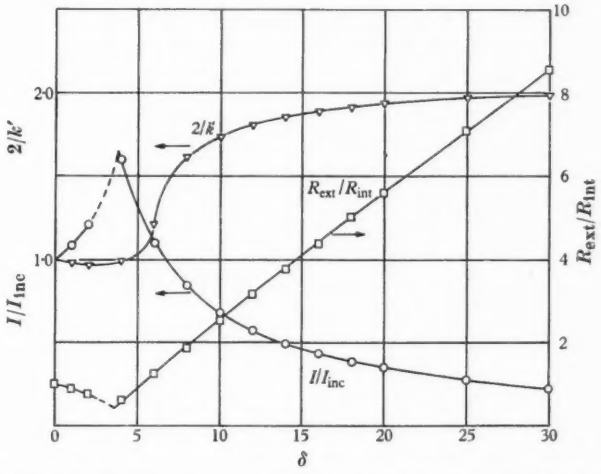

FIGURE 2. Resistance, terminal voltage and current ratios against magnetohydrodynamic interaction parameter δ. $M_0 = 0{\cdot}3$, $\gamma = \frac{5}{3}$.

to some fluid mechanical interaction), that one cannot approximate the interaction by simply treating the fluid as incompressible. For example, it is seen from the figure, that for δ very large, the external load required at optimum power is close to an order of magnitude larger than the corresponding incompressible load.

Figure 3 is a plot of the efficiency of the plasma generator as defined above. As is expected, for small δ, when the effect of the magnetic field on the fluid flow is small, the efficiency is small. It increases as δ increases approaching a value slightly over 20 % in the neighbourhood of $\delta_{\max}$.

Finally, let us consider briefly the effect of the interaction on the fluid dynamical variables. The distribution of all of the fluid dynamical variables with distance along the channel was obtained for every δ in each of the two branches with the view to determining whether any of the solutions belonging to the two branches corresponded to any peculiar phenomena, e.g. choking. In every case, the dynamical variables were single valued and varied continuously with channel distance so that behaviour peculiar to choking (Resler & Sears 1958) was absent.

Figure 4 shows the variation of the normalized fluid dynamical variables with fractional distance along the channel for the case $\delta = 20$. It is seen that the pressure and density decrease while the velocity and Mach number increases downstream of the entrance. It appears that, as far as the direction of change of

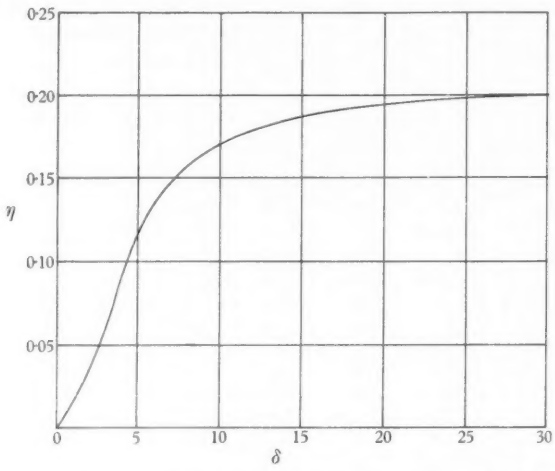

FIGURE 3. Efficiency against magnetohydrodynamic interaction parameter δ. $M_0 = 0{\cdot}3$, $\gamma = \frac{5}{3}$.

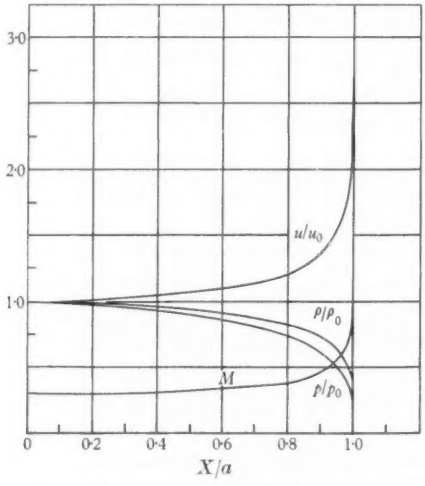

FIGURE 4. Variation of normalized fluid dynamical state variables with dimensionless distance along channel. $M = 0{\cdot}3$, $\gamma = \frac{5}{3}$, $\delta = 20$.

the fluid variables are concerned, the effect of the interaction is analogous both to channel flow with friction and no heat transfer or to channel flow with heat addition and no frictional forces (see, for example, Shapiro 1953). The velocity increase along the channel leads to a very interesting conclusion concerning power delivery

to the external load. It was seen in § 3 that the contribution to the power delivered to the external load per unit channel length at station x is $k\sigma\{uB - k/y_0\}$. Since k, σ and B are constants, the power contributed depends on the magnitude of the velocity at that station. We conclude, therefore, that most of the power delivered to the external load comes from the induction taking place near the exit region of the channel.

6. Conclusion

In this paper, solutions for the compressible generator were obtained for only one particular value of the entrance Mach number. It is planned to obtain a family of solutions over a wide range of Mach numbers both subsonic and supersonic. Interest here is not only toward the determination of the effect on the interaction of the various states of compressibility of the entering plasma, but to see whether the asymptotic behaviour occurs for other Mach numbers as well, and at what values of δ. The reason for, and the physical significance, if any, of the asymptotic behaviour itself should be investigated. Further, a thorough examination should be made into the validity of the assumptions made in § 1 directed towards estimating the practicality of the results. In particular, the effect of the possible development of space charge and the formation of space charge sheaths near the walls should be thoroughly investigated.

In conclusion, it is hoped that, while this paper concerned itself mainly with the theoretical treatment of a very highly idealized but interesting problem in hydromagnetics, it will also serve in giving a first insight into the behaviour of a type of generator which may prove to have future practicality.

The writer thanks Drs William McIlroy and Philip M. Mostov for their suggestions, clarifying discussions and helpful criticisms during the preparation of this paper. Thanks are also extended to Mr Sol Broder and Miss Eleanor Ditzler for their kind help in performing the numerical computations.

This research was supported in part by the U.S. Air Force through the Air Force Office of Scientific Research.

REFERENCES

KUNEN, A. 1958 Electromagnetic pinch effect as a space propulsion system. Paper presented at the American Astronautical Society, Western Regional Meeting, Stanford University.

NEURINGER, J. L. 1958 The formulation of a problem in optimum power generation using a plasma as the working fluid. *Tech. Note Republic Aviation Corp. Sci. Res. Staff* no. 17.

POST, R. F. 1956 An application of the physics of high temperature plasmas. *Rev. Mod. Phys.* **28**, 338.

RESLER, E. L. & SEARS, W. R. 1958 The prospects for magneto-aerodynamics. *J. Aero. Sci.* **25**, 235.

SHAPIRO, A. H. 1953 *The Dynamics and Thermodynamics of Compressible Fluid Flow*, vol. 1. New York: Ronald.

Motion of a bore over a sloping beach

By H. B. KELLER, D. A. LEVINE AND G. B. WHITHAM
Institute of Mathematical Sciences, New York University

(Received 29 May 1959)

The results of numerical calculations are presented for the motion of a bore over a uniformly sloping beach. The shallow water equations are solved in finite difference form, and a technique is developed for fitting in the bore at each step. The results are compared with the approximate formula given by Whitham (1958) and close agreement is found. The approximate theory is considered further here; the main addition is a rigorous proof that, within the shallow water theory, the height of the bore always tends to zero at the shoreline.

1. Introduction

This paper gives an account of numerical solutions of the shallow water equations for the motion of a bore on a uniformly sloping beach. In a previous paper (Whitham 1958), an approximate formula was derived for the variation in the strength and height of the bore. The predictions were seen to contain specially interesting features, one of the main ones being that the height of the bore always tends to zero as it approaches the shoreline. Indeed, in the earlier account these predictions were viewed with a certain amount of suspicion, even though checks of the analogous theory in certain problems of gas dynamics show extremely high accuracy. Subsequently, it was realized that the predicted behaviour is correct† (within the shallow water theory at least) and the result that the bore height tends to zero at the shoreline can be proved rigorously. This proof, together with recapitulation and further discussion of the approximate method, is given in § 2.

The numerical investigation confirms the previous results completely. In fact the agreement is quite remarkable; the differences are of the same order as the probable errors in the numerical work. In addition to this check, the numerical solution provides the full details of the flow behind the bore; these were not obtained previously. Furthermore, the solution is found for various starting conditions whereas it is assumed in the approximate theory that the bore is initially moving with constant speed and height in water of uniform depth. For these other starting conditions, it is found that the solutions eventually settle down and follow the approximate formula; the appropriate choice of the arbitrary constant factor in that formula varies considerably with the starting conditions for the same initial bore strength, but the functional dependence near the shoreline is the same. A similar insensitivity to the detailed initial conditions is well known for the analogous problem of the converging cylindrical shock in gas dynamics. The numerical results are discussed in detail in § 4.

† In this connexion we are grateful for discussions with G. F. Carrier and H. P. Greenspan.

For this problem, it was decided to develop a numerical method which uses fixed equal space intervals rather than the characteristics method which is not well suited to machine calculations. Stable ways of differencing the equations are well known, and the only question is how to fit in the bore at each step. This requires special care, but the method adopted here seems to be satisfactory in every respect. The details of the numerical scheme are given in § 3. It is planned to extend this method for use in the analogous shock-wave problems in gas dynamics.

2. Approximate formula and behaviour near the shoreline

If $h(x,t) = h_0(x) + \eta(x,t)$ denotes the depth of the water, where $h_0(x)$ is the undisturbed depth ahead of the bore, and $u(x,t)$ is the particle velocity, the equations of the shallow water theory are

$$\eta_t + \{(h_0+\eta)\,u\}_x = 0, \tag{1}$$

$$u_t + uu_x + g\eta_x = 0. \tag{2}$$

The bore conditions are

$$U = \sqrt{\frac{gh(h_0+h)}{2h_0}}, \tag{3}$$

$$u = \frac{h-h_0}{h}\,U, \tag{4}$$

where U is the bore velocity. Along a positive characteristic it is readily found from (1) and (2) that

$$du + 2dc - \frac{gdh_0}{u+c} = 0 \tag{5}$$

on

$$\frac{dx}{dt} = u + c, \tag{6}$$

where $c = \sqrt{(gh)}$. The approximate formula may be derived by applying the differential relation (5) to the flow quantities immediately behind the bore. Since these quantities are given in terms of U by (3) and (4) we have, then, a differential equation for U as a function of h_0. The arbitrary constant in the integration is fixed from the initial value of U.

This simple rule and its motivation are discussed in detail in the previous paper (Whitham 1958). It has not been justified in general, although it is easily shown to be the correct answer in a linearized perturbation theory for the effects of small changes in the depth on a bore initially moving with constant speed in a uniform region. In the linearized theory, the coefficient $(u+c)^{-1}$ in (5) is replaced by its unperturbed value $(u_1+c_1)^{-1}$ say. Then (5) can be integrated to

$$\Delta u + 2\Delta c - \frac{g\Delta h_0}{u_1+c_1} = 0, \tag{7}$$

where Δu, Δc, Δh_0 denote the perturbations $u-u_1$, etc.; the right-hand side of (7) is set equal to zero since all the positive characteristics C_+ come from the initial uniform region in which $\Delta u = \Delta c = \Delta h_0 = 0$ (see figure 1). Since the combination in (7) vanishes on each characteristic, it follows that it vanishes everywhere. In

particular, therefore, it applies to the flow quantities just behind the bore. Substituting from the bore conditions we have a relation of the form

$$f(U_1)\,\Delta U = \Delta h_0 \tag{8}$$

for the change in bore speed $\Delta U = U - U_1$ in terms of the change in depth Δh_0. This result is exactly the linearized form of the above rule. The more general form of the rule corresponds to replacing (8) by the differential equation

$$f(U)\frac{dU}{dh_0} = 1. \tag{9}$$

From this point of view, the rule would be expected to hold if the depth varies sufficiently slowly even though the total change in depth is not small. But it turns out to be much better and applies equally well to quite extreme cases. This will be seen in the results presented in this paper.

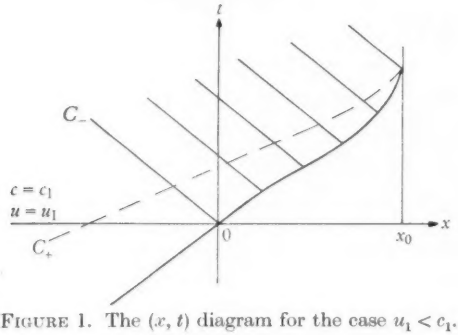

FIGURE 1. The (x, t) diagram for the case $u_1 < c_1$.

In substituting the bore conditions into (5) to get a differential equation corresponding to (9), it is convenient to work with $M = U/\sqrt{(gh)}$. In terms of M, we have

$$\left.\begin{aligned} \frac{U}{\sqrt{(gh_0)}} &= M\sqrt{(2M^2-1)}, \\ \frac{u}{\sqrt{(gh_0)}} &= \frac{2M(M^2-1)}{\sqrt{(2M^2-1)}}, \\ \frac{c}{\sqrt{(gh_0)}} &= \sqrt{(2M^2-1)}, \\ \frac{\eta}{h_0} &= \frac{h-h_0}{h_0} = 2(M^2-1). \end{aligned}\right\} \tag{10}$$

On substitution in (5), the following equation for M as a function of h_0 is obtained:

$$\frac{1}{h_0}\frac{dh_0}{dM} = -4\,\frac{(M+1)(M-\frac{1}{2})^2(M^3+M^2-M-\frac{1}{2})}{(M-1)(M^2-\frac{1}{2})(M^4+3M^3+M^2-\frac{3}{2}M-1)}. \tag{11}$$

The range of M is $1 < M < \infty$, weak bores corresponding to small values of $(M-1)$ and strong bores to large values of M. In this range, the right-hand side of (11) is

always negative so that M increases monotonically as h_0 decreases. However this is not true of the height η. When $M-1$ is small, (11) is approximately

$$\frac{1}{h_0}\frac{dh_0}{dM} = -\frac{4}{5}\frac{1}{M-1},$$

and it gives

$$M-1 \propto h_0^{-\frac{4}{5}}, \quad \eta \propto h_0^{-\frac{1}{5}}. \tag{12}$$

Whereas, when M is large, we have

$$\frac{1}{h_0}\frac{dh_0}{dM} = -\frac{4}{M}, \quad M \propto h_0^{-\frac{1}{4}}, \quad \eta \propto h_0^{\frac{1}{2}}. \tag{13}$$

This is the result noted earlier that the bore height tends to zero when $h_0 \to 0$. For weak bores, η increases as h_0 decreases, but for strong bores η decreases with h_0. Thus in the beach problem, if η is initially less than the critical value $0{\cdot}6262\,h_0$ (see the determination below), the height first increases and then ultimately decreases with a maximum at some intermediate position; at the maximum $\eta/h_0 = 0{\cdot}6262$. If η/h_0 exceeds this value initially, the height decreases all the way to the shoreline. The bore velocity U has a similar change in behaviour, but at a different critical value given by $\eta/h_0 = 2{\cdot}076$, $U/\sqrt{(gh_0)} = 2{\cdot}504$. If $U < 2{\cdot}504\sqrt{(gh_0)}$ initially, U first decreases, but then ultimately increases to a finite value at the shoreline; at the minimum $U/\sqrt{(gh_0)} = 2{\cdot}504$. If $U > 2{\cdot}504\sqrt{(gh_0)}$ initially, U increases all the way to the shore.

The result that $\eta \to 0$ as $h_0 \to 0$ is surprising at first sight and certainly the validity of the rule might be suspected in this extreme limiting case. However, an independent proof can be given as follows:

First, from the bore conditions (3) and (4), the bore height η must tend to zero with h_0 if u is to remain finite. We now show that u must remain finite. For a uniformly sloping beach we may take $h_0 = \alpha(x_0 - x)$, where α is the slope and $x = x_0$ is the shoreline. Then, the characteristic relations (5) and (6) give

$$du + 2dc + \alpha g\,dt = 0 \quad \text{i.e.} \quad u + 2c + \alpha g t = \text{constant}, \tag{14}$$

on a positive characteristic. Thus, if $u \to \infty$ at the shoreline, $u + 2c + \alpha g t \to \infty$ at *all* points of the characteristic which reaches the bore just at the shoreline. This is clearly impossible in the solution of our problem. (It should be noted that if $u \to \infty$, $U \to \infty$ so the bore reaches the shoreline in finite time.) Therefore, u remains finite as $h_0 \to 0$; hence, from the bore conditions, $\eta \to 0$. It is interesting to note that this method of fixing the behaviour near the shore, by the absence of a singularity on the characteristic, is completely analogous to the method for determining the exponent in Guderley's similarity solution for the converging cylindrical shock (see the discussion in Whitham (1958)).

The relation (14) can be written in a further convenient form if we assume that the depth is uniform in $x < 0$ and that the bore is initially moving with constant speed in that region. The (x, t) diagram is shown in figure 1 for the case when the initial constant values $u = u_1$, $c = c_1$ behind the bore are such that $u_1 < c_1$. Then the flow is undisturbed to the left of the negative characteristic $x = (u_1 - c_1)t$ shown as C_- in the figure. If $u_1 > c_1$ the flow is undisturbed with $u = u_1$, $c = c_1$ in $x < 0$

until a reflected bore appears. In the absence of such secondary bores (which would modify the result somewhat), we have from (14)

$$u + 2c + \alpha g t = u^*(\tau) + 2c^*(\tau) + \alpha g \tau,$$

where $t = \tau$ is the time when the characteristic crosses $x = 0$ and u^*, c^* are the corresponding values of u and c. But, $u + 2c$ is constant on the characteristic in $x < 0$ since $h_0 =$ constant, therefore $u^* + 2c^* = u_1 + 2c_1$ and we have

$$u + 2c + \alpha g(t - \tau) = u_1 + 2c_1. \tag{15}$$

M	$\frac{h_0}{A} = f(M)$	$\frac{\eta}{A}$	$\frac{U}{\sqrt{(gA)}}$	$\frac{c}{\sqrt{(gA)}}$	$\frac{u}{\sqrt{(gA)}}$
1·01	5·360	0·2155	2·385	2·361	0·092
1·02	3·006	0·2429	1·839	1·802	0·137
1·03	2·124	0·2586	1·590	1·543	0·173
1·04	1·649	0·2692	1·440	1·385	0·202
1·05	1·350	0·2767	1·339	1·275	0·228
$\sqrt{1·125}$	1·130	0·2825	1·261	1·188	0·252
1·08	$8·696 \times 10^{-1}$	0·2894	1·163	1·077	0·290
1·1	$6·988 \times 10^{-1}$	0·2935	1·096	0·996	0·324
1·146	$4·733 \times 10^{-1}$	0·2964	1·005	0·877	0·387
1·2	$3·342 \times 10^{-1}$	0·2941	0·951	0·793	0·445
1·3	$2·055 \times 10^{-1}$	0·2836	0·909	0·699	0·527
1·428	$1·285 \times 10^{-1}$	0·2668	0·898	0·629	0·606
1·5	$1·028 \times 10^{-1}$	0·2570	0·900	0·600	0·643
2·0	$3·308 \times 10^{-2}$	0·1985	0·962	0·481	0·825
$\sqrt{6}$	$1·602 \times 10^{-2}$	0·1602	1·028	0·420	0·935
3·0	$7·909 \times 10^{-3}$	0·1265	1·100	0·367	0·035
3·5	$4·637 \times 10^{-3}$	0·1043	1·155	0·330	1·106
4·0	$2·916 \times 10^{-3}$	0·0875	1·203	0·301	1·164
5·0	$1·335 \times 10^{-3}$	0·0641	1·279	0·256	1·253
6·0	$6·992 \times 10^{-4}$	0·0489	1·337	0·223	1·318
7·0	$4·023 \times 10^{-4}$	0·0386	1·383	0·198	1·368
8·0	$2·480 \times 10^{-4}$	0·0312	1·420	0·177	1·408
10·0	$1·094 \times 10^{-4}$	0·0217	1·476	0·148	1·468
20·0	$8·058 \times 10^{-6}$	0·0064	1·605	0·080	1·603
∞	0	0	1·763	0	1·763

TABLE 1. Calculations from approximate formula for bore motion: general A

From this form it is immediately obvious that u remains bounded since all terms on the left are positive. However, this form is limited to the particular case of an initially uniform bore and the earlier argument is more general. With this result that u remains bounded, the bore conditions (3) and (4) show that h and η are proportional to $h_0^{\frac{1}{2}}$ as $h_0 \to 0$. It should also be noted that the particle velocity u and the bore velocity U approach the same limiting value when $h_0 \to 0$.

Turning to the details of the solution given by (11), we see that the maximum of η occurs when

$$\frac{d\eta}{dh_0} = 2(M^2 - 1) + 4h_0 M \frac{dM}{dh_0} = 0. \tag{16}$$

The value of M is found to be 1·146, and from the bore conditions the corresponding η, etc. are

$$\left.\begin{aligned} &\text{Maximum } \eta\text{: } M = 1{\cdot}146, \quad \eta/h_0 = 0{\cdot}6262, \quad U/\sqrt{(gh_0)} = 1{\cdot}461,\\ &\frac{u}{\sqrt{(gh_0)}} = 0{\cdot}5627, \quad \frac{c}{\sqrt{(gh_0)}} = 1{\cdot}275. \end{aligned}\right\} \tag{17}$$

(In the earlier paper (Whitham 1958), M was taken erroneously to be approximately 1·2 and this led to a large error in η/h_0). The minimum bore speed occurs at a larger value of M; we have:

$$\left.\begin{aligned} &\text{Minimum } U\text{: } M = 1{\cdot}428, \quad \eta/h_0 = 2{\cdot}076, \quad U/\sqrt{(gh_0)} = 2{\cdot}504,\\ &\frac{u}{\sqrt{(gh_0)}} = 1{\cdot}690, \quad \frac{c}{\sqrt{(gh_0)}} = 1{\cdot}754. \end{aligned}\right\} \tag{18}$$

M	$H_0 = \dfrac{h_0}{h_0(0)}$	$N = \dfrac{\eta}{h_0(0)}$	$V = \dfrac{U}{\sqrt{(gh_0(0))}}$	$\dfrac{c}{\sqrt{(gh_0(0))}}$	$v = \dfrac{u}{\sqrt{(gh_0(0))}}$
$\sqrt{1{\cdot}125}$	1·0000	0·2500	1·186	1·118	0·237
1·08	0·7696	0·2561	1·094	1·013	0·273
1·1	0·6184	0·2597	1·031	0·937	0·305
1·146	0·4189	0·2623	0·946	0·825	0·364
1·2	0·2957	0·2602	0·895	0·746	0·419
1·3	0·1819	0·2510	0·855	0·658	0·496
1·428	0·1137	0·2361	0·844	0·591	0·570
1·5	0·0910	0·2275	0·846	0·564	0·605
2·0	0·0293	0·1757	0·905	0·453	0·776
4·0	0·0026	0·0774	1·131	0·283	1·095
8·0	0·0002	0·0276	1·336	0·167	1·325
∞	0	0	1·659	0	1·659

TABLE 2*a*. Calculations from approximate formula for bore motion: $A = 0{\cdot}8850$, $N(0) = 0{\cdot}25$

M	$H_0 = \dfrac{h_0}{h_0(0)}$	$N = \dfrac{\eta}{h_0(0)}$	$V = \dfrac{U}{\sqrt{(gh_0(0))}}$	$\dfrac{c}{\sqrt{(gh_0(0))}}$	$v = \dfrac{u}{\sqrt{(gh_0(0))}}$
$\sqrt{6}$	1·0000	10·000	8·12	3·317	7·39
3·0	0·4936	7·897	8·69	2·897	8·18
3·5	0·2894	6·511	9·13	2·608	8·74
4·0	0·1820	5·459	9·50	2·375	9·19
5·0	0·0833	3·998	10·10	2·020	9·90
6·0	0·0436	3·055	10·56	1·760	10·41
7·0	0·0251	2·410	10·92	1·560	10·81
8·0	0·0155	1·950	11·22	1·402	11·13
10·0	0·0068	1·352	11·66	1·166	11·60
20·0	0·0005	0·401	12·68	0·634	12·66
∞	0	0	13·93	0	13·93

TABLE 2*b*. Calculations from approximate formula for bore motion: $A = 62{\cdot}41$, $N(0) = 10{\cdot}0$

Equation (11) integrates to

$$h_0 = A\,\frac{(M^2-\frac{1}{2})\exp\{a_1\tan^{-1}(M+a_2)/a_3\}}{(M-1)^{\frac{1}{2}}(M-a_4)^{\varkappa}(M^2+a_5M+a_6)^{\beta}(M+a_7)^{\gamma}}, \tag{19}$$

where A is a constant of integration to be determined from the initial strength of the bore, and

$$a_1 = 0{\cdot}2808, \quad a_2 = 0{\cdot}6769, \quad a_3 = 0{\cdot}3179, \quad a_4 = 0{\cdot}7471, \quad a_5 = 1{\cdot}354,$$
$$a_6 = 0{\cdot}5593, \quad a_7 = 2{\cdot}393, \quad \alpha = 1{\cdot}180, \quad \beta = 1{\cdot}173, \quad \gamma = 1{\cdot}673.$$

The flow quantities at the bore are determined from equations (10); their values are given in table 1. For a given strength of bore initially, M is determined from the bore conditions and then A is determined from (19). The results for $\eta/h_0 = 0{\cdot}25$ and 10 initially are given in tables $2a$ and $2b$. They are discussed in detail in § 4.

3. Numerical method

It is assumed that the beach has slope α, starts at $x = 0$ and has the shoreline at $x = x_0$; the depth is constant and equal to αx_0 in $x \leqslant 0$. We introduce the dimensionless quantities:

$$\left.\begin{aligned} X = \frac{x}{x_0}, \quad T &= \frac{t}{x_0}\sqrt{(gh_0(0))}, \\ v(X,T) = \frac{u(x,t)}{\sqrt{(gh_0(0))}}, \quad V &= \frac{U}{\sqrt{(gh_0(0))}}, \\ H(X,T) = \frac{h(x,t)}{h_0(0)}, \quad N(X,T) &= \frac{\eta(x,t)}{h_0(0)}, \end{aligned}\right\} \tag{20}$$

where $h_0(0) = \alpha x_0$. In terms of these variables

$$H_0(X) = \begin{cases} 1, & X \leqslant 0, \\ 1 - X, & 0 \leqslant X \leqslant 1. \end{cases} \tag{21}$$

The shallow water theory equations (1), (2) can now be written as

$$H_T + (Hv)_X = 0, \tag{22}$$

$$v_T + \tfrac{1}{2}(v^2)_X + H_X = H_{0X}, \tag{23}$$

and the bore conditions (3), (4) become

$$V = \sqrt{\frac{H(H_0 + H)}{2H_0}}, \tag{24}$$

$$v = \left(\frac{H - H_0}{H}\right) V. \tag{25}$$

The numerical procedure is, in outline, to compute the flow quantities behind the bore on a set of net points (X_i, T_k) by means of finite difference approximations of (22) and (23). The bore quantities and its propagation between net points are computed from a special set of difference equations which include the bore conditions (24) and (25), and couple the flow variables at the bore to those behind it by means of the equations of motion. Of course this procedure assumes that the initial state contains a bore and in its present form is not capable of treating problems in which bores develop.

In detail the spatial net is chosen to be uniform, $X_i = i\Delta X$, for convenience, and the time net, $T_{k+1} = T_k + \Delta T_k$, must then satisfy the stability condition stated

below. If ξ_k is the position of the bore at time T_k, we let $X_{s(k)}$ be that net point for which

$$X_{s(k)} \leqslant \xi_k < X_{s(k)+1}.$$

At all net points $X_i < X_{s(k)}$ the flow quantities are computed from the difference forms of (22) and (23) (see figure 2*a*):

$$H(P) = \tfrac{1}{2}[H(R')+H(Q')] - \frac{\Delta T_k}{2\Delta X}[v(R')\,H(R') - v(Q')\,H(Q')], \tag{26}$$

$$v(P) = \tfrac{1}{2}[v(R')+v(Q')] - \frac{\Delta T_k}{2\Delta X}\{\tfrac{1}{2}[v^2(R')-v^2(Q')]+[H(R')-H(Q')]\}$$
$$-\begin{cases} 0, & X_i < 0, \\ \tfrac{1}{2}\Delta T_k, & X_i = 0, \\ \Delta T_k, & X_i > 0. \end{cases} \tag{27}$$

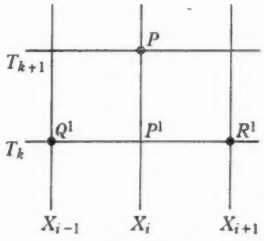

FIGURE 2*a*. Mesh points for differencing the equations.

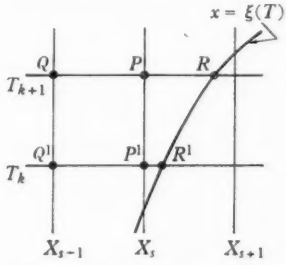

FIGURE 2*b*. Mesh points for fitting in the bore.

These equations are obtained from (22), (23) by replacing the T-derivatives by forward differences and the X-derivatives by centred differences. If in the T-differences the average values $\frac{1}{2}[H(R')+H(Q')]$, etc., are replaced by the actual values $H(P')$, etc., the difference equations become unconditionally unstable. However, using these average values it has been shown (Lax 1954) that the equations are stable provided the time mesh satisfies the so-called Courant condition

$$\Delta T_k \leqslant \min_{P'}\left(\frac{\Delta X}{v(P')+\sqrt{\{H(P')\}}}\right).$$

It is clear from (21) that $\partial H_0/\partial X$ is discontinuous at $X = 0$ and as a consequence it follows that $\partial v/\partial X$ and $\partial H/\partial X$ must satisfy the jump conditions

$$\left[\frac{\partial H}{\partial X}\right]_{X=0-}^{X=0+} = \frac{-H}{H-v^2}, \quad \left[\frac{\partial v}{\partial X}\right]_{X=0-}^{X=0+} = \frac{v}{H-v^2}. \tag{28}$$

In these dimensionless variables, $v^2 = H$ when the particle velocity is equal to the propagation speed. In fact this condition never occurs at $x = 0$; if it holds initially, a reflected bore is produced when the main bore meets the change in depth, and this second bore establishes values of v and H, with $v^2 \neq H$, at $x = 0$. This whole question of perturbations on sonic conditions behind a shock has been elucidated by M. P. Friedman (1959). This particular feature of the problem is not under discussion here and we compute only cases with $v^2 - H$ well away from zero.

Again the discontinuity in the bottom and corresponding discontinuities in v_X and H_X are not of primary interest here, since we are mainly concerned with the motion of the bore as it approaches the shoreline. Accordingly no special account of these discontinuities has been taken in (26) and (27). As a consequence we expect and indeed find in the results that the numerical solution suffers from relatively large truncation errors near $X = 0$. These effects could be eliminated either by smoothing the corner in the bottom profile or by modifying the difference equations to include the jump conditions (28). However, the errors introduced in this way at $X = 0$ are not large enough to warrant these detailed corrections for the present purposes.

The net points which enter into the bore fitting procedure are shown in figure 2*b*. All relevant quantities are known at Q, Q', P' and R' and the unknowns are $v(P)$, $H(P)$, $v(R)$, $H(R)$, $V(R)$ and $\xi_{k+1} = \xi(R)$. Thus in order to have a determined system we must add to the equations of motion and bore conditions two additional relations. We use the definition of the bore speed

$$\frac{d\xi(T)}{dT} = V(T), \tag{29}$$

and the bore acceleration, obtained by differentiating (24) and using (22)–(25),

$$\frac{dV(T)}{dT} = \frac{1}{4V}\left\{[VH_X - (vH)_X]\left(1 + 2\frac{H}{H_0}\right) - VH_{0X}\left(\frac{H}{H_0}\right)^2\right\}. \tag{30}$$

The equations of motion are approximated at P using *backward* T-differences and, for simplicity, X-differences centred at $\frac{1}{2}(Q+R)$ rather than at P. These implicit equations are unconditionally stable and so impose no further restriction on the time mesh. The bore conditions (24) and (25) are to be satisfied at R and the subsidiary equations (29) and (30) are centred on the bore at $\frac{1}{2}(R+R')$. The system of equations obtained in this manner is non-linear and is solved by iterations. In the form and order in which these equations are used they are:

$$\xi(R) = \xi(R') + \tfrac{1}{2}(\Delta T_k)\,[V(R) + V(R')], \tag{31}$$

$$H(R) = \tfrac{1}{2}\{\sqrt{\{H_0(R)\,[H_0(R) + 8V^2(R)]\}} - H_0(R)\}, \tag{32}$$

$$v(R) = \left(1 - \frac{H_0(R)}{H(R)}\right) V(R), \tag{33}$$

$$H(P) = H(P') - \frac{\Delta T_k}{\Delta X + (\xi(R) - X_s)}\,[v(R)\,H(R) - v(Q)\,H(Q)], \tag{34}$$

$$\begin{aligned} v(P) = v(P') &- \frac{\Delta T_k}{\Delta X + (\xi(R) - X_s)}\{\tfrac{1}{2}[v^2(R) - v^2(Q)] + [H(R) - H(Q)]\} \\ &+ \begin{cases} 0, & \xi(R) \leqslant 0, \\ \dfrac{\xi(R) - X_s}{\Delta X + (\xi(R) - X_s)}\,\Delta T_k, & \xi > 0, \quad X_s < \Delta X, \\ \Delta T_k, & X_s \geqslant \Delta X, \end{cases} \end{aligned} \tag{35}$$

$$V(R) = V(R') + \frac{\Delta T_k}{2}\,[W(R) + W(R')]. \tag{36}$$

Equations (32) and (33) are the bore conditions, equations (34) and (35) are the equations of motion and equations (31) and (36) are the difference forms of (29) and (30). Here $W(R)$ and $W(R')$ are the lengthy but obvious difference forms of the right side of (30). In these evaluations the appropriate X-differences must be extrapolated to R and R'. By this procedure the fitting method yields the correct uniform flow over a uniform bottom. Any other procedure seems to require special considerations in order to obtain this steady solution.

The iterations proceed from an initial estimate of $V(R)$, say $V(R) = V(R')$, in (31). With the $\xi(R)$ thus determined $H_0(R) = H_0(\xi(R))$ is computed from (21) and the quantities in (32)–(36) can then be evaluated in order. This procedure is repeated, using the latest value of $V(R)$ to start each new iteration, until the successive iterates of all quantities are sufficiently close. In actual computations it is found that the number of iterations required to satisfy a prescribed convergence criterion decreases with the mesh widths and initial bore strength, and increases as the bore gets very close to the shoreline.

When the iterations have converged the bore may have crossed one or more net points; i.e. $\xi(R) > X_{s+1}$ in figure 2*b*. If this is the case, v and H at the intermediate net points are evaluated by linear interpolation between their values at P and R. To aid in smoothing the calculation the time mesh was restricted, in addition to the Courant condition, by

$$\Delta T_k \leqslant \frac{\Delta X}{2V(R')}.$$

In this manner at least two time steps are required for the bore to traverse a mesh width and the above interpolation procedure is used at most every other time step. For all of the calculations reported here it was observed that this latter condition determined ΔT.

4. Discussion of the results

In the calculations a value is chosen for the initial ratio of the bore height to the undisturbed depth, η/h_0, and the other quantities at the bore then follow from the bore conditions. In the first calculations, the bore is started at $x = 0$ (or in some cases one or two mesh lengths to the left) with flow quantities behind the bore constant and equal to the values at the bore. The results are shown here for the cases with initial values $\eta/h_0 = 0{\cdot}25$ and $\eta/h_0 = 10$. The first case is typical of those where η/h_0 is less than the critical value 0·6262 so the height η increases and the bore speed U decreases at first; also the initial flow behind the bore is subsonic, $u_1 < c_1$. The second case is typical of strong bores with η/h_0 above both critical values so that η decreases and U increases all the way to the beach; the initial flow behind the bore is supersonic, $u_1 > c_1$.

The results for the dimensionless bore height $\eta/h_0(0) = N$ and the dimensionless bore speed $U/\sqrt{(gh_0(0))} = V$ are shown in figures 3*a* and 3*b*; V_s indicates the value at the shoreline according to the approximate formula. In these calculations, the mesh width was $\Delta X = 0{\cdot}01$. Each calculation of the flow up to the arrival of the bore at the shoreline took about 45 min on a Univac. It should be remembered that in the dimensionless variables the initial undisturbed depth $h_0(0)$ is 1, the shoreline is at $X = 1$ and the slope of the beach is 1. Any other depth $h_0(0)$,

distance x_0 or slope α (where $h_0(0) = \alpha x_0$), can be obtained from the scaling in (20), but the initial ratio of bore height to depth is fixed. In the first case, figure 3*a*, a small oscillation appears on the curve of N near $\xi = 0$. This is the effect of the truncation error introduced by the discontinuities in the derivatives at $X = 0$

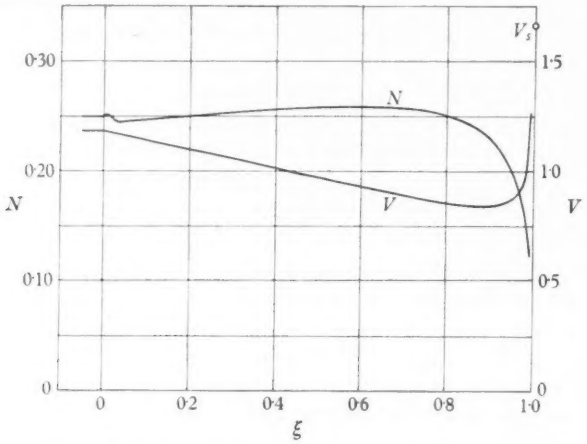

FIGURE 3*a*. Variation of the bore height N and bore velocity V in the case $N(0) = 0{\cdot}25$.

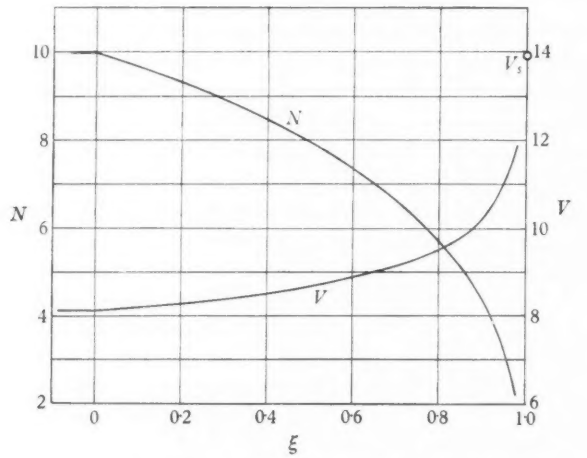

FIGURE 3*b*. Variation of the bore height N and bore velocity V in the case $N(0) = 10{\cdot}0$.

noted in § 3. Corresponding disturbances in the other quantities could not be accurately detected in the numerical results. The observed oscillation in N has a magnitude of about 2 % and is exceptionally large because of the small absolute value of N in this case. As noted in § 3 it did not seem worthwhile to modify the calculation specially to eliminate this particular inaccuracy.

There is no point in plotting the corresponding values given by the approximate formula of § 2 since they lie almost on the curves. Instead the corresponding values

are given in tables 2*a* and 2*b*. In the case $N(0) = 0{\cdot}25$, it is interesting to compare the predictions of the approximate formula for the maximum η and minimum U with the numerical calculations. They are shown in table 3. The numerical calculations can be taken with good accuracy to within a mesh width of the shoreline. In fact reasonable results are obtained at $\xi = 0{\cdot}996$. The limiting values of V at $X = 1$ may be obtained by extrapolation; this gives $V = 1{\cdot}568$, for the case $N(0) = 0{\cdot}25$ and $V = 13{\cdot}20$, for the case $N(0) = 10{\cdot}0$. Since V varies very rapidly in the last few mesh widths, we consider also an indirect method of extrapolation derived as follows:

From the characteristic relation (14), we expect $u + 2c$ to vary little over the last few mesh lengths because the variation in t is extremely small. Thus, since $c \to 0$, a convenient prediction of u at the shoreline is the value of $u + 2c$ (or its

		ξ	N	V	$\frac{N}{H_0} = \frac{\eta}{h_0}$	$\frac{V}{\sqrt{H_0}} = \frac{U}{\sqrt{(gh_0)}}$
Maximum η	Approximate formula	0·5811	0·2623	0·9457	0·6262	1·461
	Numerical calculation	0·5938	0·2587	0·9363	0·6367	1·469
Minimum U	Approximate formula	0·8863	0·2361	0·8444	2·076	2·504
	Numerical calculation	0·8835	0·2349	0·8401	2·017	2·462

TABLE 3. Comparison of critical values

extrapolation) over the last few mesh widths. As $h_0 \to 0$, u and U approach the same limiting value. The values obtained by this method for V at the shoreline are $V = 1{\cdot}681$ for the first case, and $V = 13{\cdot}99$ for the second case; the corresponding values from tables 2*a* and 2*b* are 1·659 and 13·93, respectively. In connexion with this extrapolation method it may be noted that the approximate characteristic rule also reduces approximately to $u + 2c =$ constant for strong bores.

Turning now to details of the flow behind the bore, the height N and particle velocity v are shown for typical times in figures 4*a* and 4*b*. Again the effect of the truncation error introduced by the discontinuities at $X = 0$ is noticeable in figure 4*a*. In this first case, $u_1 < c_1$ so that a reflected wave moves back into $X \leqslant 0$; in the second case, figure 4*b*, $u_1 > c_1$ so that the flow quantities in $X \leqslant 0$ remain equal to their initial values.

Figures 5*a* and 5*b* show the results of different starting conditions. The initial bore height is kept at $N(0) = 0{\cdot}25$, as for the case shown in figure 3*a*, but behind the bore two different initial distributions of N and v are chosen in place of the constant values. First N and v are taken to fall linearly in $-0{\cdot}1 \leqslant X \leqslant 0$ to $\frac{9}{10}$ of their values at the bore, and then remain constant in $X \leqslant -0{\cdot}1$; secondly, N and v fall in the same distance to $\frac{1}{2}$ their values at the bore. The results for the bore height N and bore speed V are shown as curves 2 and 3 in figures 5*a* and 5*b*, respectively, and compared with the original curves 1 of figure 3*a*. At the points where V is minimum the values of $V/\sqrt{H_0} = U/\sqrt{(gh_0)}$ are 2·462, 2·539, and 2·674, for curves 1, 2 and 3, respectively. These are reasonably close to each other and to the value 2·504 given by the approximate formula in (18). This indicates that the formula (19) still applies near the shore even though the starting conditions are not the ones assumed in that approximate theory. Of course the values of A will

be different for the three different cases shown. Curves 1 have A determined from the initial bore height according to §2. For curves 2 and 3, the approximate formula does not apply in the early stages and some other choice of A must be

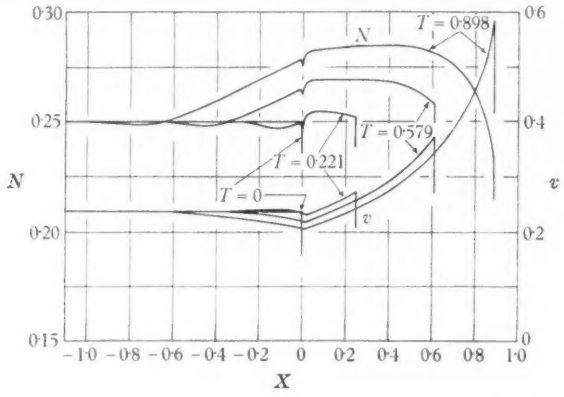

FIGURE 4*a*. The flow behind the bore: height N and particle velocity v in the case $N(0) = 0{\cdot}25$.

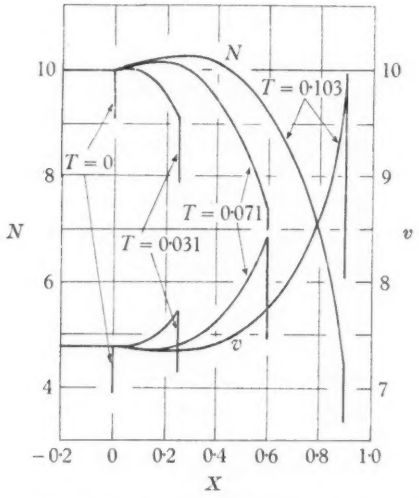

FIGURE 4*b*. The flow behind the bore: height N and particle velocity v v in the case $N(0) = 10{\cdot}0$.

made to see if the formula can describe the curves near the shore. It is convenient to choose A in each case so that the minimum of V agrees. The corresponding curves are drawn dashed in figures 5*a* and 5*b* using the values in table 1 with the appropriate choice of A, which is 0·8004 for curves 2 and 0·5325 for curves 3. These show to what extent the motion of the bore depends on the detailed initial distribution of N and V, before tending to one of the curves (19) as the shoreline is approached. It is interesting to see (figure 5*a*) that in each case the curve goes

approximately to the value in the uniform region *behind* the linear profile. This might have been expected of course. It should be remarked that these initial constant values of N and v in $X \leqslant -0{\cdot}1$ do not satisfy the bore conditions exactly; for $N = 0{\cdot}225$, the bore conditions give $v = 0{\cdot}2627$, whereas it was taken to be 0·2135; for $N = 0{\cdot}125$, the bore conditions give $v = 0{\cdot}1367$, whereas it was taken to be 0·1186.

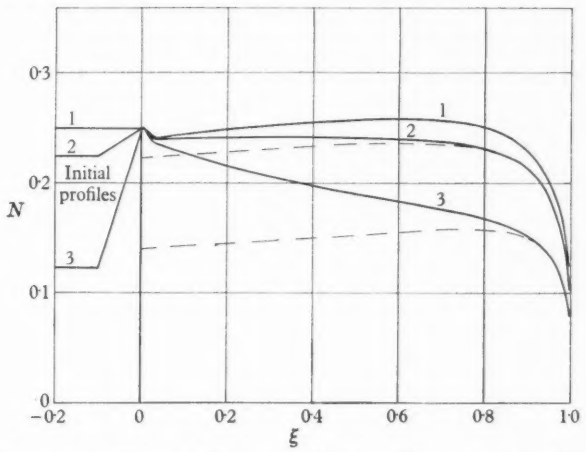

FIGURE 5*a*. Effect of different starting conditions: bore height N.

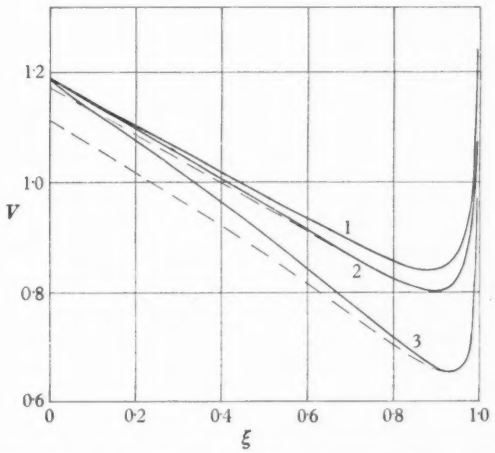

FIGURE 5*b*. Effect of different starting conditions: bore velocity V.

Finally figures 6 and 7 show on a greatly magnified scale, the oscillations due to the truncation errors at $X = 0$ for the case $N(0) = 0{\cdot}25$. These calculations were run until the bore reached $\xi = 0{\cdot}159$ for different mesh sizes and the convergence as $\Delta X \to 0$ is clearly indicated. It was observed (figure 7) that while the mesh size changed by a factor of 8 the value of N at the bore changed by only 4 %. The value $\Delta X = 0{\cdot}01$ was used for the full calculations described above.

All these calculations were performed on the A.E.C. Univac at New York University.

This research was supported by the United States Air Force under Contract No. AF 49(638)-446, monitored by the AF Office of Scientific Research of the Air Research and Development Command.

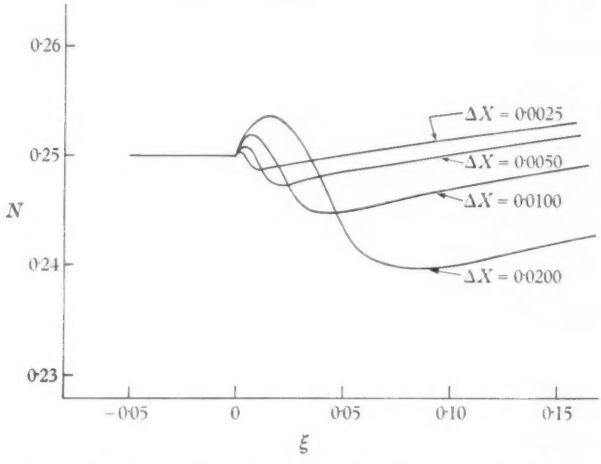

FIGURE 6. Convergence of oscillation in bore height $N(\xi)$.

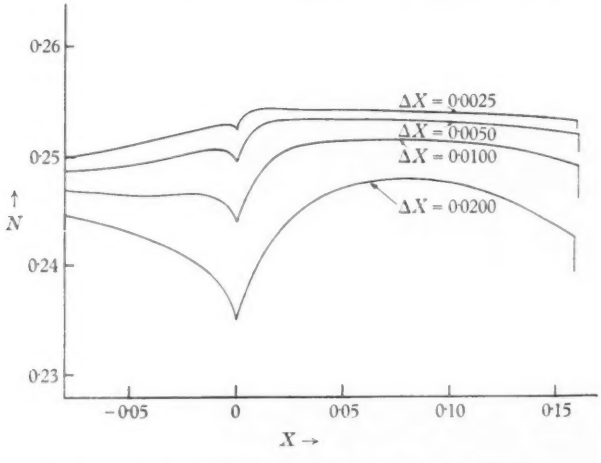

FIGURE 7. Convergence of oscillation in height $N(X, t)$.

REFERENCES

FRIEDMAN, M. P. 1959 An improved perturbation theory for shocks propagating through non-uniform regions. (To be published.)

LAX, P. D. 1954 *Commun. Pure appl. Math.* **7**, 159–93.

WHITHAM, G. B. 1958 *J. Fluid Mech.* **4**, 337–60.

REVIEWS

Applied Hydrodynamics. By H. R. VALENTINE. London: Butterworth's Scientific Publications, 1959. 272 pp. 50*s*.

In the preface the author states that the book is intended 'as an introduction to Hydrodynamics for students of Applied Mathematics and as a course in Fluid Dynamics for senior and post graduate students in Civil, Mechanical and Aeronautical Engineering'. He also states that 'the book has a bias towards practical application' and that 'particular attention has been paid to the provision of detailed physical explanations'.

Broadly speaking, it can be said that the author has written a book which is suitable for senior engineering and applied mathematics students as regards level and treatment, but there are serious omissions in the subject matter. Each aspect is taken slowly and illustrated by worked examples. From a mathematical stand-point the treatment is reasonably rigorous and the physical background is kept well in mind. References are given to further reading and there is a list of problems (with answers) at the end of each chapter. The book is limited to incompressible flow and, apart from a short chapter on the effects of viscosity, is mainly concerned with the irrotational flow of an inviscid fluid in two dimensions. It is attractively produced, being well illustrated with diagrams, and the use of headings in heavy type makes it easy to find any particular subject.

Chapter 1, headed 'The flow of an ideal fluid', introduces a variety of topics, including fluid properties, continuity, stream lines, streak lines and path lines (or filament lines), rotational and irrotational flow, the stream function and velocity potential, Laplace's equation, flow nets, Euler's equation for inviscid flow, Bernoulli's equation and its applications. The treatment of these topics is in keeping with the author's intentions and is generally satisfactory, but Kelvin's theorem (relating to the circulation in a circuit moving with the fluid) should have been proved after the derivation of Euler's equation for inviscid flow. There is only a passing reference to this important theorem in a later chapter.

Chapter 2 is entitled 'The flow of a real fluid' and deals with the effects of viscosity, with the distinction between laminar and turbulent flow, and with boundary layers. Results for velocity distributions are quoted and not derived, which is unconvincing for the student. I consider this the least satisfactory chapter in the book, largely because too little space is devoted to it, with the result that the discussion of the various themes is inadequate. For instance, in dealing with stresses in a viscous fluid there is no reference to the deformation of a fluid element and the rates of strain. A fuller discussion of the laminar and turbulent boundary-layer flows, from both theoretical and experimental aspects, would have helped this chapter very much, and the derivation of the two-dimensional equation of motion might have been given in an appendix. These modifications would require a good deal of space and it might be argued that such a treatment is outside the scope of the title of the book, but the book is

intended for engineers who have to deal with real fluids; in any case, where a problem can be treated by inviscid flow methods it is important to understand why this is so!

Chapter 3, on 'Graphical flow nets, numerical analysis and experimental analogies', is a very welcome chapter which is quite well done. There is a variety of examples of the appropriate construction of flow nets by graphical methods and a short account of the solution of Laplace's equation by numerical methods. There is a useful account of the membrane analogy and of Hele-Shaw's viscous flow analogy, but more space should have been given to the electrical analogy. This is the most useful analogy for engineers, since it is capable of yielding fairly precise quantitative information and it can be applied to a wide variety of problems.

Chapter 4 deals with the 'Standard patterns of flow'. There are both graphical and analytical treatments of the elementary flows such as source, sink, doublet, point vortex and the combinations with a uniform stream. The concept of circulation, which is introduced here for the first time in the book, would have been much better placed in the first chapter of the book.

Chapters 5 and 6 are headed 'Conformal transformation' and together occupy about one-third of the book. Chapter 5 introduces complex numbers and functions of a complex variable leading to the solution of Laplace's equation in two dimensions. There is a reasonable account of analytic functions and of singular points, but, surprisingly, nothing is said about multi-valued functions, the need to ensure a point-to-point correspondence between corresponding regions of the various planes, and the use of 'cuts' or Riemann surfaces. This I regard as a grave defect, since in my experience this is where engineering students often have difficulty. The potential functions for the elementary flows are established in this chapter, and, finally, the Joukowski transformation is used to derive the flow about a normal flat plate and the Joukowski family of aerofoils. The chapter ends with an account of the lift on a two-dimensional aerofoil. I think it is a pity that the pressure distribution round an inclined flat plate at a small angle of attack was not dealt with in detail, because this is fundamental to the understanding of flow past an aerofoil. Chapter 6 is devoted to flows involving straight boundaries. The Schwarz–Christoffel theorem is stated and its meaning is explained. It is then applied to the mapping of semi-infinite and infinite strips and a number of flows involving straight boundaries are dealt with in detail. These include sink flows in infinite and semi-infinite channels, the flow past a normal flat plate and the flow into a rectangular channel. Finally, an account is given of free streamline theory and there are examples of its application, including the flow through a slot in a plane wall, Borda's mouthpiece and flow past a normal flat plate.

The last chapter is headed 'Three-dimensional irrotational flow'. It is really devoted to axisymmetric flows, and it begins by developing the equation of continuity and the equations governing the stream function and velocity potential for cylindrical and spherical polar co-ordinates. The elementary flows are then developed and followed by their combination with the flow due to a uniform stream. Lastly, there is a short account of the numerical analysis of axisymmetric flows.

At the end of the book there are three appendices, one on the theorems of Green, Stokes, Cauchy and Blasius (to which Kelvin's theorem might have been added), one on exponential, trigonometric and hyperbolic functions (useful although hardly necessary), and one summarizing the main relations and equations governing the flow of an inviscid incompressible fluid.

In addition to the omissions I have mentioned under various chapter headings, there are two others which I regard as very important in a book at this level intended for engineers. First, I should like to have seen some account of the approximate methods which are used in aerofoil theory; for example, the development of fairings using continuous distributions of sources and sinks, and the development of camber line theory using the concept of a bound vortex sheet. Secondly, there should have been an account of vortices in three dimensions, together with their application to the theory of wings of finite span.

My conclusions are that as a text-book on applied fluid dynamics it is too narrow in the selection of subjects, particularly for mechanical and aeronautical engineering students. A number of practically important aspects of inviscid incompressible hydrodynamics have not been dealt with and the effects of viscosity merit a more detailed and comprehensive treatment. On the other hand, there are useful aspects of the subject which have been dealt with and which are not usually found in text-books. The level and treatment of the subjects selected are entirely suited to the students which the author had in mind and there is much in the book which will be of great value to them, even though it cannot be regarded as a comprehensive text-book for a course in incompressible fluid dynamics.

J. H. Preston

The Potential Theory of Unsteady Supersonic Flow. By J. W. Miles. Cambridge University Press, 1959. 220 pp. 45*s*.

This book is the eleventh in the series of Cambridge Monographs on Mechanics and Applied Mathematics (edited by G. K. Batchelor and H. Bondi) to be issued, and is in a sense complementary to the monograph by Ward on *Linearised Theory of High-Speed Flow* which was published some time ago. Whereas, however, many books have been written on high-speed steady flow, no comprehensive treatise exists on the theory of unsteady flow. For this reason this monograph will be welcomed by all who are concerned with flutter problems which require a knowledge of unsteady aerodynamic forces at supersonic speeds. It supplements the general information on unsteady flow problems included by I. E. Garrick in Section F, entitled 'Nonsteady wing characteristics', of Vol. VII of *High Speed Aerodynamics and Jet Propulsion*, by A. T. van de Vooren in an article on 'Unsteady aerofoil theory' published in Vol. V of *Advances in Applied Mechanics*, and by G. Temple in a chapter written for *Modern Developments in Fluid Dynamics: High Speed Flow*. Related information is also to be found in comprehensive treatises on aeroelasticity by R. L. Bisplinghoff, H. Ashley and R. L. Halfman and by Y. C. Fung. In addition, a recent series of papers on unsteady transonic flow theory by M. Landahl contains much valuable informa-

tion. There still remains, however, a need for a comprehensive account of unsteady subsonic theory.

The present monograph is mainly concerned with supersonic flow and only draws attention to corresponding subsonic solutions where comparison is of value in giving further information on the problem. It starts with a discussion of the basic assumptions made in the development of the linearized equations used in the theory, and the validity of various approximations are considered by extending the method of analysis used by Lin, Reissner and Tsien in their classic paper on two-dimensional non-steady motion of a slender body in a compressible fluid (*J. Math. Phys.*, 1948). Then follows a discussion of various transformations which have been used in subsonic theory and it is shown how similar methods can be used in the theory of unsteady supersonic flow. Supersonic problems are much simpler than those of subsonic flow because the effect of the wake can be neglected when the component of flow normal to the trailing edge is supersonic. In many cases exact solutions can be obtained, and four chapters are devoted to a discussion of such solutions. For many of the problems alternative solutions exist but most of those described are due to the author who has made very many important contributions in this field of research.

The chapter on slender wing methods and their application to unsteady flow problems is fairly comprehensive and is a most valuable part of the monograph. In the following chapters solutions are obtained for oscillating delta wings, low aspect ratio rectangular wings and slender non-planar bodies. The monograph concludes with a brief discussion of non-linear problems, and reverse flow theorems are discussed in the Appendix. A very extensive and useful list of references is included.

The monograph is an authoritative account of the subject and one that should be studied by all interested in unsteady supersonic flow theory.

W. P. Jones

Proceedings of the Sixth Midwestern Conference on Fluid Mechanics. The University of Texas, 1959. 465 pp. $12.50.

The above conference and the Fourth Midwestern Conference on Solid Mechanics were held simultaneously at the University of Texas in September 1959, and copies of both sets of proceedings are now available. The original typescripts and drawings submitted by authors have been reproduced photographically, which certainly makes for speed of publication although not for attractiveness of appearance. The volume on fluid mechanics contains 29 contributed papers and the text of an invited lecture by S. F. Schaaf on rarefied gas dynamics.

THE BORROWER WILL BE CHARGED AN OVERDUE FEE IF THIS BOOK IS NOT RETURNED TO THE LIBRARY ON OR BEFORE THE LAST DATE STAMPED BELOW. NON-RECEIPT OF OVERDUE NOTICES DOES NOT EXEMPT THE BORROWER FROM OVERDUE FEES.

THE QUÉRE TITRATOR

has wide applications in recording physico-chemical processes

The Quére Titrator is a precision instrument for recording titrations accurately. Equipped with an automatically variable recording table to suit the gradient of the curve, it permits the rate of advance to be reduced when the rate of change increases. Reagent flow is controlled by the table mechanism and by changing the jet of the syringe, the volume being represented by the abscissa of the graph and the state of mixture by the ordinate. The circle method determines accurately the end points of titration. *The circuits permit all kinds of potentiometric titrations and with special attachments it is possible to perform conductimetric or polarised-electrode titrations.*

- **PHOTOMETRY** The Quére strip photometer attachment is provided with filters and a vacuum type photocell giving accurate and stable readings.
- **USING A LIQUID MEDIUM** photometric attachment to this Recorder allows any photocolourimetric titration, recording photometric variations instead of equivalent points.
- **INTEGRATION** The Recorder automatically integrates the curve as it is traced. The results are entered on the axis of the ordinate of the curve by means of an electric pen marking 'tens' and 'units'.
- **RECORDING TIME FUNCTIONS** The Titrator is fitted with a zero drift correcting circuit using an automatic potentiometer. To make accurate measurements it is necessary only to check the zero periodically; the instrument itself will then introduce the necessary corrections.

Write for fully illustrated and descriptive leaflet

Tinsley

H. TINSLEY & CO. LTD.

Werndee Hall, South Norwood, London, S.E.25

Telephone: ADDiscombe 6046–8

JSP 5719

JOURNAL OF FLUID MECHANICS

Volume 7, Part 2 February 1960

CONTENTS

Behaviour of small regions of different gases carried in accelerated gas flows
by GEORGE RUDINGER and LOWELL M. SOMERS *page* 161

Taylor instability of finite surface waves
by H. W. EMMONS, C. T. CHANG and B. C. WATSON 177

Dispersion due to molecular diffusion and macroscopic mixing in flow through a network of capillaries
by P. G. SAFFMAN 194

Wave resistance to vertical motion in a stratified fluid
by F. W. G. WARREN 209

The viscosity of a suspension of spheres
by A. D. MAUDE 230

Force-momentum fields in a dual-jet flow
by DAVID R. MILLER and EDWARD W. COMINGS 237

The boundary layer near the stagnation point in hypersonic flow past a sphere
by T. K. HERRING 257

A presentation of cnoidal wave theory for practical application
by R. L. WIEGEL 273

Optimum power generation from a moving plasma
by JOSEPH L. NEURINGER 287

Motion of a bore over a sloping beach
by H. B. KELLER, D. A. LEVINE and G. B. WHITHAM 302

REVIEWS

Applied Hydrodynamics 317

The Potential Theory of Unsteady Supersonic Flow 319

Proceedings of the Sixth Midwestern Conference on Fluid Mechanics 320

Printed in Great Britain at the University Press, Cambridge
(Brooke Crutchley, University Printer)